

NORTHWESTERN UNIVERSITY

Patterning and Characterization of Reconfigurable Nanoparticle Assemblies

A DISSERTATION

SUBMITTED TO THE GRADUATE SCHOOL
IN PARTIAL FULFILLMENT OF THE REQUIREMENTS

for the degree

DOCTOR OF PHILOSOPHY

Field of Materials Science and Engineering

By

Benjamin Daniel Myers

EVANSTON, ILLINOIS

September 2018

© Copyright by Benjamin D. Myers 2018
All Rights Reserved

Abstract

The assembly of nanoscale building blocks into larger ensembles with well-defined architecture has the potential to create entirely new classes of designer photonic and plasmonic metamaterials with unique properties not found in nature. Electromagnetic metasurfaces, or 2D metamaterials, operating at optical wavelengths are of particular interest due to ease of integration with current fabrication processes for electronic and optical devices. The fabrication of metasurfaces with nanometer-scale meta-atoms has largely been limited to top-down lithographic processes. However, directed assembly approaches offer an alternative route utilizing colloidal nanoparticles as the meta-atoms, deterministically positioned by a combination of top-down lithography and bottom-up self-assembly. Nanoparticle metasurfaces have the potential for higher performance due to reduced scattering at grain boundaries by utilizing single-crystal nanoparticles. In addition, nanoparticles can be synthesized with complex 3D shapes and compositional engineering (Janus particles, core-shell structures, etc.), providing a large parameter space for metasurface design. Moreover, directed assembly provides the ability to manipulate the short-range forces that drive particle assembly to achieve reconfigurable, stimuli-responsive architectures. In tandem with new patterning and assembly strategies for reconfigurable directed assembly, the development of new tools to analyze the assembly process *in situ* is critical for constructing a detailed and mechanistic understanding of these systems.

While structural tunability has been demonstrated in metamaterials at longer wavelengths, most of these approaches fail at nanometer-length scales due to the increased surface forces and difficulty in addressing the individual meta-atoms. Similarly, self-assembly strategies can produce a range of structures with short- and long-range order, but the degree of architectural control and

ability to register these assemblies for device applications is limited. In this work, the top-down lithographic control provided by electron beam lithography (EBL) is combined with a bottom-up assembly strategy using DNA hybridization. DNA-functionalized substrates are modified by grayscale EBL patterning (DNA-EBL) to achieve local control over the surface density of the DNA to modulate interactions with complementary DNA-grafted colloidal gold nanoparticles. By this approach, the thermodynamics and kinetics of nanoparticle binding can be manipulated to achieve nanoparticle configurations that change as a function of temperature. First, the DNA-EBL process is described and characterized, demonstrating patterning of DNA density with high spatial resolution to direct nanoparticle assembly at the single-particle length scale. Second, the DNA-EBL approach is utilized to drive temperature-dependent size-selective nanoparticle assembly from a bimodal suspension of spherical gold nanoparticles. Third, this patterning strategy is extended to drive temperature-dependent ordering, alignment and positioning of both gold nanorods and spherical gold nanoparticles in 2D arrays. Finally, the ability to image these processes *in situ* is explored by the development of a liquid-cell platform based on microelectromechanical systems (MEMS) technology compatible with scanning electron microscopy (SEM), transmission electron microscopy (TEM) and correlative techniques.

Acknowledgement

My path to a doctorate has been somewhat atypical. The notion of a part-time PhD student who was also a full-time University employee was a relatively novel concept and would not have been possible without the advocacy and support of many people. In particular, I owe a huge debt of gratitude to my advisor and mentor, Professor Vinayak Dravid. He has been tireless in his support of my academic pursuits and professional development for more than 15 years. He has provided me with an enormous amount of freedom to pursue my own scientific interests, with just the right balance of encouragement and skepticism. Others in the MatSci department and graduate school also deserve acknowledgment for helping make this happen including Professor Lincoln Lauhon, Professor Kenneth Shull, Jeannine Hall and Kate Veraldi. I would like to acknowledge my PhD committee members Professor Erik Luijten, Professor Derk Joester and Professor Horacio Espinosa, who have been fantastic advisors and even collaborators on some of this work. I would also like to thank Professor Chad Mirkin and Professor Koray Aydin for their valuable insight and input on this work.

Most research does not happen in a vacuum. Well, much of mine did, but you can read about that in subsequent chapters. The point is that most research today requires a team approach and I have had the pleasure of working with a number of excellent students, staff and faculty throughout my PhD. First, I have worked closely with a number of VPD group members over the years. There are too many to mention them all, but recent students Karl Hujsak, Dr. Qingyuan Lin, Dr. Eve Hanson and Jann Grovogui have been great collaborators on this work and other recent projects. I have also had the pleasure of collaborating with students and researchers from other groups on my PhD research including Huanxin Wu, Edgar Palacios, Dr. Stas Dogel and Dr. Serkan

Butun. I would also like to thank those with whom I worked with on a number of research projects during my PhD, but unrelated to this dissertation including Dr. Blake Stevens, Dr. Lanhe Zhang, Dr. Zhiqiang Luo, Dr. Layla Jaber-Ansari and Dr. Andy Mannix. In addition, the fantastic facility staff at Northwestern are the unsung heroes of much of the work that comes out of this institution. I would like to recognize Dr. Carla Shute, Dr. Jinsong Wu, Karl Hagglund, Tirzah Abbott, Dr. Nasir Basit, John Ciraldo, Dr. Keith MacRenaris, Dr. Xinqi Chen, Jeff Sundwall and John Bussan for their contribution to this work and that of many others over the years. In addition to the technical staff, the *NUANCE* administrative team (past and present) also deserves a lot of credit including Chad Goeser, Amy Morgan, Joyce Park and Raymond Bailey.

Finally, I would like to thank my family, namely my parents Richard and Stephanie and my sister and brother, Leah and Daniel. However, the greatest thanks goes to my wife, Dorota. Our relationship began in the laboratory and we still discuss science almost daily. In addition to picking up plenty of slack during the production of this work, she has contributed scientific insight (and even some data) and has been a sounding board for many ideas throughout this process. In addition to being a great scientist, she is also a great mom. Our son, Maxwell, was born just a few months after I began this process and he is now the center of our lives. I hope to be able to spend more time with both of them now that this chapter is coming to an end.

- Ben

(April 2018)

Dedication

To my wife and son.

Table of Contents

Abstract	3
Acknowledgement	5
Dedication	7
Table of Contents	8
List of Figures	11
List of Tables	22
Chapter 1: Nanoparticle Directed Assembly and <i>In Situ</i> Characterization	23
1.1 Chapter Summary.....	23
1.2 Overview of Nanoparticle Directed Assembly Strategies.....	24
1.2.1 Capillary Force Directed Assembly.....	25
1.2.2 Electrostatic Force Directed Assembly.....	28
1.2.3 Directed Assembly through Intermolecular Forces	30
1.3 DNA Nanotechnology for Nanoparticle Assembly	31
1.4 Methods for <i>In Situ</i> Characterization of Nanoparticle Assembly	36
1.4.1 In Situ Scattering Techniques	36
1.4.2 In Situ Microscopy Techniques	38
1.5 Scope of Dissertation	40
Chapter 2: Grayscale Electron Beam Patterning of DNA for Directed Assembly.....	42
2.1 Chapter Summary and Motivation	42
2.2 Introduction	43
2.3 Results and Discussion.....	45
2.3.1 Nanoparticle Assembly on DNA-EBL Patterned Surfaces	45
2.3.2 Characterization of DNA Damage Caused by Electron Irradiation.....	48
2.3.3 Single-Particle Resolution DNA-EBL with Suspended Membranes	53
2.3.4 Electron-Scattering Monte Carlo Simulations of Energy Deposition.....	57
2.4 Summary and Outlook	60
2.5 Experimental Methods	61
2.5.1 Substrate Fabrication and Functionalization.....	61
2.5.2 Nanoparticle Functionalization and Assembly	64
2.5.3 Electron Beam Patterning	65
2.5.4 X-ray Photoelectron Spectroscopy	66

2.5.5	Fluorescence Microscopy	67
2.5.6	Spectrophotometry of Nanorod Desorption.....	67
Chapter 3:	Size-Selective Nanoparticle Assembly by DNA Density Patterning	69
3.1	Chapter Summary and Motivation.....	69
3.2	Introduction	70
3.3	Results and Discussion.....	71
3.3.1	Nanoparticle Assembly Strategy.....	71
3.3.2	Nanoparticle Adsorption Studies	73
3.3.3	Particle-Substrate Interaction Calculations.....	79
3.3.4	Molecular Dynamics Simulation Results.....	82
3.4	Summary and Outlook	84
3.5	Experimental Methods	85
3.5.1	DNA Design and Nanoparticle Functionalization	85
3.5.2	Substrate Functionalization and Nanoparticle Assembly	86
3.5.3	Electron-Beam Modification	87
3.5.4	Scanning Electron Microscopy and Image Analysis	87
3.5.5	Spectrophotometry of Nanoparticle Film Melting.....	88
3.5.6	Molecular Dynamics Simulation	89
Chapter 4:	Programmable Surfaces for Reconfigurable Nanoparticle Assembly	92
4.1	Chapter Summary and Motivation.....	92
4.2	Introduction	93
4.3	Results and Discussion.....	96
4.3.1	Temperature-Controlled Ordering in 2D Gold Nanorod Arrays	96
4.3.2	Reconfigurable Assembly of Gold Nanorods on 2D Square Grids	106
4.3.3	Reconfigurable and Size-Selective Assembly of Spherical Gold Nanoparticles..	113
4.4	Summary and Outlook	116
4.5	Experimental Methods	119
4.5.1	Substrate Fabrication, DNA Functionalization and Nanoparticle Assembly	119
4.5.2	DNA-EBL Patterning.....	119
4.5.3	Optical Microscopy and Spectroscopy	120
4.5.4	Autocorrelation Analysis	120
4.5.5	Image Processing and Analysis	122
4.5.6	Random Sequential Adsorption Simulations	123

Chapter 5: MEMS Platform for <i>In Situ</i> Characterization of Nanoparticle Assembly	124
5.1 Chapter Summary and Motivation	124
5.2 Introduction	125
5.3 Results and Discussion.....	129
5.3.1 Design of MEMS Chips and Holders	129
5.3.2 SEM Liquid Cell.....	132
5.3.3 Sparse Imaging for Dose Reduction	138
5.3.4 Nanofluidic TEM Liquid Cell.....	140
5.4 Summary and Outlook	145
5.5 Experimental Methods	146
5.5.1 MEMS Fabrication.....	146
5.5.2 Liquid-Cell SEM Imaging	149
5.5.3 Nanofluidic Liquid-Cell Imaging	150
5.5.4 Thermal Imaging.....	150
Chapter 6: Concluding Remarks.....	151
References.....	153
Appendix A.....	173
<i>Curriculum Vitae</i>	181

List of Figures

Figure 1.1 Schematic illustration of free-energy landscape for nanoparticle assembly indicating energy barriers (e.g. ΔG_1) and energy gaps (e.g. ΔG_2) between metastable or kinetically trapped states (1 and 2) and the thermodynamic equilibrium state (3). ^{3,4}	24
Figure 1.2 Illustration of a) lateral capillary forces and b) hydrodynamic drag forces acting on colloidal particles during convective assembly. ^{1,2}	26
Figure 1.3 Illustration of a) electrophoretic force (<i>FEP</i>) on charged particles and b) dielectrophoretic force (<i>FDEP</i>) due to induced dipole as a result of surface-charge patterning..	29
Figure 1.4 Schematic illustration of the various schemes for DNA-linked nanoparticle assembly involving a) direct linkage with self-complementary DNA for A-A assembly, b) direct linkage with non-self-complementary DNA for A-B assembly and the analogous structures utilizing linker DNA strands for c) A-A assembly and d) A-B assembly. Self-assembly in these systems results in the e) FCC structure for A-A assembly and BCC structure for A-B assembly.	33
Figure 1.5 Conceptual illustration of the scope of this dissertation.....	41
Figure 2.1 Schematic illustration of a) anchor DNA immobilized on substrate, b) DNA-EBL grayscale patterning of anchor DNA, c) selective hybridization of surface linker DNA on undamaged anchor DNA and d) subsequent nanoparticle assembly with surface density dependent on surface linker density.	45
Figure 2.2 Nanoparticle density patterning by dose-controlled electron beam exposure showing a) control of 140 nm edge-length gold nanoprism density (scale bar is 5 μm), b) higher magnification of patterned low-density region (scale bar is 2 μm), c) control of 30 nm spherical gold nanoparticle density from 10 $\mu\text{C}/\text{cm}^2$ (top-left) to 10,000 $\mu\text{C}/\text{cm}^2$ (bottom-right) and illustrating proximity	

effects at high dose (scale bar is 10 μm) and d) higher magnification of lower density region with contaminant particles and agglomerates in the patterned area (scale bar is 2 μm)..... 47

Figure 2.3 Fluorescence microscopy evaluation of electron beam exposure showing a) schematic illustration of the Anchor-B immobilization (top), electron irradiation of Anchor-B DNA (center) and hybridization of Linker-BCy5 DNA, b) fluorescence microscopy image with Cy5 filter to show decrease in intensity with increasing electron dose from 20 (top-left) to 10,000 $\mu\text{C}/\text{cm}^2$ (bottom-right) (scale bar is 100 μm) and c) relative intensity of the exposed regions as a function of electron dose. 50

Figure 2.4 (a) XPS data showing high resolution C 1s scans for an unmodified DNA monolayer compared to DNA exposed with doses of 1000 and 5000 $\mu\text{C}/\text{cm}^2$ showing significant change in the ratio of the C 1sA and 1sB peaks. (b) XPS data showing an exponential decay in the fitted peak-area ratio for C 1sB/C 1sA. 52

Figure 2.5 Nanorod assembly and alignment scheme using a) a series of vertical and horizontal line exposures with 2-5 lines and 10 nm pitch positioned in a rectangular grid with 100 nm (X) and 210 nm (Y) overall pitch. Images and autocorrelation (insets) for b) bulk substrate with 3 lines and 1.5 nC/cm dose, c) suspended membrane with 5 lines and 2 nC/cm dose and d) bulk substrate with 5 lines and 2 nC/cm dose. (Scale bar is 1 μm)..... 55

Figure 2.6 High resolution patterning of Au nanorods by high-dose (4333 $\mu\text{C}/\text{cm}^2$) binary patterning with 20 nm-wide landing sites showing a) 2D arrays with 200 \times 300 nm periodicity, b) split-ring design and c) twisting orientations with d-f) corresponding hard-threshold FFT-filtered images. (Scale bars are 1 μm)..... 56

Figure 2.7 Monte Carlo electron-trajectory simulation data showing 2D simulations of scattering in a) bulk substrate and b) suspended membrane structure (note different scales). Contour maps of

energy deposition in the Au layer for 3D simulation replicating lithographic conditions on c) bulk substrate and d) suspended membrane structure. Line profiles extracted from a 500 nm-wide region for energy deposition in the e) Au layer and f) carbon layer for both bulk and suspended membrane substrates..... 58

Figure 2.8 Microfabrication and functionalization of suspended silicon nitride substrates showing a) silicon wafer (gray) with 50 nm LPCVD silicon nitride (red), b) backside photolithography and RIE etching of silicon nitride, c) DRIE etching of silicon substrate, d) KOH wet etching of remaining silicon to stop on silicon nitride, e) deposition of Cr/Au (2 nm/8 nm) layers by thermal evaporation through a shadow mask and f) functionalization of gold surface with alkanethiol-modified DNA. 61

Figure 3.1 Nanorod (NR1) melting experiment showing a) UV-Vis spectra pre (25 °C) and post (70 °C) melting, indicating blue-shift and decrease in intensity of the longitudinal plasmon peak and b) melting curve, showing an inflection (melting) point at 47.5 °C. 68

Figure 3.1 Schematic illustration of size-selective assembly process. (a) Thiol coupling of surface anchor DNA to Au-coated Si substrate. (b) DNA-EBL for dose-controlled electron-beam patterning of surface anchor DNA. (c) Hybridization of surface linker strands, showing reduced coverage in electron-irradiated regions. (d) Assembly of nanoparticles with different sizes but with the same surface functionalization. Larger particles are selectively adsorbed to regions that present a lower density of sticky ends. 72

Figure 3.2 DNA-density directed assembly of small (30 nm) and large (80 nm) nanoparticles. (a) Size-selective assembly from a solution with a bimodal distribution of particles (small-to-large particle ratio of 42:1) by exposing a 5 μm square with an electron dose of 990 $\mu\text{C}/\text{cm}^2$ (assembled at 35 °C). (b) Size-selective assembly with 500-nm line patterns with an electron dose of 510

$\mu\text{C}/\text{cm}^2$ (assembled at $40\text{ }^\circ\text{C}$). (c-d) High-resolution line patterning for 1D particle chains with control over particle size distribution. These patterns were created on the same substrate by exposing lines with a pitch of 110 nm and varying the linewidth (c – 60 nm linewidth and $730\ \mu\text{C}/\text{cm}^2$, d – 80 nm linewidth and $710\ \mu\text{C}/\text{cm}^2$; both assembled at $40\text{ }^\circ\text{C}$). (Scale bars are $1\ \mu\text{m}$.)

..... 74

Figure 3.3 UV-Vis melting curves for 30 and 80 nm nanoparticle films on gold-coated quartz substrates..... 75

Figure 3.4 Temperature dependence of size-selective assembly. (a) Areal density of small and large particles as a function of electron dose showing a decrease in transition dose D_T (defined in the main text) with increasing assembly temperature. (Y-axis scales are adjusted to account for particle size and show equivalent surface coverage) (b) Selected images of nanoparticle films showing electron-dose effects on small-to-large particle ratio for assembly at $35\text{ }^\circ\text{C}$. (Scale bar is $1\ \mu\text{m}$.)..... 76

Figure 3.5 Areal density as a function of electron dose for lower-concentration and lower-ratio size-selective assembly at $35\text{ }^\circ\text{C}$ for a) $500\ \text{pM}$ 30 nm/ $100\ \text{pM}$ 80 nm and b) $500\ \text{pM}$ 30 nm/ $50\ \text{pM}$ 80 nm. 77

Figure 3.6 Effects of linker concentration on size-selective assembly with $500\ \text{pM}$ 30 nm/ $50\ \text{pM}$ 80 nm particle solutions containing a) $120\ \text{pmol}$ linker DNA and $125\ \mu\text{C}/\text{cm}^2$ electron dose, b) $370\ \text{pmol}$ linker DNA and $125\ \mu\text{C}/\text{cm}^2$ electron dose and c) linker DNA removed by centrifugation and resuspension and $425\ \mu\text{C}/\text{cm}^2$ electron dose. All particles were assembled at $35\text{ }^\circ\text{C}$. (Scale bar is $2\ \mu\text{m}$)..... 79

Figure 3.7 Illustration of geometric interaction between a “fuzzy” nanoparticle and substrate showing relevant variables in calculating the total interaction area for nanoparticle films: R is the

hydrodynamic radius of the DNA-functionalized nanoparticle, L is the fully extended length of the DNA on the substrate, d is the nanoparticle-substrate separation when bound by hybridized DNA, r is the gold nanoparticle radius and h is the overlap of the two “fuzzy” surfaces giving rise to the concept of a contact area. 80

Figure 3.8 Molecular dynamics simulation of size-selective assembly. (a) Schematic illustration of simulated particles and substrate. (b) Size dependence of nanoparticle adsorption with decreasing DNA surface density (axes adjusted for equivalent projected area). (c) Average number of bonds involved in nanoparticle immobilization and (d) retention time for adsorbed particles for small and large particles. 83

Figure 3.9 Image processing routine showing a) cropped region of interest, b) regions with contaminants edited out of analyzed area, c) image with contrast threshold and watershed filter applied and d) histogram of particle size. (Scale bars are 1 μm) 88

Figure 4.1 Schematic illustration of patterning schemes used in this work showing qualitative electron dose profiles for a) rectangular grid patterns (section 4.3.1) with transverse and longitudinal pitch (P_X and P_Y) and linewidth (L), b) square grid patterns with $P_X = P_Y$ and circle arrays with diameter (D) and $P_X = P_Y$ 95

Figure 4.2 SEM images and FFT (inset) of gold nanorods assembled on suspended silicon nitride substrates patterned by DNA-EBL. This is a representative example of assembly conditions demonstrating a large change in ordering as a function of assembly temperature with NR3 (a-d) and NR2 (e-h). The substrates were exposed with a 1000 $\mu\text{C}/\text{cm}^2$ dose to create 40 nm-wide landing sites. Assembly temperatures are 25, 32.5, 40 and 47.5 $^\circ\text{C}$ from left to right. (Scale bar is 1 μm) 98

Figure 4.3 Change in ordering parameter ($\Delta\xi$) from low-to-high temperature (25 – 47.5 °C) for a) NR2 and b) NR3 in the transverse and longitudinal directions with different landing site widths and electron doses.	99
Figure 4.4 Box plots showing nanorod orientation for a) NR2 and b) NR3 as a function of assembly temperature and electron dose for 40 nm-wide landing sites.....	100
Figure 4.5 Change in nanorod orientation ($\Delta\theta$) for a) NR2 and b) NR3 shown for different landing site widths and electron doses. As these distributions are highly skewed (see Figure 4.4 and Appendix A), the median is the most reasonable metric and mean values with error bars ($\pm\sigma$) are plotted for reference.....	101
Figure 4.6 Violin plots of nanorods on rectangular grid patterns with 40 nm-wide landing sites and 1000 $\mu\text{C}/\text{cm}^2$ electron dose showing a) bimodal distribution of NR2 nanorods at low temperature compare to b) more random orientation of the NR3 nanorods. Both converge to a skewed unimodal distribution at high temperature. (Additional violin plots for other conditions are shown in Appendix A, Figure A.7 – Figure A.10).....	102
Figure 4.7 Optical spectroscopy and imaging of assembled NR3 nanorod arrays showing reflectance as a function of polarization (transverse – P_T , longitudinal – P_L) and electron dose for a) high temperature and c) low temperature. The arrow in c) indicates an increase in the change in reflectance with temperature for lower dose patterns. The FDTD simulations results (b) show reflection, transmission and absorption for aligned nanorods and reflection data correspond well with experiment. The optical images show polarization-dependence for NR3 assembled at 40 °C with 40 nm-wide landing sites in transmission with d) P_L , e) P_T and reflection with f) P_L and g) P_T . The electron dose is varied from 500 to 2000 $\mu\text{C}/\text{cm}^2$ counter-clockwise from lower-left. (Scale bar is 30 μm).....	105

Figure 4.8 SEM images and FFT (inset) of reconfigurable assembly of Au nanorods on 2D square grids for 40 nm-wide landing sites and 1000 $\mu\text{C}/\text{cm}^2$ electron dose for NR2 (a-d) and NR3 (e-h). The assembly temperatures are 25, 32.5, 40 and 47.5 °C from left-to right (scale bar is 1 μm). Plots of nanorod orientation for the experiments in (a-h) showing the change in percentage of rods with each orientation for i) NR2 and j) NR3. 107

Figure 4.9 Results of RSA simulations for combination of nearest and next-nearest neighbor adsorption with four assembly schemes where a) orthogonal orientations are preferred and the adsorption probability for diagonal orientation is varied, b) diagonal orientations are preferred and the adsorption probability for orthogonal orientation is varied, c) horizontal orientation is preferred and adsorption probability for vertical and diagonal orientations are varied and d) adsorption at alternating column sites is preferred and the probability for adsorption at the other sites is varied with no direct change in orientation probability. Jamming limits (e-f) and particle occupancy by orientation (i-l) are shown for the corresponding adsorption schemes. 110

Figure 4.10 High-angle annular dark field (HAADF) STEM images of randomly assembled a) NR2 and b) NR3 nanorods showing differences in shape and size. Note the out-of-plane NR2 nanorods in a) identified by increased brightness, indicating larger thickness along beam direction. (Scale bars are 200 nm)..... 112

Figure 4.11 SEM images (with FFT inset) of small (30 nm) and large (80 nm) spherical gold nanoparticles assembled on circle-array patterns with both circle diameter and x/y pitch of 200 nm. This results in a temperature-dependent transformation in surface coverage with a) 25, b) 32.5, c) 40 and d) 47.5 °C. These images are processed to produce the corresponding hard-threshold FFT-filtered images shown in (e-f). (Scale bar is 1 μm) 114

Figure 4.12 SEM images (with FFT inset) of small (30 nm) and large (80 nm) spherical gold nanoparticles assembled on circle-array patterns with circle diameter of 220 nm and x/y pitch of 400 nm. This results in a temperature-dependent transformation in surface coverage with a) 25, b) 32.5, c) 40 and d) 47.5 °C. These images are processed to produce the corresponding hard-threshold FFT-filtered images shown in (e-f). (Scale bar is 1 μm) 115

Figure 4.13 Comparison of typical ACF profiles from ordered assembly (NR3, 47.5 °C, 50 nm linewidth, 1500 $\mu\text{C}/\text{cm}^2$) in the transverse direction (black) and longitudinal direction (red) with nanorod assembly on an unpatterned substrate (blue). 121

Figure 5.1 Schematic illustrations of various liquid cell approaches using silicon nitride membranes (green) including a) standard TEM liquid cell, b) SEM liquid cell and c) suspended nanochannel TEM liquid cell. (Adapted with permission from an illustration by Serkan Butun) 127

Figure 5.2 Liquid-cell MEMS chips showing a) example electrode configuration and b) bare silicon nitride window. The custom-built SEM liquid cell holder c) prior to loading, d) after loading and e) mounted on the Peltier stage in the SEM with heaters and temperature sensor. The custom-built electrical biasing TEM holder showing f) electrical connectors and g) loaded with nanofluidic TEM liquid cell. 130

Figure 5.3 Simulated backscattered electron images generated by 3D Monte Carlo image simulations for Au nanoparticles suspended in water below a) a 50 nm-thick silicon nitride membrane and b) a 50 nm-thick silicon nitride membrane with an 8 nm-thick Au layer. The particles are at different distances from the bottom surface: 100 nm (top-left), 50 nm (bottom-left), 20 nm (top-right), 10 nm (bottom-right) and on the membrane (center). Images are simulated with different incident beam energy from 5 – 30 keV. 133

Figure 5.4 Thermal microscopy of the SEM liquid cell loaded with chip and water for testing showing a) temperature reference from silicon nitride window (region 1) at 44.5 °C and aluminum liquid cell surface (region 2) at 44.3 °C and b) histogram of region 1 showing temperature uniformity within about 1 °C (at a slightly higher average temperature). 135

Figure 5.5 BSE images of prism adsorption experiments in the SEM liquid cell at approximately a) 30 min, b) 1 hour and c) 3 hours near the center of the window and d) 3 hours near the edge of the window. (Scale bar is 1 μm) 136

Figure 5.6 BSE images from SEM liquid cell prism desorption experiments at a) 27, b) 42, c) 48 and d) 60 °C. (Scale bar is 1 μm)..... 137

Figure 5.7 Sparse imaging results showing a) a fully sampled BSE image of 80 and 30 nm gold nanoparticles adsorbed on a gold-coated silicon nitride membrane; b) a sparse 30% sampled experimental image collected for reconstruction of the same sample; c) the reconstruction of the sparsely sampled image showing strong similarity and dramatically reduced background noise as compared with (a). Zoomed in image d) of the inset in (c) highlighting the noise present in most BSE images from the SEM liquid cell and e) the same inset from the reconstruction, which was experimentally collected after the fully sampled image. The highlighted region displays features that are present and observable in the sparse imaging method, that were attracted to the region when capturing fully sampled images..... 139

Figure 5.8 SEM images of fluid-filled nanochannel on bulk substrate showing a) filled (dark) and empty (light) regions of the channel, b-c) higher magnification of area indicated in (a) showing changes in the fluid distribution after imaging and d) images of nanoparticles on the surface (blue) and interior (red) distinguishable by their relative sharpness. (Scale bars are 1 μm (a-c) and 200 nm (d)) 142

Figure 5.9 Suspended nanochannel filled with colloidal gold suspension imaged by STEM in a) SE, b) BF and c) HAADF modes showing d) air bubbles formed by radiolysis of the water in the nanochannel with a focused probe and e) discrimination of surface (blue) and interior (red) particles by SE imaging. (Scale bars are 2 μm (a-d) and 1 μm (e))..... 143

Figure 5.10 COMSOL simulations of the nanofluidic TEM liquid cell with a heating trace next to a water-filled suspended nanochannel showing a) top of the chip, b) bottom of the chip, c) mesh configuration and d) temperature map resulting from Joule heating..... 144

Figure 5.11 MEMS process flow for liquid-cell chips showing a) starting wafer with low-stress silicon nitride, b) sacrificial Cr deposition, c) silicon nitride deposition, d) dry etching silicon nitride for access to nanochannel, e) electrode deposition, f) SU8 microfluidic layer deposition, g) backside etching to release silicon nitride window, h) Cr etching to release nanochannel, i) filling and sealing of microfluidic channels. (Figure adapted with permission from an illustration by Serkan Butun) 147

Figure 5.12 PECVD silicon nitride stress-control demonstrated by measurement of wafer curvature and application of Stoney's formula for different ratios of high and low frequency deposition..... 148

Figure A.1 Ordering parameter as a function of temperature for NR2 on rectangular grid patterns with electron dose of a) 500, b) 1000, c) 1500 and d) 2000 $\mu\text{C}/\text{cm}^2$ 173

Figure A.2 Ordering parameter as a function of temperature for NR3 on rectangular grid patterns with electron dose of a) 500, b) 1000, c) 1500 and d) 2000 $\mu\text{C}/\text{cm}^2$ 174

Figure A.3 Box plots of nanorod orientation on rectangular grid patterns for NR2 with 50 nm-wide landing sites..... 175

Figure A.4 Box plots of nanorod orientation on rectangular grid patterns for NR3 with 50 nm-wide landing sites.....	175
Figure A.5 Box plots of nanorod orientation on rectangular grid patterns for NR2 with 60 nm-wide landing sites.....	176
Figure A.6 Box plots of nanorod orientation on rectangular grid patterns for NR3 with 60 nm-wide landing sites.....	176
Figure A.7 Violin plots for NR2 assembly on rectangular grid patterns with electron dose of 1000 $\mu\text{C}/\text{cm}^2$ and a) 40, b) 50 and c) 60 nm-wide landing sites.....	177
Figure A.8 Violin plots for NR3 assembly on rectangular grid patterns with electron dose of 1000 $\mu\text{C}/\text{cm}^2$ and a) 40, b) 50 and c) 60 nm-wide landing sites.....	177
Figure A.9 Violin plots for NR2 assembly on rectangular grid patterns with 40 nm-wide landing sites and a) 500, b) 1000, c) 1500 and d) 2000 $\mu\text{C}/\text{cm}^2$ electron dose.	178
Figure A.10 Violin plots for NR3 assembly on rectangular grid patterns with 40 nm-wide landing sites and a) 500, b) 1000, c) 1500 and d) 2000 $\mu\text{C}/\text{cm}^2$ electron dose.	178
Figure A.11 Histograms of NR2 orientation for square grid patterns with 40 nm-wide landing sites and a) 500, b) 1000, c) 1500 and d) 2000 $\mu\text{C}/\text{cm}^2$ electron dose.....	179
Figure A.12 Histograms of NR3 orientation for square grid patterns with 40 nm-wide landing sites and a) 500, b) 1000, c) 1500 and d) 2000 $\mu\text{C}/\text{cm}^2$ electron dose.....	180

List of Tables

Table 1. List of DNA sequences and their function.....	63
Table 2. List of nanoparticles and their properties	65

Chapter 1: Nanoparticle Directed Assembly and *In Situ* Characterization

1.1 Chapter Summary

The development of nanoparticle assembly strategies has been an active area of research for the better part of two decades. Nevertheless, the ability to precisely position nanoparticles with control over particle orientation and both short- and long-range order remains a challenging task. A large number of strategies have been developed for assembling a range of different types of nanoparticles in solution as well as strategies for synthesizing nanostructures on patterned surfaces.⁵⁻⁸ However, this section will be limited to a review of approaches designed to deterministically position nanoparticles from colloidal suspensions on planar substrates.⁹⁻¹² In addition, the discussion will be largely limited to gold nanoparticle assembly, as the vast majority of such techniques have focused on gold nanoparticles due to the facile synthesis of a wide range of shapes and sizes as well as the ease of surface functionalization.¹³⁻¹⁵ The general strategy for directed assembly in this context combines top-down patterning to define the nanoparticle arrangement with bottom-up assembly to control the short-range forces that drive the immobilization process. These directed assembly processes can be categorized based on the primary forces involved in particle positioning and immobilization: capillary, electrostatic and intermolecular. The first section (1.2) will focus on a brief theoretical description of these forces and specific applications of each in the directed assembly of nanoparticles on surfaces. The second section (1.3) will describe DNA-based methods for nanoparticle assembly. The third section (1.4) will review the various approaches for *in situ* characterization of nanoparticle assembly processes.

1.2 Overview of Nanoparticle Directed Assembly Strategies

The forces acting on nanoparticles during self- and directed-assembly processes are legion and relate to particle-particle, particle-solvent and particle-surface interactions as well as potential interactions between particles and external stimuli (e.g. electric fields, magnetic fields, light). The ultimate configuration in a given assembly process results from the complex interplay between these competing forces and the resulting kinetic and thermodynamic interactions. The fundamental criterion for successful directed assembly is that the assembly forces are large enough to overcome the thermal energy ($k_B T$) of the particles. The overall architecture is then dependent on the free energy landscape of the system, which can result in metastable, kinetic or thermodynamic equilibrium structures, as illustrated in Figure 1.1. As the focus of this dissertation is reconfigurable assemblies, it is ultimately the switching between these different local and global

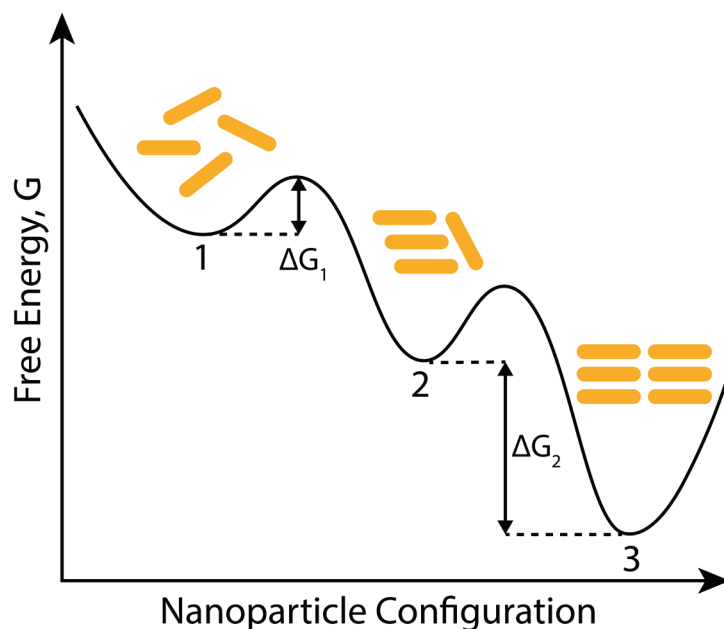


Figure 1.1 Schematic illustration of free-energy landscape for nanoparticle assembly indicating energy barriers (e.g. ΔG_1) and energy gaps (e.g. ΔG_2) between metastable or kinetically trapped states (1 and 2) and the thermodynamic equilibrium state (3).^{3,4}

energy minima that will drive the range of possible structures. In addition, it is possible to maintain dissipative non-equilibrium states provided a constant energy input.¹⁶ Such dynamic assemblies are not explicitly considered here, but there is significant potential in their application for reconfigurable assembly, which may benefit from the strategies and characterization tools developed herein.

While a large number of different forces are important for colloidal stability and can play an important role in particle assembly such as depletion/solvation forces, van der Waals forces, hydrophobic forces and steric effects, this section will be limited to those forces that dominate in terms of achieving positioning control and high yield in directed assembly. In fact, there is often a balance between positioning precision and yield, which is directly related to the balance between the substrate patterning (top-down) and the stochastic nature of nanoparticle assembly (bottom-up). This section will focus on the application of three generalized sets of forces most commonly applied for directed assembly of nanoparticles: capillary forces, electrostatic forces and intermolecular forces (chemical bonding).

1.2.1 Capillary Force Directed Assembly

Capillary forces, which can be described as the set of interactions between particles and fluid interfaces have been defined in literature and are summarized below.^{1,2} For the purposes of directed assembly on substrates, the primary capillary forces of interest are lateral capillary forces that act on particles in the presence of a liquid meniscus as illustrated in Figure 1.2a. For example, the capillary force (F_C) between two particles (with small separation distance) can be described as:

$$F_C = -\frac{2\pi\sigma Q_1 Q_2}{L} \quad r_k \ll L \ll q^{-1} \quad (1)$$

where

$$Q_i = r_i \sin \psi_i \quad (i = 1,2). \quad (2)$$

The magnitude of the force is driven by the surface tension (σ), the center-to-center distance (L), and the capillary charge (Q), which is a function of the radii (r) of the contact lines and angles (ψ) of the menisci. Depending on the menisci angles, this force can be either attractive or repulsive and hence depends on the hydrophilicity of the particle surface. These forces act within a characteristic capillary length (q^{-1}), which depends on the particular liquid-fluid interface and the liquid film thickness. This length is on the order of 2.7 mm for the water-air interface with thick films, but can be less than 1 μm for nanometer-scale liquid films.¹⁷ A similar description can be derived for the force between a particle and a fixed wall, in which the wall produces a capillary “image” charge and results in either attractive or repulsive forces depending on the wetting characteristics of the wall. In addition, most applications of capillary forces for nanoparticle assembly processes rely on evaporation-induced hydrodynamic drag forces (F_D) driven by a hydrodynamic flux (J_W) to supply particles to the thin liquid layers where capillary forces are

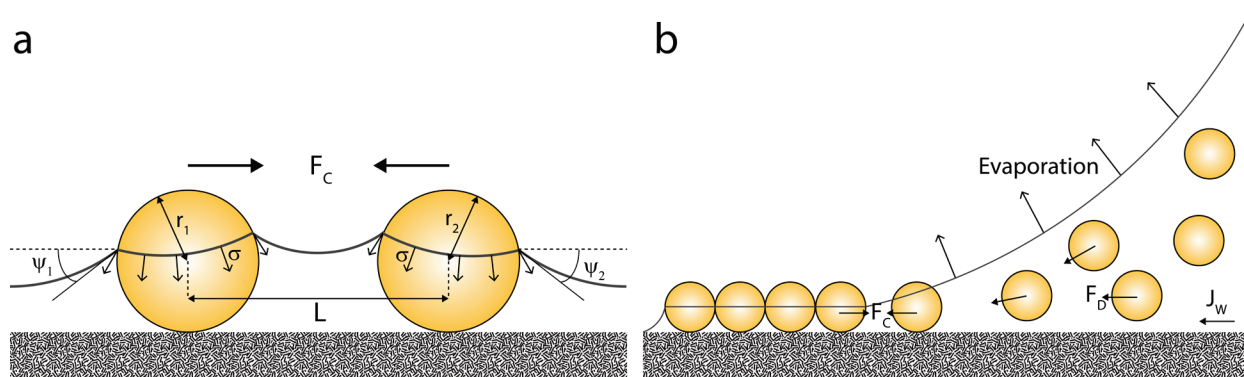


Figure 1.2 Illustration of a) lateral capillary forces and b) hydrodynamic drag forces acting on colloidal particles during convective assembly.^{1,2}

present (Figure 1.2b). In general, these capillary and convective assembly processes rely on careful engineering of the shape of the solid-liquid interfaces and the evaporation rates.

In the absence of any surface patterns, capillary forces can drive 2D and 3D crystallization of nanoparticle films. Early work on micron-size latex particles^{18,19} was later extended to gold nanoparticle assembly on unpatterned substrates.²⁰⁻²³ One application of capillary forces for nanoparticle assembly involves the use of surfaces with patterned wettability.^{24,25} These techniques typically involve the patterning of hydrophobic and hydrophilic regions on a substrate by microcontact printing and selective wetting of the hydrophilic regions by a colloidal suspension followed by controlled drying. This approach has also been extended to allow some degree of orientation control in assembly of Pd nanorods.²⁶ Another approach for directed assembly using capillary forces involves the fabrication of substrates with topographical templates, which provide local control over particle position as the liquid contact line moves across the surface. Cui, *et al.* demonstrated some of the first template-assisted assembly of nanoparticles by patterning trenches in PMMA by EBL and exploiting capillary forces during controlled solvent evaporation.²⁷ Similar techniques using different lithographic methods were subsequently developed in other groups with EUV lithography²⁸ and interference lithography.²⁹ Malaquin, *et al.* used PDMS templates along with a motorized assembly to drag the liquid meniscus across the surface to provide further control of the solvent evaporation.³⁰ This approach was successful in positioning spherical gold nanoparticles in trap structures by tuning the substrate temperature (evaporation rate), contact angle (surface energy) and particle concentration. A similar process was used to load nanoparticles onto a printing plate with patterned topographical features, which was then used to transfer the particles to plain substrates.³¹ Flauraud, *et al.* recently refined this approach by the fabrication of

surfaces with more complex “funnel traps,” which allow both high filling fractions and superb orientation control.³²

1.2.2 Electrostatic Force Directed Assembly

Electrostatic forces are attractive for nanoparticle assembly due to their long-range interactions and potential for broad application with multiple material systems. In this section, the discussion will focus on approaches that rely on patterning surface potential to drive assembly, rather than the use of external electric fields. The electrostatic assembly of nanoparticles on a charged surface is driven by a combination of dielectrophoretic and electrophoretic forces as illustrated in Figure 1.3.³³⁻³⁵ The electrophoretic force is described by

$$F_{EP} = Q_{ef}E \quad (3)$$

where the effective charge of the particles Q_{ef} is

$$Q_{ef} = 4\pi\xi\epsilon_1\epsilon_0r \quad (4)$$

where ξ is the zeta potential of the colloidal suspension, ϵ_1 is the solvent relative permittivity, ϵ_0 is the vacuum permittivity and r is the particle radius. For the dielectrophoretic case, the patterning of patches of charge on a surface present a non-uniform electric field E to particles in solution, which induces a dipole moment p . This results in a dielectrophoretic force F_{DEP} on the particles, which can be either attractive or repulsive, depending on their permittivity ϵ_2 (for dielectric particles) or conductivity σ_2 (for conductive particles) relative to the solvent (ϵ_1, σ_1). This force is described by

$$F_{DEP} = p \cdot \nabla E \quad (5)$$

where (for a homogenous spherical particle)

$$p = 4\pi r^3 \varepsilon_1 \varepsilon_0 K E . \quad (6)$$

The Clausius-Mossotti factor K defines the magnitude of the dipole moment

$$K = \frac{\varepsilon_2 - \varepsilon_1}{\varepsilon_2 + 2\varepsilon_1} , \quad (7)$$

for dielectric particles and

$$K = \frac{\sigma_2 - \sigma_1}{\sigma_2 + 2\sigma_1} , \quad (8)$$

for conductive particles. In most cases, the particle/solvent system is designed such that the dielectrophoretic force is attractive (*i.e.* $\varepsilon_2 > \varepsilon_1$ or $\sigma_2 > \sigma_1$).³⁴

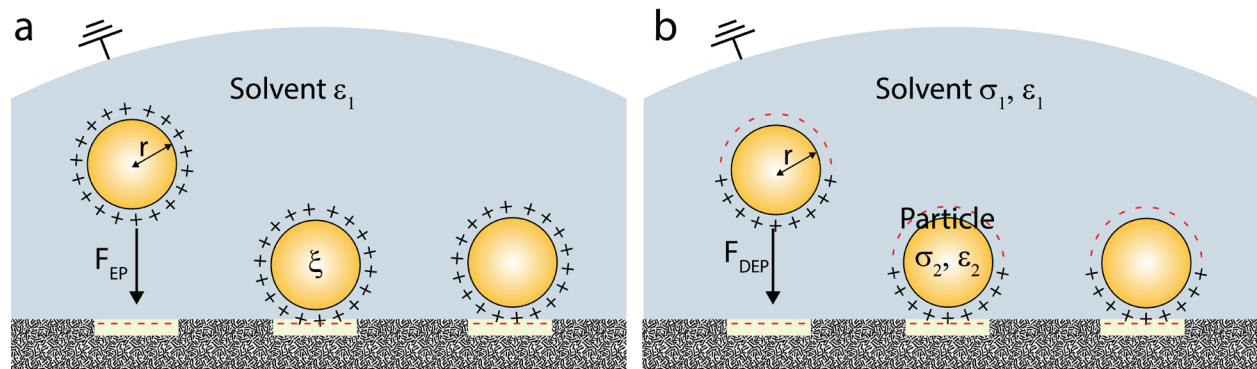


Figure 1.3 Illustration of a) electrophoretic force (F_{EP}) on charged particles and b) dielectrophoretic force (F_{DEP}) due to induced dipole as a result of surface-charge patterning.

Electrophoretic assembly of 2D lattices from colloidal gold particles was first accomplished 25 years ago.³⁶ However, site-specific patterning using these forces remains an active area of research and the means of generating high spatial-resolution surface-charge patterns is the major differentiating factor in the various approaches. Fudouzi, *et al.* used electron-beam patterning of an insulating substrate (CaTiO_3) to create persistent charged lines capable of attracting both dielectric and conductive nanoparticles with micrometer-scale fidelity.³⁴ This approach has also been extended to both electron and ion-beam exposure³⁷ and has been used to

capture DNA-functionalized gold nanoparticles with nanometer-scale resolution.^{38,39} Electron-beam exposure has also been used to selectively modify nitro groups in a SAM, converting them to amino groups that become protonated under acidic conditions, leading to electrostatic capture of gold nanoparticles.⁴⁰ Jacobs, *et al.* develop a nanoxerography technique using a flexible, electrically conductive stamp to pattern charge in a thin film of PMMA.^{41,42} Particles were then assembled on the charged patterns by direct immersion of the substrate in nanoparticle powder or in a gas or liquid-phase suspension of the particles. This process was later refined by using a nanostructured, thin silicon stamp to create sub-100 nm patterns.⁴³ AFM-based techniques have also been applied to directly pattern surface charge for directed assembly.³³ One approach takes advantage of the AFM to selectively pattern self-assembled monolayers to present positively charged amino groups, which can immobilize negatively charged gold nanoparticles.⁴⁴⁻⁴⁶ Another approach uses AFM to write charge directly into an electret structure followed by particle assembly in solution.⁴⁷⁻⁴⁹

1.2.3 Directed Assembly through Intermolecular Forces

Surface forces based on molecular interactions are attractive for nanoparticle directed assembly due to the rapid development in nanoparticle functionalization capabilities and the robust nature of these interactions. However, since chemical bonds provide short-range interactions, nanoparticle assembly using molecular forces often result in glassy, disordered configurations.⁵ This provides one of the major motivations for the use of elongated linkers, such as DNA (see section 1.3), which provide weak, polyvalent interactions which are long-range relative to the particle size.⁸ Nevertheless, chemically patterned surfaces have been widely applied for directed nanoparticle assembly *via* covalent binding, hydrogen bonding or specific biomolecular

interactions.^{50,51} For covalent binding, amide formation is the most common approach and has been applied for amino-functionalized gold nanoparticle assembly by patterning mercaptohexadecanoic acid (MHA) on a substrate by dip-pen nanolithography (DPN) or microcontact printing (μ CP).⁵² Other approaches use an amino-functionalized substrate patterned by nanoimprint lithography (NIL) and carboxylate-functionalized SiO₂ particles⁵³ or μ CP followed by heterobifunctional dithiocarbamate chemistry to immobilize gold particles.⁵⁴ Thiol chemistry has also been applied for selective nanoparticle immobilization using AFM-based patterning and dithiol linkages⁵⁵ or thiol-modification of silane monolayers on silicon.⁵⁶ Weaker interactions, such as hydrogen bonding, while less robust, have the advantage of being stimuli-responsive (*e.g.* pH) and have been applied in directed assembly using Hamilton-type receptors.^{57,58} While biomolecular interactions can also be exploited including biotin-streptavidin⁵⁹ and antibody-antigen, with the exception of DNA, most of these interactions have been limited to unpatterned thin-film, 3D-templated assembly (*e.g.* on viruses or proteins), or solution-based assembly/aggregation.⁶⁰⁻⁶²

1.3 DNA Nanotechnology for Nanoparticle Assembly

One of the most remarkable developments in nanoscience over the past two decades has been the development of DNA nanotechnology, which utilizes the programmable interactions of synthetic oligonucleotides to build and assemble complex nanostructures.⁶³⁻⁶⁶ The structure of the DNA molecule, which forms the basis for all life, can be engineered to produce highly specific, tunable and reversible linkages through Watson-Crick base-pairing interactions. The field can be divided into two subfields: 1) structural DNA nanotechnology, which takes advantage of these specific interactions to build complex 2D and 3D architectures based on tiling or folding of DNA

and 2) assembly of nanoparticles with densely grafted DNA containing complementary sequences, called programmable atom equivalents. In the structural DNA nanotechnology approach, rigidity and structure are derived from the specific DNA sequences, which produce double-stranded regions with multiple crossovers. The DNA folding (“origami”) approach uses a single large DNA strand, which is folded into a predetermined shape with the use of staple strands.⁶⁷ This approach has been utilized for directed assembly of gold nanoparticles by first assembling DNA origami triangles on patterned hydrophilic regions of a substrate. The corners of the DNA triangles were modified to present A₈ or A₃₀ single-stranded DNA (ss-DNA) sequences, which could bind to gold nanoparticles with complementary T₈ or T₃₀ grafted oligonucleotides.⁶⁸ In comparison, the tiling approach can produce large-area periodic structures from a small number of different DNA building blocks.⁶⁹ Such 2D self-assembled DNA arrays have also been fabricated to present short sequences of ss-DNA to immobilize nanoparticles grafted with a complementary sequence into periodic arrays.^{70,71}

In comparison, nanoparticle assembly using grafted oligonucleotides has a number of advantages for 2D and 3D assembly as the “bond” is a result of the polyvalent interactions of multiple DNA strands. These interactions preserve much of the specificity, tunability and reversibility from native DNA interactions, but demonstrate distinct and rich thermodynamics. Much of the literature on DNA-nanoparticle assembly is related to solution-based assembly of 3D structures and two such approaches are described in Figure 1.4 (one of the nanoparticles can be replaced with a substrate for 2D assembly). In general, the DNA binding occurs either directly between the grafted DNA strands or by using one or more “linker” strands. The relevant general results of the 3D assembly work as well as strategies for assembling nanoparticles into 2D arrays

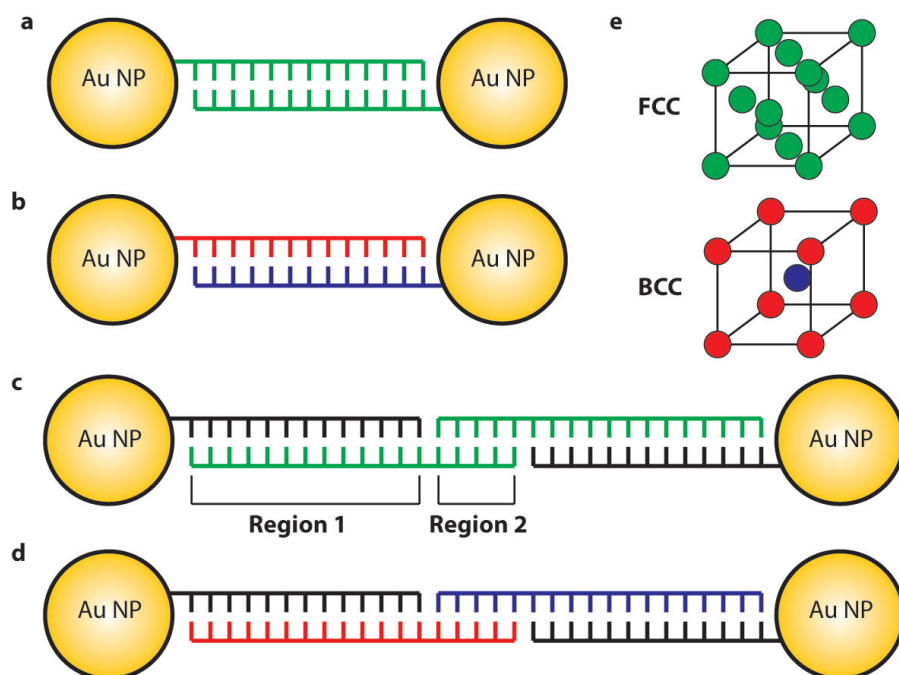


Figure 1.4 Schematic illustration of the various schemes for DNA-linked nanoparticle assembly involving a) direct linkage with self-complementary DNA for A-A assembly, b) direct linkage with non-self-complementary DNA for A-B assembly and the analogous structures utilizing linker DNA strands for c) A-A assembly and d) A-B assembly. Self-assembly in these systems results in the e) FCC structure for A-A assembly and BCC structure for A-B assembly.

are summarized in this section. First, to assemble structures from DNA-functionalized nanoparticles it is necessary to achieve sufficiently high grafting density to minimize nonspecific interactions and improve binding kinetics. Gold nanoparticles are functionalized by reaction with an excess of thiolated DNA in buffered solutions with high salt concentration. Typically, the salt concentration is increased gradually through a salt aging process and the high salt concentration screens the negative charge on the phosphate backbone of the DNA allowing higher grafting densities.^{72,73} In addition, due to steric effects, the grafting density is dependent on the particle size⁷⁴ (radius of curvature) and can be tuned by the addition of a spacer (e.g. non-complimentary DNA or PEG).⁷⁵ Alternatives to the salt aging process using a low pH citrate buffer⁷⁶ or an oligoethylene glycol spacer⁷⁷ have also demonstrated high grafting densities.

A number of factors determine the melting (aggregation/disaggregation) properties of DNA-linked gold nanoparticle assemblies.⁷⁸ These properties have been most thoroughly evaluated for 3D assembly, but are generally relevant for 2D directed assembly as well. The collective binding due to polyvalent interactions results in a significant increase in melting temperature and a sharper melting transition compared to native DNA. This is due to both energetic effects as a larger number of base-pair interactions are participating and entropic effects as the configurational entropy of the DNA strands increases (even though their translational entropy decreases) as they are able to reversibly explore multiple binding sites.⁷⁹ The melting temperature increases with the particle size,⁷⁵ the number of base pairs^{75,80,81} and both the melting temperature and sharpness of the transition increase with DNA grafting density.⁸² In addition, with increasing salt concentration, both the melting temperature and the kinetics of aggregation increase.^{82,83} Finally, by increasing the length of the DNA strands through addition of spacers, the melting temperature also increases.^{81,83}

As a consequence of the longer-range interactions and the reversible and programmable binding, DNA-linked nanoparticles can self-assemble into a wide range of superlattice structures with control of crystal structure and habit.^{65,84-87} Monodisperse spherical colloids have been assembled into a large range of cubic structures (FCC, BCC, HCP)⁸⁶⁻⁸⁸ and, recently, a diamond cubic structure by a hybrid nanoparticle/origami assembly strategy.⁸⁹ By changing the size of the nanoparticles, the hydrodynamic radius (by varying DNA length) and/or the complementarity (AB vs. AA interactions), a large number of binary crystal structures can be produced (*e.g.* isostructural with CsCl, AlB₂, Cr₃Si and Cs₆C₆₀).⁸⁶ The range of structures and properties can be further expanded by the use of anisotropic nanoparticles.⁷ Here, the structures depend not only on size but

also on the particle shape, which controls packing density and the curvature, which controls the number of DNA interactions between particles.^{85,90-92} Due to the reversibility and programmability of the DNA interactions, reconfigurable systems have been constructed that enable switchable lattice parameters, which can provide tunable plasmonic properties.⁹³⁻⁹⁶

Various strategies for DNA-directed nanoparticle assembly in 2D have also been developed using patterned planar surfaces grafted with complementary DNA. Early work by Hartmann, *et al.* used UV photolithography to selectively damage DNA in a manner conceptually similar to the electron-beam exposure method described in Chapter 2.⁹⁷ Similarly, micrometer-scale gold patterns were used to selectively adsorb DNA-functionalized nanoparticles by Kannan, *et al.*⁹⁸ Surface patterning has been used to direct surface-driven assembly of superlattices by selective immobilization of a bi-functional linker.⁹⁹ To control assembly at the individual nanoparticle level, EBL has been used to pattern gold “landing sites,” which can then be functionalized with DNA and enable site-specific adsorption.¹⁰⁰ This approach has been extended to promote the growth of superlattice structures epitaxially from 2D pre-patterned arrays.¹⁰¹ One of the challenges in assembling 2D arrays of arbitrary geometry with this approach is the competition between high pattern fidelity in the assembled array and high occupancy of surface sites.¹⁰² In general, smaller landing sites and higher immobilization temperatures increase pattern fidelity, but both of these also decrease occupancy. This has been addressed to some degree by creating landing sites within trenches, providing better alignment of the particle with the landing site.¹⁰³ This approach allows high enough precision to exploit plasmonic lattice modes and exhibits tunable optical absorption by changing solvent polarity, which controls the particle-particle separation.¹⁰⁴ A similar approach uses tunable plasmonic coupling between DNA-functionalized

colloidal nanorods and EBL-patterned nanorods to achieve electromagnetically-induced transparency.¹⁰⁵

1.4 Methods for *In Situ* Characterization of Nanoparticle Assembly

The development of a mechanistic understanding of nanoparticle assembly requires the development of tools for the direct visualization and analysis of the assembly process *in situ*. This is particularly critical for reconfigurable assembly where one is interested in switching between different equilibrium configurations in addition to metastable and kinetically trapped configurations. In addition to optical techniques such as spectrophotometry, which provide ensemble information, tools are needed to probe structural changes at the single-particle level. These can be divided into techniques that provide structural information based on scattering (x-ray, neutron) through reciprocal-space analysis and microscopic techniques (electron, scanning probe) that provide real-space information. In general, these approaches are complimentary, probing different interactions with different spatial and temporal resolution and correlative techniques are key to building a complete understanding of a given system.¹⁰⁶

1.4.1 *In Situ* Scattering Techniques

X-ray scattering techniques are among the most widely applied and useful methods for *in situ* characterization of nanoparticle assembly processes. Synchrotron-based x-ray transmission and reflectance measurements using small-angle x-ray scattering (SAXS) and wide-angle x-ray scattering (WAXS) have been widely applied in this area.¹⁰⁷ SAXS provides information about the average nanoparticle size and shape (form factor) as well as the positional correlation of particle assemblies (structure factor). SAXS analysis can be used to determine a nanoparticle superlattice crystal structure (unit cell) in a manner similar to atomic x-ray diffraction.^{87,88} This technique can

also be extended to evaluate the crystal quality (grain size and microstrain) as a function of the DNA-nanoparticle system design and assembly conditions.^{91,108} For 2D assemblies, this is typically carried out with grazing-incidence (GISAXS or GIWAXS) and can provide information about the nanoparticle-substrate distance as well as in-plane and out-of-plane ordering. For example, this approach has been used to characterize the dehydration and rehydration of monolayer and multilayer superlattice DNA-linked nanoparticle films.¹⁰⁹ GIWAXS can provide complementary information about orientational ordering within the lattice.¹¹⁰ Small-angle neutron scattering (SANS) often provides complementary information to SAXS as well. For example, SAXS can be used to probe the average nanoparticle size while SANS provides the size of the nanoparticle and a surrounding surfactant layer.¹¹¹

In situ x-ray scattering techniques can provide information about the dynamics of nanoparticle assembly and response of assembled structures to various stimuli. Synchrotron sources provide high flux, enabling time-resolved studies with temporal resolution at the picosecond time-scale and can be coupled to a range of different spectroscopic techniques (Raman, UV-Vis, mass spectrometry, etc.).¹⁰⁷ Experimental setups have been designed for *in situ* fluidic studies of nanoparticle synthesis by simultaneous SAXS/WAXS.¹¹² Vapor-pressure controlled cells have been built specifically for the *in situ* study of solvent-mediated assembly on surfaces.¹¹³ Similar systems have been used for the *in situ* study of convective assembly^{114,115} and structural evolution^{116,117} in 2D nanoparticle films upon drying. Similar fluidic cells have been built for SANS experiments enabling the study of dielectrophoretic ordering in polystyrene nanoparticles.¹¹⁸ However, *in situ* evaluation of DNA-nanoparticle assembly will require the development of temperature-controlled fluidic stages that retain appropriate assembly conditions.

In comparison to solution-based or convective-assembly processes, characterization of 2D assembly in solution poses additional challenges as the substrate must be exposed to the x-ray source in grazing incidence while maintaining complete fluid immersion, which may require the use of MEMS-based stages similar to those described in Chapter 5. In addition, *in situ* experiments must be carefully designed to minimize beam damage to the DNA during long-term exposure to the high flux x-ray source.^{119,120}

1.4.2 *In Situ Microscopy Techniques*

While x-ray scattering techniques provide structural information in reciprocal space through diffraction techniques, real-space analysis by microscopic techniques can provide complementary information. In general, x-ray scattering techniques probe larger sample volumes, providing superior statistics, but cannot evaluate samples at the individual-particle level. Microscopic image techniques (electron, scanning probe, super-resolution optical) can provide high spatial resolution analysis in real-space with a range of imaging modalities and complementary spectroscopic information. Scanning probe microscopy (SPM) with fluidic cells provides one of the more direct routes to imaging nanoparticle assembly on substrates *in situ*. This technique has been used to probe gold nanoparticle adsorption^{121,122} and pH-induced changes in self-assembled alkanethiol-functionalized gold nanoparticle films.¹²³ Fluidic-cell AFM has also been used for the visualization of gold nanoparticle “cargo” moved by a DNA walker on a DNA origami assembly line.¹²⁴ However, such *in situ* SPM techniques have not been widely adopted as they suffer from limited temporal resolution (typically seconds to minutes)^{125,126} and strong interactions between the cantilever tip and the fragile nanoparticle assemblies.¹²⁷ Recent advances in super-resolution optical microscopy¹²⁸ have attracted attention for sub-diffraction limit optical

microscopy of colloidal nanoparticle assemblies.¹²⁹ Such photoswitching-based far-field fluorescence microscopy techniques have been used to study organic core-shell nanoparticle assembly.¹³⁰ Dynamics of assembly can also be captured with high temporal resolution (milliseconds) as has been demonstrated for the convective assembly of fluorescent polystyrene nanoparticles.¹³¹ However, these techniques require the immobilization of a fluorophore on the nanoparticles and the use of high-intensity laser sources to achieve sufficient intensity for dynamic studies at high spatial resolution. These requirements are challenging for DNA-nanoparticle assembly, where the functionality is driven by the surface chemistry and the high intensity laser will cause local temperature changes due to photothermal effects.¹³²

In situ liquid-cell electron microscopy has emerged as a powerful new tool for the direct visualization of fluidic processes with high spatial and temporal resolution.^{133,134} Typically performed in the scanning transmission or transmission electron microscope (S/TEM), this technique isolates the fluidic environment from the vacuum of the microscope chamber by the use of thin electron-transparent membranes. These systems allow for fluidic mixing, heating and electrical biasing while imaging and collecting spectroscopic data at the millisecond time-scale.^{135,136} The electron microscope is particularly well suited for imaging metallic nanoparticles in a liquid environment due to the high contrast, which can enable spatial resolution even down to the atomic level.^{137,138} Nanoparticle aggregation and assembly in a number of different systems has been studied by liquid cell S/TEM.¹³⁹⁻¹⁴³ These techniques can be used to track individual particles, providing quantitative information about the assembly process not accessible by other techniques.^{138,140,144} However, in the vast majority of such *in situ* nanoparticle assembly studies, energy from the electron beam is used to trigger the assembly process. The effects of the electron

beam interactions are numerous and are outlined in more detail in Chapter 5. However, the power of correlative analysis can provide some insight into how to design experiments to account for such effects. Recently, Kim, *et al.* showed that the particle-particle distance in nanoparticle superlattices is modulated even at very low doses of $0.2\text{-}5\text{ e}^-/\text{Å}^2$ by comparing liquid cell S/TEM data with SAXS analysis.¹⁰⁶ These dose levels are well within (or below) the regime of what is considered “low-dose” electron microscopy^{145,146} and emphasize the need for adequate controls and further investigation of dose and dose-rate impact on these systems. Nevertheless, significant progress has been made designing liquid-cell systems that can mitigate some of the beam-induced artifacts. For example, radical scavengers (graphene/graphene oxide) have recently enabled the direct imaging of DNA-nanoparticle superlattices in solution for the first time.¹⁴⁷

1.5 Scope of Dissertation

The scope of this dissertation is summarized in Figure 1.5 and organized as follows: **Chapter 1** (above) describes the state-of-the-art in directed assembly of nanoparticles with a focus on the details of DNA-based nanoparticle assembly and provides an overview of strategies for *in situ* characterization tools for studying these processes. **Chapter 2** describes the grayscale DNA-EBL process that is utilized in subsequent chapters to drive nanoparticle assembly. This includes characterization of the electron-beam damage of the DNA as well as the development of high-resolution patterning on suspended membranes, which enables single-particle resolution. **Chapter 3** introduces the capability of DNA-EBL to control thermodynamics in DNA-linked nanoparticle assembly by tuning the surface density of DNA. This process drives a temperature-dependent size-selective assembly process from bimodal suspensions of spherical particles. **Chapter 4** extends the single-particle assembly work in Chapter 2 and the thermodynamic tenability described in

Chapter 3 to the reconfigurable assembly of both spherical and rod-shaped nanoparticles by creating programmable surfaces with different levels of DNA density. **Chapter 5** provides an overview of liquid cell capabilities developed for electron microscopy to enable the *in situ* observation of nanoparticle assembly and other fluidic processes.

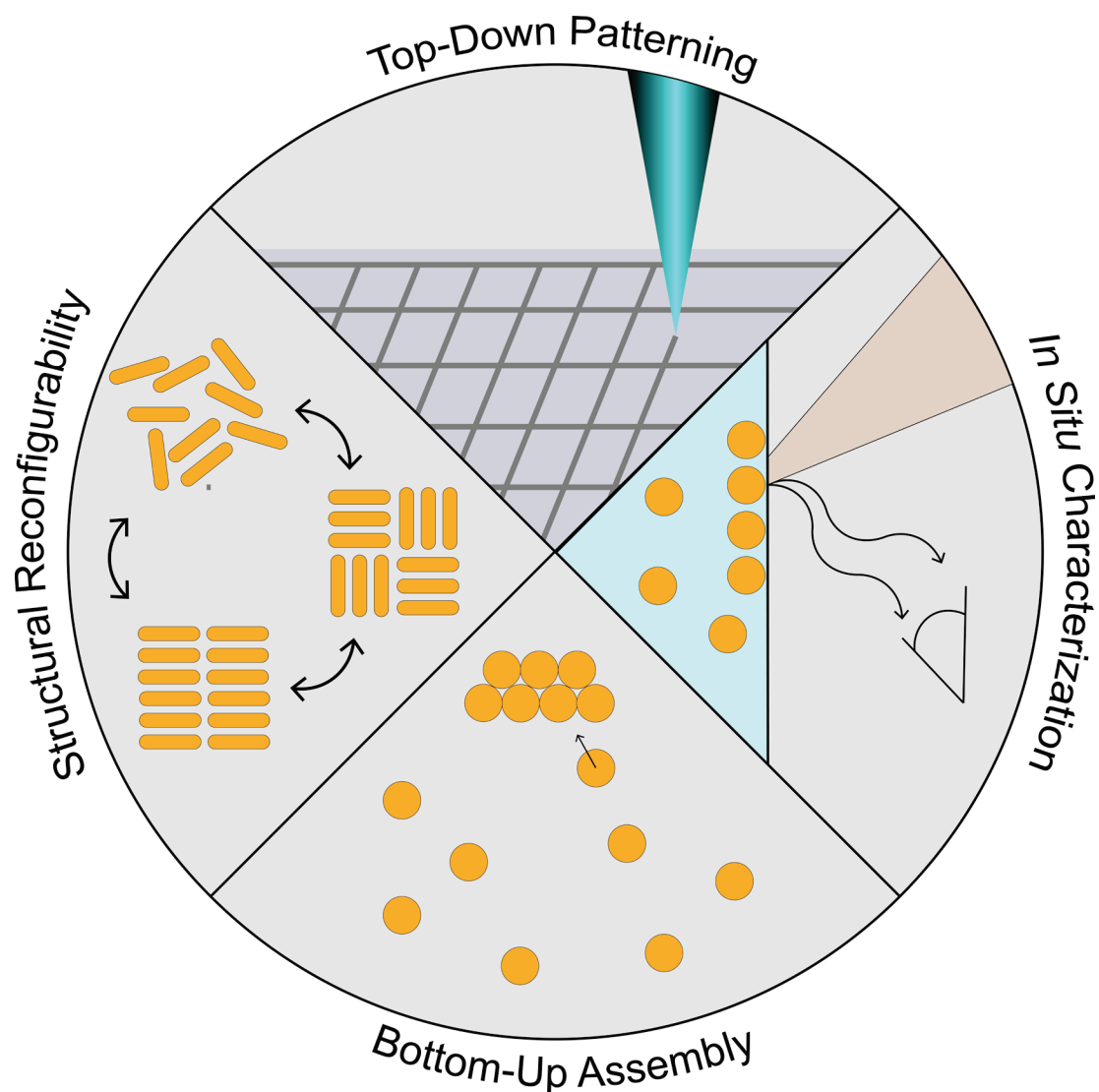


Figure 1.5 Conceptual illustration of the scope of this dissertation.

Chapter 2: Grayscale Electron Beam Patterning of DNA for Directed Assembly

Parts of this chapter are adapted with permission from: Myers, B. D., Lin, Q.-Y., Wu, H., Luijten, E., Mirkin, C. A. & Dravid, V. P. Size-Selective Nanoparticle Assembly on Substrates by DNA Density Patterning. ACS Nano 10, 5679-5686, (2016)¹⁴⁸ Copyright 2016 American Chemical Society

2.1 Chapter Summary and Motivation

High-resolution patterning techniques are critical for the effective implementation of directed assembly strategies. Direct patterning of DNA monolayers by DNA-EBL offers several unique advantages compared with other techniques. DNA-EBL provides grayscale patterning by achieving precise control over the density of active DNA strands through dose-controlled DNA damage. Fluorescence microscopy and x-ray photoelectron spectroscopy (XPS) are employed to characterize the DNA damage in this process. DNA-EBL also provides patterning resolution down to the single-nanoparticle level (< 20 nm) with the precise alignment and registry afforded by this top-down technique. High spatial resolution is achieved by patterning on suspended silicon nitride membrane substrates and Monte Carlo electron scattering simulations are employed to compare the differences in proximity effects with bulk substrates. Unlike most nanoparticle assembly strategies, which rely on topographical templates or binary chemical patterning, grayscale patterning by DNA-EBL enables manipulation of kinetic and thermodynamic interactions to drive assembly in 2D DNA-linked nanoparticle films.

2.2 Introduction

EBL has become a standard tool in the nanofabrication toolbox, allowing nanometer-scale patterning for a number of different applications. The standard implementation of EBL relies on the use of an electron-sensitive resist layer, typically a polymer. This resist layer can either be a positive or negative resist, meaning that the exposed region is removed or remains on the substrate after developing, respectively. Common positive resists include poly(methyl methacrylate) (PMMA),¹⁴⁹ ZEP520 (α -chloromethacrylate and α -methylstyrene copolymer)¹⁵⁰ and EBR-9 (poly(2,2,2-trifluoroethyl- α -chloroacrylate)),¹⁵¹ which undergo bond scission upon electron beam irradiation. Common negative resists include chemically amplified resists such as SAL601,¹⁵² epoxy-based resists such as SU-8¹⁵³ and organosilicon compounds such as hydrogen silsesquioxane (HSQ),¹⁵⁴ which undergo cross-linking reactions, either directly during exposure or during a post-exposure bake. In general, all such resist materials are either designed to either transfer patterns to an underlying substrate or template subsequent material deposition. Self-assembled monolayers (SAM) have been applied as EBL resists as well, including thiol-derived aromatic¹⁵⁵⁻¹⁵⁷ and aliphatic¹⁵⁸ SAMs, which tend to have negative and positive resist characteristics, respectively. Electron-beam patterned alkylsilane SAMs such as n-octadecyltrimethoxysilane (ODS/OTS) have been applied as silicon etch masks^{159,160} and for the subsequent immobilization of DNA in unexposed areas.^{161,162} Fluorinated silanes have also been demonstrated as self-developing electron beam resists.¹⁶³

While standard EBL processes result in binary patterns, the modification of surfaces with chemical gradients is an active area of research as such surfaces enable the ability to interrogate surface phenomena and drive surface transport.¹⁶⁴ Patterning of gradients at the microscale has

been achieved by application of inkjet,¹⁶⁵ microfluidic^{166,167} and microcontact printing¹⁶⁸ with applications ranging from cell culture¹⁶⁹ to diagnostics.¹⁷⁰ At the nanoscale, most patterning methods tend to be binary in nature and the production of chemical gradient patterns is more challenging. Scanning probe microscope based techniques such as ThermoChemical NanoLithography (TCNL) have been developed for the patterning of chemical¹⁷¹ and biochemical gradients.¹⁷² EBL is an excellent candidate for such applications due to the capability for high spatial resolution, precise dose control and rapid patterning over a relatively large field-of-view. Variable dose patterning by EBL is referred to as grayscale EBL and has typically referred to the ability to control the depth of resist exposure in polymer resists by modulating electron dose to generate 3D structures.^{173,174} Grayscale or gradient chemical patterning methods have also been developed using electron beam patterning of aminosilane¹⁷⁵ and alkanethiol¹⁷⁶⁻¹⁷⁸ SAMs, usually followed by subsequent chemical modification.

In this chapter, the details of patterning DNA monolayers by dose-controlled DNA-EBL are examined. The effects of electron dose on the DNA monolayer are analyzed by XPS as well as fluorescence microscopy. One of the primary challenges associated with patterning of organic monolayers by EBL is that of limited contrast and the associated deleterious effects of proximity dose, particularly for high-density patterns over large areas. This results in a significant reduction in pattern fidelity and reduces precision in nanoscale gradients. This limitation is overcome by patterning on microfabricated suspended silicon nitride membranes, which is compared to patterning on bulk silicon substrates and supported by Monte Carlo simulations of electron scattering in these systems. In addition, the technique will be utilized to explore the high-resolution site-specific assembly of individual gold nanoparticles functionalized with complementary DNA.

2.3 Results and Discussion

2.3.1 Nanoparticle Assembly on DNA-EBL Patterned Surfaces

To assess the impact of the electron-beam exposure of DNA-functionalized substrates on the subsequent binding of nanoparticles functionalized with complementary DNA. The general nanoparticle assembly scheme by DNA-EBL is outlined in Figure 2.1. The DNA sequences are listed in Table 1 and include four oligonucleotides: two anchor strands and two linker strands. Anchor-A and Anchor-B strands are immobilized by alkanethiol linkages on the particles and substrate, respectively. The Linker-A and Linker-B strands bind to the respective anchor strands with an 18-base complementary sequence. The linkers each present complementary 5-base sticky ends, which are responsible for immobilization of particles on the substrate. Large-area patterns

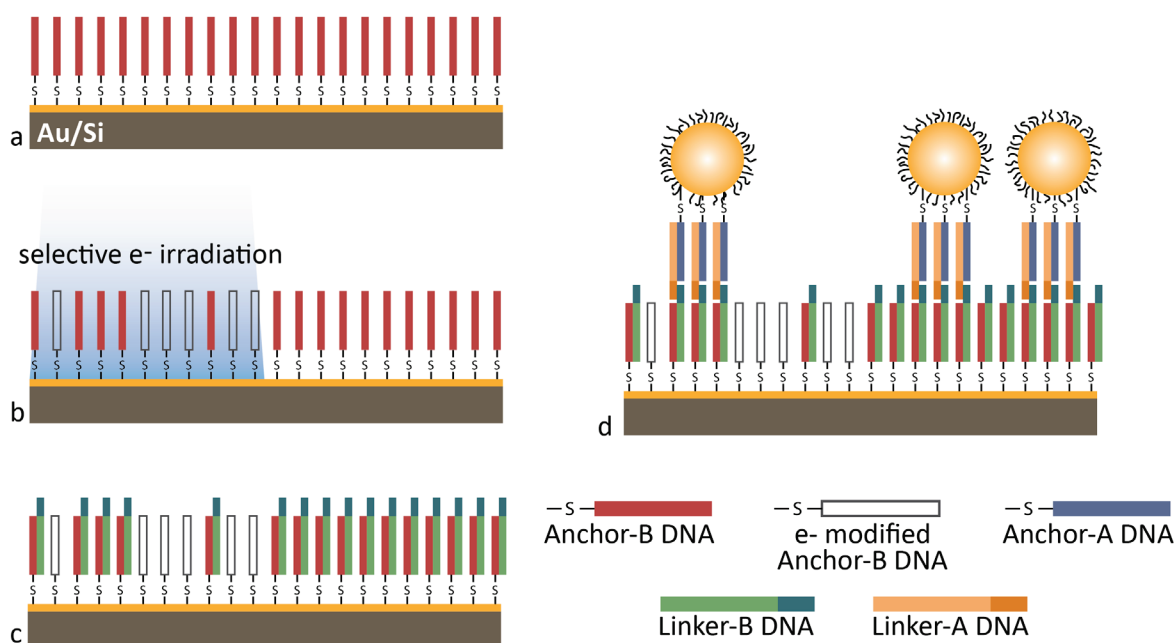


Figure 2.1 Schematic illustration of a) anchor DNA immobilized on substrate, b) DNA-EBL grayscale patterning of anchor DNA, c) selective hybridization of surface linker DNA on undamaged anchor DNA and d) subsequent nanoparticle assembly with surface density dependent on surface linker density.

were generated to produce surfaces with patches of different nanoparticle density or nanoparticle gradients. Patterned substrates were immersed in colloidal suspensions of nanoparticles functionalized with complementary DNA, which preferentially assembled in regions with higher DNA density. First, Anchor-B DNA-functionalized silicon substrates were exposed to electron doses from 10 – 10,000 $\mu\text{C}/\text{cm}^2$. These were subsequently hybridized with Linker-B DNA and immersed in a solution of Au nanoprisms (nominal 140 nm edge-length and 7 nm thickness) grafted with Anchor-A and Linker-A DNA at room temperature. Figure 2.2a shows the gradual change in nanoparticle surface density that can be achieved by grayscale DNA-EBL. A higher magnification view in Figure 2.2b shows the dense monolayer coverage in the unexposed regions. Similar effects are shown in Figure 2.2c for 30 nm spherical gold nanoparticles, similarly functionalized with complementary DNA. In general, it is more difficult to achieve zero coverage at high electron dose with the nanoprisms, presumably due to nonspecific adsorption and the very high surface area for the nanoparticle interaction. In addition to the decreasing nanoparticle density, as the electron dose is increased, there is significant rounding of the edges and corners of the nominal 5 μm square patterns due to proximity effects. Proximity effects result from scattered electrons that contribute an effective electron dose to areas near the exposed region. This can be clearly seen in Figure 2.2d, in addition to the presence of larger contaminant particles and agglomerates of the spherical particles in the exposed region. This observation is the origin for the discovery of the size-selective assembly behavior discussed in detail in Chapter 3.

The general explanation for the decrease in nanoparticle density with decreasing DNA density is due to the collective binding effects in the DNA-DNA interactions between the nanoparticles and the substrate. As previously shown for particle-particle and particle-substrate

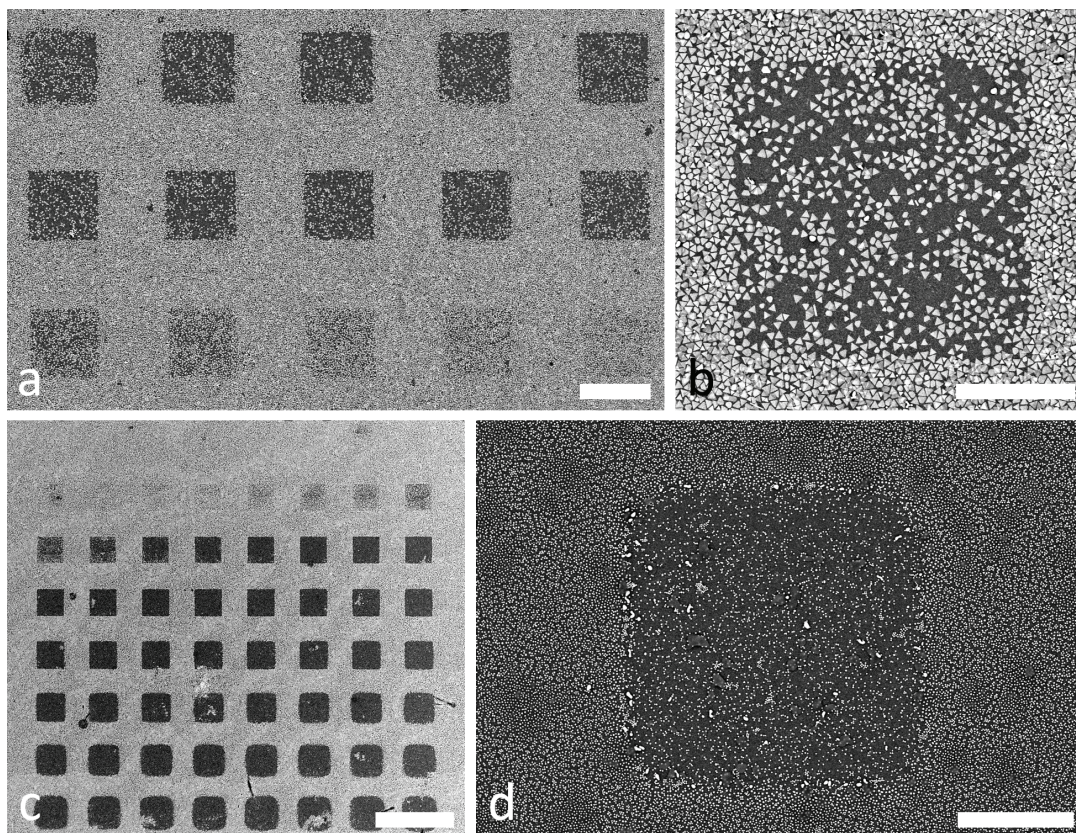


Figure 2.2 Nanoparticle density patterning by dose-controlled electron beam exposure showing a) control of 140 nm edge-length gold nanoprism density (scale bar is 5 μm), b) higher magnification of patterned low-density region (scale bar is 2 μm), c) control of 30 nm spherical gold nanoparticle density from 10 $\mu\text{C}/\text{cm}^2$ (top-left) to 10,000 $\mu\text{C}/\text{cm}^2$ (bottom-right) and illustrating proximity effects at high dose (scale bar is 10 μm) and d) higher magnification of lower density region with contaminant particles and agglomerates in the patterned area (scale bar is 2 μm).

interactions,⁸² the melting point of these systems decreases with decreasing DNA loading. This is directly due to a decrease in the binding enthalpy associated with DNA hybridization when fewer strands are participating. In general, both the enthalpy (ΔH°) and entropy (ΔS°) become more negative as additional DNA strands hybridize with the enthalpic term dominating below the melting point (T_m), resulting in adsorption/aggregation. From a statistical standpoint, this increases the desorption rate of particles in the lower density regions, leading to a decrease in the equilibrium surface coverage with increasing temperature. The different behavior of nanoprism and spherical

particles was previously studied in detail for particles with equivalent DNA coverage and calculation of the free energy (ΔG°) by measuring T_m at different particle concentrations according to the Van't Hoff equation:

$$\frac{1}{T_m} = \frac{R}{\Delta H^\circ} \ln(C) + \frac{\Delta S^\circ}{\Delta H^\circ}, \quad (9)$$

where R is the ideal gas constant and C is the nanoparticle concentration. By plotting $1/T_m$ vs. $\ln(C)$, ΔH° and ΔS° can be calculated from the slope and intercept, allowing ΔG° and the equilibrium constant (K_{eq}) to be calculated from the following:

$$\Delta G^\circ = \Delta H^\circ - T \Delta S^\circ \quad (10)$$

$$K_{eq} = e^{-\frac{\Delta G^\circ}{RT}}. \quad (11)$$

This analysis showed much larger binding constants for the anisotropic particles, presumably due to the differences in curvature resulting in a larger number of strands available for binding on the flat faces of the nanoprisms.⁹⁰ Subsequent work showed that this effect is somewhat less significant for particle-surface interactions, likely due to surface roughness or the fact that only one face of each particle is interacting with the surface.¹⁰² For future work, it would be interesting to use this approach to compare the ΔG° and K_{eq} as a function of DNA surface density. This could be possible either by large area electron exposures on transparent substrates (typical UV-Vis spot is about 4 mm²) or by using a microspectrophotometer measurement system with temperature control.

2.3.2 Characterization of DNA Damage Caused by Electron Irradiation

To control binding of nanoparticles to the substrate, the density of linkers is modulated by selectively damaging the anchor DNA strands by electron beam exposure. A series of studies were

conducted to gain a better understanding of the mechanism of DNA damage and the impact of DNA density on nanoparticle assembly. First, fluorescence microscopy was utilized to visualize the degree of linker DNA binding to the damaged anchor DNA. A 15 kV accelerating voltage was used to expose 40 μm square regions of Anchor-B DNA on a silicon substrate with doses from 20 – 10,000 $\mu\text{C}/\text{cm}^2$ in exponentially increasing dose-steps. Fluorescently-labeled Linker-BCy5 strands with sequences complementary to the Anchor-B strands were then hybridized on the exposed substrate and imaged by fluorescence microscopy as shown in the schematic illustration in Figure 2.3a. The fluorescence microscopy image in Figure 2.3b clearly shows a gradual and smooth decrease in intensity with increasing electron dose, with some decrease even at the lowest exposure dose of 20 $\mu\text{C}/\text{cm}^2$. To provide a semi-quantitative measure of the degree of hybridization as a function of electron dose, the fluorescence intensity from the exposed regions was compared to the intensity of the nearby unexposed regions. This ratio approach minimized the influence of overall intensity variations in the image and the resulting data are plotted in Figure 2.3c. These data show a bi-exponential decay in fluorescence intensity with increasing electron dose. This behavior is similar to the radiation damage of DNA in biological systems described by Target Theory and as applied to radiation damage of organic scintillator detectors.¹⁷⁹ The deviation from this behavior at low electron dose may be due to fluorescence quenching effects at high DNA density. At high electron dose (above 1,000 $\mu\text{C}/\text{cm}^2$), it is likely that the microscope camera system has an insufficient signal-to-noise ratio (SNR) to produce meaningful data. A significant decrease in fluorescence intensity was seen with an electron dose as low as 20 $\mu\text{C}/\text{cm}^2$, which corresponds to approximately 22 incident electrons per DNA strand (assuming a DNA density of 9.6 pmol/cm^2).⁷⁴ Unfortunately, there is no simple way of quantifying the DNA damage in terms of the actual linker density as a function of electron dose. Attempts were made to use fluorimetric

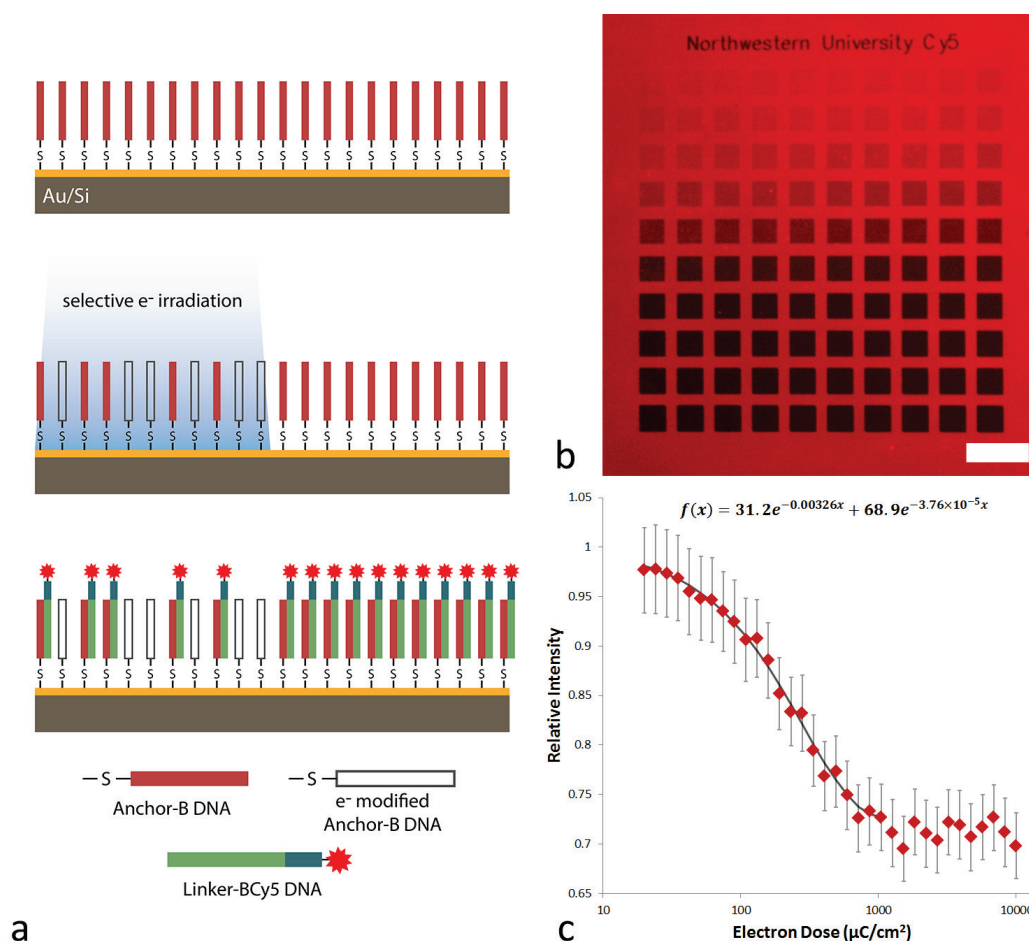


Figure 2.3 Fluorescence microscopy evaluation of electron beam exposure showing a) schematic illustration of the Anchor-B immobilization (top), electron irradiation of Anchor-B DNA (center) and hybridization of Linker-BCy5 DNA, b) fluorescence microscopy image with Cy5 filter to show decrease in intensity with increasing electron dose from 20 (top-left) to 10,000 $\mu\text{C}/\text{cm}^2$ (bottom-right) (scale bar is 100 μm) and c) relative intensity of the exposed regions as a function of electron dose.

methods⁷² to quantify the density of linkers by hybridizing fluorescent linker strands, heating above the melting point and quantifying the concentration by using a series of reference standards.

By this method, one could determine the surface density of linker strands given a well-defined surface area. However, to achieve reasonable measurements, relatively large (cm^2 -scale) substrates are required. Even electron beam exposures of mm^2 -scale regions take on the order of several hours and did not provide sufficient signal intensity for these measurements.

The fluorescence microscopy methods show that dose-controlled electron beam irradiation is able to provide a highly tunable linker strand surface density. However, these studies do not elucidate the mechanism by which linker binding is prevented. Damage to individual nucleobases in the TEM has been studied by electron energy loss spectroscopy (EELS) showing significant changes to the spectra upon electron irradiation. Notably, this work also found differences between the nucleobases with relative degree of damage following the general trend thymine > cytosine > guanine > adenine, which corresponds to the relative resonance energy per π electron.¹⁸⁰ This may indicate the possibility for engineering the degree of damage based on DNA sequence in the future. While many studies have been done to explore electron radiation damage to DNA, the vast majority investigate the damage inside cellular DNA or in some form of aqueous media.^{119,120} These studies indicate a huge number of potential molecular damage mechanisms including chain scission by single- and double-strand breaks and base damage that can be caused either by direct electron irradiation effects or by indirect effects from irradiation of the DNA environment.¹⁸¹ However, radiation damage of dry DNA under vacuum conditions has not been as thoroughly studied as the more biologically/physiologically relevant conditions. Early work showed that electron beam irradiation of dry DNA in the absence of oxygen resulted in cross-linking of double-stranded DNA (ds-DNA).^{182,183} Recently, a DNA origami approach was used to probe electron-induced DNA damage in a dry state inside a TOF-SIMS chamber and suggested damage by single-strand breaks.¹⁸⁴ Other work on low energy electron irradiation of plasmid DNA followed by gel electrophoresis shows both single- and double-strand breaks as well as crosslinking.¹⁸⁵

The same challenge of sample size exists in determining the DNA damage mechanism in this work as were present in the fluorescence measurements of active DNA surface density. It is

simply not feasible to produce a large enough sample volume of damaged DNA to probe the damage mechanism by gel electrophoresis or high performance liquid chromatography (HPLC). To examine the damage mechanism in this work more closely, XPS analysis was used to probe the damage mechanism by evaluating the changes in carbon bonding. High-resolution XPS scans of the C 1s peak were captured for DNA monolayers as a function of increasing electron dose as shown in Figure 2.4a. The C 1s scan was fitted by four peaks, which correspond well to the characteristic peaks for DNA oligomers previously identified.¹⁸⁶ These peaks are attributed to the following carbon bonding: hydrocarbon (C–H/ C–N, 284.5 eV, C 1sA), carbon/nitrogen bonding (C–N/N–C–N, 286 eV, C 1sB), amide (N–C=O, 287.5 eV, C 1sC) and urea (N–C(=O)–N, 289 eV, C 1sD). Similar to previous XPS studies on radiation damage of DNA¹⁸⁷ a significant increase in hydrocarbon bonding (C 1sA) accompanied by a decrease in the peak associated with carbon

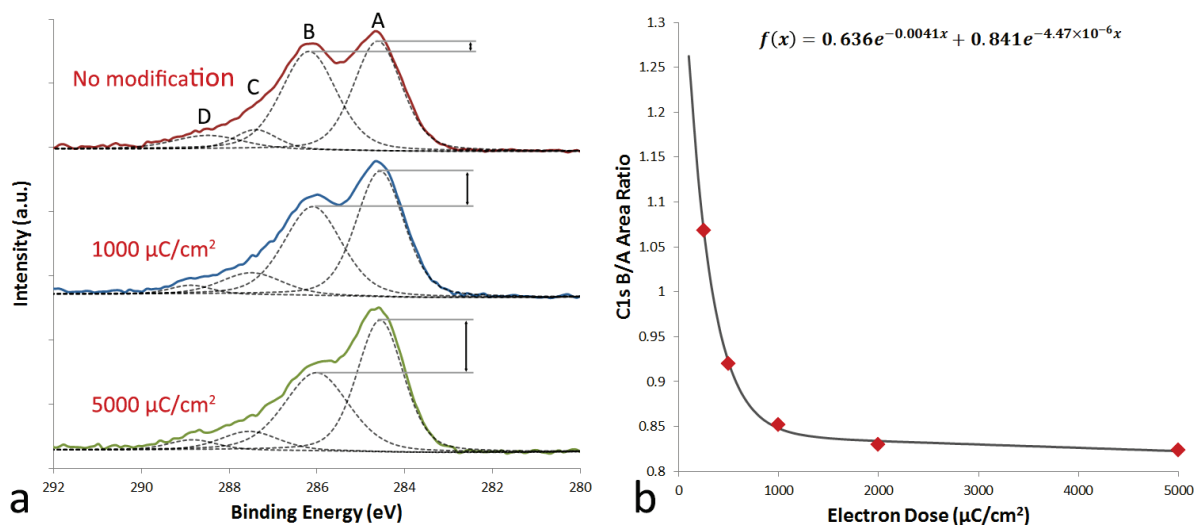


Figure 2.4 (a) XPS data showing high resolution C 1s scans for an unmodified DNA monolayer compared to DNA exposed with doses of 1000 and 5000 $\mu\text{C}/\text{cm}^2$ showing significant change in the ratio of the C 1sA and 1sB peaks. (b) XPS data showing an exponential decay in the fitted peak-area ratio for C 1sB/C 1sA.

bound to nitrogen (C 1sB) was found with increasing electron dose. This change in carbon bonding indicates a cross-linking mechanism, which is consistent with previous studies that suggest this as the dominant damage mechanism for dry DNA irradiated in the absence of oxygen.¹⁸² With increasing electron dose, an exponential decay in the C 1sB/C 1sA peak area ratio was noted (Figure 2.4b). These data, coupled with the fluorescence data, show that DNA-EBL is capable of grayscale patterning of active DNA surface density *via* direct electron-irradiation-induced damage.

2.3.3 *Single-Particle Resolution DNA-EBL with Suspended Membranes*

As evidenced by Figure 2.2c above, the effects of proximity dose on these systems can be quite significant. Given that doses as low as $20 \mu\text{C}/\text{cm}^2$ can have an effect on the density of active DNA on the surface, the patterning of dense, small features on bulk substrates is a significant challenge. In an effort to characterize this effect and establish a method for reliable high-resolution DNA patterning, suspended silicon nitride membrane samples were prepared according to the process outlined Figure 2.8 and compared to bulk substrates. In addition, Monte Carlo modeling of the energy deposition profile in these two substrates was employed to support the experimental results. The electron range (R) in a solid is dependent on the beam energy (E_0) and the sample properties and can be estimated by the Kanaya-Okayama range equation:

$$R \text{ (nm)} = 27.6 \left(\frac{A}{Z^{0.89} \rho} \right) E_0^{1.67}, \quad (12)$$

where A is the atomic mass (g/mol), Z is the atomic number and ρ is the density (g/cm^3).¹⁸⁸ For silicon with an incident beam energy of 30 keV, this results in an electron range of about $9.2 \mu\text{m}$. This, coupled with the fact that the gold top-layer has a very high secondary electron (SE) yield,¹⁸⁹ means that the DNA attached to the gold layer are subject to significant irradiation not only from

forward-scattering of the primary beam, but from backscattering and fast SE¹⁹⁰ from nearby regions.

To test these effects, optimization experiments were run on bulk substrates to attempt patterning of 2D arrays of aligned gold nanorods. Assembly temperatures were set below the melting points for the nanorod films, which were found to be above 45 °C for the nanorods used in these studies (details are in section 2.5.6 for NR1 nanorods). These patterns, shown in Figure 2.5a, were written by exposing a groups of vertical and horizontal lines with 10 nm pitch in a 2D grid with a differential X/Y pitch (X – 100 nm, Y – 210 nm) to provide a nominal 60 nm spacing between rods (NR2 in Table 2). A design of experiments (DOE) was configured to analyze ordering in these samples as a function of the number and dose of the exposed lines. The degree of ordering in these samples can be analyzed by comparison of the 2D autocorrelation function, which is described in more detail in Chapter 4. For bulk substrates, the optimum configuration was found to be three lines with a dose of 1.5 nC/cm as shown in Figure 2.5b. This resulted in an assembled structure exhibiting some degree of ordering, but additional exposure dose degraded the nanorod alignment significantly, presumably due to proximity effects. A similar DOE was conducted on suspended membrane samples, resulting in a significant improvement in the overall ordering of the nanorod assembly for an exposure with five lines and 2 nC/cm dose (more than twice the dose in Figure 2.5b) as illustrated in Figure 2.5c. The same exposure conditions on the same sample, but in a region with bulk substrate result in the disordered and low-occupancy assembly shown in Figure 2.5d.

These data highlight the dramatic differences between patterning and assembly on bulk substrates compared to suspended membranes. Further refinement was achieved by using patterns

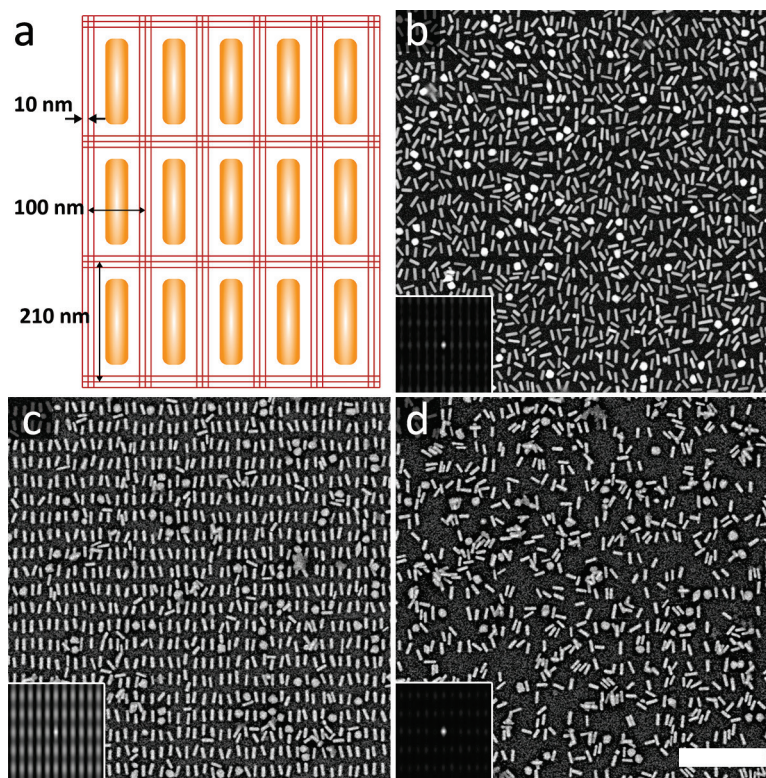


Figure 2.5 Nanorod assembly and alignment scheme using a) a series of vertical and horizontal line exposures with 2-5 lines and 10 nm pitch positioned in a rectangular grid with 100 nm (X) and 210 nm (Y) overall pitch. Images and autocorrelation (insets) for b) bulk substrate with 3 lines and 1.5 nC/cm dose, c) suspended membrane with 5 lines and 2 nC/cm dose and d) bulk substrate with 5 lines and 2 nC/cm dose. (Scale bar is 1 μm)

with finer pixel spacing (~ 3.5 nm) in a similar overlapping rectangular array. A DOE was developed around this approach to compare the linewidth and dose to optimize assembly on the suspended membranes. This resulted in the discovery that the effective contrast of the DNA patterning is much higher when patterning on the suspended membrane. This high contrast enables very high-dose patterning while retaining high spatial resolution, which minimizes the adsorption of particles between landing sites. Figure 2.6 shows the assembly of NR3 nanorods (nominally 40×125 nm) on patterns with landing site widths of only 20 nm (120 nm length) and arbitrary

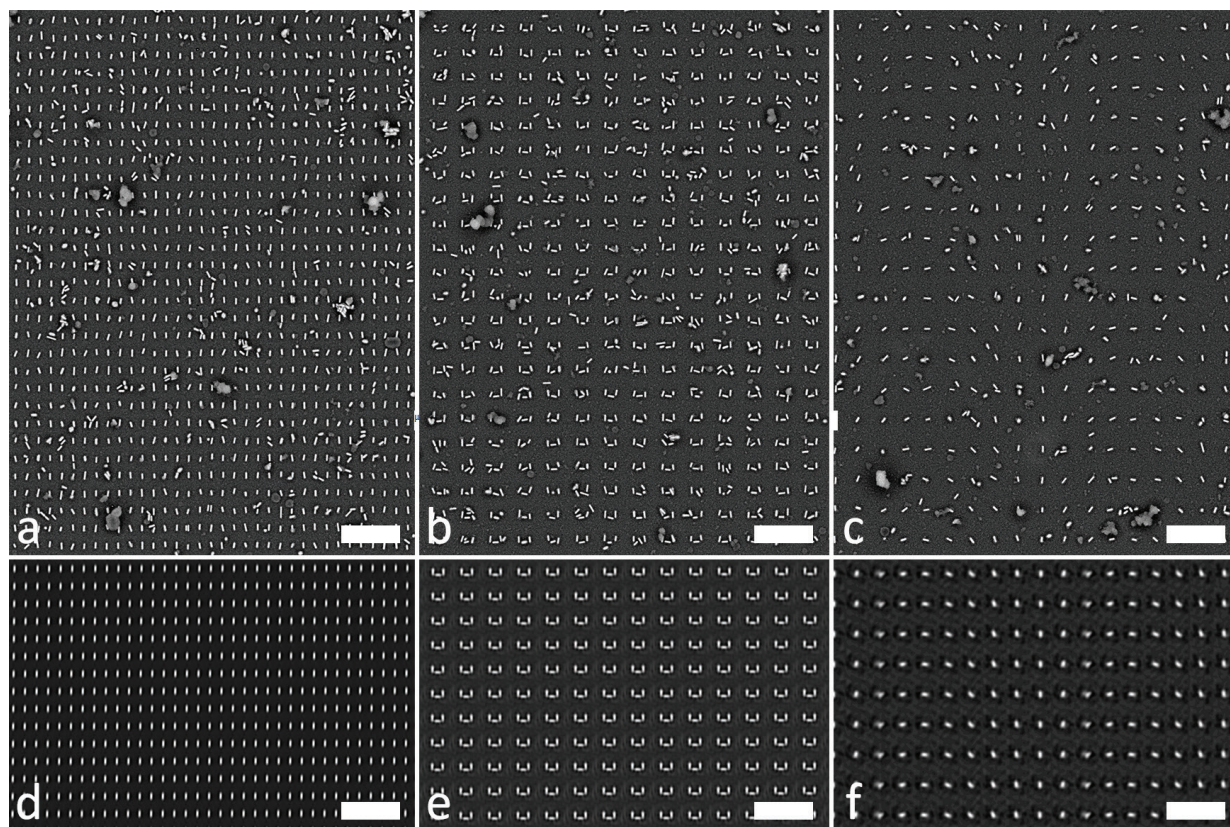


Figure 2.6 High resolution patterning of Au nanorods by high-dose ($4333 \mu\text{C}/\text{cm}^2$) binary patterning with 20 nm-wide landing sites showing a) 2D arrays with $200 \times 300 \text{ nm}$ periodicity, b) split-ring design and c) twisting orientations with d-f) corresponding hard-threshold FFT-filtered images. (Scale bars are $1 \mu\text{m}$)

orientation. The 2D arrays (Figure 2.6a) and twisting orientation (Figure 2.6c) were patterned with large periodicity ($200 \times 300 \text{ nm}$) to avoid particles interacting with multiple sites as occurs in the split-ring patterns (Figure 2.6b). In contrast, patterns on bulk substrates reach a limit at area doses of $1000 \mu\text{C}/\text{cm}^2$ and landing sites of about 40 nm, above which pattern fidelity is lost due to proximity effects. However, pattern fidelity remains high for membrane patterning at much higher doses (over $4000 \mu\text{C}/\text{cm}^2$) and for smaller landing sites (20 nm width). The result of this is not simply improved resolution, but also a much greater degree of control over local dose gradients.

2.3.4 *Electron-Scattering Monte Carlo Simulations of Energy Deposition*

To support these experimental results, Monte Carlo simulations were used to analyze the energy deposition profile of electron scattering in both bulk and suspended membrane samples. To carry out these simulations, an electron scattering Monte Carlo package (Casino 3.3 and 2.48)¹⁹¹ was used to replicate the lithography conditions and sample composition/geometry. Monte Carlo methods have been used to simulate electron trajectories in solids for some time¹⁹² and the three-dimensional (3D) implementation has been applied to study proximity effects in PMMA.¹⁹³ In general, this simulation method uses elastic scattering cross sections to track individual electron trajectories (single-scattering model). The Rutherford elastic scattering model determines the distance between scattering events and the angle of electron scattering. In the simplest implementation, the energy lost by electron due to inelastic scattering is simulated as a continuous energy loss, the rate of which is called the stopping power. By tracking the individual trajectories of electrons, the energy deposition due to the stopping power of the sample can be calculated and compared between different beam conditions, sample composition and geometry. To compare patterning on bulk substrates and suspended membranes, simulations were run in both 2D and 3D implementations.

The results of the 2D simulations are shown in Figure 2.7a for carbon (10 nm - top), gold (10 nm - middle) and chromium (2 nm - bottom) layers on bulk silicon and in Figure 2.7b for the same layers on a 50 nm silicon nitride membrane. The carbon layer is used as a proxy for DNA. The simulation for the silicon substrate shows both a larger scattering volume and more backscattered electrons (red lines), which result in proximity dose effects. For 3D simulations, a simplified version of the line patterning scheme (Figure 2.5a) was constructed as an exposure

mask. This simulation evaluated the exposure of a $5 \times 5 \mu\text{m}$ area with 60 nm wide parallel lines with a 100 nm pitch. Each line was simulated as a series of points on a 10 nm square grid with an

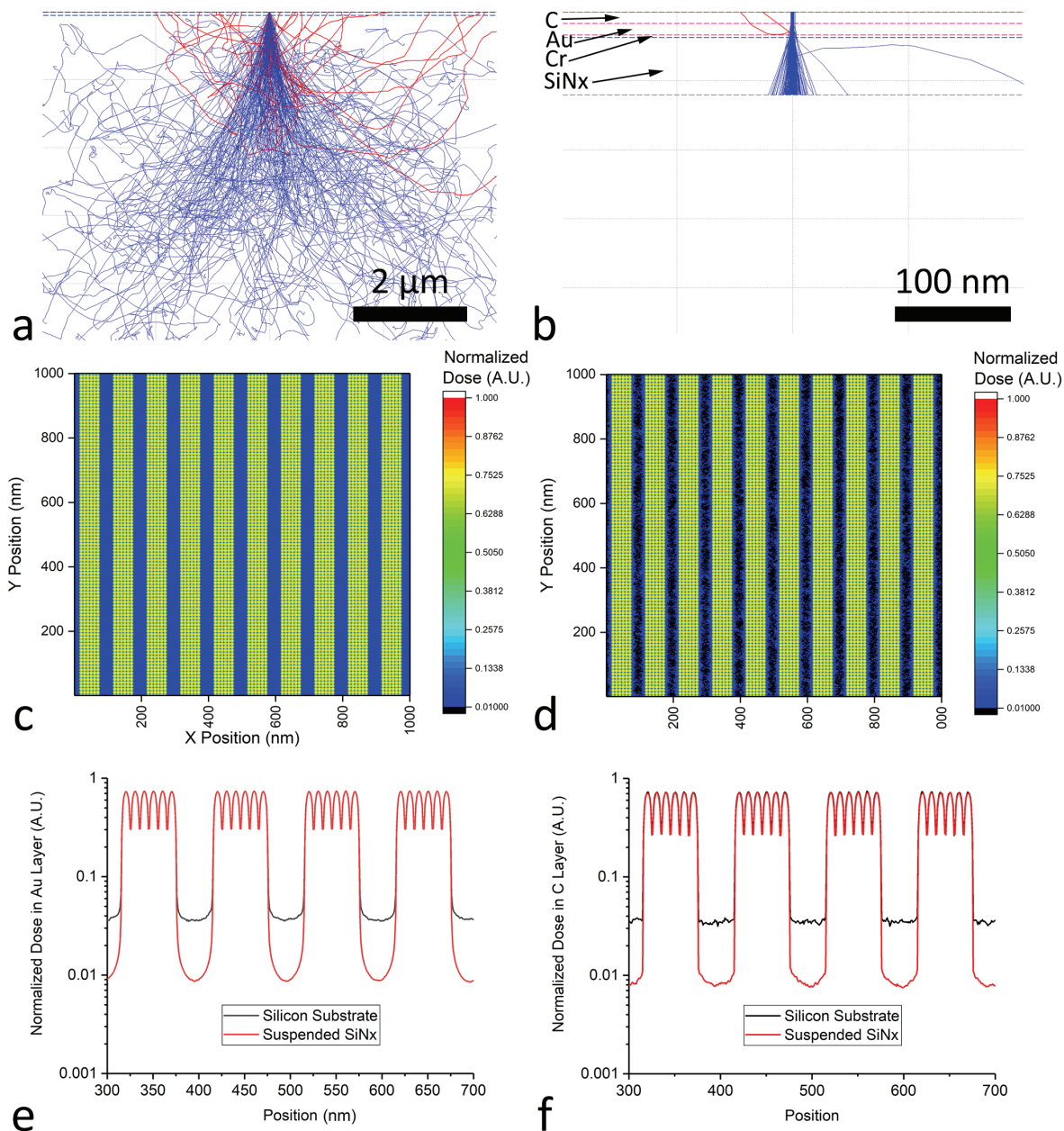


Figure 2.7 Monte Carlo electron-trajectory simulation data showing 2D simulations of scattering in a) bulk substrate and b) suspended membrane structure (note different scales). Contour maps of energy deposition in the Au layer for 3D simulation replicating lithographic conditions on c) bulk substrate and d) suspended membrane structure. Line profiles extracted from a 500 nm-wide region for energy deposition in the e) Au layer and f) carbon layer for both bulk and suspended membrane substrates.

effective beam diameter of 10 nm and a total of 12,500 electrons with 30 keV energy at each point for a dose of 2000 $\mu\text{C}/\text{cm}^2$. The energy deposition data were captured for the central $1 \times 1 \mu\text{m}$ region with 1 nm X/Y lateral resolution and 10 nm Z resolution. Contour plots of the energy deposition profile in the gold layer are shown in Figure 2.7c for bulk silicon and Figure 2.7d for the suspended membrane. These data are normalized to the maximum energy deposition to effectively compare relative dose in the two cases. Given that the majority of the damage to the DNA is likely caused by SE with relatively low energy ($< 100 \text{ eV}$),¹²⁰ the energy deposited in the gold layer is the best proxy for DNA damage as gold has a high secondary electron yield.¹⁸⁹ Normalized energy deposition profiles in both the gold and carbon layers are shown in Figure 2.7d and Figure 2.7e, respectively, for both substrate types. The gold profiles have more significant tails than carbon due to forward scattering in the gold layer, while the carbon profiles have more noise due to the lower stopping power (lower total energy deposition). These data clearly show an increase in the energy deposition between the exposed lines due to electron scattering from the substrate. However, it should be noted that these simulation data only capture the effects of long-range proximity dose due backscattering and do not capture other substrate contributions, such as fast SE generation. In addition, given that the range of the primary electrons in silicon is larger than the $5 \mu\text{m}$ exposed area, the simulations also underestimate energy deposition relative to the large-area exposures (up to $100 \mu\text{m}$) used in experiments. Nevertheless, these data support the conclusion that suspended-membrane patterning results in a significant reduction in proximity effects and subsequent improvement of pattern fidelity and local dose-control for grayscale patterning.

2.4 Summary and Outlook

This chapter introduced grayscale patterning of DNA monolayers by DNA-EBL. While the exact mechanism of DNA damage is not clear, XPS analysis indicates that the electron beam likely results in cross-linking of the ss-DNA, which adversely affects the subsequent hybridization of complementary DNA strands. The amount of damage varied exponentially with electron-beam dose as confirmed by both XPS and fluorescence microscopy. Fluorescence microscopy also revealed the capability for fine control over the extent of DNA hybridization over two orders of magnitude in electron dose. Control of the surface density of active DNA strands enables the assembly of nanoparticle films with controlled density and density gradients. In addition, by patterning on suspended membranes the spatial resolution and contrast of DNA-EBL are dramatically improved. This enables patterning at the single-particle level with control over both particle position and orientation for gold nanorods.

Further work on DNA-EBL would be greatly assisted by continued research in several key areas. First, it would be useful to understand the mechanism of electron beam damage in these systems to better optimize exposure conditions and DNA engineering. One possible avenue to explore would be the use of large-area electron flood exposures followed by cleavage of the thiol linkage and gel electrophoresis on the cleaved DNA. Similarly, flood exposures of large areas in conjunction with fluorimetric measurements could be used to develop a quantitative understanding of the relationship between electron dose and the density of active DNA strands. In addition, to these large area measurements, it would be very useful to understand the *local* changes in DNA density for high-resolution patterning. While the single-particle patterning work demonstrates the ability to write features about 20 nm wide, it is not clear how the density of DNA varies locally

around these 20 nm features. A better understanding of the local DNA gradients would allow fine-tuning of exposure conditions to exploit these gradients for reconfigurable assembly. Super-resolution optical microscopy or some variant of scanned probe microscopy may be possible directions for further investigation.

2.5 Experimental Methods

2.5.1 Substrate Fabrication and Functionalization

Two types of substrates were utilized for DNA-EBL experiments: bulk silicon (100) substrates and silicon nitride membranes suspended across “windows” in silicon (100) substrates. The suspended silicon nitride membrane substrates were prepared by a series of microfabrication

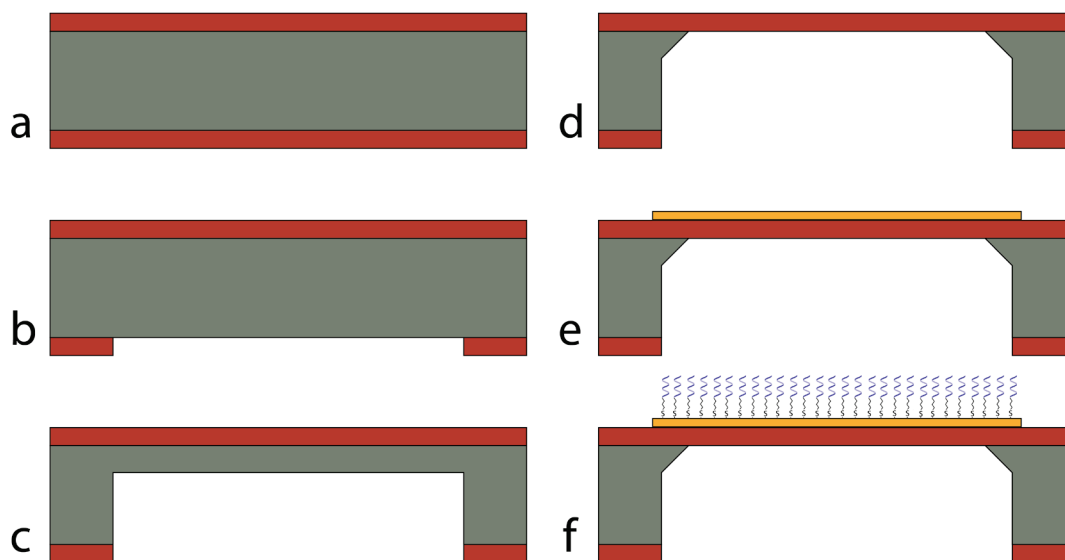


Figure 2.8 Microfabrication and functionalization of suspended silicon nitride substrates showing a) silicon wafer (gray) with 50 nm LPCVD silicon nitride (red), b) backside photolithography and RIE etching of silicon nitride, c) DRIE etching of silicon substrate, d) KOH wet etching of remaining silicon to stop on silicon nitride, e) deposition of Cr/Au (2 nm/8 nm) layers by thermal evaporation through a shadow mask and f) functionalization of gold surface with alkanethiol-modified DNA.

steps as illustrated in Figure 2.8. First, silicon substrates with 50 nm low-stress silicon nitride deposited by low pressure chemical vapor deposition (LPCVD) were purchased (Rogue Valley Microdevices). These substrates were then patterned by photolithography (Suss MABA6) to open windows in the backside and in the “streets” to assist in separating individual die. The exposed backside silicon nitride was then etched with reactive ion etching (SAMCO RIE-10NR) using CF_4/O_2 . The exposed silicon substrate was then etched either by deep RIE (DRIE) with Bosch process and KOH wet etching or by KOH etching alone. While KOH etching alone is sufficient to remove the silicon, it takes more than 8 hours to etch through the 500 μm silicon wafer. The DRIE was applied to reduce this cycle time, but was typically stopped 20 – 30 μm short of the silicon nitride as KOH has much higher selectivity to silicon over silicon nitride compared to DRIE.¹⁹⁴ Depending on the process, a square mask area of 500 μm edge-length resulted in a suspended silicon nitride membrane of about 300 μm edge-length. The wafer was then separated into smaller groups of die, which were batch-processed through the metal deposition and DNA functionalization steps to provide fresh substrates as needed for experiments. Metal deposition was performed by thermal evaporation (Kurt J. Lesker Nano38) of chromium (2 nm) followed by gold (8 nm) through a laser-cut stainless steel shadow mask with 1 mm square openings which were manually aligned to the silicon nitride windows. This patterned metal deposition process was utilized to minimize the area to which DNA was immobilized to conserve nanoparticles in the subsequent assembly processes. Bulk silicon substrates were fabricated by applying a similar metal deposition process through 2mm square openings on bare silicon after oxygen plasma cleaning (South Bay Technologies, Inc.) and then separated into individual die by scribe and break separation.

Gold-coated substrates were functionalized with DNA in a similar fashion to methods developed by the Mirkin group^{102,108} and the DNA sequences used are listed in Table 1. Immediately following gold deposition, preparation of the as-synthesized DNA (Integrated DNA Technologies) was begun by cleaving the mercapto-propanol protecting group. This was accomplished by mixing 5 nmol Anchor-B DNA with 100 mM dithiothreitol (DTT) in a 100 μ L of a 170 mM sodium phosphate buffer (pH = 8.0) for one hour to reduce the disulfide bond. This solution was then desalted using a Nap-5 size exclusion column (GE Healthcare) and eluted with 600 μ L HPLC-grade deionized (DI) water. A 60 μ L aliquot of the DNA solution was immediately added to 440 μ L of a 1 M NaCl, 5 mM sodium phosphate buffer (pH = 7.4) for a DNA concentration of 1 μ M in each of 10 standard or screw-top 1.5 mL microcentrifuge tubes with one substrate per tube. Screw-top tubes are recommended for the suspended silicon nitride membrane substrates to avoid breakage of the windows. The substrates were then placed on a shaker at 600-700 RPM overnight or up to several days, until they were needed. Prior to subsequent processing, substrates were cleaned by washing in 0.01% sodium dodecyl sulfate (SDS) followed by rinsing twice in DI water and were then blown dry with nitrogen.

Table 1. List of DNA sequences and their function

DNA Function	DNA Sequence (5' to 3')
Anchor-A (NP)	TCA ACT ATT CCT ACC TAC AAA AAA AAA A – (CH ₂) ₃ – SH
Linker-A (NP)	GTA GGT AGG AAT AGT TGA ATC TCT
Anchor-B (Substrate)	TCC ACT CAT ACT CAG CAA AAA AAA AAA A – (CH ₂) ₃ – SH
Linker-B (Substrate)	TTG CTG AGT ATG AGT GGA AAG AGA
Linker-BCy5 (Substrate)	TTG CTG AGT ATG AGT GGA AAG AGA – Cy5

2.5.2 Nanoparticle Functionalization and Assembly

Spherical gold nanoparticles (BBI Solutions) and gold nanorods (Nanopartz, Inc.) were purchased for use in this work with nominal sizes and properties outlined in Table 2. The spherical particles are citrate stabilized, while the nanorods are stabilized by hexadecyltrimethylammonium bromide (CTAB), which require somewhat different functionalization procedures. In general, the citrate ligands are more easily exchanged for the thiolated DNA, and can be functionalized directly as synthesized. The nanorods require careful centrifugation to remove as much CTAB as possible without causing aggregation. Typically, as-received nanorod suspensions were centrifuged at 8-10K RPM for 10 minutes, supernatant was removed and they were resuspended in DI water (the exact speed and time are somewhat dependent on the nanorod size and concentration of CTAB present in the as-received suspensions). Gold nanoprisms were supplied by collaborators in the Mirkin group¹⁹⁵ and treated similarly to the gold nanorods. Anchor-A DNA (see Table 1) was deprotected and desalted in a manner similar to that in section 2.5.1 and added to nanoparticles in a ratio of 5 nmol/mL of as-received suspension (nanorod suspensions were often concentrated 10:1 to achieve higher loading). This was then placed on a shaker for 30 min to several hours and then brought to 0.01 M sodium phosphate buffer (pH = 7.4) and 0.01 wt. % SDS. Salting buffer (2 M NaCl, 0.01 M sodium phosphate, 0.01 wt. % SDS, pH = 7.4) was then added stepwise over the course of several hours to bring the final salt concentration to 0.5 M. The nanoparticle solution was then placed on a shaker overnight and centrifuged twice in 0.01 wt. % SDS. After a third centrifugation, the nanoparticles were resuspended in a phosphate storage buffer (PSB - 0.5 M NaCl, 0.01 M sodium phosphate, 0.01 wt. % SDS, pH = 7.4). The nanoparticle solutions at this stage were typically left quite concentrated (100-200 μ L per mL of as-received nanoparticle

suspension) to achieve dense linker hybridization. An excess concentration of Linker-A strands (100 μM in PSB) were then added to concentrated nanoparticle suspensions in ratios that depended on the nanoparticle size (typically, 1000 per 30 nm particle, 5000 per 80 nm particle and 10,000 per nanorod). The linker strands were hybridized to the anchor strands by heating on a shaker at 700 RPM to 70 $^{\circ}\text{C}$ for 30 minutes and then slowly cooling to room temperature. Excess linkers were removed by gentle centrifugation and resuspension in storage buffer (twice). Nanoparticles were assembled by immersing substrates in the nanoparticle suspensions at the desired temperature and placed on a shaker at 700 RPM overnight.

Table 2. List of nanoparticles and their properties

Nanoparticle ID	Size (nm)	SPR (nm) (TSPR for NR)	LSPR (nm)
NS1	30	525	-
NS2	80	550	-
NR1	25 \times 93	514	850
NR2	40 \times 148	520	850
NR3	40 \times 124	520	780

Note: Surface plasmon resonance (SPR) for transverse axis of nanorods (TSPR) and longitudinal axis (LSPR)

2.5.3 Electron Beam Patterning

Dose-controlled electron beam exposure was applied to form density gradient patterns in the DNA monolayers. This was carried out with either a Quanta 600F or Quanta 650 FEG (FEI Company) integrated with a NPGS beam control system (JC Nability Lithography Systems) and a high-speed (5 MHz) electrostatic beam blanker. This system is capable of achieving sub-20 nm feature sizes in PMMA resists.¹⁹⁶ High-resolution patterns were exposed using a small spot size, low beam current (\sim 150-200 pA) and small pixel spacing (\sim 3 nm). Large-area patterns were

exposed with a large beam current (~ 8 nA) and larger pixel spacing (~ 100 nm). Since the beam size may be smaller than the pixel size under the latter conditions, the beam was defocused $25 \mu\text{m}$. This defocus was determined empirically to be sufficient to minimize pixel-size artifacts in subsequent nanoparticle assembly. Most patterns were exposed with a 30 kV accelerating voltage and 6-7 mm working distance. The electron dose was controlled by changing the dwell-time per pixel to achieve doses ranging from 10 to $10,000 \mu\text{C}/\text{cm}^2$, depending on the application. Basic characterization of the DNA exposure process by XPS and fluorescence microscopy was carried out by exposing square regions of different sizes with uniform dose and either a small pixel size or defocused electron beam. Single-particle resolution patterns for nanorod assembly were carried out by leaving small unexposed areas (< 50 nm) between exposed regions. This high-resolution patterning was carried out using a finely focused electron beam and small pixel size (< 5 nm).

2.5.4 *X-ray Photoelectron Spectroscopy*

XPS analysis was carried out with an ESCALAB 250Xi (Thermo Scientific). Large (1 mm^2) regions on Anchor-B DNA functionalized silicon substrates were exposed to ensure no overlap of the $500 \mu\text{m}$ X-ray probe with unexposed regions. C 1s scans were carried out by averaging 100 scans with a pass energy of 20 eV, dwell time of 100 ms, and energy step size of 0.1 eV with electron-beam flood for charge suppression. While charging was minimal, an energy shift was applied according to Au 4f reference scans for each sample. A Gaussian/Lorentzian mixed peak fit was carried out for the four characteristic peaks near 284.5, 286, 287.5, and 289 eV.

2.5.5 *Fluorescence Microscopy*

To probe the relative degree of DNA damage, a fluorophore labeled linker strand (Linker-BCy5 in Table 1) was hybridized to the Anchor-B strands on silicon substrates after electron beam exposure. This was accomplished by adding the substrate to 0.5 μM Linker-BCy5 in PSB and heating to 70 °C for 30 minutes followed by slowly cooling to room temperature. Cy5 is a cyanine fluorescent dye with peak absorbance at 648 nm and emission at 668 nm,¹⁹⁷ although this could shift depending on the interaction with the gold substrate.¹⁹⁸ Fluorescence microscopy was carried out with an IX83 inverted fluorescent microscope (Olympus) using a Cy5 filter. Semiquantitative analysis was performed by calculating relative intensity values for the modified regions compared to an immediately adjacent unmodified region. This method minimized the effects of uneven illumination and any long-range variations or gradients in DNA loading on the substrate.

2.5.6 *Spectrophotometry of Nanorod Desorption*

Melting curves for nanorod desorption were carried out using an Agilent/HP 8453 UV-visible spectrophotometer with a Peltier stage. Quartz substrates were first prepared by the same method outlined in section 2.5.1. Nanorods were assembled on the substrates at room temperature and then placed in a quartz cuvette with phosphate storage buffer. The cuvette was heated from 25 – 70 °C at a rate of 0.1 °C/min and extinction spectra were captured at each step. The melting curve was calculated by measuring the change in intensity of the longitudinal plasmon resonance (~825-850 nm) referenced to the intensity at 600 nm (this provided better signal intensity than either the transverse peak at ~520 nm or the DNA peak at 260). The inflection point in this curve is considered the melting temperature. Examples of pre- and post-melt spectra and the melting curve for NR1 nanorods is shown in Figure 3.1.

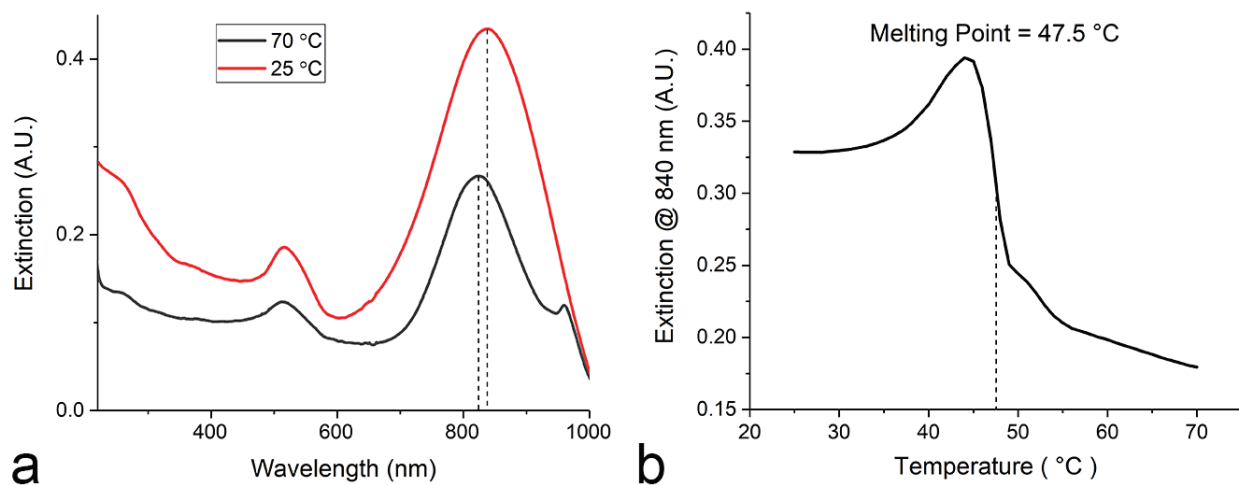


Figure 3.9 Nanorod (NR1) melting experiment showing a) UV-Vis spectra pre (25 °C) and post (70 °C) melting, indicating blue-shift and decrease in intensity of the longitudinal plasmon peak and b) melting curve, showing an inflection (melting) point at 47.5 °C.

Chapter 3: Size-Selective Nanoparticle Assembly by DNA Density Patterning

Parts of this chapter are adapted with permission from: Myers, B. D., Lin, Q.-Y., Wu, H., Luijten, E., Mirkin, C. A. & Dravid, V. P. Size-Selective Nanoparticle Assembly on Substrates by DNA Density Patterning. ACS Nano 10, 5679-5686, (2016)¹⁴⁸ Copyright 2016 American Chemical Society

3.1 Chapter Summary and Motivation

The vision of nanoscale self-assembly research is the programmable synthesis of macroscale structures with controlled long and short-range order that exhibit a desired set of properties and functionality. However, strategies to reliably isolate and manipulate the nanoscale building blocks based on their size, shape or chemistry are still in their infancy. Among the promising candidates, DNA-mediated self-assembly has enabled the programmable assembly of nanoparticles into complex architectures. In particular, two-dimensional assembly on substrates has potential for the development of integrated functional devices and analytical systems. Here, the high-resolution patterning capabilities afforded by electron-beam lithography are combined with the DNA-mediated assembly process to enable direct-write grayscale DNA density patterning. This method allows modulation of the functionally active DNA surface density to control the thermodynamics of interactions between nanoparticles and the substrate. Size-selective directed assembly of nanoparticle films from solutions containing a bimodal distribution of particles is demonstrated by exploiting the cooperativity of DNA binding in this system. To support this result, the temperature-dependence of nanoparticle assembly is studied and molecular dynamics simulations are employed to explore the size-selection behavior.

3.2 Introduction

The assembly of nanoparticles into larger ensembles with well-controlled architecture^{87,88,199} has enabled the development of new materials for potential application in plasmonics,²⁰⁰⁻²⁰² sensing,^{203,204} photovoltaics²⁰⁵ and data storage.²⁰⁶ Among the various assembly strategies,^{6,207,208} DNA-mediated nanoparticle assembly has emerged as a powerful and versatile approach due to the highly specific, tunable and reversible nature of DNA binding.^{63,87,88} DNA-programmable self-assembly has resulted in the development of a range of interesting structures from clusters to three-dimensional (3D) colloidal crystals with control over lattice parameter, symmetry and crystal habit.^{65,84,86} Specific macroscopic crystal structures based on nanoparticle motifs can be synthesized by following a well-defined set of design rules and tuning parameters such as nanoparticle size and DNA length.⁸⁶ Two-dimensional (2D) DNA-mediated nanoparticle assembly on surfaces^{209,210} has been applied in microarray technology,^{204,211} and recently interest has emerged in this technique for the fabrication of structures with novel optical properties.^{103,212,213} Many of the critical parameters in 3D assembly have been identified, notably the effect of DNA density on the melting (particle-dissociation) temperature of colloidal crystals,^{83,214,215} but its role in 2D assembly has not been studied and exploited systematically.

EBL has matured as a flexible nanopatterning tool^{196,216} and electron irradiation has been shown to cause damage to DNA and individual nucleobases.^{180,182} Therefore, one could envision that selectively damaging a DNA monolayer by electron-beam patterning would give rise to controlled particle-substrate interactions and the effectiveness of DNA-EBL in the grayscale patterning of DNA monolayers was shown in Chapter 2. DNA-EBL enables patterning of DNA density with high spatial resolution for multiplexed analysis of 2D nanoparticle assembly. This

approach differs from yet complements previous studies on 3D assembly which require multiple batches of nanoparticles with different DNA densities and analysis by indirect methods of spectrophotometry⁸² or fluorimetry.⁷² In this work, the design rules in the complementary contact model (CCM)⁸⁶ are extended to understand particle-surface interactions. Specifically, DNA density patterning by DNA-EBL drives the size-selective assembly of nanoparticles from a solution with a bimodal distribution of particles. For nanoparticles with the same surface chemistry, the size distribution of particles can be controlled such that smaller particles preferentially associate with areas of high DNA density and larger particles assemble in lower density regions. The former observation is substantiated with a thermodynamic argument based on geometric surface coverage akin to the CCM and show that the transition from small to large particles with decreasing DNA density occurs due to particle-size effects and collective binding at the individual particle level, as supported by molecular dynamics (MD) simulations.

3.3 Results and Discussion

3.3.1 Nanoparticle Assembly Strategy

The assembly method in this study relies on four oligonucleotides, which include two anchor strands and two linker strands, as used in previous work and shown in Table 1.^{88,102} The DNA anchor strands are attached to the gold nanoparticles (Anchor-A) and the gold-coated silicon surface (Anchor-B) and subsequently the Linker-A and -B strands are hybridized with the particle and surface-bound anchor strands, respectively. The anchor strands have an A₁₀ spacer and an 18-base sequence complementary to the respective linker strand. The linker strands present five-base complementary “sticky ends” which enable the assembly of nanoparticles on the substrate. The key innovation in this work, as illustrated in Figure 3.1, is the use of DNA-EBL to modify the

Anchor-B DNA monolayer, which modulates the subsequent hybridization with Linker-B DNA, effectively modulating the surface density of functionally active DNA. An EBL system is used to pattern arbitrary features with nanometer-scale resolution and precise electron-dose control over a wide range (20–10,000 $\mu\text{C}/\text{cm}^2$). This results in a high degree of control over the surface density of active DNA on the substrate and thereby enables tunable thermodynamic interactions during the subsequent nanoparticle-assembly process. Size-selective assembly is achieved due to strong size-dependent effects, which drive small particles to areas of high DNA density and large particles to regions with lower density of active DNA. The influence of electron dose, temperature and relative nanoparticle concentration on the size-selective assembly process are explored.

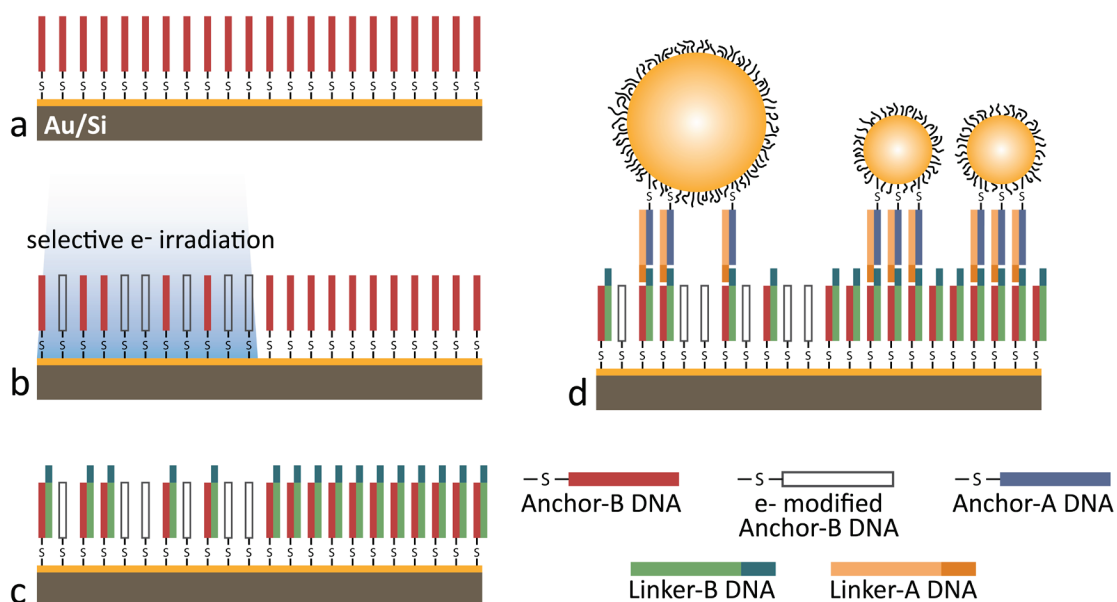


Figure 3.1 Schematic illustration of size-selective assembly process. (a) Thiol coupling of surface anchor DNA to Au-coated Si substrate. (b) DNA-EBL for dose-controlled electron-beam patterning of surface anchor DNA. (c) Hybridization of surface linker strands, showing reduced coverage in electron-irradiated regions. (d) Assembly of nanoparticles with different sizes but with the same surface functionalization. Larger particles are selectively adsorbed to regions that present a lower density of sticky ends.

3.3.2 Nanoparticle Adsorption Studies

The ability to tune the DNA surface density, as introduced in Chapter 2, is in itself a powerful tool with many potential applications. Here, the DNA-EBL technique is applied by controlling the adsorption from solutions with bimodal distributions of spherical DNA-modified gold nanoparticles in 0.5 M NaCl, 0.01 M sodium phosphate buffer (pH = 7.4). As shown in Chapter 2, for monodisperse suspensions this results in the ability to control the surface density of adsorbed particles (Figure 2.2), which enables the site-specific tuning of nanoparticle monolayer density and the creation of surfaces with nanoparticle surface-density gradients. However, for solutions with a bimodal distribution of particles, a complex competitive adsorption process is observed in which the combined effects of particle size, DNA density and temperature-dependent adsorption make it possible to control the relative surface density of particles based on their size (Figure 3.2a). This technique enables both binary size separation of particle mixtures on a surface and tuning of the size distribution for mixed monolayer nanoparticle films. In addition to the larger micrometer-scale features, the EBL system affords the ability to pattern features with length scales that are relevant to the study of photonic and plasmonic interactions and even down to the scale of individual particles. To demonstrate this capability, line patterns with controlled periodicity (Figure 3.2b) and linear arrays of 1D nanoparticle chains (Figure 3.2c-d) were created. In these nanoparticle chains, the linewidth and pitch of the exposed lines not only arranged the particles in chains, but also allowed control of the size distribution of particles in the chain.

To study the impact of DNA density on the competitive adsorption of nanoparticles of different sizes in detail, nanoparticle adsorption on DNA monolayers with no electron-beam modification was investigated. Nanoparticles were assembled at different temperatures on

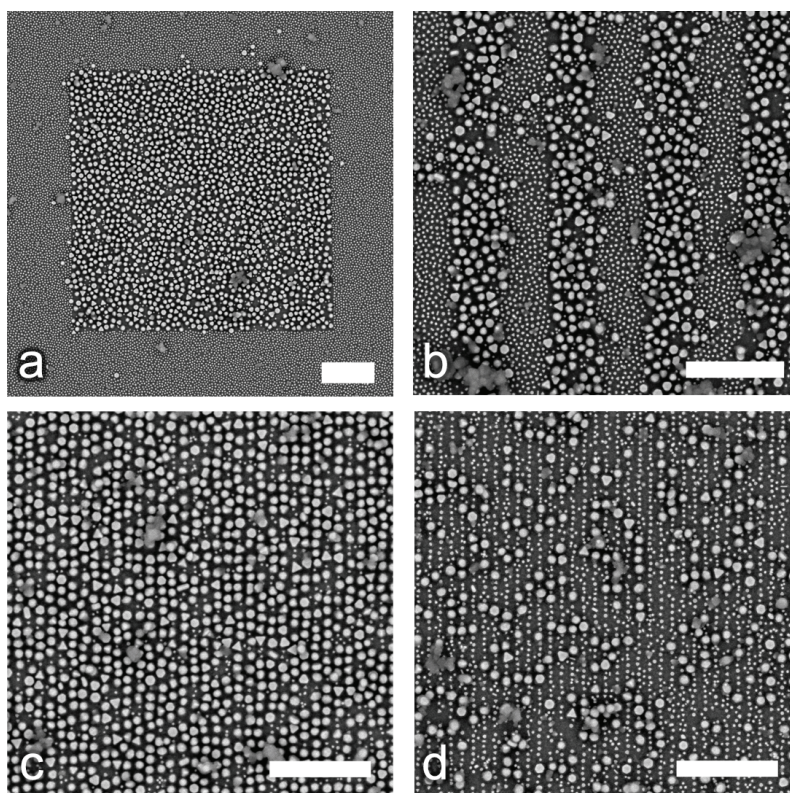


Figure 3.2 DNA-density directed assembly of small (30 nm) and large (80 nm) nanoparticles. (a) Size-selective assembly from a solution with a bimodal distribution of particles (small-to-large particle ratio of 42:1) by exposing a 5 μm square with an electron dose of 990 $\mu\text{C}/\text{cm}^2$ (assembled at 35 $^\circ\text{C}$). (b) Size-selective assembly with 500-nm line patterns with an electron dose of 510 $\mu\text{C}/\text{cm}^2$ (assembled at 40 $^\circ\text{C}$). (c-d) High-resolution line patterning for 1D particle chains with control over particle size distribution. These patterns were created on the same substrate by exposing lines with a pitch of 110 nm and varying the linewidth (c – 60 nm linewidth and 730 $\mu\text{C}/\text{cm}^2$, d – 80 nm linewidth and 710 $\mu\text{C}/\text{cm}^2$; both assembled at 40 $^\circ\text{C}$). (Scale bars are 1 μm .)

unmodified DNA-functionalized substrates from a solution with a bimodal distribution of small (30 nm) and large (80 nm) particles. The concentration of this mixed suspension was controlled to achieve small-to-large ratio of particles of approximately 42:1, with a total particle concentration of 2.56 nM. The results of these experiments showed nearly complete exclusion of the larger particles on the surface with a small-to-large ratio of $2.05 \times 10^4:1$ at 30 $^\circ\text{C}$. As the assembly temperature was increased, this ratio decreased to $1.09 \times 10^4:1$ at 35 $^\circ\text{C}$ and $2.89 \times 10^3:1$ at 40 $^\circ\text{C}$

and the overall density of the nanoparticle monolayers decreased by about 16% from 30 to 40 °C. This trend correlates with the size-dependent melting in these nanoparticle films as measured by spectrophotometry as shown in Figure 3.3. The melting temperature (50% absolute change in absorbance) was found to be 48.9 °C for 30 nm particles and 53.1 °C for 80 nm particles. The difference in melting points has been exploited in previous work for particle–particle binding, enabling size separation of particles by sedimentation.²¹⁷

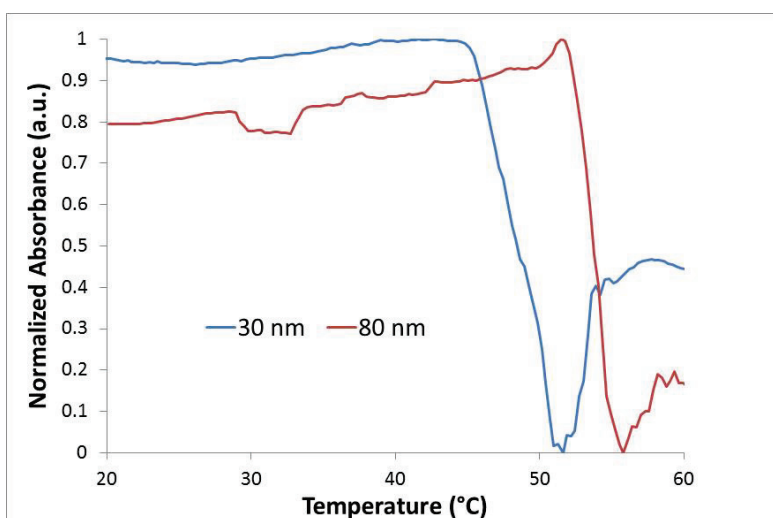


Figure 3.3 UV-Vis melting curves for 30 and 80 nm nanoparticle films on gold-coated quartz substrates.

The combined effects of temperature- and size-dependent adsorption show a clear and tunable response when coupled with the precise control over local active DNA surface density afforded by DNA-EBL. A 15 keV electron beam was used to expose a series of 5- μm wide square regions with doses ranging from 150 to 2040 $\mu\text{C}/\text{cm}^2$ in 30 $\mu\text{C}/\text{cm}^2$ steps. The number density of particles was calculated as a function of electron dose at 30, 35 and 40 °C *via* image analysis. These data show a size-selective adsorption effect with a transition electron dose (D_T , defined as the dose resulting in equal areal coverage of small and large particles) that is temperature

dependent as shown in Figure 3.4a. At low electron doses, the small particles dominate as in the unmodified films. As the dose is increased, the surface density of small particles decreases while the density of large particles increases, until the films are almost completely devoid of small particles. At higher doses, the density of the large particles also begins to decrease. A similar

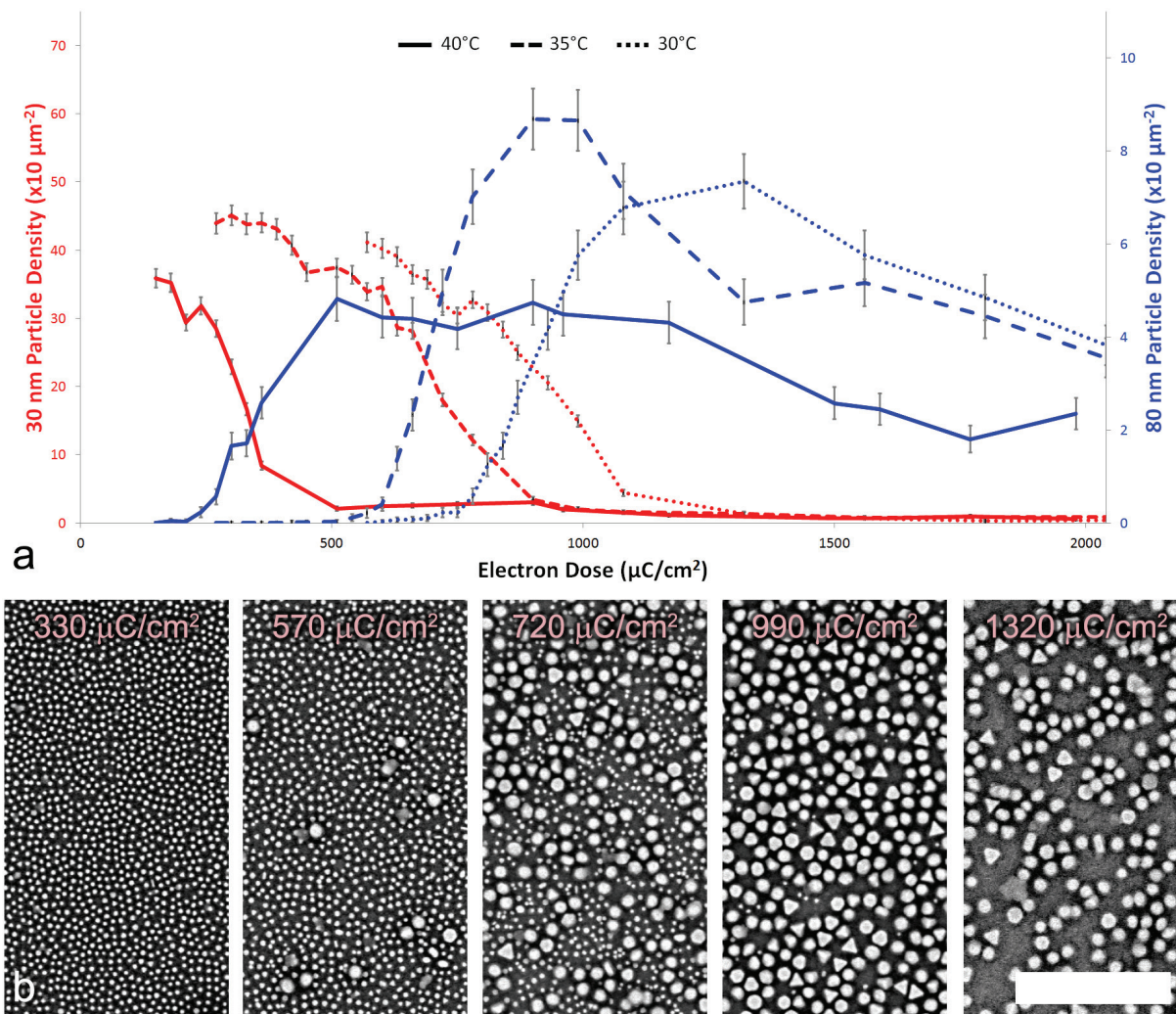


Figure 3.4 Temperature dependence of size-selective assembly. (a) Areal density of small and large particles as a function of electron dose showing a decrease in transition dose D_T (defined in the main text) with increasing assembly temperature. (Y-axis scales are adjusted to account for particle size and show equivalent surface coverage) (b) Selected images of nanoparticle films showing electron-dose effects on small-to-large particle ratio for assembly at 35 $^{\circ}\text{C}$. (Scale bar is 1 μm .)

overall behavior is observed at all three assembly temperatures, but D_T shifts to lower doses as the temperature is increased.

This phenomenon enables the tuning of nanoparticle film size distribution from a situation dominated by small particles to one with predominantly large particles in one step and on the same substrate, starting from a mixed suspension as shown in Figure 3.4b. These data show that the sensitivity of the adsorption and desorption rates to particle size can be varied dramatically by tuning the DNA density on the surface. *Via* this method, ratios of 30-nm to 80-nm particles greater than 1:100 are achieved from a 42:1 ratio in the nanoparticle suspension, even without any optimization of the DNA sequences or immobilization chemistry. The actual discrimination is

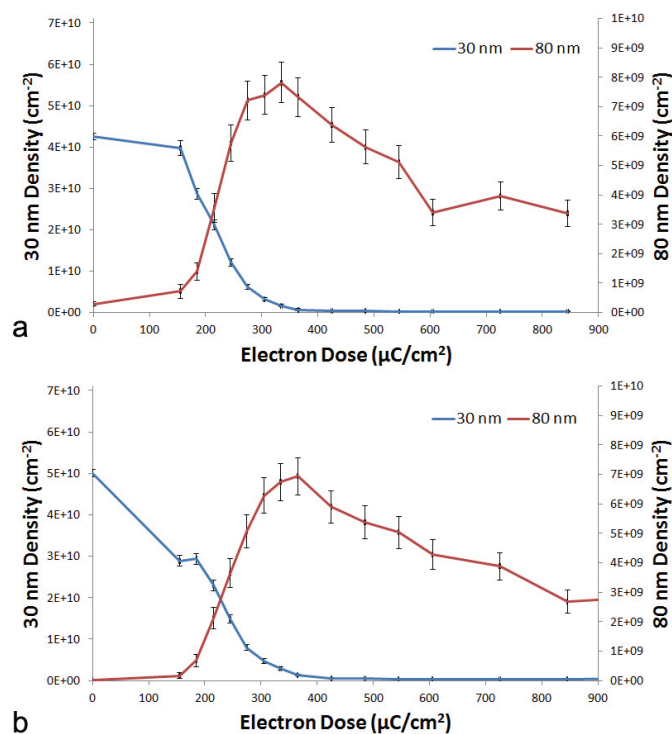


Figure 3.5 Areal density as a function of electron dose for lower-concentration and lower-ratio size-selective assembly at 35 °C for a) 500 pM 30 nm/100 pM 80 nm and b) 500 pM 30 nm/50 pM 80 nm.

likely much higher as there are a significant number of agglomerated small particles that appear to behave as larger particles, but are still classified as small particles in the image analysis. Similar effects were seen with lower overall concentrations and lower small-to-large particle ratios as well (10:1 and 5:1), indicating that this effect is driven primarily by particle–surface interactions rather than concentration imbalance. Separate batches of 30 nm and 80 nm nanoparticles and substrates were functionalized and mixed in concentration ratios (30 nm:80 nm) of 5:1 and 10:1 with lower total concentrations of 600 pM and 550 pM, respectively. Similar size-selectivity was noted as in the high-concentration, high-ratio study as shown in Figure 3.5.

However, the concentration of linker DNA relative to the nanoparticle concentration was found to be critical to observe size-selective assembly. Initial linker concentrations were adapted from the literature,¹⁰⁸ but in experiments with lower particle concentration this linker concentration proved insufficient for effective size selection as shown in Figure 3.6a. This is likely due to insufficient loading of linker oligonucleotides on the nanoparticles in the relatively dilute conditions. On the other hand, at higher linker concentrations, size-selective assembly was still not observed, likely due to excess linker in solution competing with nanoparticle assembly as shown in Figure 3.6b. In fact, the excess linker prevented nearly all adsorption of the 30 nm particles and strongly affected the adsorption of 80 nm particles in the electron-beam modified regions, even at a significantly lower dose than in other experiments. However, after the nanoparticles were centrifuged and resuspended three times to remove excess linker, strong size-selective assembly was observed as shown in Figure 3.6c. This indicates that the particles were densely loaded and supports the notion that free linker strands can compete with nanoparticles and impact adsorption properties.

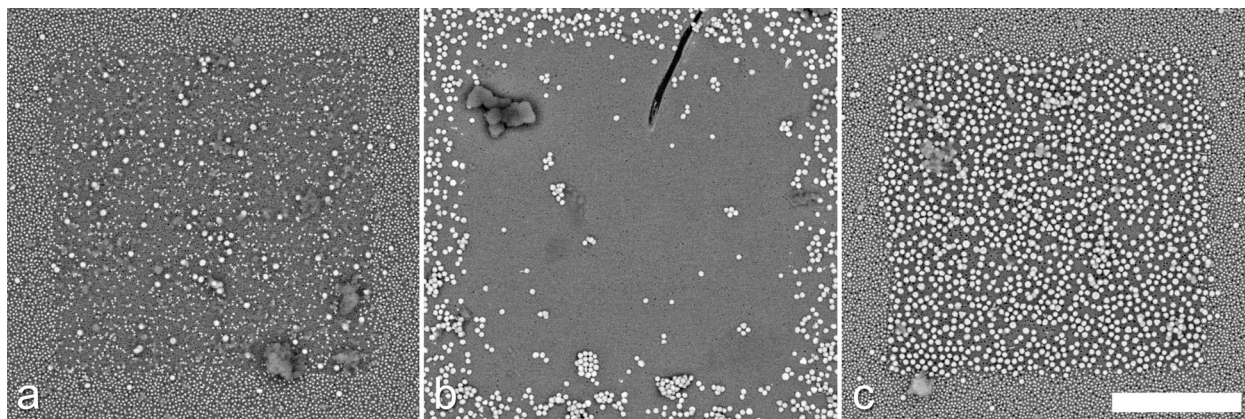


Figure 3.6 Effects of linker concentration on size-selective assembly with 500 pM 30 nm/50 pM 80 nm particle solutions containing a) 120 pmol linker DNA and $125 \mu\text{C}/\text{cm}^2$ electron dose, b) 370 pmol linker DNA and $125 \mu\text{C}/\text{cm}^2$ electron dose and c) linker DNA removed by centrifugation and resuspension and $425 \mu\text{C}/\text{cm}^2$ electron dose. All particles were assembled at 35°C . (Scale bar is $2 \mu\text{m}$)

3.3.3 Particle-Substrate Interaction Calculations

A thermodynamic driving force to maximize the number of hybridized DNA strands can explain the preferential adsorption of smaller particles in regions of high DNA density from a bimodal suspension. The total enthalpic contribution of the adsorbed particles is directly proportional to the total contact area between the particles and the surface and the density of DNA. Following previous calculations,⁸⁶ the ratio of surface interaction area for close-packed particles of different sizes (30 and 80 nm) on a substrate are compared. The DNA-functionalized nanoparticles and substrate are treated as having “fuzzy” surfaces where the sticky ends of the DNA linkers exist in some predictable range of distances from their respective surfaces. As a result, the degree of binding between particles and surfaces depends on the number of DNA linkages in the region where the two “fuzzy” surfaces interpenetrate as illustrated in Figure 3.7. Since the substrate DNA density is lower than the particles due to curvature effects,⁷⁴ the substrate DNA density will limit the total particle-surface interaction. Therefore, the surface area of the particle

can be ignored and only the area of interaction on the substrate is considered when comparing the favorability of adsorption for small and large particles.

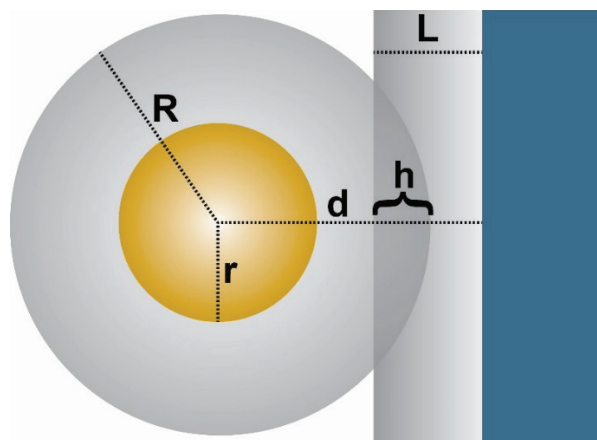


Figure 3.7 Illustration of geometric interaction between a “fuzzy” nanoparticle and substrate showing relevant variables in calculating the total interaction area for nanoparticle films: R is the hydrodynamic radius of the DNA-functionalized nanoparticle, L is the fully extended length of the DNA on the substrate, d is the nanoparticle-substrate separation when bound by hybridized DNA, r is the gold nanoparticle radius and h is the overlap of the two “fuzzy” surfaces giving rise to the concept of a contact area.

The particle-to-surface distance (d , in nm) can be calculated by the following:

$$d = r + 0.255(x) + 0.8, \quad (13)$$

where r is the radius of the inorganic nanoparticle core, x is the total number of nucleobases in the DNA connecting the particles and substrate and 0.8 nm represents the length of two propyl-thiol moieties. The multiplier of 0.255 nm indicates the rise per base pair and has been determined experimentally to represent typical particle separation distances.²¹⁸ To determine the region of overlap between the two “fuzzy” surfaces, the distance, d , is compared to the hydrodynamic radius (R , in nm) of the “fuzzy” nanoparticle, which is defined as:

$$R = r + 0.34(y) + 0.4 \quad (14)$$

and the thickness of the DNA layer on the substrate (L , in nm) can be calculated similarly:

$$L = 0.34(y) + 0.4, \quad (15)$$

where y is the total number of nucleobases attached to the nanoparticle and 0.4 nm represents the length of the propyl-thiol moiety. The multiplier of 0.34 nm indicates the rise per base pair for canonical B-form DNA. While the actual value of the rise per base pair was not measured in this work, the values used in Equations (13) and (14) should be reasonable estimates and even if there is some deviation, the relative comparison between small and large particles is still valid. The overlap of the two “fuzzy” surfaces, h , can then be calculated as:

$$h = L - (d - R) \quad (16)$$

and the area of intersection on the substrate, A , can then be calculated by:

$$A = \pi h(2R - h). \quad (17)$$

To compare the relative surface coverage for particles of different size, a hexagonally close-packed 2D nanoparticle film is used as a reference. Given this arrangement, the maximum surface coverage can be calculated from the following:

$$\%Coverage = 100 \left(\frac{A}{2\sqrt{3}R^2} \right). \quad (18)$$

The results of this calculation indicate that a nanoparticle film made of entirely small (30 nm) particles will result in approximately 41.3% surface coverage while the large (80 nm) particles provide only 23.0% coverage, resulting in a 1.8-fold larger number of DNA linkages for a small particle film.

3.3.4 *Molecular Dynamics Simulation Results*

To verify the hypothesis that the size-selective behavior is due to a competition between overall thermodynamics and the adsorption behavior of individual particles, coarse-grained molecular dynamics simulations were performed and the effects of particle size and DNA surface density on equilibrium nanoparticle adsorption were examined. As shown in the rendering in Figure 3.8a, the system was modeled as a bimodal distribution of nanoparticles matching the experimental setup, grafted with semiflexible bead–spring chains (each 14 beads long) that are capable of reversible attachment to surface binding sites. The solvent was modeled implicitly, with a Langevin thermostat for temperature control, whereas the modification of the DNA surface density was mimicked through variation of the density of binding sites. To account for the slow diffusion of the extended nanoparticles, the surface coverage was monitored for long times. Size-dependent adsorption was observed as a function of DNA surface density (Figure 3.8b), with the smaller species dominating at low surface modification, but then monotonically decreasing and gradually being displaced by the larger species as the number of adsorption sites decreases—in agreement with the experimental observations. The coverage by the larger species grows steady until curtailed by the sheer lack of binding sites. Accordingly, this mechanism could be exploited to segregate mixtures that contain additional species of different sizes or possibly binding strengths. The computational modeling also provides information that is less easily accessible experimentally. At the highest coverage by the smaller species, adsorbed nanoparticles were bound to the surface by more than three bonds (Figure 3.8c). This number dropped gradually with increasing modification level, preceding the decrease in nanoparticle coverage. As the larger species gradually replaced the smaller ones, their number of bonds per particle also surpassed the

smaller species, reflecting stronger binding to the surface. Notably, for modification levels between 60% and 80%, the number of bonds continued to drop whereas the coverage of the species increased. The surface residence time decreases more quickly with decreasing DNA surface density for small particles than for large particles (Figure 3.8d), which supports the notion of an enhanced desorption rate for small particles and an equilibrium nanoparticle film size distribution that becomes dominated by large particles.

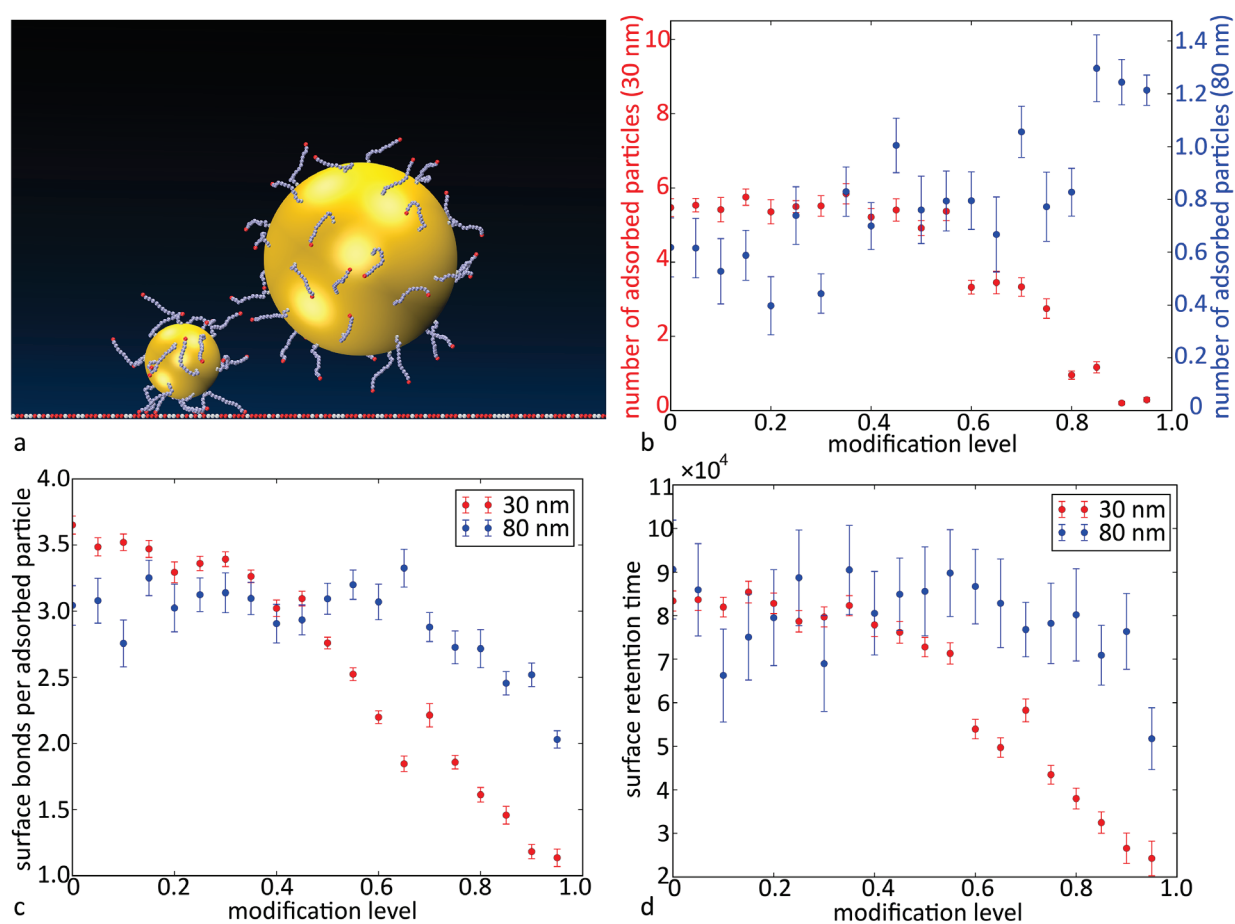


Figure 3.8 Molecular dynamics simulation of size-selective assembly. (a) Schematic illustration of simulated particles and substrate. (b) Size dependence of nanoparticle adsorption with decreasing DNA surface density (axes adjusted for equivalent projected area). (c) Average number of bonds involved in nanoparticle immobilization and (d) retention time for adsorbed particles for small and large particles.

3.4 Summary and Outlook

In summary, this work builds on the use of DNA-EBL as a method for tuning the local density of active DNA strands in a monolayer by high-resolution, dose-controlled electron-beam irradiation. DNA-EBL was applied for the size-selective assembly of DNA-functionalized gold nanoparticles on substrates functionalized with complementary DNA. The thermodynamics of polyvalent DNA binding interactions coupled with differences in particle surface area drive this phenomenon. The larger surface coverage by small particles provides a thermodynamic advantage for assembly with high DNA density but that large particles dominate at low density where small particles cannot access a sufficient number of linkages for immobilization, as supported by molecular dynamics simulations. The technique can be utilized to further the understanding of thermodynamic and kinetic factors in DNA-linked nanoparticle assembly and to create complex and technologically interesting structures with potential photonic, plasmonic and bioanalytical applications. For future work, it would be interesting to explore the size-difference threshold at which the selective assembly behavior is triggered. This could then be extended to application of size-selectivity by DNA density engineering as a method for sorting or filtering nanoparticles, since even the best synthetic methods result in some polydispersity. In addition to size-selectivity, the role of nanoparticle geometry could also be explored to look at the selective assembly of particles of the same volume, but different shape (*i.e.* curvature). For example, the switchable assembly of cubic and spherical nanoparticles could have application in tunable metasurfaces as strong nanocavity modes exist for cube-substrate plasmon coupling, but not for spheres.

3.5 Experimental Methods

3.5.1 DNA Design and Nanoparticle Functionalization

Nanoparticle and substrate functionalization and nanoparticle assembly procedures are similar to previous protocols and those in Chapter 2.^{102,108,219} Briefly, oligonucleotides were either synthesized with a MerMade 48 (MM48) automated oligonucleotide synthesizer (BioAutomation) using reagents purchased from Glen Research or purchased (Integrated DNA Technologies). The DNA sequences used are the same as those shown in Table 1. Immediately prior to use, the thiolated oligonucleotides were deprotected by treatment with 100 mM dithiothreitol (DTT) in 170 mM sodium phosphate buffer (pH = 7.4) and purified with Nap-5 size-exclusion columns (GE Healthcare). The purified oligonucleotides were added to gold nanoparticles (British Biocell International) in a ratio of approximately 5 nmol per mL of nanoparticle solution. The solution was placed on a shaker for 2 hours to overnight and then brought to 0.01 M sodium phosphate buffer (pH = 7.4) and 0.01 wt. % sodium dodecyl sulfate (SDS) in water. Salting buffer (2 M NaCl, 0.01 M sodium phosphate, 0.01 wt. % SDS, pH = 7.4) was added stepwise over the course of several hours to bring the final salt concentration to 0.5 M. The nanoparticle solution was placed on shaker overnight and then centrifuged twice and resuspended in 0.01 wt. % SDS to remove excess DNA. After a third centrifugation, the nanoparticles were resuspended in storage buffer (0.5 M NaCl, 0.01 M sodium phosphate buffer (pH = 7.4) with 0.01 wt. % SDS) at their final concentrations, which were determined by UV-vis. A-type linker strands were added to the nanoparticle suspensions and allowed to fully hybridize by heating the suspension to 60–70 °C and then slowly cooling to room temperature. The linker concentration was 300 per 30-nm nanoparticle and 2000 per 80-nm nanoparticle for most experiments.

3.5.2 *Substrate Functionalization and Nanoparticle Assembly*

Silicon substrates were cleaved, cleaned by oxygen plasma treatment (South Bay Technology, Inc.) and coated with 2 nm of chromium followed by 8 nm of gold in a thermal evaporator (Kurt J. Lesker Company). Following gold coating, substrates were immersed in a substrate buffer (1 M NaCl, 5 mM sodium phosphate buffer (pH = 7.4)) and freshly cleaved and desalted Anchor-B oligonucleotides were added to achieve a DNA concentration of 1 μ M. Substrates were placed on a shaker and allowed to react with the thiolated DNA for 24 hours followed by rinsing three times in DI water and then were blown dry with nitrogen. After electron-beam exposure, substrates were immersed in storage buffer with 0.5 μ M B-type linker oligonucleotides. This solution was heated to 60–70 °C for 30 minutes and allowed to slowly cool to room temperature to fully hybridize the anchor and linker strands. Substrates were then rinsed three times in storage buffer to remove any unbound DNA.

Nanoparticles were assembled by immersing patterned substrates in the desired nanoparticle mixture, which were placed on a shaker and heated to the desired temperature for a minimum of 5 hours. The standard nanoparticle mixture included 2.5 nM small (30 nm) particles and 60 pM large (80 nm) particles for a concentration ratio of 41.7:1. After nanoparticle assembly, substrates were rinsed three times with storage buffer and then embedded in silica²²⁰ to preserve the monolayer structure. For silica embedding, substrates were immersed in 1 mL storage buffer, 2 μ L (7.2 μ mol) N-trimethoxysilylpropyl-N,N,N-trimethylammonium chloride (Gelest) was added and substrates were placed on a shaker for 20 min at 700 RPM. Following this reaction, 4 μ L (21.7 μ mol) triethoxysilane (Sigma-Aldrich) was added and substrates were placed on a shaker for a

minimum of 4 hours. After silica embedding each substrate was rinsed three times in DI water and blown dry with nitrogen.

3.5.3 *Electron-Beam Modification*

Substrates functionalized with Anchor-B oligonucleotides were patterned by electron-beam exposure in a Quanta 600F scanning electron microscope (FEI Company) with an NPGS beam control system (JC Navity Lithography Systems) and high-speed beam blanker (5 MHz) for pattern generation. All exposures were carried out with a 15 kV accelerating voltage and 6.5 mm working distance. High-resolution patterns were exposed using a small spot size and low beam current (~ 200 pA) and small pixel spacing (~ 3 nm). Large-area patterns were exposed with a large beam current (~ 8 nA) and larger pixel spacing (~ 100 nm). Since the beam size may be smaller than the pixel size under the latter conditions, the beam was defocused $25\ \mu\text{m}$. This defocus was determined empirically to be sufficient to minimize pixel-size artifacts in subsequent nanoparticle assembly.

3.5.4 *Scanning Electron Microscopy and Image Analysis*

SEM analysis was performed with a SU8030 cold-cathode field-emission SEM (Hitachi) with 5 kV accelerating voltage and upper backscattered electron detector to minimize contrast from the silica sol-gel. Image analysis was performed with a custom MatLab script to extract the areal densities of both large and small particles as a function of electron dose. The procedure (Figure 3.9) involves cropping a region of interest and manually removing polygonal regions from the image, which include sol-gel debris, etc. These regions are stored as a mask layer to calculate the total area removed for the areal density calculation. The mask layer is applied to the original image and a threshold operation is applied to create a binary image, which is then processed by a

watershed filter to separate particles that may be touching. Due to the polydispersity of the nanoparticles, small particles with diameters of 20–40 nm and large particles with diameters of 65–90 nm were counted and divided by the total analyzed area (original image area less the masked regions) to compute the areal density.

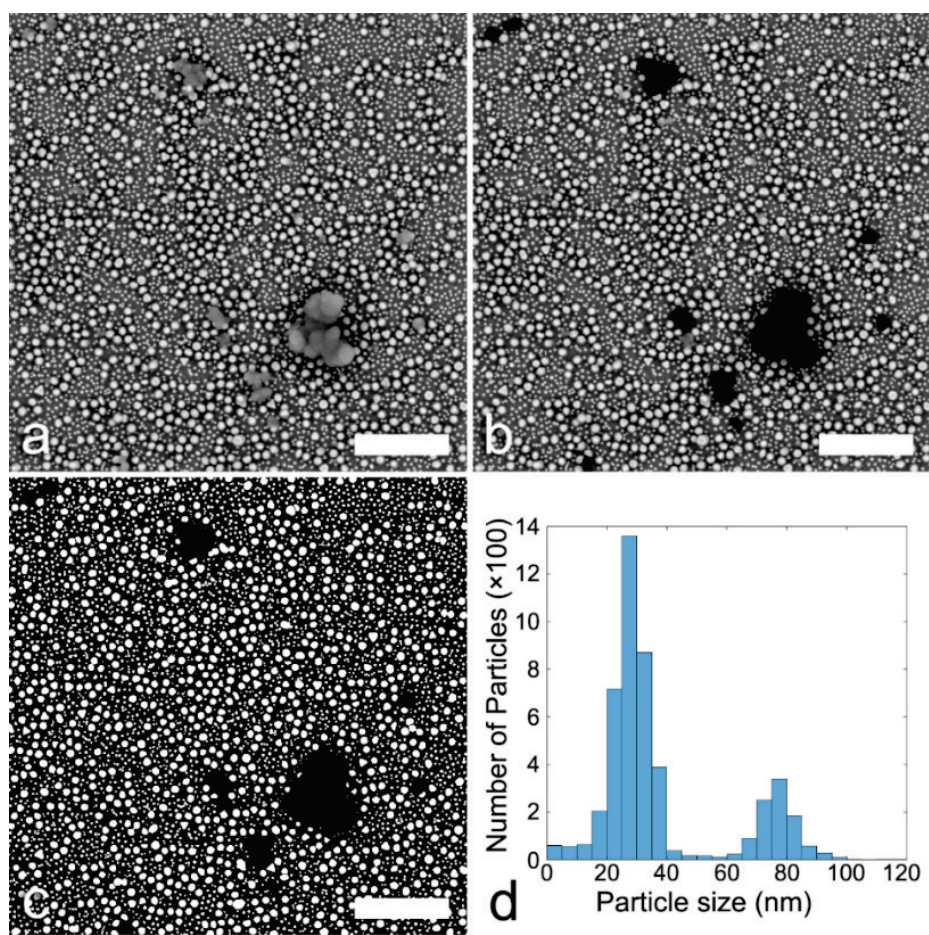


Figure 3.9 Image processing routine showing a) cropped region of interest, b) regions with contaminants edited out of analyzed area, c) image with contrast threshold and watershed filter applied and d) histogram of particle size. (Scale bars are 1 μm)

3.5.5 Spectrophotometry of Nanoparticle Film Melting

Temperature-controlled spectrophotometry was used to study the melting behavior of nanoparticle films. The same nanoparticle assembly procedure described above was used to create

uniform nanoparticle films (no electron-beam patterning) on Cr/Au coated quartz substrates. The quartz substrates with nanoparticle films were immersed in storage buffer in quartz cuvettes. A spectrophotometer (Cary 5000) was used to monitor the absorption peak for the gold nanoparticles as the samples were heated from 20 °C to 60 °C at a rate of 0.1 °C/min. The absorption peak for 30 nm nanoparticles was near 534 nm, and near 540 nm for 80 nm nanoparticles.

3.5.6 *Molecular Dynamics Simulation*

Molecular dynamics simulations using a coarse-grained model were performed to study the microscopic bonding behavior of DNA-functionalized nanoparticles on the DNA-coated substrate as a function of surface modification level. Each grafted DNA strand was modeled as a bead-spring polymer consisting of 14 beads, each of diameter $\sigma = 2$ nm, approximately representing the width of ds-DNA. In accordance with experiment, the diameters and the masses of the gold cores of the small and large colloids were chosen to be 15σ (mass $1100m_0$) and 40σ (mass $27500m_0$), respectively, where m_0 is the mass of a DNA bead. The mass ratio does not exactly correspond to the size ratio, but this is immaterial for static properties. For simulation, 20 chains were grafted on each small colloid and 40 chains on each large colloid. The chains were evenly distributed on the spherical surfaces, according to a modified spiral algorithm²²¹. The coverage on the larger colloids (relative to the smaller colloids) was scaled down compared to experiment to reduce the computing time; nevertheless, this choice provides a qualitative correspondence to the experimental system. Each chain was grafted to the sphere at a single point. The excluded-volume interactions between all particles were modeled with an expanded shifted-truncated Lennard-Jones potential with repulsive strength equal to the thermal energy $k_B T$,

$$u_{\text{LJ}}(r_{ij}) = \begin{cases} \infty & \text{if } r_{ij} \leq \Delta_{ij} \\ 4k_{\text{B}}T \left[\left(\frac{\sigma}{r_{ij} - \Delta_{ij}} \right)^{12} - \left(\frac{\sigma}{r_{ij} - \Delta_{ij}} \right)^6 + \frac{1}{4} \right] & \text{if } \Delta_{ij} < r_{ij} < \Delta_{ij} + 2^{1/6} \sigma \\ 0 & \text{if } r_{ij} \geq \Delta_{ij} + 2^{1/6} \sigma \end{cases} \quad (19)$$

Here, $\Delta_{ij} = r_i + r_j - \sigma$, where r_i and r_j are the radii of two particles. Additionally, the beads within each grafted DNA chain are bonded *via* a harmonic potential,

$$u_{\text{bond}} = k(r - r_o)^2, \quad (20)$$

with $r_o = 0.84\sigma$ and $k = 165 k_{\text{B}}T/\sigma^2$.²²²

In experiments, the DNA is grafted to the colloid by a thiol linkage and consists of a length ss-DNA, which acts as a spacer, followed by a length of ds-DNA and ss-DNA “sticky end” for binding to the substrate. To model the stiffness of the ds-DNA portion, a dihedral potential was applied with $\theta_o = \pi$ and $k_\theta = 5 k_{\text{B}}T$ between beads number 4 through 13 in each grafted chain,

$$u_{\text{angle}} = k_\theta(\theta - \theta_o)^2. \quad (21)$$

To maintain conditions similar to the experiment, 8 large colloids and 88 small colloids were placed in a rectangular simulation box ($140 \times 140 \times 280\sigma^3$) with periodic boundary conditions in the X and Y directions. At the upper and lower Z boundaries, repulsive Lennard-Jones walls were placed. To represent the substrate, a 2D lattice of particles of size σ with lattice spacing 3σ was placed at the lower Z boundary and served as potential binding sites. A fraction of lattice particles were randomly selected to be inactive to represent a certain degree of surface modification by electron beam irradiation. To simulate the DNA hybridization, dynamic bonding functions are employed to form and break bonds between the active surface sites and the tail bead of any grafted DNA. When separated by a distance equal to or less than $2^{1/6}\sigma$, a harmonic bond was formed with $r_o = 2^{1/6}\sigma$ and $k = 165k_{\text{B}}T/\sigma^2$. Such a bond would break if subsequently the bond length equaled

or exceeded 1.4σ with a critical energy of $12.7 k_B T$. Each active surface site could only bind with one DNA strand at any given time.

Starting from an initial configuration, the time step was gradually increased to 0.015τ , where $\tau = (m_0\sigma^2/k_B T)^{1/2}$ is the reduced time unit. A Langevin thermostat with damping time 10τ was used for temperature control. For each simulation, the grafted DNA chains were first allowed to equilibrate over 84τ , during which the colloids were kept fixed in space. This was followed by a global equilibration period of $4.5 \times 10^5 \tau$. Statistics were then collected for another $4.5 \times 10^5 \tau$ with the surface binding configurations collected every 7.5τ . For 20 equally spaced modification levels between 0 and 100% 20 independent runs were performed.

Chapter 4: Programmable Surfaces for Reconfigurable Nanoparticle Assembly

4.1 Chapter Summary and Motivation

Remarkable progress has been made in the development of self- and directed-assembly approaches for construction of complex nanoparticle architectures. Strategies have been developed that enable precise control over the composition and geometry of 2D and 3D assemblies with potential application in optical metamaterials, among other areas. However, the resulting structures are typically static, offering only a single structural arrangement of the nanoparticle building blocks. In this work, the power of DNA-linked nanoparticle assembly is coupled with a grayscale patterning technique to create programmable surfaces for reconfigurable assembly of gold nanoparticles. Direct grayscale patterning of DNA monolayers by DNA-EBL enables the production of surfaces with nanometer-scale control over the density of functional DNA. This enables thermodynamic tuning of the surface with spatial resolution at the scale of individual nanoparticles. Three proof-of-concept schemes are presented to illustrate the potential in this approach to achieve temperature-dependent structural reconfiguration in 2D nanoparticle arrays. First, oriented assemblies of gold nanorods in rectangular arrays show temperature-dependent ordering effects that result in temperature-controlled polarization-dependent optical properties. Second, gold nanorods are assembled on a 2D square grid and exhibit orientation reconfiguration with increasing temperature. Finally, 2D circle-array patterns drive the size-selective assembly from a bimodal suspension of spherical particles to produce temperature-dependent array configurations.

4.2 Introduction

There is significant technological interest in nanoparticle-based devices for diverse applications in fields from optoelectronics^{223,224} to energy harvesting^{225,226} and even medical diagnostics and therapeutics.²²⁷⁻²²⁹ Research exploring self-assembly of complex architectures from nanoscale building blocks is helping define new ways to build materials with novel properties. A great deal of progress has been made in understanding and manipulating the fundamental forces⁵ responsible for governing these processes and a large number of different self-assembly strategies have been developed.⁷ Among these myriad assembly strategies, DNA-based assembly offers unrivaled flexibility in tuning the structure and properties in such nanoparticle superstructures.^{85,86,88} However, in applications such as the fabrication of optical metasurfaces, top-down lithographic approaches have dominated due to the ability to fabricate arbitrary structures with precise control over the short- and long-range order.²³⁰⁻²³³ The resulting structures, however, are typically polycrystalline with significant edge and surface roughness, which limit optical performance due to scattering losses.^{234,235} In addition, they are usually planar, monolithic structures and strongly adhered to the substrate, which limit the range of optical properties and preclude structural tunability, respectively. Directed assembly strategies make the large diversity of nanoparticle sizes, shapes and compositions available for fabrication of metasurfaces and other devices by combining the site-specific positioning of a top-down process to define local forces that guide the assembly of individual nanoparticles. In particular, anisotropic nanoparticles such as gold nanorods hold particular interest due to their polarization-dependent optical properties²³⁶⁻²³⁹. Several directed assembly methods for oriented nanorod assembly have been developed, including

nanoscale chemical patterning,²⁴⁰ capillary assembly in nanoscale trenches^{32,241,242} and block copolymer lithography.²⁴³

One of the most exciting advances in optical metasurfaces is the development of structurally reconfigurable systems that allow the tuning of optical properties based on a modification of the spatial organization of the optical elements.²⁴⁴ This has been achieved by a number of different approaches, including the use of MEMS-based devices that can change the distance between elements²⁴⁵⁻²⁴⁸ or their orientation^{249,250}. Other approaches include mechanical deformation of metasurfaces with flexible substrates,^{251,252} manipulation of multiple, stacked metasurfaces to change their relative in-plane^{253,254} or out-of-plane²⁵⁵ positions and the use of phase-change materials.²⁵⁶⁻²⁵⁸ However, most of these approaches have only been demonstrated in the GHz and low-THz regimes and adapting these techniques to visible light frequencies is a formidable task. The main challenge with structural reconfiguration for metasurface devices operating at shorter wavelength is that the size and periodicity of the elements approaches the nanometer length-scale. At such small feature sizes, most of the aforementioned reconfiguration strategies are not effective due to the high precision required to manipulate the elements. Reconfigurable systems that do operate at visible frequencies do so by controlling the surrounding materials, rather than the individual elements.^{252,257} Directed assembly of nanoparticles with DNA offers an opportunity to bridge this divide by using top-down processes to guide assembly globally with bottom-up assembly for local structural control by tuning thermodynamic interactions. Recently, a directed assembly approach combining EBL and DNA-based assembly was applied to fabricate arrays of stacked nanoparticles with tunable interparticle and particle-substrate distances.¹⁰⁴ This work demonstrates one type of structural reconfigurability for dynamic

modulation of optical properties by changing the nanoparticle-substrate plasmonic coupling. However, as with most top-down fabrication processes, the position of each stack of particles remains fixed according to the 2D lattice prescribed by the EBL patterning step.

The DNA-EBL process described in previous chapters is fundamentally different from most top-down lithographic approaches as it allows grayscale patterning. This chapter demonstrates the use of grayscale DNA-EBL to modulate local thermodynamic interactions, thereby achieving temperature-controlled in-plane reorganization of nanoparticle arrays toward the fabrication of structurally reconfigurable metasurfaces. Reconfigurable assembly in these systems is demonstrated by three separate patterning and assembly strategies illustrated in Figure 4.1. First, temperature-controlled ordering is shown in 2D rectangular arrays of oriented gold nanorods (Figure 4.1a) that transition from a more disordered state at low temperature to a more ordered state at high temperature. This transition results in a modification of the optical properties with the more ordered structures providing stronger polarization-dependent light scattering.

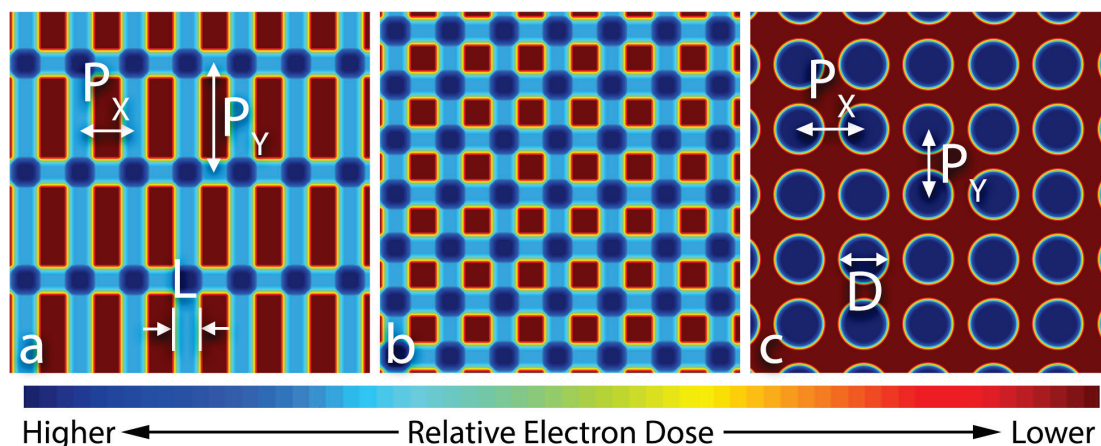


Figure 4.1 Schematic illustration of patterning schemes used in this work showing qualitative electron dose profiles for a) rectangular grid patterns (section 4.3.1) with transverse and longitudinal pitch (P_x and P_y) and linewidth (L), b) square grid patterns with $P_x = P_y$ and circle arrays with diameter (D) and $P_x = P_y$.

Second, gold nanorods are assembled onto a patterned square grid (Figure 4.1b) where the preferred nanorod orientation (vertical, horizontal, diagonal and out-of-plane) is strongly temperature-dependent. Finally, spherical particles from a mixed suspension containing a bimodal distribution are assembled on grids of circular patterns (Figure 4.1c) such that the system switches between multiple lattice configurations with increasing temperature.

4.3 Results and Discussion

4.3.1 *Temperature-Controlled Ordering in 2D Gold Nanorod Arrays*

The oriented assembly of gold nanorods was achieved by the general strategy outlined in section 2.3.3. However, rather than expose the DNA monolayer with high doses ($>4000 \mu\text{C}/\text{cm}^2$) to achieve binary patterning with isolated landing sites, lower doses were applied to achieve grayscale patterning. For these experiments, the goal was to pattern a regular grid of rectangular landing sites and study the degree of nanorod ordering on these sites to find the largest response to changes in temperature. The parameter space for these experiments is quite large including a number of potential variables related to the nanorods (size, aspect ratio, end curvature, concentration and polydispersity), the DNA (binding energy, length and nominal surface density), the patterned substrate (length/width of landing sites, pitch in x/y directions, dose and dose profile) and the assembly conditions (pH, salt concentration and temperature). For the purposes of simplification, many of these conditions were fixed based on previous experiments and these studies focus on just a few, namely nanorod size (and, indirectly, nanorod end-curvature), patterning conditions (geometry, dose) and temperature. Two batches of nanorods were selected with nominal lengths of 148 and 124 nm, both with nominal widths of 40 nm (NR2 and NR3 in Table 2). The nanorods with higher aspect ratio (NR2) were hypothesized to demonstrate improved

orientation control, however, the longitudinal plasmon resonance of the shorter rods (NR3) is blue-shifted (from 850 nm to 780 nm), which is within a reasonable range for optical measurements. The pattern geometry was fixed to provide landing sites with a pitch in both directions (transverse and longitudinal – P_X and P_Y) such that there would be a nominal 60 nm spacing between particles in both directions. This pitch was chosen intentionally to provide a small enough spacing between lattice sites such that particles could interact with more than one site. This is in contrast to the binary patterned surface in Figure 2.6a, where the pitch was controlled to specifically avoid particles interacting with multiple sites. A series of screening experiments was conducted to determine reasonable patterning conditions for electron dose (500, 1000, 1500, 2000 $\mu\text{C}/\text{cm}^2$), linewidth ($L = 40, 50, 60$ nm) and assembly temperature (25, 32.5, 40, 47.5 °C). The landing site sizes were effectively controlled by the linewidth to provide different degrees of geometric confinement: from 40 – 60 nm wide \times 150 – 170 nm long for NR3 and 40 – 60 nm wide \times 130 – 150 nm long for NR2.

An example of one such experiment for both types of nanorods is shown in Figure 4.2 for patterns with $L = 60$ (40 nm-wide landing sites) and electron dose of 1,000 $\mu\text{C}/\text{cm}^2$ at four different assembly temperatures from 25 – 47.5 °C. Visual inspection of the SEM images and FFT shows increased ordering with increasing temperature and the degree of ordering was quantified by application of two different image analysis approaches. First, a 2D autocorrelation function (ACF) approach was applied to investigate the periodic ordering in both horizontal and vertical directions. Second, a particle detection approach was applied to analyze the orientation of individual nanorods. Autocorrelation methods have been previously applied to quantify the degree of ordering in self-assembled systems.²⁵⁹⁻²⁶² In this work, a modified approach is used and described

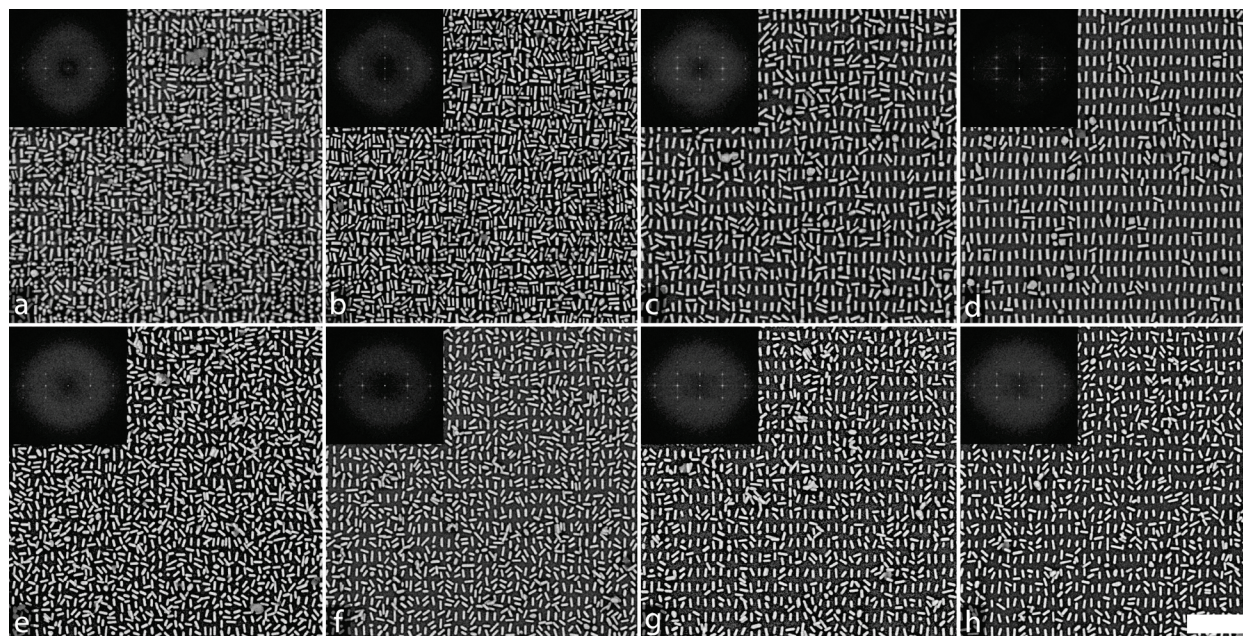


Figure 4.2 SEM images and FFT (inset) of gold nanorods assembled on suspended silicon nitride substrates patterned by DNA-EBL. This is a representative example of assembly conditions demonstrating a large change in ordering as a function of assembly temperature with NR3 (a-d) and NR2 (e-h). The substrates were exposed with a $1000 \mu\text{C}/\text{cm}^2$ dose to create 40 nm-wide landing sites. Assembly temperatures are 25, 32.5, 40 and 47.5 °C from left to right. (Scale bar is $1\mu\text{m}$)

in detail in section 4.5.4, which establishes ordering parameters, ξ_T and ξ_L , as measures of the degree of ordering in the 2D lattice. These values are plotted for all experimental conditions in Appendix A (Figure A.1 and Figure A.2) and clearly show that ordering increases with increasing dose and decreasing landing site width. These results confirm the hypothesis that a higher degree of geometric confinement results in a higher degree of ordering. In addition, aspect ratio plays an important role as the longer nanorods (NR2) show higher overall ordering parameters than the shorter nanorods (NR3). The results also indicate that the degree of ordering increases with increasing temperature, but this effect saturates at high doses and small landing site widths. This illustrates a key metric for this work where the goal is to find conditions where the *change* in ordering (*i.e.* $\Delta\xi_T$ and $\Delta\xi_L$) is greatest over a given temperature range as shown in Figure 4.3. These

data provide information related to the maximum reconfigurability, which still occurs at smaller landing site widths, but at more moderate conditions in terms of electron dose.

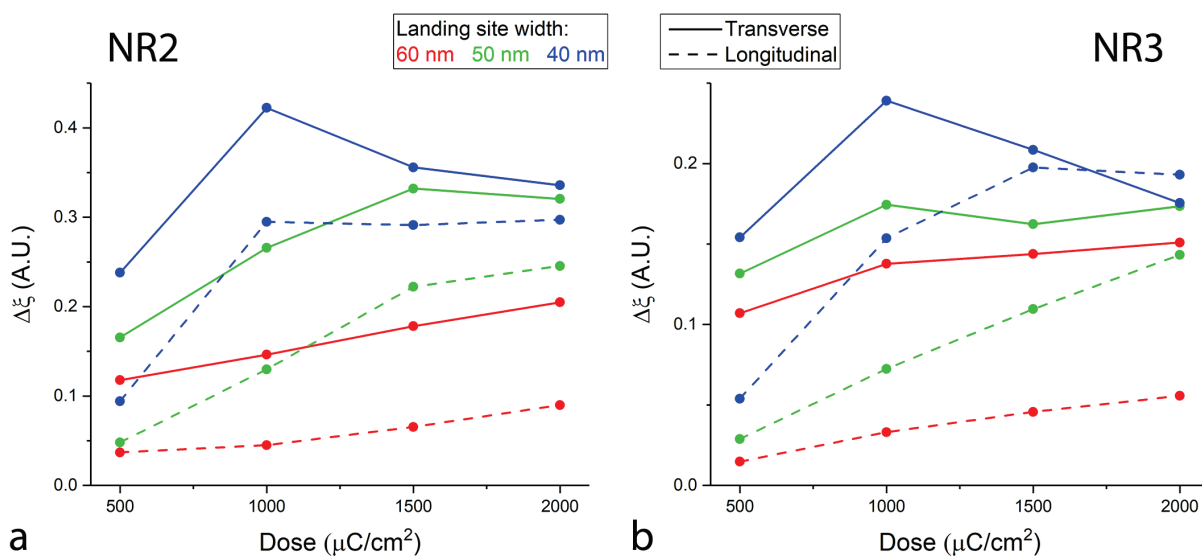


Figure 4.3 Change in ordering parameter ($\Delta\xi$) from low-to-high temperature (25 – 47.5 °C) for a) NR2 and b) NR3 in the transverse and longitudinal directions with different landing site widths and electron doses.

While the ACF data provide useful insight into the correlation between nanoparticle positions and the patterned landing sites, the degree of orientation control is only indirectly evaluated based on the amplitude of the ACF profile. In terms of optical properties, the precision of the assembled 2D lattice is critical when plasmonic coupling results in the development of surface lattice resonance (SLR) modes. However, for the arrays presented here, this type of coupling is not expected to be strong as the lattice periodicity is significantly smaller than the wavelength of the plasmon resonance.²⁴⁴ Instead, the degree of orientation control likely has a greater impact on the optical properties of these arrays due to polarization-dependent light scattering. As such, a different image analysis method is applied to extract the orientation of the

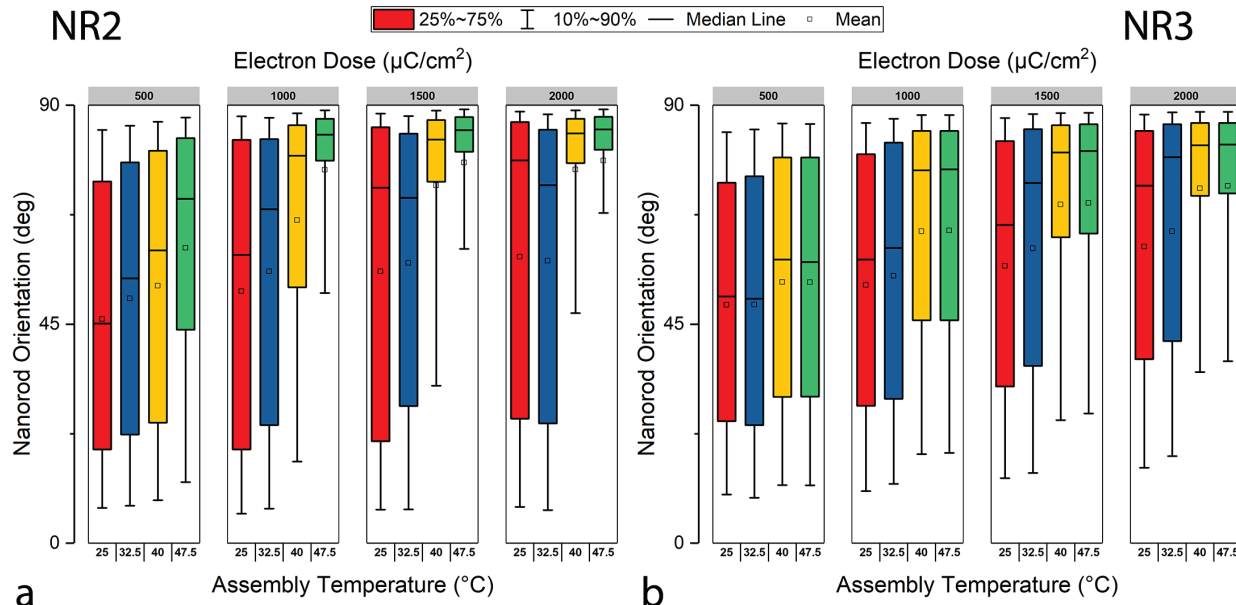


Figure 4.4 Box plots showing nanorod orientation for a) NR2 and b) NR3 as a function of assembly temperature and electron dose for 40 nm-wide landing sites.

nanorods in each experiment by a particle detection method. The orientation data for the 40 nm-wide landing sites are shown in Figure 4.4 (the data for other experiments are included in Appendix A, Figure A.3-Figure A.6) and the total change in orientation ($\Delta\theta$) with temperature is shown in Figure 4.5. Similar to the ACF data, these data show improved alignment with increasing temperature, increasing dose and decreasing landing site dimensions. They also show that the higher aspect ratio nanorods achieve a greater degree of alignment overall and show larger maximum $\Delta\theta$. However, these data also indicate that the transition to increased alignment with increasing temperature is more abrupt compared to the change in ξ .

The reconfigurable assembly in these systems can be described as competition between maximization of the binding enthalpy and the dynamics of particle adsorption, desorption and surface diffusion. As shown in the size-selective assembly work in Chapter 3, the equilibrium

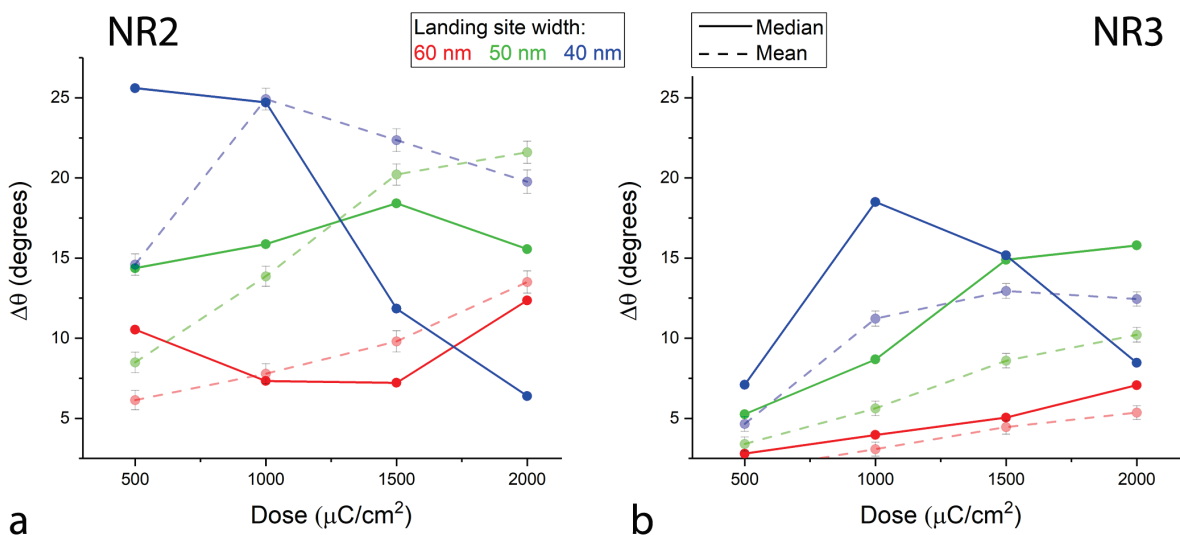


Figure 4.5 Change in nanorod orientation ($\Delta\theta$) for a) NR2 and b) NR3 shown for different landing site widths and electron doses. As these distributions are highly skewed (see Figure 4.4 and Appendix A), the median is the most reasonable metric and mean values with error bars ($\pm\sigma$) are plotted for reference.

surface density of particles is directly dependent on the surface DNA density. In the case of a surface with nanometer-scale DNA-density gradients, this has direct implication on the position and orientation of the adsorbed particles. In effect, the grayscale patterning by DNA-EBL creates a surface with a thermodynamic landscape that changes with temperature. This can be illustrated by close examination of the images in Figure 4.2a-d for NR2 nanorod assembly, which show significant variations in the character of the nanoparticle films that are not fully captured by either the ACF or orientation analysis. At low temperature (Figure 4.2a), there are three distinct nanoparticle orientations: vertical, horizontal and out-of-plane. These configurations arise due to the geometric confinement due to patterning and the relatively high strength of the individual DNA linkages at low temperature. In addition to the higher bond strength at low temperature, the out-of-plane orientation for the NR2 nanorods is also related to the large radius of curvature on nanorod ends, which will be explored and explained further in section 4.3.2. The horizontal particles bridge

neighboring landing sites and result in a bimodal distribution at low temperature as shown in the violin plots in Figure 4.6a. As the temperature is increased, both of these configurations become energetically unfavorable due to the lower DNA density between landing sites and the vertical orientation dominates, resulting in a skewed unimodal distribution. However, for larger landing sites, the NR2 nanorods also show a significant number of nanorods with orientation near 60° at higher temperature (see violin plot in Figure A.7). This can also be seen in the images in Figure 4.2c,d where there are pairs of angled particles occupying single landing sites. In comparison, the assemblies of the shorter NR3 nanorods (Figure 4.2e-h) exhibit neither the out-of-plane assembly, nor the bimodal distribution due to horizontal alignment at low temperature (Figure 4.6b). This is likely due to the shorter nanorod length and higher end-curvature, resulting in a more gradual increase in ordering and alignment. In general, there are two components to the nanoparticle assembly process on the rectangular grid patterns. The first component relates to the registry between particles and the landing sites, which is refined with increasing temperature as evidenced by the gradual change in ξ and θ for the NR3 nanorods. The second component is a more abrupt

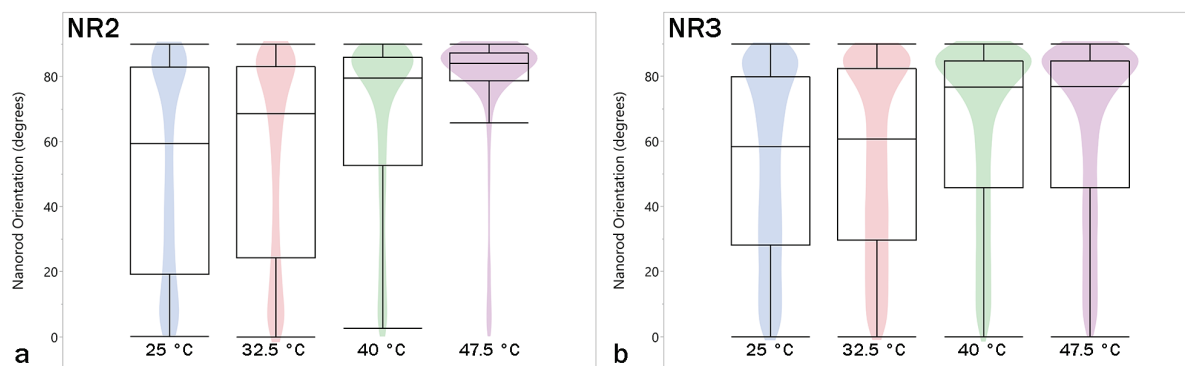


Figure 4.6 Violin plots of nanorods on rectangular grid patterns with 40 nm-wide landing sites and $1000 \mu\text{C}/\text{cm}^2$ electron dose showing a) bimodal distribution of NR2 nanorods at low temperature compare to b) more random orientation of the NR3 nanorods. Both converge to a skewed unimodal distribution at high temperature. (Additional violin plots for other conditions are shown in Appendix A, Figure A.7 – Figure A.10)

orientation switching behavior favoring a single orientation along the landing sites at higher temperature as seen with the NR2 nanorods.

The optimization of patterning conditions achieved by these experiments indicates that small landing-site widths are favorable for better orientation control and larger changes in orientation with temperature. However, while this work provides some guidance for general application, even in the simple case of a rectangular grid of oriented nanorods, the optimum pattern parameters will depend on several factors including the nanorod size (and size distribution), aspect ratio, DNA length and the desired periodicity. While the magnitude of the electron dose primarily sets the relative difference in DNA density between the landing sites and the interstices, it also has an indirect influence on the landing-site size due to proximity effects. Even though the elimination of the bulk substrate reduces proximity effects, there is still some electron scattering, which effectively increases the linewidth with increasing dose. This explains the general trend of increased ordering with electron dose for the larger landing sites (50 – 60 nm) as the landing-site size is effectively decreasing with increasing dose. However, for the smallest landing sites, the effect of grayscale patterning can clearly be seen as the change in ordering (both by $\Delta\xi$ and $\Delta\theta$) decreases at higher doses as the patterns become more binary and highly ordered assemblies are generated even at lower temperatures. It should also be noted that this low-temperature ordering behavior is probably enhanced by the “overlapping” nature of the exposures as shown in Figure 4.1a. This results in three nominal dose levels and the lower DNA-density overlapping regions have an impact on nanoparticle adsorption even at low temperature, an effect that is exploited in section 4.3.2. The overall change in ordering would likely be enhanced by eliminating (or modifying) the relative dose in these regions.

Optical spectroscopy and finite-difference time-domain (FDTD) simulations were applied to investigate the effects of nanorod ordering and alignment on the optical properties of these arrays. The NR3 samples were used for these studies as the longitudinal plasmon resonance is blue-shifted to approximately 780 nm, which is within range of the spectrometer. Specifically, the polarization dependence of the reflectance was measured for the nanorod arrays assembled at low and high temperatures to assess the impact of ordering on the optical properties. The data shown in Figure 4.7 highlight the impact of the reconfigurable assembly on the optical properties. First, the data show a significant increase in reflectance with polarization along the longitudinal axis (P_L) of the nanorods compared to the transverse direction (P_T) which is accompanied by a change in spectral shape. This can be seen in the optical microscope images in Figure 4.7 as well for both transmitted (d-e) and reflected (f-g) light, which show significant changes compared to the randomly oriented nanorod film that surrounds the four patterned regions. While arrays at both high and low temperature show some polarization-dependence, the magnitude is significantly larger for the high temperature case in Figure 4.7a compared to the low temperature case in Figure 4.7c due to a greater degree of nanorod alignment. For example, the change in reflectance with polarization (P_L vs P_T) is about 89% larger at 540 nm and about 61% larger at 650 nm for the high temperature case. The importance of grayscale patterning can be illustrated by analyzing the change in P_L reflectance with electron dose for the low temperature case (indicated by arrow in Figure 4.7c). As the electron dose increases, the DNA density for the landing sites increases relative to the patterned interstitial regions. As a result, the patterns show strong ordering and thereby strong polarization-dependent optical reflectance even at low temperatures, resulting in a less significant difference for the same patterning conditions when the temperature is increased. FDTD simulations of the NR3 nanorods are shown in Figure 4.7b and illustrate a polarization-

dependent reflectance that corresponds well to the experimental data. Light scattering by broadband reflection dominates the change in optical properties, while changes in absorption are

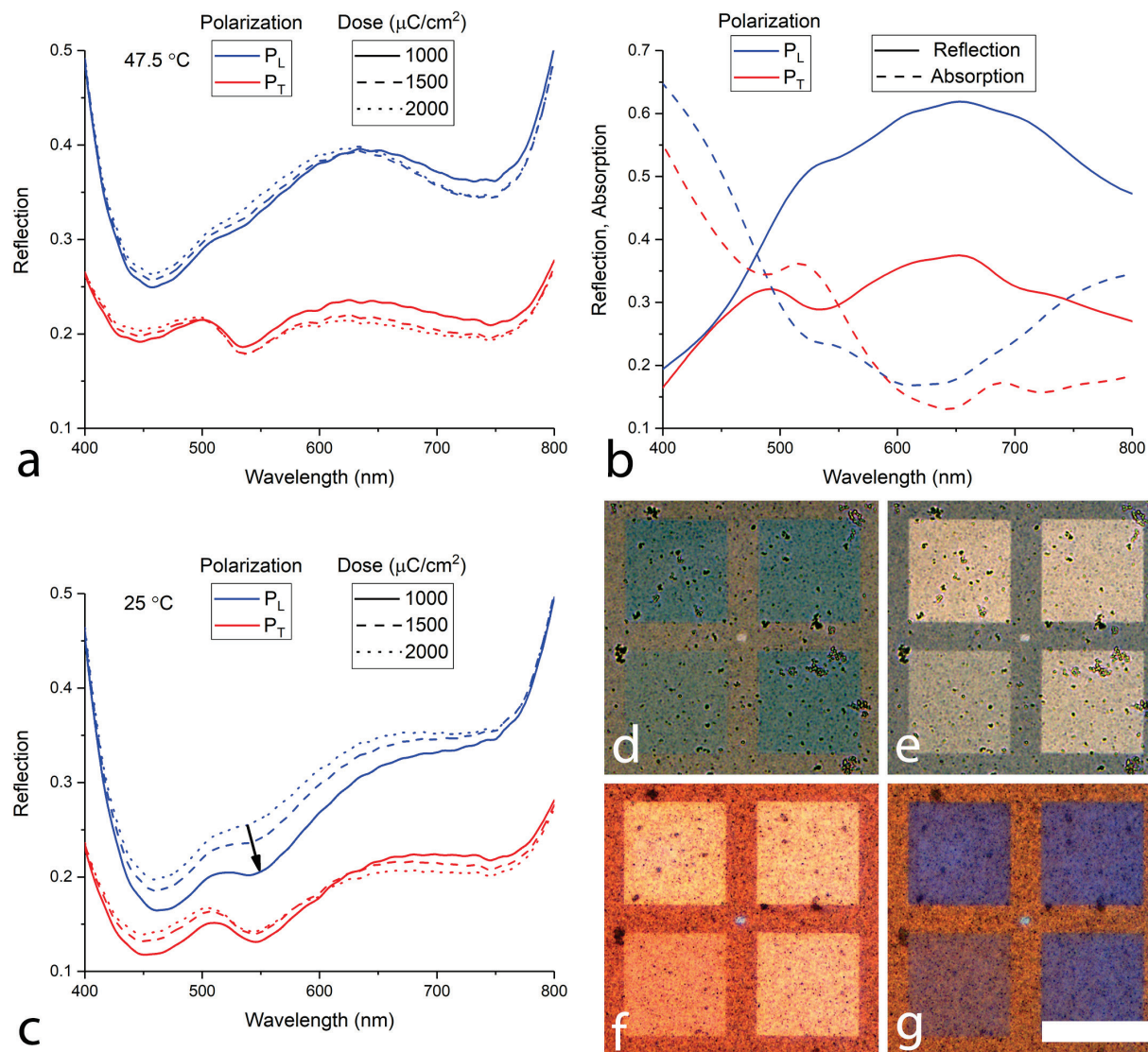


Figure 4.7 Optical spectroscopy and imaging of assembled NR3 nanorod arrays showing reflectance as a function of polarization (transverse – P_T, longitudinal – P_L) and electron dose for a) high temperature and c) low temperature. The arrow in c) indicates an increase in the change in reflectance with temperature for lower dose patterns. The FDTD simulations results (b) show reflection, transmission and absorption for aligned nanorods and reflection data correspond well with experiment. The optical images show polarization-dependence for NR3 assembled at 40 °C with 40 nm-wide landing sites in transmission with d) P_L, e) P_T and reflection with f) P_L and g) P_T. The electron dose is varied from 500 to 2000 μC/cm² counter-clockwise from lower-left. (Scale bar is 30 μm)

relatively small and correspond to the transverse (520 nm) and longitudinal (780) SPR modes. Differences between the experiment and simulation are likely due to the assumption of perfect nanorod alignment in the simulation and scattering from the rough silica sol-gel in experiments. In addition, while the simulation approximates all of the primary geometric and materials parameters of the experiments (nanorod size/shape, spacing, silica coating, substrate materials and thickness), it is not feasible to simulate the disordered structures for comparison, given the periodic boundary conditions.

4.3.2 Reconfigurable Assembly of Gold Nanorods on 2D Square Grids

The second patterning scheme for reconfigurable nanorod assembly is based on a square grid design as illustrated in Figure 4.1b. The patterning methodology is essentially the same as that in section 4.3.1, with $P_X = P_Y = 80$ nm. This spacing provides approximately 40 nm between parallel nanorods to minimize particle-particle interactions, but provides a close enough spacing such that particles can align in-plane along horizontal, vertical or diagonal directions and only occupy two landing sites. A DOE was constructed for the 2D grid patterns to evaluate the effects of landing site width (30, 40, 50 nm), electron dose (500, 1000, 1500, 2000 $\mu\text{C}/\text{cm}^2$) and temperature (25, 32.5, 40, 47.5 $^\circ\text{C}$). The results indicate that a moderate landing site width and dose was most effective in driving temperature-dependent reconfiguration. One such condition is examined here in detail (40 nm-wide landing site with 1000 $\mu\text{C}/\text{cm}^2$) as shown in Figure 4.8. Compared to the rectangular arrays studied in section 4.3.1, the grid-patterned surfaces do not have the large interstitial regions and as a result, the nanorod films are generally well ordered even at low temperatures. However, the preferred orientation of the nanorods changes based on temperature and nanorod geometry. Specifically, the nanorod arrays exhibit three distinct

orientations (orthogonal, diagonal and out-of-plane), with temperature-dependent probabilities. The orientation of each nanorod was extracted using image analysis and the percentage of each orientation is plotted in Figure 4.8i-j corresponding to the experiments in Figure 4.8a-h. Histograms of these orientations for both types of nanorods with 40 nm-wide landing sites at all

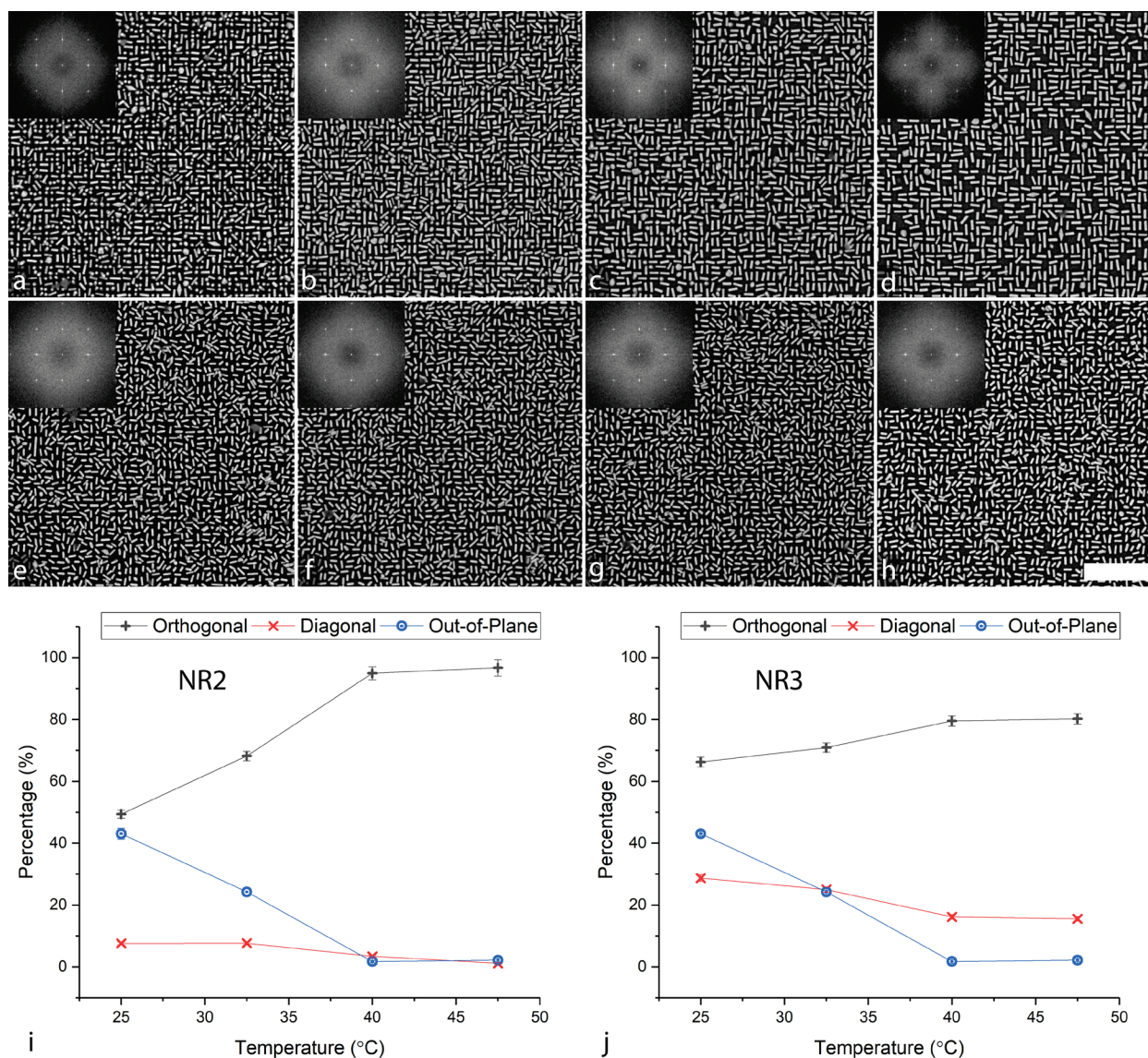


Figure 4.8 SEM images and FFT (inset) of reconfigurable assembly of Au nanorods on 2D square grids for 40 nm-wide landing sites and 1000 $\mu\text{C}/\text{cm}^2$ electron dose for NR2 (a-d) and NR3 (e-h). The assembly temperatures are 25, 32.5, 40 and 47.5 °C from left-to right (scale bar is 1 μm). Plots of nanorod orientation for the experiments in (a-h) showing the change in percentage of rods with each orientation for i) NR2 and j) NR3.

four doses are shown in Appendix A (Figure A.11 and Figure A.12) to illustrate the three preferred orientations and their evolution with assembly temperature.

The temperature-dependent nanorod orientation in these arrays is driven by a combination of factors including the patterning methodology and the nanorod geometry. The patterning scheme as outlined in Figure 4.1b shows that the 2D grid is patterned as a series of overlapping rectangles on a square grid, with the overlapping regions receiving twice the nominal dose. As a result, the surfaces in these 2D grids effectively have three levels of DNA-density in the unexposed, single-exposed and double-exposed regions. This results in a general decrease in the likelihood of diagonal adsorption with increasing temperature as the interstitial regions between next-nearest-neighbor lattice sites have lower DNA density than those between nearest-neighbor sites. Thus at higher temperatures, where the number of particle-surface linkages required for immobilization is higher, orthogonal orientations are preferred. At the lowest temperature for NR2, a significant number of out-of-plane oriented nanorods are present. This orientation is not observed at higher temperatures due to surface area differences following the same general mechanism that drives the size-selective assembly in Chapter 3. However, it is not clear at lower temperatures whether the out-of-plane rods are simply occupying “empty” spaces between the orthogonally and diagonally oriented rods or if they are competing for surface coverage. In addition, it is not clear why diagonally oriented rods are favored as the interstitial DNA density is lower for this orientation. To address these questions, one can look to the general problem of assembling anisotropic structures (dimers) on a 2D grid, which has conceptual significance in a number of fields from chemisorption on atomic lattices to thin film deposition and phase transformations.²⁶³ This problem has been studied extensively by random sequential adsorption (RSA) theory and

simulation for rod-shaped n-mers on different types of lattices. This includes square lattices with either nearest²⁶⁴ or next-nearest²⁶⁵ neighbor adsorption and, more recently, adsorption on triangular lattices.²⁶⁶ In general, most such studies are concerned with percolation across the surface and the jamming limit, defined as the maximum filling of a lattice for a given particle geometry. For 2-mers on a square lattice with nearest-neighbor alignments, this jamming limit is about 90.7%.²⁶⁷ However, there are no results in literature that consider the combination of nearest-neighbor and next-nearest-neighbor adsorption on a square grid, particularly with differential adsorption probabilities.

To study this more closely, a RSA simulation was developed which considered the nanorods as dimers randomly and irreversibly adsorbed on a 2D square lattice (50×50). This model makes several important physical assumptions and simplifications and considers only geometric effects of nanorod packing. First, the simulation assumes a sufficiently low temperature such that there is irreversible binding and no surface diffusion or desorption. Second, it simplifies the substrate as a square lattice of binding sites, ignoring the surface diffusion that necessarily plays a role in nanorod alignment on the grayscale-patterned surface. Third, as the simulation is run in the low temperature limit, no energetics are calculated to drive the simulation, rather the geometric effects on packing in different orientations were explored by changing the relative adsorption probability of the orthogonal and diagonal orientations. The jamming limit and relative numbers of orthogonally and diagonally oriented rods were calculated as a function of the diagonal adsorption probability, which directly (but nonlinearly) correlates to the fraction of rods with diagonal orientation (Figure 4.9a,e,i). These data confirm the previous literature reports and show a jamming limit of 90.6% ($\sigma = 0.246\%$) for the limit of no diagonal adsorption. As the probability of diagonal adsorption increases, the jamming limit quickly increases to 93.1% with a relative

adsorption rate of only $\sim 10\%$. As the thermodynamics of the DNA interactions alone should dominate in this system²⁶⁸ (i.e. ignoring the configurational entropy of the particles), these

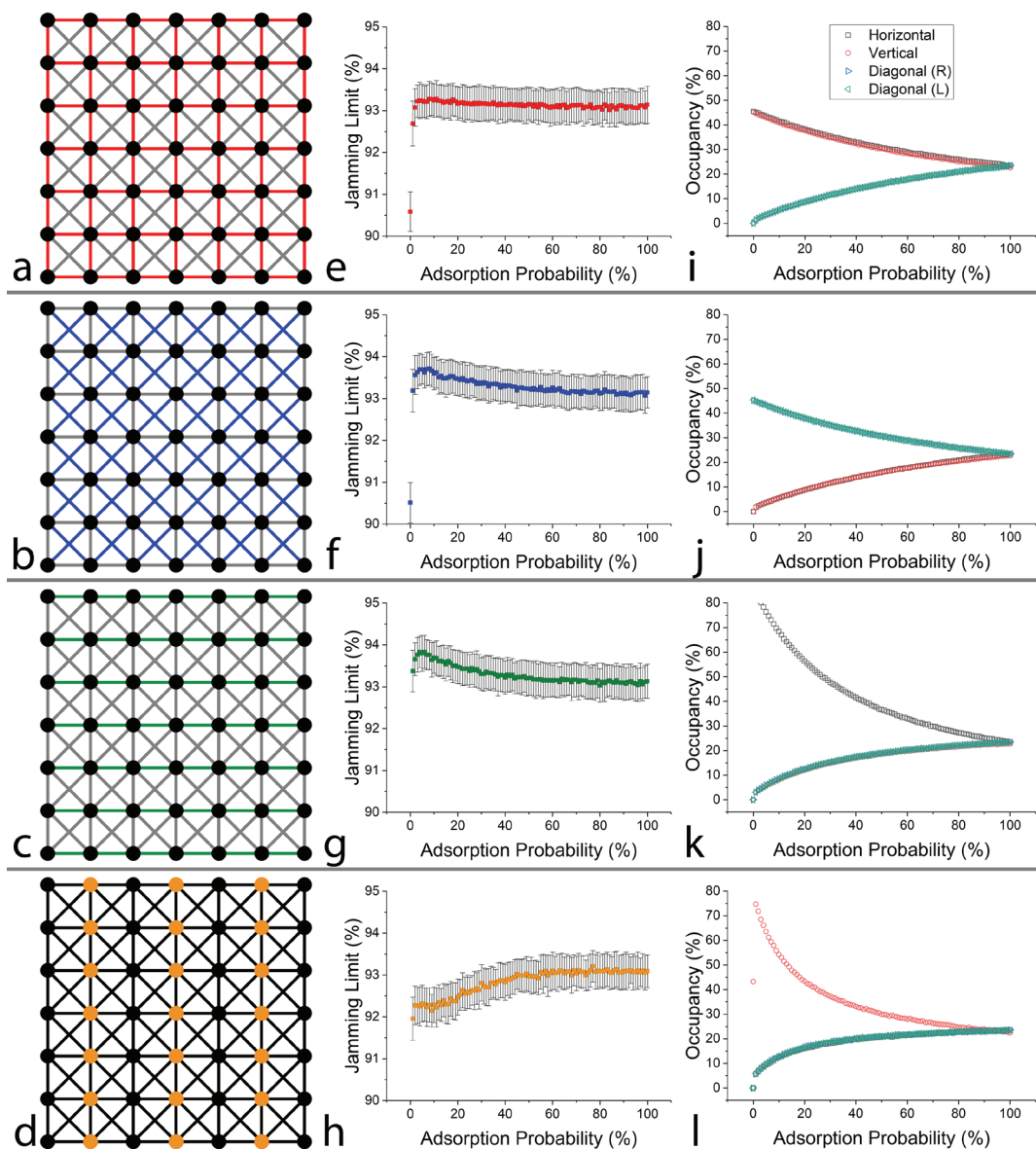


Figure 4.9 Results of RSA simulations for combination of nearest and next-nearest neighbor adsorption with four assembly schemes where a) orthogonal orientations are preferred and the adsorption probability for diagonal orientation is varied, b) diagonal orientations are preferred and the adsorption probability for orthogonal orientation is varied, c) horizontal orientation is preferred and adsorption probability for vertical and diagonal orientations are varied and d) adsorption at alternating column sites is preferred and the probability for adsorption at the other sites is varied with no direct change in orientation probability. Jamming limits (e-f) and particle occupancy by orientation (i-l) are shown for the corresponding adsorption schemes.

simulations can assist in interpreting the experimental results in the low temperature limit by considering increasing surface coverage as the primary driving force. First, the higher jamming limit achieved with a small concentration of diagonally bound rods indicates a small, but significant energetic driving force for a 2D assembly with both orthogonal and diagonally orientated rods. Second, the jamming limits calculated from the simulations indicate that the out-of-plane rods are in competition with in-plane rods for lattice sites as their numbers (over 40% in experiments) far exceed the 7-10% of expected vacancies.

The RSA simulations can also provide insight into other potential patterning schemes, as the interstitial DNA density in all directions and the landing-site DNA density can be precisely controlled. The approach of overlapping rectangles was chosen out of experimental convenience, but it is trivial to control the DNA density in arbitrary patterns and at high spatial resolution (~ 10 nm). Three simple variations on the experimental patterning scheme are investigated with RSA simulation as illustrated in Figure 4.9b-d. In the first case, diagonal orientation is preferred over orthogonal orientation and in the second, horizontal orientation is preferred over both diagonal and vertical, with equal probability for diagonal or vertical orientation. These are analogous to changing the interstitial DNA density with the landing-site DNA density unchanged. In the third case, adsorption at every other row of lattice sites is preferred with no specific preference for nanorod orientation. This is analogous to changing the DNA density on every other row of landing sites with uniform interstitial DNA density. The jamming limit is evaluated for all three of these scenarios and it is found that, in the first three cases (orthogonal, diagonal and horizontal preference), the jamming limit increases for mixtures of orthogonal and diagonal particles exceeds the nominal 93.1% jamming limit to different degrees at low concentrations ($< 10\%$) of the minor

orientations. At these concentrations, the jamming limit reaches values of $\sim 93.3\%$ (orthogonal preferred) and $\sim 93.8\%$ (both diagonal and horizontal preferred). While these are small increases, this could nevertheless be important in DNA-nanoparticle systems as the overall system tends toward maximum coverage (maximum enthalpic interaction of DNA-DNA hybridization) and could thus drive toward configurations that maximize the jamming limit. This behavior is distinct from the fourth case (every other column sites preferred) where the $\sim 93.1\%$ jamming limit is reached more gradually as adsorption probabilities at alternating rows approach parity.

The second primary consideration for evaluating the reconfigurable assembly in Figure 4.8 is related to the end-curvature of the nanorods. The scanning transmission electron microscope (STEM) images in Figure 4.10 show significant differences between the two batches of nanorods. The ends of NR2 nanorods have a significantly larger radius of curvature than the NR3 nanorods, which can have significant implications on DNA loading and subsequent assembly. It is clear from the preceding analysis that the out-of-plane NR2 nanorods must be competing with other

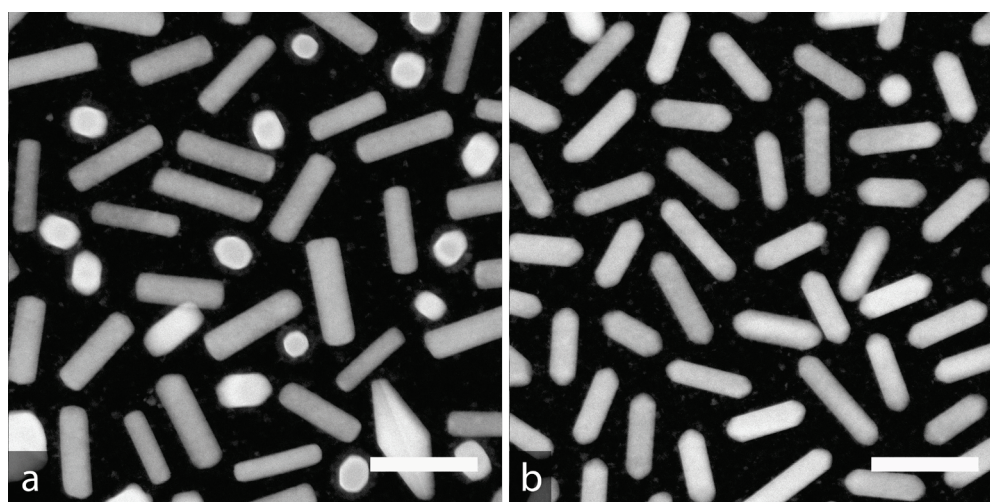


Figure 4.10 High-angle annular dark field (HAADF) STEM images of randomly assembled a) NR2 and b) NR3 nanorods showing differences in shape and size. Note the out-of-plane NR2 nanorods in a) identified by increased brightness, indicating larger thickness along beam direction. (Scale bars are 200 nm)

orientations for lattice sites at low temperatures. However, a geometric analysis similar to that in section 3.3.3 reveals that even though the radius of curvature is different, both the sides and ends of a 40 nm-wide nanorod would fully intersect the DNA on a 40 nm-wide landing site, to achieve maximum DNA binding. The in-plane oriented rods, however, interact with a surface area of about 6853 nm² each, while two out-of-plane rods interact with about 6418 nm² (these calculations assume the rods are perfect 40 × 148 nm cylinders with uniform DNA coverage). This geometric analysis coupled with an expected lower DNA loading on the flattened ends,⁷⁴ results in a small, but significant energetic favorability for the in-plane orientation. One likely explanation for high concentration of out-of-plane rods is that the low temperature structures are in a kinetically trapped state. Since a stochastic process determines the initial orientations of adsorbed nanorods and at low temperature, the out-of-plane nanorods may be effectively “frozen” in their initial conformation (although some surface diffusion must occur given the degree of ordering). The interstitial DNA between landing sites should result in a driving force for edge-bound nanorods to maximize DNA-DNA interactions, but the out-of-plane nanorods block this transformation. While the more curved ends of the NR3 nanorods appears to prevent them from standing on-end, a close examination of Figure 4.8e reveals that there are rods occupying single sites, but they have “fallen over” to some extent. In addition, the assembly of the NR3 nanorods does not appear to be as sensitive to temperature changes in the range of this study. This is likely due to the increased curvature of the nanorod ends resulting in higher DNA density and a stronger interaction with the lattice sites relative to the interstitial DNA.

4.3.3 *Reconfigurable and Size-Selective Assembly of Spherical Gold Nanoparticles*

The third approach for reconfigurable assembly is based on the circle-array patterning

scheme outlined in Figure 4.1c. In addition to the different patterning geometry, a different nanoparticle system was applied in this work utilizing spherical gold nanoparticles of two different sizes (30 and 80 nm diameter). This approach allows the combination of high-resolution patterning at the individual particle level with the size-selective assembly shown in Chapter 3. Similar to the nanorod patterning schemes, the parameter space is quite large and a DOE was conducted to find combinations of electron dose, circle diameter (D) and the x/y pitch (P_X and P_Y) that provide large configuration changes with temperature. However, unlike the nanorod assemblies, it is difficult to quantify the changes in assembly as they can be quite diverse depending on the changes in geometry. Instead, two specific cases are examined here which illustrate some of the diversity that

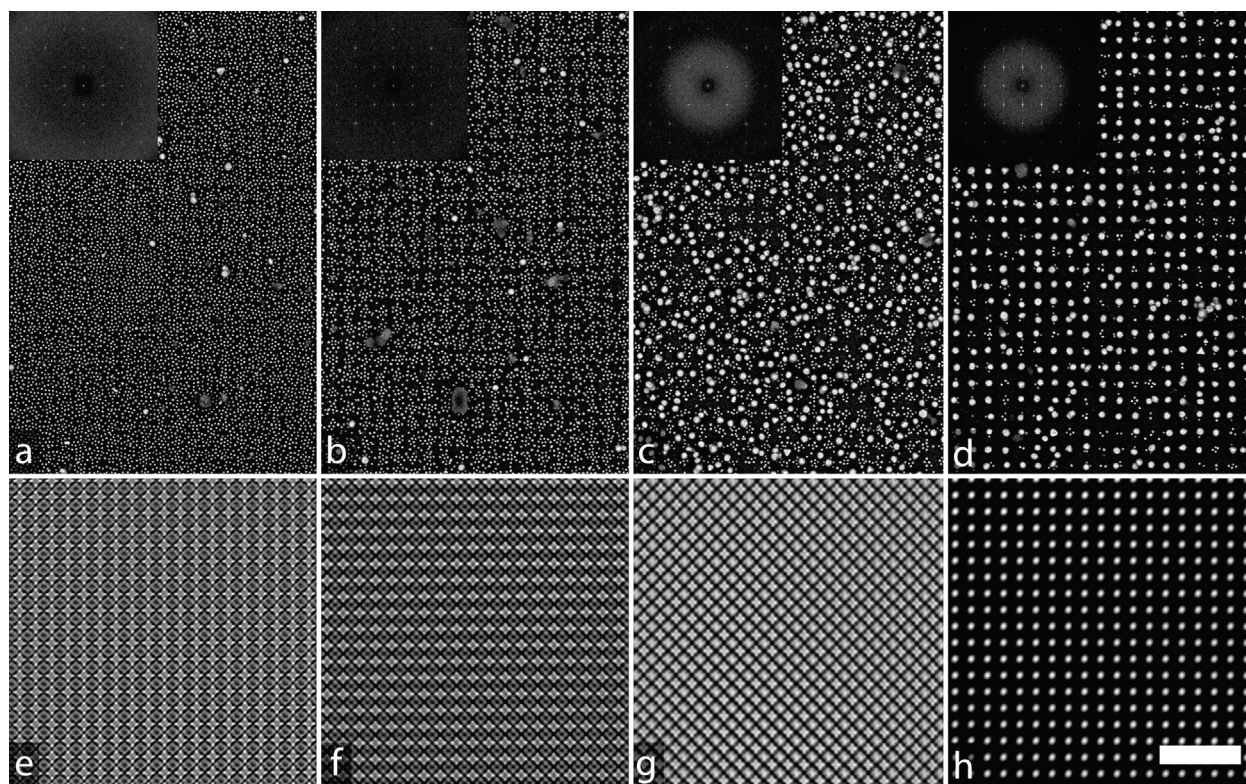


Figure 4.11 SEM images (with FFT inset) of small (30 nm) and large (80 nm) spherical gold nanoparticles assembled on circle-array patterns with both circle diameter and x/y pitch of 200 nm. This results in a temperature-dependent transformation in surface coverage with a) 25, b) 32.5, c) 40 and d) 47.5 °C. These images are processed to produce the corresponding hard-threshold FFT-filtered images shown in (e-f). (Scale bar is 1 μm)

result from a combination of size-selectivity and geometric confinement effects. The first example is shown in Figure 4.11 for patterns with an array of 200 nm-wide circles with an x/y pitch of 200 nm and an electron dose of 1000 $\mu\text{C}/\text{cm}^2$. The resulting patterns show a nearly homogenous disordered film dominated by small particles at 25 °C, with some ordering of “vacancies” where the DNA density is lower. At 32.5 °C, the film is still dominated by small particles, but a somewhat ordered hole-array emerges. At 40 °C, the film begins to shift to a somewhat disordered mix of small and large particles. The patterned circles are largely devoid of any small particles and instead many of the large particles are positioned at these sites, however the large particles are also competing with the small particles in the unexposed regions. At 47.5 °C, most of the small particles

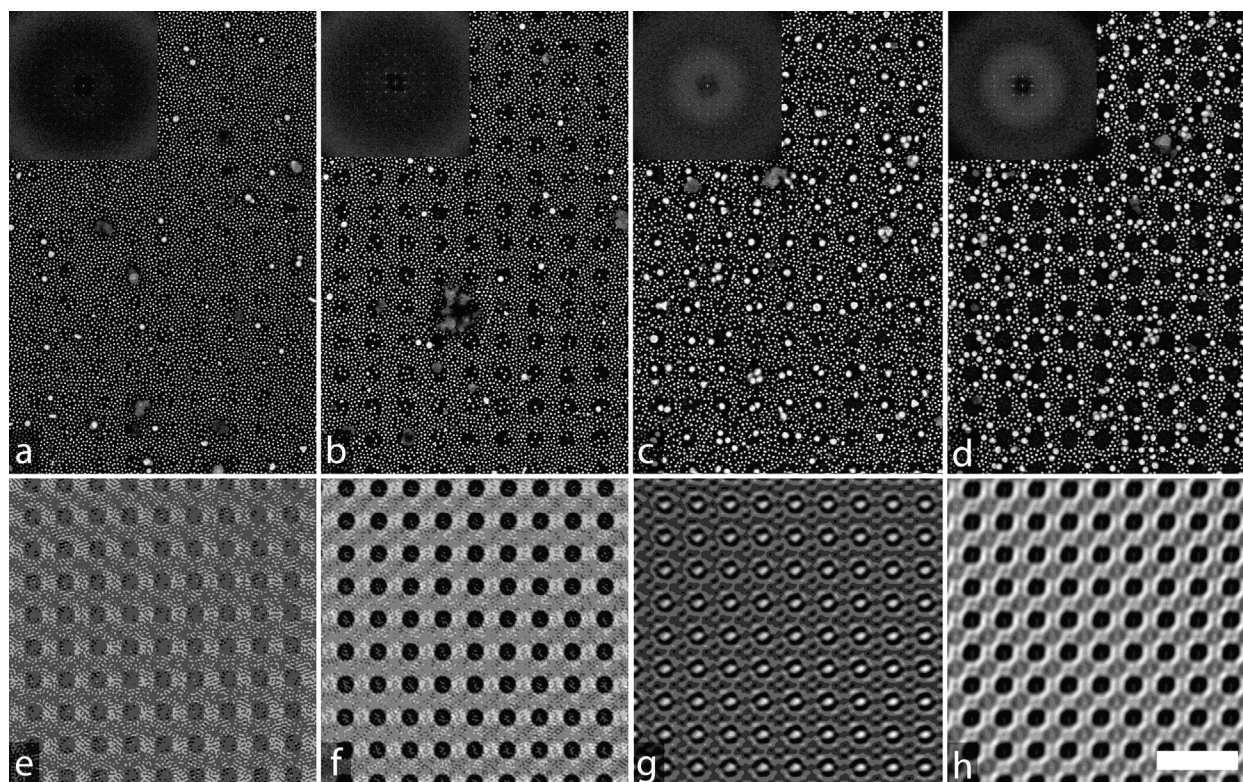


Figure 4.12 SEM images (with FFT inset) of small (30 nm) and large (80 nm) spherical gold nanoparticles assembled on circle-array patterns with circle diameter of 220 nm and x/y pitch of 400 nm. This results in a temperature-dependent transformation in surface coverage with a) 25, b) 32.5, c) 40 and d) 47.5 °C. These images are processed to produce the corresponding hard-threshold FFT-filtered images shown in (e-f). (Scale bar is 1 μm)

have desorbed and the lower DNA density inside the circles results in large particles adsorbed in an ordered array at the interstitial sites that received no electron irradiation (other than proximity dose).

The second example is shown in Figure 4.12 for a circle-array pattern with a circle diameter of 220 nm, an x/y pitch of 400 nm and an electron dose of 900 $\mu\text{C}/\text{cm}^2$. At low temperature (25 °C), this results in a small particle-dominated film with lower density of small particles in the exposed regions. At 32.5 °C, the film is still dominated by small particles, but the circles become a fairly well-defined hole array, with just a few small particles in each circle. At 40 °C, a transition occurs and the circles are mostly filled with large particles due to the size-selective assembly mechanism described in Chapter 3. At 47.5 °C, the circles are devoid of particles, but the proximity dose at the edges of the circles causes preferential adsorption of the large particles along their perimeter. In general, both of the patterning examples shown here are very sensitive to small changes in dose, circle diameter and x/y pitch. The hard-threshold FFT filtering also exaggerates the ordering in these films, but is useful in guiding observation.

4.4 Summary and Outlook

This work demonstrates the use of DNA-EBL to create programmable surfaces for reconfigurable nanoparticle assembly by grayscale patterning. Three different patterning strategies were demonstrated as a proof-of-concept and illustrate the power and potential of this method for creating nanoparticle assemblies that can undergo structural reconfiguration with changes in temperature. The grayscale patterning methods that enable nanometer-scale control of DNA density are fundamental to this capability as none of these strategies would be possible with traditional binary-patterned surfaces. In the first example, structural reconfigurability was

demonstrated by transformation of relatively disordered films of gold nanorods into oriented 2D arrays. The ordering and alignment in these systems was characterized by autocorrelation and particle analysis from SEM images and confirms the role of interstitial DNA enabled by grayscale patterning in driving the reconfigurability. These arrays showed polarization-dependent light scattering properties that is tunable with assembly temperature due to increased ordering and alignment at higher temperatures. Assembly of nanorods on 2D square grids resulted in three general particle orientations (orthogonal, diagonal and out-of-plane), which occur in different ratios at different temperatures. This phenomenon was shown to depend on nanorod geometry in addition to patterning and assembly conditions. RSA simulations were applied to investigate the details of jamming in these systems, which allow both nearest neighbor and next-nearest neighbor configurations. The results of these simulations coupled with thermodynamic considerations of DNA binding (i.e. drive to maximize surface coverage) indicate that the low temperature configurations are likely kinetically trapped non-equilibrium states. Finally, exposure of circle-array patterns was coupled with size-selective assembly from a bimodal suspension of spherical nanoparticles. These studies demonstrated the ability to switch between different 2D structures as a function of temperature by carefully controlling the patterning geometry and dose relative to the particle size.

Future work in this area should focus on developing systems that are likely to drive stronger changes in optical properties. The primary considerations should be selection of nanoparticles with uniform size distributions and faceted shapes that will couple strongly with the substrate to form nanocavity modes. This would enable coupling the in-plane reconfigurability of these systems with the out-of-plane reconfigurability shown in similar systems.¹⁰⁴ In addition, methods for *in situ*

observation of these structures would be critical for better understanding of critical temperatures rather than the rather large discrete steps examined here. Both *in situ* electron microscopy for visualization of the individual particle assembly as well as *in situ* optical spectroscopy to capture changes in optical properties would be invaluable. It would also be interesting to compare experimental results from the 2D grid patterns with a more sophisticated Monte Carlo approach.^{269,270} Compared to the simple geometric considerations in the low-temperature RSA simulations presented herein, such an approach can take into consideration the configurational energy of the system and account for temperature-dependent transformations through surface diffusion and desorption as well as particle-particle interactions. Such dimer models of nearest-neighbor and next-nearest-neighbor systems have been studied in the context of understanding confinement effects in strongly correlated quantum systems.²⁷¹ It is possible that Molecular Dynamics simulations could be utilized to extract some of the fundamental parameters (diffusion constants, etc.) that could then be applied to the more computationally efficient Monte Carlo methods. Finally, engineering the DNA sequences used in this type of assembly should enable improvements in the fidelity of assembly (shorter DNA length) and modify the useful temperature range (different number or strength of base-pair interactions) for particles of different sizes. In addition, this work focuses only on particle-substrate interactions, but coupling this with particle-particle interactions by appropriate DNA design could result in self-assembled 2D assemblies with crystal structures not present in 3D superlattices.

4.5 Experimental Methods

4.5.1 Substrate Fabrication, DNA Functionalization and Nanoparticle Assembly

Substrate fabrication, substrate functionalization, nanoparticle functionalization and nanoparticle assembly were carried out according to the procedures outlined in sections 2.5.1 and 2.5.2.

4.5.2 DNA-EBL Patterning

DNA-EBL patterning was carried out at 30 kV and a beam current of approximately 150 pA. The dose range for these studies (500-2000 $\mu\text{C}/\text{cm}^2$) was determined by screening experiments that analyzed doses from 100-10,000 $\mu\text{C}/\text{cm}^2$. For sections 4.3.1 and 4.3.2, the patterns were exposed as a series of overlapping rectangles with variable width (according to target landing-site size) and pixel size of ~ 5 nm. For section 4.3.1, the pitch of the patterns in the transverse direction (P_x) was fixed at 100 nm for both types of nanorods, while the longitudinal pitch (P_y) was fixed at 210 nm for NR2 and 190 nm for NR3 to achieve approximately the same ratio of landing-site size to nanorod size for each. The target landing-site width was varied from 40 – 60 nm. The resulting patterns provided a nominal particle-particle distance of 60 nm in both longitudinal and transverse directions. For section 4.3.2, the pattern pitch was fixed at 80 nm in both x/y directions and the landing-site width was varied from 30 – 50 nm. The range of appropriate landing site widths was also determined from screening experiments with high-dose (binary) patterning (section 2.3.3), and indicated a minimum of ~ 20 nm before proximity effects became an issue. For section 4.3.3, the diameter of the circles was varied from 180 – 220 nm and the pitch was varied from 200 – 400 nm.

4.5.3 *Optical Microscopy and Spectroscopy*

Optical microscopy was carried out in both reflection and transmission modes using a Leica DMi8A inverted optical microscope adjusting the polarizer to align parallel (P_L) and perpendicular (P_T) to the pattern orientation.

4.5.4 *Autocorrelation Analysis*

ACF methods have been applied to characterize ordering in a number of applications in nanoparticle assembly and other fields. In general, a different metric is applied to calculate an ordering parameter that can be used to interpret the ACF depending on the details of each system. One common approach is to fit a radial ACF to an exponential decay and determine a correlation length.^{261,262} Another approach involves fitting the peak envelope of the ACF decay as two Gaussian functions where the asymptotic peak level and amplitude of the decay are combined to extract an ordering parameter.²⁶⁰ A third approach calculates an ordering parameter from the slope between the first peaks in the normalized ACF.²⁵⁹ However, in all these cases, the ordering in the systems is derived from close packing of individual objects that results in lattice formation. This is distinctly different from the present work where the long-range ordering is anisotropic and defined lithographically by electron-beam exposure. This can be illustrated by examining typical ACF profiles as shown in Figure 4.13. The ACF profiles are constructed by plotting the normalized intensity averaged across a 5-pixel-wide (~20 nm) line in the desired direction.

The periodicity of the sinusoidal profiles from the patterned assembly corresponds to the pitch defined by DNA-EBL. The profile in the longitudinal direction does exhibit noticeable decay

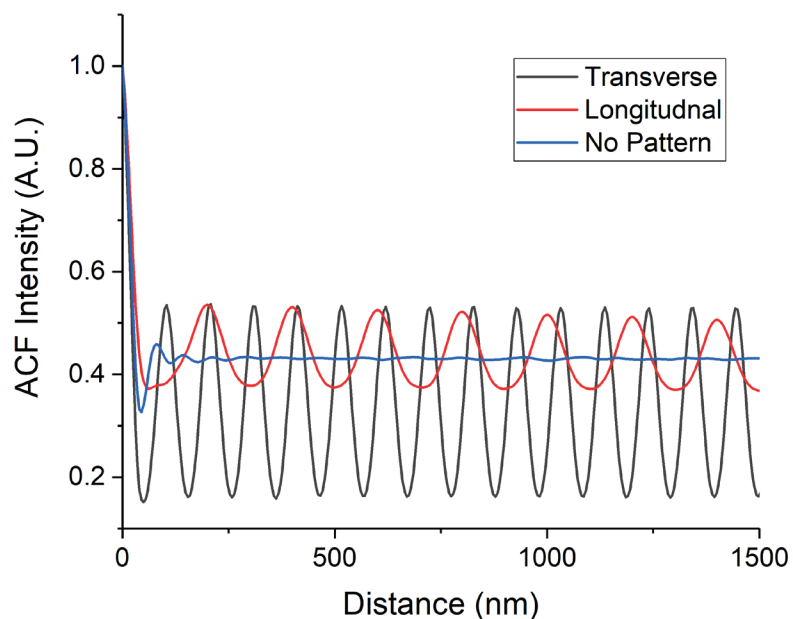


Figure 4.13 Comparison of typical ACF profiles from ordered assembly (NR3, 47.5 °C, 50 nm linewidth, 1500 $\mu\text{C}/\text{cm}^2$) in the transverse direction (black) and longitudinal direction (red) with nanorod assembly on an unpatterned substrate (blue).

with increasing distance, but this is not useful for comparing ordering effects. In more disordered systems, the decay is actually less significant as the initial amplitude is significantly lower. A more accurate metric for ordering in these systems can be extracted by comparing the amplitude of the sinusoidal profile near the central peak. However, as can be seen in the ACF from the unpatterned substrate, there is significant structure in the profile near the central peak due to short-range order as a result of close packing. Therefore, the amplitude of the ACF envelope for the patterned substrates is extracted at a sufficient distance from the central peak (> 400 nm) to avoid convolution with this short-range ordering effect. Ordering parameters are defined as:

$$\xi_T = \alpha_4 - \beta_5 \quad (22)$$

and

$$\xi_L = \alpha_2 - \beta_3, \quad (23)$$

where ξ_T and ξ_L are the ordering parameters in the transverse and longitudinal directions with α and β representing the intensities of peaks (peak number indicated by the subscript) for the upper and lower bounds of the ACF, respectively. This ordering parameter requires some modification due to the fact that the ACF for less ordered systems often has structure between the main peaks (particularly in the longitudinal direction due to nanorods assembled across multiple sites), which is representative of a less ordered system. As such, the actual value measured for β is the intensity at the midpoint between two consecutive peaks, rather than the lower envelope value. In more ordered systems, such as that in Figure 4.13, these are effectively the same value.

4.5.5 *Image Processing and Analysis*

To analyze the precision of assembly and alignment in the nanorod films, a custom MATLAB script was written to extract the number and orientation of nanorods from SEM images. This was accomplished by first applying a contrast threshold to each image and extracting isolated nanorods based on their size (separate subsets for out-of-plane and in-plane orientations). The subset with the in-plane rods was filtered based on eccentricity to remove large circular particles that fell into the same size range. The nanorods in this filtered subset were then analyzed for orientation by fitting each rod as an ellipse and measuring the angle of the major axis. The orientation of all nanorods was logged and nanorods within ± 5 degrees of the nominal orientation (horizontal, vertical, etc.) were categorized as such.

Fast Fourier transforms (FFT) were calculated using ImageJ for 1024×1024 or 2048×2048 regions of SEM images. The inset FFT's were produced by applying a maximum filter (0.5 pixel radius), cropping and adjusting brightness/contrast. For the FFT-filtered images, a contrast

threshold was applied to the raw FFT and an inverse Fourier transform was performed. This results in hard-threshold FFT-filtered images that highlight even low-level periodic structures in the original images.

4.5.6 *Random Sequential Adsorption Simulations*

RSA simulations were carried out with a custom MATLAB script. The patterned surface was simulated as a dimensionless square grid with 50×50 points and periodic boundary conditions. Each rod was simulated as a 2-mer that could adsorb at nearest and next-nearest neighbor sites. The simulation was carried out by selecting a random permutation of lattice positions and then attempting to adsorb rods at each site. For each position, an orientation was chosen at random and the rod would attempt to adsorb if the lattice sites were both available. If the lattice sites were available, the probability of “sticking” would depend on the particular simulation conditions. For example, in the simulations with orthogonal adsorption preferred, the probability of adsorption for particles with diagonal orientation was varied from 0% (all orthogonal) to 100% (equal probability of orthogonal and diagonal) in 1% steps. After attempting to place rods at every lattice site in random order, the process was repeated until only isolated single lattice points remained (i.e. the jamming limit was reached). For each probability step, the simulation was repeated 200 times. The number of rods with each orientation and the jamming limit was recorded for each repetition of the simulation.

Chapter 5: MEMS Platform for *In Situ* Characterization of Nanoparticle Assembly

Parts of this chapter are adapted with permission from: Myers, B. D., Lin, Q., O'Brien, M., Mirkin, C. A. & Dravid, V. P. Temperature-Controlled Fluidic-Cell Scanning Electron Microscopy. Microscopy and Microanalysis 22, 764-765, (2016)²⁷² and Hujsak, K., Myers, B. D., Roth, E., Li, Y. & Dravid, V. P. Suppressing Electron Exposure Artifacts: An Electron Scanning Paradigm with Bayesian Machine Learning. Microscopy and Microanalysis 22, 778-788, (2016).²⁷³

5.1 Chapter Summary and Motivation

One of the primary challenges in developing a mechanistic understanding of nanometer-scale assembly is the lack of methods for the direct visualization of the assembly processes. Liquid-cell microscopy in the TEM has emerged in recent years as a potential gateway for real-time and real-space interrogation of fluidic systems.^{133,134} TEM evaluation provides ultra-high spatial resolution information in liquids, even down to the atomic scale.^{138,274} However, there are significant concerns related to replication of relevant experimental conditions due to artifacts resulting from the liquid-cell architecture (geometric confinement, concentration depletion, surface effects, flow control)²⁷⁵⁻²⁷⁸ and electron-beam irradiation (radiolysis and electrostatic charging).²⁷⁹⁻²⁸² The relative impact of these factors is difficult to measure with TEM experiments alone and other techniques, such as liquid-cell SEM, optical microscopy, optical spectroscopy and x-ray techniques can provide complimentary information to the TEM analysis. A correlative approach using multiple imaging and analytical techniques will allow a more complete understanding of the impact of these artifacts and should allow the determination of conditions appropriate for a given liquid-cell experiment. This chapter highlights the development of a MEMS-based liquid-cell platform that can be custom tailored to the specific experiment and is

compatible with a range of different imaging techniques and modalities. Specifically, two liquid cells were designed based on a single MEMS platform utilizing silicon nitride membranes to isolate the fluidic environment from the microscope vacuum: 1) an SEM liquid cell that enables temperature-controlled experiments with a large fluidic reservoir and 2) a TEM liquid cell utilizing surface-micromachined nanochannels for precise control over liquid-layer geometry and fluid flow.

5.2 Introduction

Electron microscopy has long been a characterization method of choice for imaging nanoparticles and nanoparticle assemblies due to the high spatial resolution as well as the ability to analyze chemical and atomic structure. The high vacuum required in the standard electron microscope has generally precluded the direct imaging of liquid or samples with high vapor pressure. As a result, a number of liquid-cell approaches have been developed which isolate the liquid from vacuum while maintaining the ability to image objects in the liquid. This has been primarily accomplished through the use of MEMS-based devices with electron-transparent silicon nitride membranes. Such devices have already been used for *in situ* TEM observation of nanoparticle diffusion and beam-induced nanoparticle synthesis, movement and aggregation.^{138,279,283-285} More recently, methods have been refined to allow *in situ* observation of nanoparticle assembly from discrete building blocks.^{106,141-143} However, in almost all cases, energy deposited by the electron beam is utilized to trigger the observed processes. While these phenomena are interesting and the results may be extrapolated to a more generalized understanding of nanoparticle assembly, these devices are not yet practical tools to help develop and refine *ex situ* assembly strategies. The primary challenges in transforming liquid-cell EM into a reliable

analytical methodology revolve around the complexity of the beam-induced interactions, the complications of the liquid-cell geometry and a general lack of methods to make experiments repeatable and representative.^{133,286,287}

The standard TEM liquid cell, as shown in Figure 5.1a, requires the use of two silicon nitride membranes which isolate a thin liquid layer from the chamber vacuum. The distance between the membranes is defined by a patterned spacer layer on one of the two chips and is typically in the range of 100 nm to 1 μm .¹³⁴ These devices allow the imaging of fluidic samples, but have significant limitations in terms of spatial resolution and uniformity. In general, they are characterized by membranes that bow out under the differential pressure in the microscope, which causes variation in liquid thickness and difficulty maintaining thin, uniform liquid layers. In addition, only diffusive flow is possible in these devices, which allows flushing of the cell, but does not allow for controlled flow experiments. Finally, the standard TEM holder geometry makes it difficult to provide uniform heating or temperature control in the device. In contrast, the SEM liquid cell, as shown in Figure 5.1b, relies on a single silicon nitride membrane suspended over a fluid-filled cavity. While generally less popular than the S/TEM approach, SEM liquid cells with various membrane materials (silicon nitride, graphene, graphene oxide, polymer) have been demonstrated.²⁸⁸⁻²⁹² These devices are inherently lower in spatial resolution due to increased scattering of the lower energy ($\sim 1\text{-}30$ keV) electron beam, have lower temporal resolution (compared to TEM) due to serial scanning and provide lower sensitivity imaging. However, the high depth of focus of the SEM reduces the impact of membrane bowing and some degree of flow control should be possible, although integrated microfluidic SEM cells have not yet been constructed. Imaging is accomplished *via* a backscattered electron (BSE) signal that is sensitive to

average atomic number and can easily visualize electron-dense materials on or near the membrane surface. Further, the SEM chamber is sufficiently large to accommodate a Peltier stage or other heating/cooling stages for temperature control. Overall, *in situ* liquid cell SEM is uniquely suited for imaging structures on the membrane surface with moderate spatial resolution (>1 nm) and temporal resolution (>0.01 Hz).

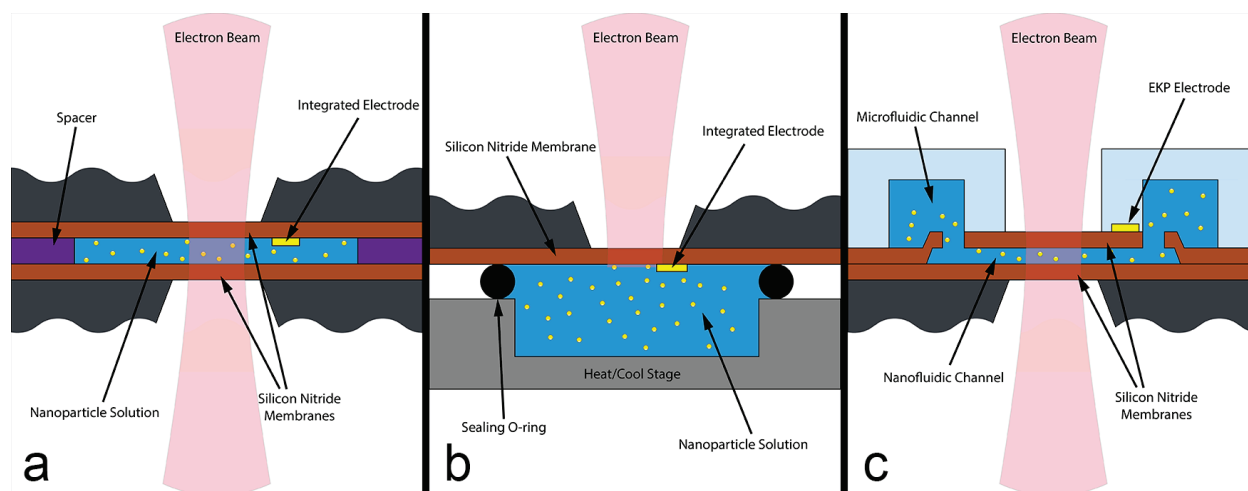


Figure 5.1 Schematic illustrations of various liquid cell approaches using silicon nitride membranes (green) including a) standard TEM liquid cell, b) SEM liquid cell and c) suspended nanochannel TEM liquid cell. (Adapted with permission from an illustration by Serkan Butun)

For the specific case of imaging DNA-linked gold nanoparticle assembly in the liquid cell, it is important to understand the types of electron-beam interactions that can influence the assembly process to inform the experimental design. First, the direct electron-beam damage mechanisms will be explored, which can be divided into two broad categories: knock-on damage and radiolysis.²⁹³ Knock-on damage occurs as a result of high-angle elastic scattering that can cause atomic displacement in the sample. This is the primary damage mechanism in conductive, inorganic materials where radiolysis is suppressed. Knock-on damage is characterized by a material-dependent threshold energy in the range of several 10's or 100's of keV and thus typically

only a concern in TEM experiments.²⁹⁴ Radiolysis is the dominant damage mechanism for organics, resulting from inelastic scattering of the primary electron beam and shows increasing scattering cross section at lower energy.²⁹³ As a result, damage by radiolysis is expected to increase with both the lower beam energy and the increased sample thickness in SEM experiments. For a given experiment, a critical dose (D_c) can be defined below which no beam-induced change is detectable. However, an additional important factor is the dose rate, which is controlled by the beam current and the imaging/scanning methodology. By carefully managing the dose rate, some systems can be imaged indefinitely without any detectable damage.²⁹⁵ The effects of radiolysis in liquid systems are myriad, but include significant changes in pH, production of radical species or other molecular products and direct bond scission.^{120,296} A second consideration for electron-specimen interactions is that of electrostatic charging effects in solution or on the silicon nitride membrane. While some obvious effects of charging have been noted including repulsion of charged nanoparticles^{279,297} and general slowing of particle movement,^{298,299} the electric fields generated in the liquid cell may also have significant effects on local reactant concentrations due to ion migration.^{300,301}

This chapter focuses on the design, fabrication and testing of two types of novel liquid cells based on a single MEMS-based platform: the SEM liquid cell (Figure 5.1b) and the nanofluidic TEM liquid cell (Figure 5.1c). The SEM liquid cell has the unique capability to provide uniform temperature control, contains a large fluidic reservoir and has electrical contacts for electrochemical studies, application of electric fields or local probing. The temperature control capability is demonstrated for the adsorption and desorption of DNA-linked gold nanoparticles. Imaging capabilities in this system are demonstrated using the BSE signal and supported by Monte

Carlo simulations. In addition, the use of sparse imaging to minimize the electron exposure dose is illustrated. Proof-of-concept studies using the nanofluidic cells (in both SEM and TEM) are demonstrated and finite element modeling of an on-chip heater will demonstrate the potential for uniform heating of the nanochannel.

5.3 Results and Discussion

5.3.1 Design of MEMS Chips and Holders

The liquid cell designs presented in this chapter are based on different implementations of a single MEMS chip platform. The design criteria for this platform include: 1) compatibility with SEM and TEM instruments (and ultimately other techniques), 2) electron-transparent imaging region, 3) integrated electrical contacts, 4) compatibility with a range of different solvents/fluidic environments, 5) customizable for a given experiment. The resulting MEMS chips are based on 5 mm × 10 mm × 500 μm silicon chips coated with low-stress LPCVD silicon nitride. This chip design is larger than most commercial liquid cells and thus provides more “real estate” for a variety of on-chip components, microfluidic channels, etc. Two primary types of liquid cell chips were fabricated for the SEM liquid cell (Figure 5.1b) and the nanofluidic TEM liquid cell (Figure 5.1b). The standard SEM liquid cell design can also be utilized as an *in situ* electrical biasing holder (with up to 8 contacts) in SEM or TEM and examples of such chips are shown in Figure 5.2a,b. The advantages of this standardized platform are numerous, including the ability to fabricate multiple chip designs on a single wafer and the ability to transfer chips between instruments. For example, it is possible to carry out an SEM liquid-cell experiment (e.g. nanoparticle assembly or beam-induced deposition), then remove the chip from the SEM liquid cell holder and image the same sample under the TEM.

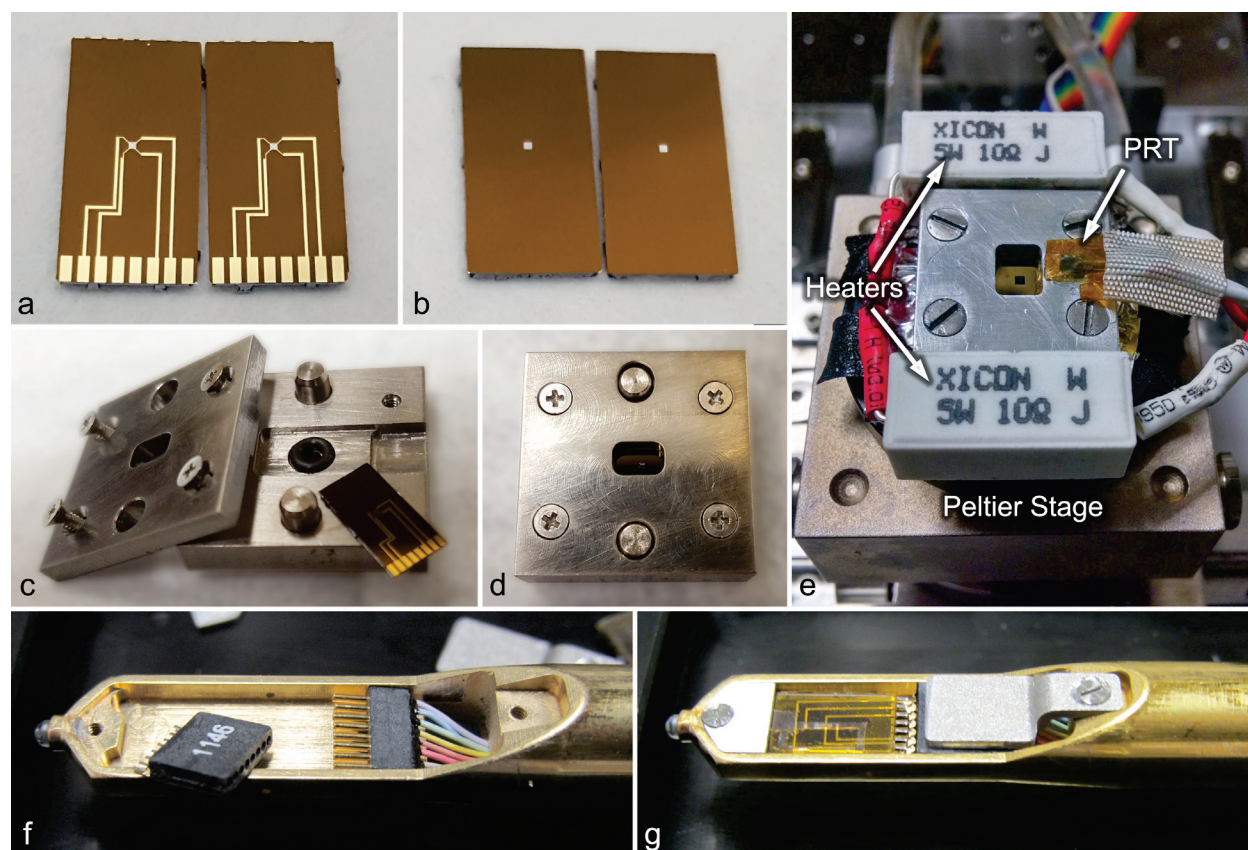


Figure 5.2 Liquid-cell MEMS chips showing a) example electrode configuration and b) bare silicon nitride window. The custom-built SEM liquid cell holder c) prior to loading, d) after loading and e) mounted on the Peltier stage in the SEM with heaters and temperature sensor. The custom-built electrical biasing TEM holder showing f) electrical connectors and g) loaded with nanofluidic TEM liquid cell.

The SEM liquid cell design is shown schematically in Figure 5.1b and consists of a single silicon nitride membrane that is suspended over a cavity, which is sealed by an o-ring. The SEM liquid cell holder is shown in Figure 5.2c-e and provides a cavity volume of approximately 8 μL , which can be decreased by using “plugs” for controlled-volume experiments. The holder is constructed of titanium to provide compatibility with a range of different experiments (a similar aluminum prototype was used for many experiments herein). The chip is sealed by securing a lid, which compresses the o-ring and secures the microfabricated electrodes (if necessary) against spring-loaded beryllium-copper contacts on an 8-pin electrical connector. These contacts are

connected to a feedthrough in the microscope chamber for external connection. For liquid-cell experiments, the electrodes can be used for a number of different applications including *in situ* Joule heating, temperature measurement, electrochemical studies and electrokinetic flow. In this preliminary design, heating is achieved by means of two power resistors (5 W, 10 Ω) placed on either side of the holder with temperature monitored *via* a local platinum resistance thermometer (PRT) placed close to the chip area. Cooling (and supplemental heating) is achieved by means of a small Peltier cooling stage provided by microscope manufacturer. The Peltier stage is controlled by the microscope software and the heaters are controlled *via* an external DC power supply either manually or by a PID pulse-controller. The automated PID control is ideal for precise temperature control, but the pulsed-DC power causes interference with microscope imaging. This setup provides temperature control in the range of approximately 15 – 100+ °C by combination of the two systems. A revised sub-stage is currently being designed and fabricated, which utilizes a larger Peltier element (300 W) and an automated controller, which should be able to achieve temperature control well below 0 °C and up to 80 °C.

The TEM sample holder is shown in Figure 5.2f,g (designed in collaboration with Hitachi High Technologies, Canada) and utilizes the same chip geometry and electrical connections as the SEM liquid cell. The TEM liquid cell design is show schematically in Figure 5.1c and the primary difference between these chips and the SEM liquid cell (and traditional TEM liquid flow cells) is that the chips are designed to be self-sealing, without an external o-ring. This approach is possible due to the controlled geometry of the nanofluidic channel and the ability to pump fluid through the channel *via* electrokinetic pumping.³⁰²⁻³⁰⁴ Given the small volume of the nanochannel, sufficient fluid can be supplied by means of an on-chip reservoir connected to the nanochannel by integrated

microfluidic channels, eliminating the need for external fluidic connections. For example, a typical channel has a cross section of $10\ \mu\text{m} \times 200\ \text{nm}$ with a length of $300\ \mu\text{m}$ in the electron-transparent region. This results in a volume of $600\ \text{fL}$ in the viewable area of the liquid cell, which could be replenished more than 16,000 times with a small on-chip reservoir of $1\ \text{mm} \times 1\ \text{mm} \times 10\ \mu\text{m}$. In addition to eliminating fluidic connections, the on-chip electrokinetic pumping system coupled with channels of well-defined geometry should enable the study of nanofluidic phenomena not previously accessible by liquid-cell TEM. The nanochannel approach also minimizes the membrane bulging effect seen in traditional liquid-cell TEM,³⁰⁵ rendering imaging possible along the entire channel at high spatial resolution. Parallel channels can be constructed to enable redundancy for conducting multiple experiments on the same chip and providing control channels to evaluate beam effects, both of which can make liquid cell TEM experiments more repeatable and representative.

5.3.2 *SEM Liquid Cell*

SEM liquid cells have been available commercially for some time, targeted toward the biological sciences with interest in studying cells by gold nanoparticle labeling techniques.²⁹² These liquid cells use polymer membranes and other variants have been developed with different membrane materials. The primary challenge of SEM liquid cell experiments with the traditional silicon nitride membrane is that they are limited to systems with high (and heterogeneous) electron density to provide sufficient imaging contrast by backscattered electron imaging. In addition, only material on or near the membrane is visible due to the scattering of the primary electron beam at the relatively low beam energies ($<30\ \text{keV}$). Fortunately, the study of directed assembly of DNA-linked gold nanoparticles on surfaces is particularly well suited for this technique: the gold

particles have high atomic number relative to the other components; the primary output is the particle position/orientation; and only particles on the membrane surface are of interest. To study the feasibility of imaging these systems, a 3D Monte Carlo image simulation¹⁹³ was performed for 50 nm diameter gold nanoparticles suspended in water in a silicon nitride liquid cell as shown in Figure 5.3. The simulation was configured to account for nanoparticles at different distances from the membrane (0, 10, 20, 50 and 100 nm) and includes a realistic simulation of the annular solid-state BSE detector used in experiments. These data show that while imaging of the particles is possible, the image is blurred as the beam energy is decreased and with the additional gold layer (required for DNA immobilization). In addition, the intensity and sharpness of the nanoparticle images depends strongly on the particle-membrane distance. This suggests the potential for quantitative analysis of the vertical position of the nanoparticles in the liquid cell based on calibrated image analysis.

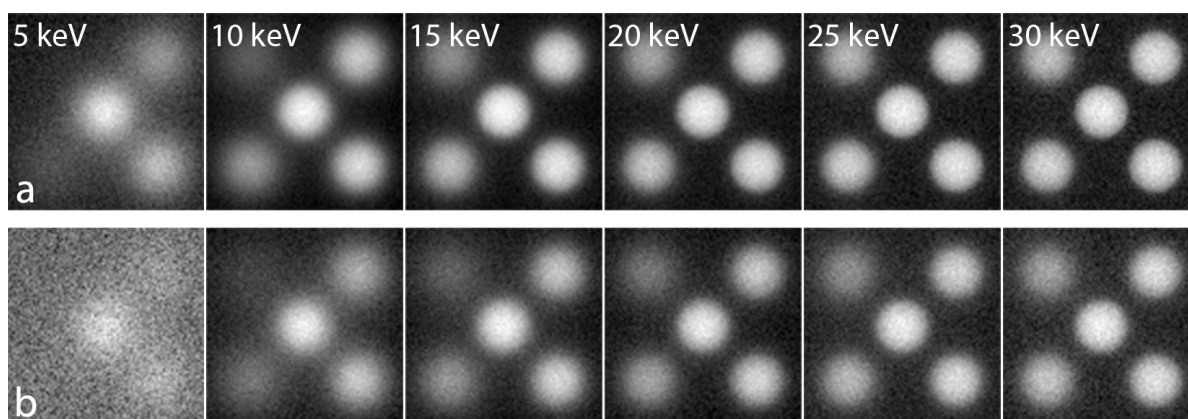


Figure 5.3 Simulated backscattered electron images generated by 3D Monte Carlo image simulations for Au nanoparticles suspended in water below a) a 50 nm-thick silicon nitride membrane and b) a 50 nm-thick silicon nitride membrane with an 8 nm-thick Au layer. The particles are at different distances from the bottom surface: 100 nm (top-left), 50 nm (bottom-left), 20 nm (top-right), 10 nm (bottom-right) and on the membrane (center). Images are simulated with different incident beam energies from 5 – 30 keV.

One of the major design considerations for the SEM liquid cell is the size of the fluidic reservoir. Compared to TEM fluidic cells, which have very thin liquid layers, with total cell volumes in the picoliter range, the SEM liquid cell can accommodate much larger fluidic volumes on the order of microliters. This makes the SEM liquid cell capable of more accurately reproducing *ex situ* experimental conditions and may ameliorate beam-induced artifacts. Specifically, the local depletion of reactants has been noted in many beam-induced nanoparticle nucleation studies inside TEM liquid cells.^{284,285} This causes reactions to become diffusion-limited and negatively affects the repeatability of liquid-cell experiments as well as the ability to correlate results with *ex situ* studies. For the case of nanoparticle assembly, designing an experiment for the TEM liquid cell presents a great challenge. If a typical monolayer adsorption experiment is considered utilizing a 1 nM solution of DNA-functionalized 30 nm (diameter) spherical particles, a particle density on the substrate on the order of $5 \times 10^{10} / \text{cm}^2$ is achieved.¹⁴⁸ At these conditions, a minimum liquid layer thickness of approximately 800 μm is required to achieve monolayer coverage. To carry out this experiment in a TEM liquid cell with a sub-micron liquid layer, either the nanoparticle concentration must be several orders of magnitude higher or flow is required to replenish the particles, neither of which is a reasonable approximation of the *ex situ* experiment. In addition, the assembly studies are often require temperature control to within 1 °C as the assembly is extremely temperature-dependent. Reports of temperature control in the TEM liquid cell are rare, but some progress has been made using sealed liquid cells and joule heating,^{306,307} cryogenic cooling³⁰⁸ or standard heating holders.³⁰⁹ However, even though these systems are capable of heating the sample, there are significant questions about the precision of temperature control and uniformity of heat distribution. Heating in the SEM liquid cell can be approached with a different strategy, as there is room in the SEM chamber for larger heating elements and additional thermal mass around

the liquid cell to maintain constant and uniform temperature control. Temperature control was verified by melting experiments with low melting point metals (Ga and Field's metal) to be within 1 °C. Temperature control and uniformity were verified by thermal imaging in Figure 5.4 and shows excellent uniformity (<1 °C) across the membrane and between the membrane and the surface of the holder where the PRT is mounted.

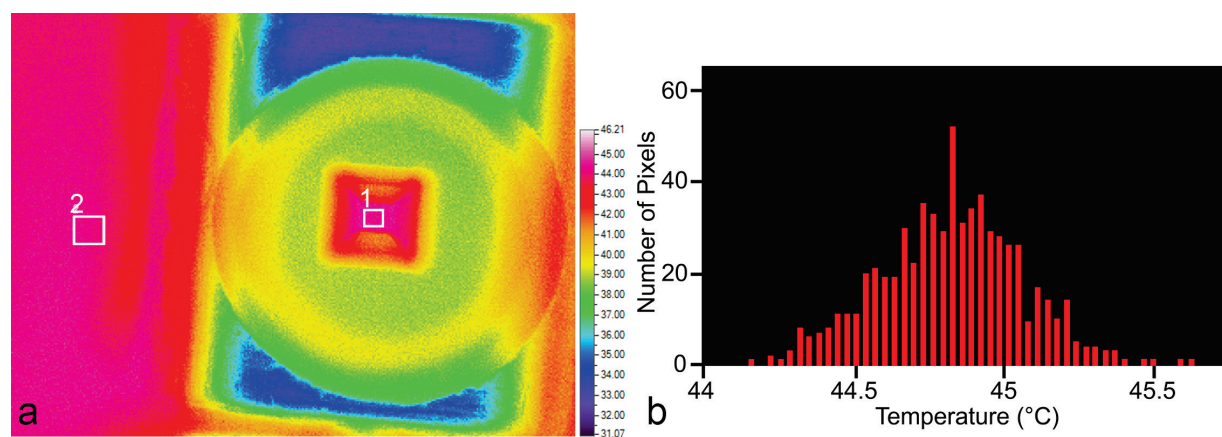


Figure 5.4 Thermal microscopy of the SEM liquid cell loaded with chip and water for testing showing a) temperature reference from silicon nitride window (region 1) at 44.5 °C and aluminum liquid cell surface (region 2) at 44.3 °C and b) histogram of region 1 showing temperature uniformity within about 1 °C (at a slightly higher average temperature).

As a proof-of-concept, the adsorption (hybridization) and desorption (melting) of DNA-linked gold nanoprism was studied by *in situ* liquid-cell SEM. The functionalization of the SEM liquid-cell chips and the nanoparticles was carried out according to the same procedures as in the preceding chapters. For the adsorption (hybridization) studies, linker strands were hybridized *ex situ* on both the DNA-functionalized liquid cell chips and the nanoparticles. The nanoparticles were then loaded into the liquid cell and the chip was loaded to seal the reservoir. It was possible to image the system within 10-15 minutes of loading, which is sufficient given the kinetics of this system. The liquid cell was heated slowly *in situ* to 40 °C to minimize non-specific adsorption and

imaged periodically as shown in Figure 5.5. Despite their minimal thickness (7 – 10 nm), the nanoprisms are clearly visible in the BSE images and even particle overlaps can be distinguished. Care was taken to image different regions of the membrane at each time step to minimize direct electron-beam exposure effects. While an increase was noted in the density of particles adsorbed on the membrane, after three hours most regions showed only a moderate increase in particle coverage. However, the nanoparticle loading was not consistent across the membrane and tended to be higher near the perimeter of the window (Figure 5.5d). Repeated experiments resulted in similar non-uniformity, which is distinctly different from *ex situ* studies, which consistently result in dense monolayer formation, with minimal particle overlap or agglomeration.

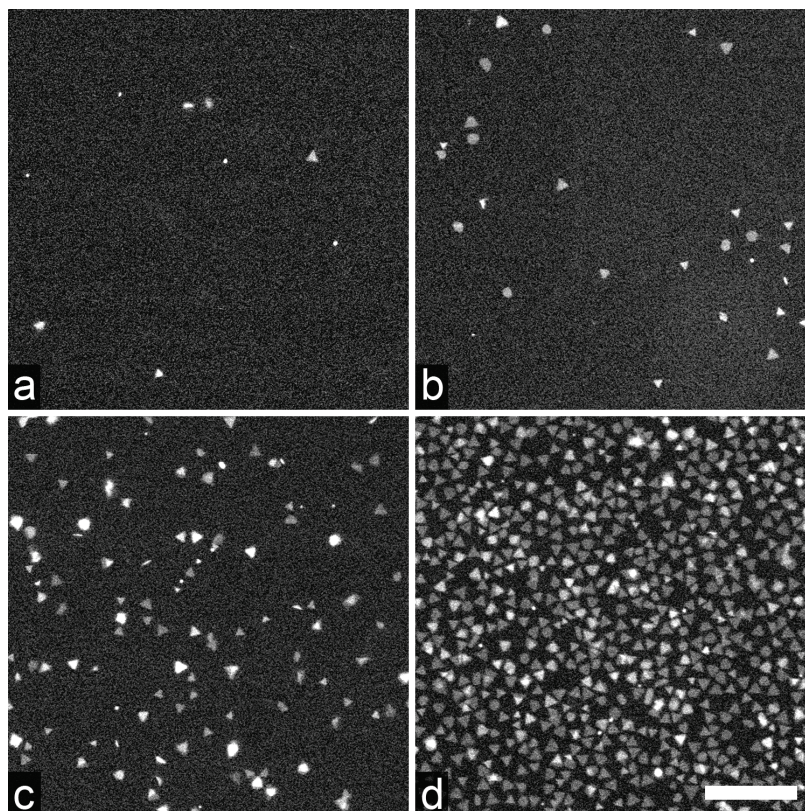


Figure 5.5 BSE images of prism adsorption experiments in the SEM liquid cell at approximately a) 30 min, b) 1 hour and c) 3 hours near the center of the window and d) 3 hours near the edge of the window. (Scale bar is 1 μm)

Particle desorption (melting) experiments were carried out by immobilizing particles on functionalized membranes *ex situ* and then loading the liquid cell with phosphate buffer (0.5 M NaCl, 0.01 M sodium phosphate, 0.01 wt. % SDS, pH = 7.4). The results of one of these studies are shown in Figure 5.6 and indicate a two-step melting process. Starting from a dense nanoparticle film, which comprises both face-bound and edge-bound prisms, the edge-bound prisms melted first in the 38-42 °C range. The face-bound prisms did not begin to desorb until a somewhat higher temperature range of 45-48 °C, which corresponds to UV-Vis melting curves for this system. However, unlike *ex situ* experiments which typically show over 90% melting above 50 °C, these films did not completely melt at high temperatures, and exhibited fairly dense films with

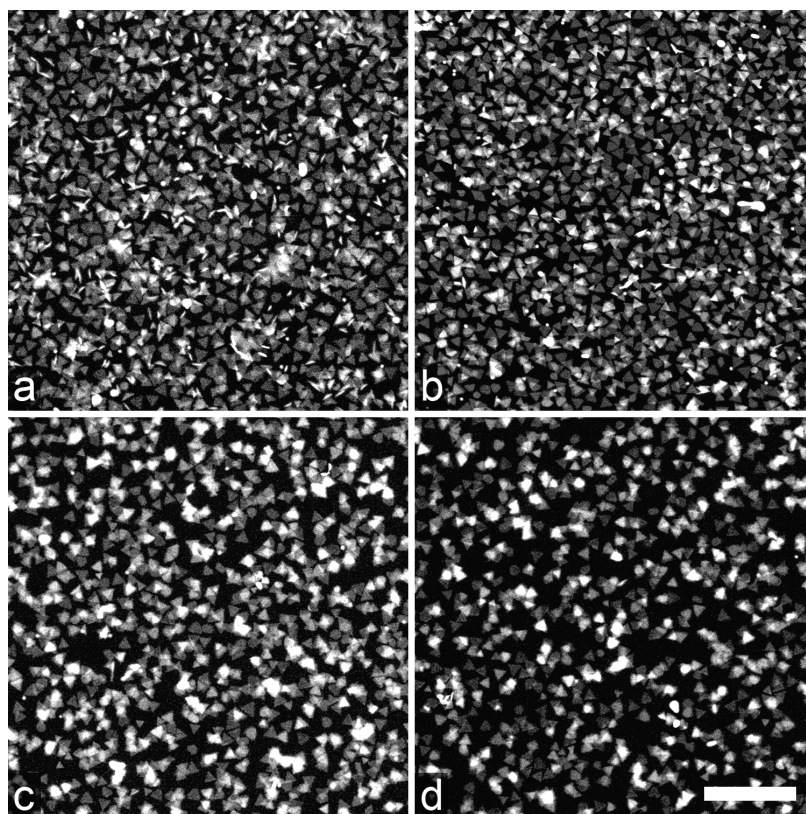


Figure 5.6 BSE images from SEM liquid cell prism desorption experiments at a) 27, b) 42, c) 48 and d) 60 °C. (Scale bar is 1 μm)

overlapping nanoprisms even at temperatures above 60 °C. These two studies (hybridization and melting) indicate some systematic discrepancy between *in situ* and *ex situ* experiments. One possible explanation is the limited sample volume. These experiments were completed with an early generation SEM liquid cell that maintained a liquid layer thickness of only 200 – 300 μm. As discussed previously, this liquid layer thickness may be insufficient to avoid concentration depletion during the adsorption experiments and may saturate during melting studies. Another possible explanation is the impact of the electron beam on this system. Even though care was taken to only expose each region a single time, electron-beam exposure can significantly decrease the pH of the solution,²⁸² which can significantly alter the DNA-DNA interactions if the pH is outside the range of 5 and 9.^{310,311} In addition, the electron beam can cause significant charging of the silicon nitride membrane, which may result in electrostatic attraction or repulsion of the charged particles and can affect the ion concentration and distribution, which is critical for DNA hybridization.

5.3.3 *Sparse Imaging for Dose Reduction*

A perennial challenge in liquid-cell electron microscopy (and electron microscopy of any beam-sensitive material) is that of beam-induced damage and imaging artifacts. In beam-sensitive materials, there is often a dose budget, above which the beam can have deleterious effects on the sample. The typical solution in a scanned-probe system is to reduce dwell time to avoid such effects, but this approach is often limited by the inherently low contrast and signal-to-noise ratio in many of these systems. However, most electron micrographs captured by standard raster scanning have relatively low information content and are effectively over-sampled. Techniques can be borrowed from the field of compressive sensing to reconstruct images by exploiting the

statistical correlations that exist in undersampled datasets.³¹²⁻³¹⁴ This approach was implemented in conjunction with the SEM liquid cell by modification of the electron scanning system in the SEM. Instead of capturing full raster-scanned images, an electrostatic beam blanker was used to rapidly deflect the beam and only acquire signal from a user-selected (typically random) sampling mask. The resulting sparse images were then reconstructed by a dictionary-learning inpainting algorithm.²⁷³ Images of DNA-functionalized 30 and 80 nm gold nanoparticles were captured by

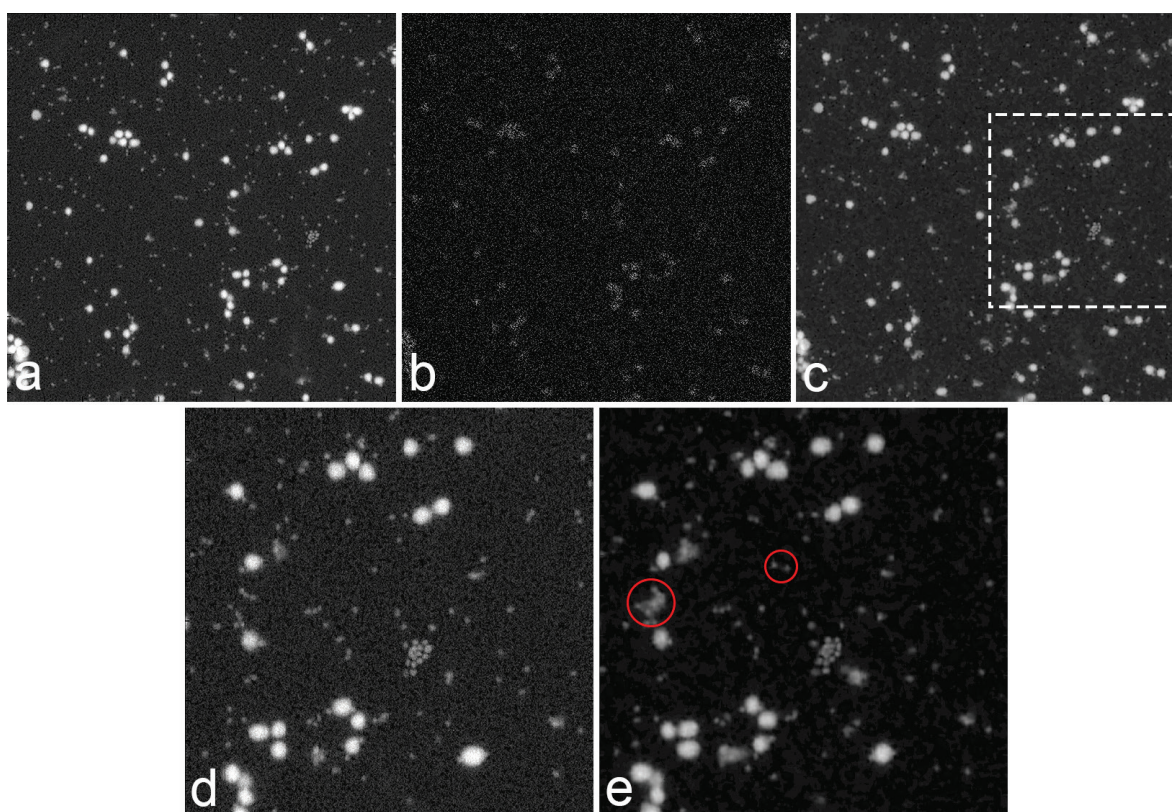


Figure 5.7 Sparse imaging results showing a) a fully sampled BSE image of 80 and 30 nm gold nanoparticles adsorbed on a gold-coated silicon nitride membrane; b) a sparse 30% sampled experimental image collected for reconstruction of the same sample; c) the reconstruction of the sparsely sampled image showing strong similarity and dramatically reduced background noise as compared with (a). Zoomed in image d) of the inset in (c) highlighting the noise present in most BSE images from the SEM liquid cell and e) the same inset from the reconstruction, which was experimentally collected after the fully sampled image. The highlighted region displays features that are present and observable in the sparse imaging method, that were attracted to the region when capturing fully sampled images.

full raster scanning followed by sparse imaging with 30% sampling as shown in Figure 5.7. These images illustrate the power of the sparse image reconstruction to recover all of the detail in the fully sampled image (including pinholes in the gold coating and all 30 nm particles) while also providing a de-noised image. The red circles in Figure 5.7e. show particles/features not present in the fully-sampled image that likely adsorbed during the imaging process, possibly due to a combination of electrostatic interactions and electron beam-induced cross-linking of the DNA linkers. While the advantage of this type of approach is likely sample-dependent, such sparse imaging routines have been shown to be superior to denoising algorithms for the same acquisition time.³¹⁵

5.3.4 *Nanofluidic TEM Liquid Cell*

The study of fluid flow in nanochannels is an active area of research with potential implication in technologies with diverse applications including DNA sequencing, energy conversion, molecular separations and oil and gas exploration.^{316,317} Fluidic interactions under extreme geometric confinement are distinct from more general fluid dynamics, but are still not completely understood. Most experimental work in literature on the fabrication of planar nanochannels utilizes bulk, optically transparent materials.³¹⁸⁻³²⁰ In comparison, the nanofluidic channels in the TEM fluidic cell must be electron transparent and thus self-supported. This presents major challenges in the design and fabrication of the nanochannels and their integration with the on-chip microfluidics. The section will cover the work to-date on the fabrication and testing of the nanochannel liquid cell.

Nanochannel fabrication is based on a surface micromachining approach utilizing sacrificial chromium layers.³²¹ Patterned chromium thin films were fabricated on the LPCVD

silicon nitride-coated substrate, defining the nanochannel dimensions. Following patterning of the chromium layer, a conformal, stress-controlled PECVD silicon nitride film was deposited on the chromium layer. Windows were opened in the silicon nitride layer and the chromium was removed with a standard chromium etchant, which contains cerium (IV) as the active component. This process can take several hours to days, but can be enhanced by galvanic coupling, if an electrode layer (i.e. electrokinetic pump) is in contact with the chromium layer.³²¹ After release, the channels were filled with a gold nanoparticle suspension and sealed on both ends with epoxy. The success of the nanochannel filling process depends on the nanochannel geometry, the release methodology and the silicon nitride stress (see Figure 5.12). Ultimately, in future devices these nanochannels will remain open and interface with a microfluidic channel for fluid transport.

Nanochannels (50 nm height) filled with the colloidal nanoparticle suspension were first imaged by BSE in SEM at 30 kV as shown in Figure 5.8 prior to backside etching of the silicon wafer to release the suspended nanochannel. These images show that the nanochannel is hermetically sealed and successfully isolates fluid from the microscope vacuum. They also illustrate the hydrophobicity of the nanochannel, which shows a contact angle in the plane of the channel of approximately 150 °. The hydrophobicity of the membrane in the air gap between the two fluid columns is modified by imaging with the electron beam (Figure 5.8b-c), which results in wetting of the unfilled region. Finally, the BSE image in Figure 5.8d highlights the ability to discriminate between particles on the surface and interior of the nanochannel based on their contrast and sharpness. The electron beam will undergo additional scattering through the silicon nitride membrane, rendering particles on the interior blurry and darker. Similar samples were imaged in STEM at 200 kV after the membrane was released by backside etching of the silicon

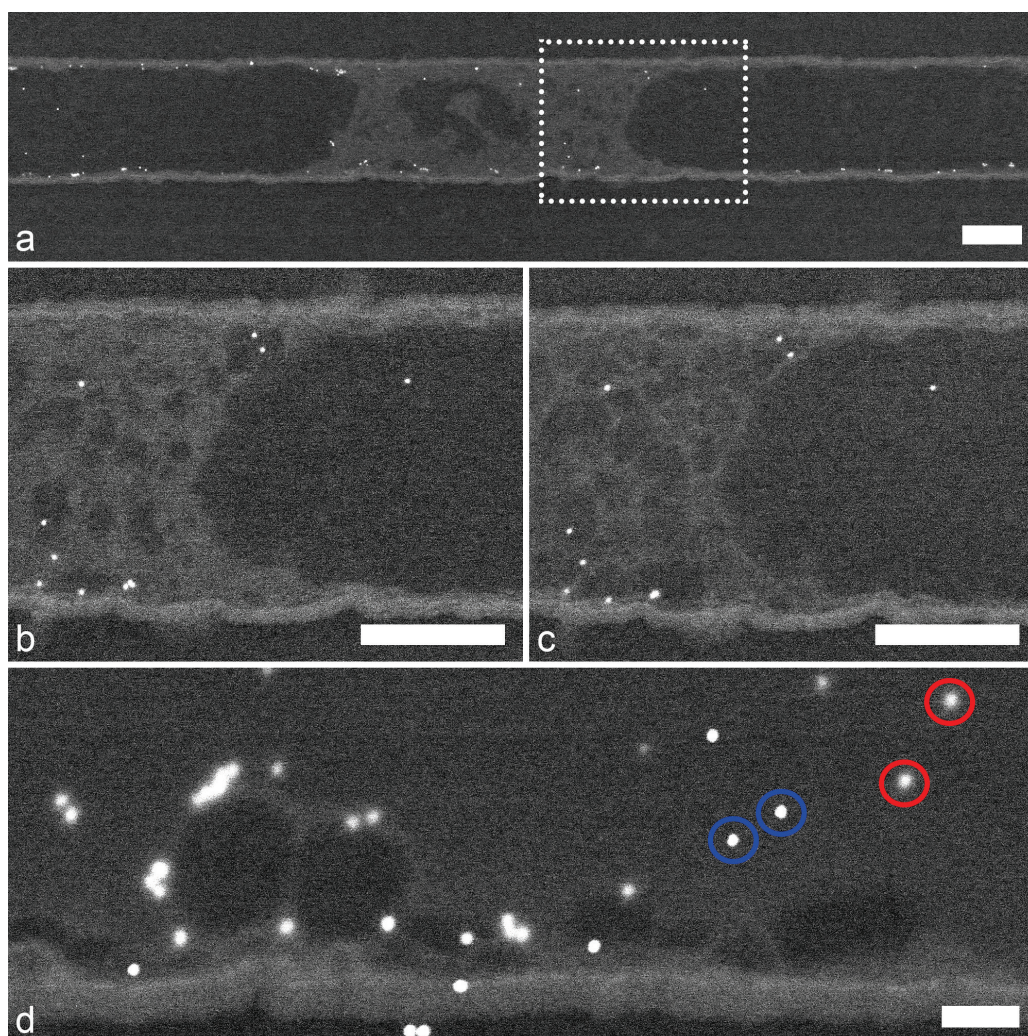


Figure 5.8 SEM images of fluid-filled nanochannel on bulk substrate showing a) filled (dark) and empty (light) regions of the channel, b-c) higher magnification of area indicated in (a) showing changes in the fluid distribution after imaging and d) images of nanoparticles on the surface (blue) and interior (red) distinguishable by their relative sharpness. (Scale bars are 1 μm (a-c) and 200 nm (d))

wafer. As shown in Figure 5.9, the presence of fluid in the channels was observed by the contrast present in either the transmitted electron (TE)/bright field (BF) or HAADF images. Prolonged exposure of the fluid in the channel by a focused electron probe resulted in air bubble formation due to radiolysis²⁸¹ as shown in Figure 5.9d. For these experiments, the exterior of the channel was also covered with the colloidal suspension of particles and SE imaging allowed for the ability to

discriminate between particles on the interior and exterior of the channel as shown in Figure 5.9e. At higher magnification, the contrast of the images showed a texture that is likely due to a replica effect by the conformation of the silicon nitride film on the polycrystalline chromium. As a result, future work may explore amorphous films (SiO_2 or $\alpha\text{-Si}$) as alternatives for the sacrificial layer. Integration of the nanofluidic channels with microfluidic channels and the evaluation of electrokinetic pumping capabilities are ongoing.

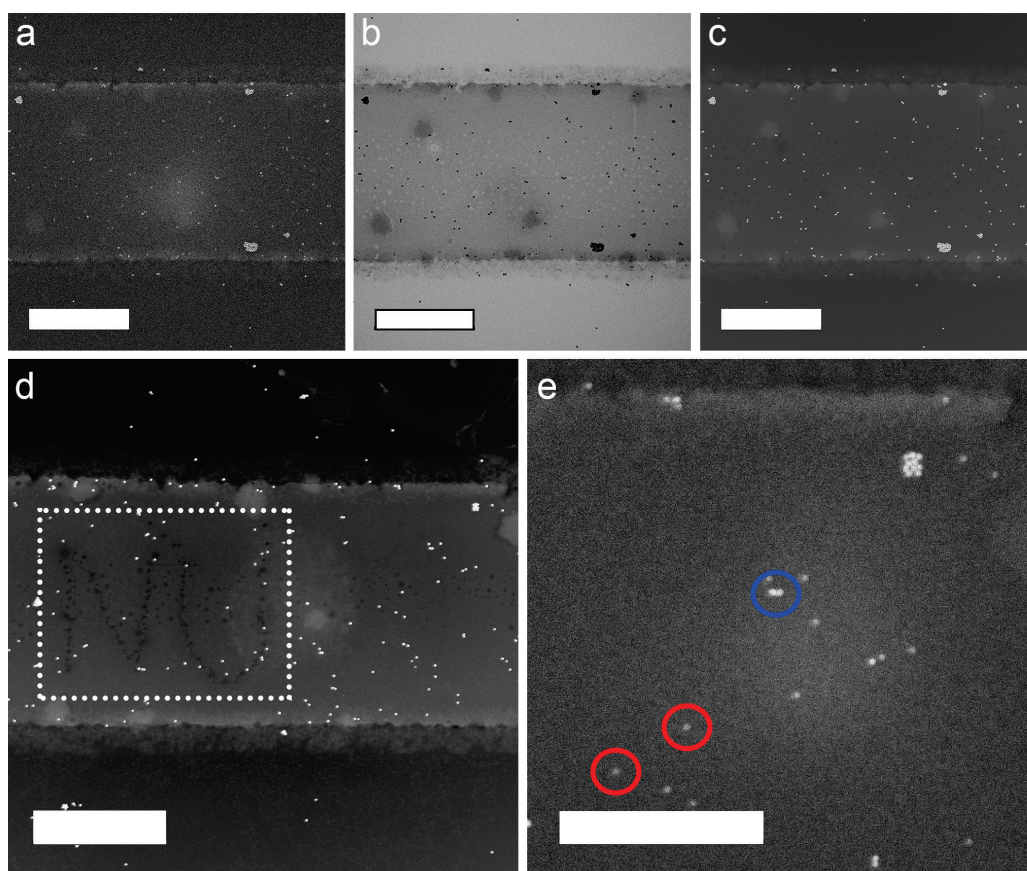


Figure 5.9 Suspended nanochannel filled with colloidal gold suspension imaged by STEM in a) SE, b) BF and c) HAADF modes showing d) air bubbles formed by radiolysis of the water in the nanochannel with a focused probe and e) discrimination of surface (blue) and interior (red) particles by SE imaging. (Scale bars are 2 μm (a-d) and 1 μm (e))

Temperature control in the nanofluidic TEM liquid cell is more challenging to execute than in the SEM liquid cell, due to the limited sample holder size. As a result, it may be preferable to

provide on-chip temperature control by Joule heating with a resistive heating element. In the traditional TEM liquid cell, it is difficult to design a heating element that provides a uniform temperature profile over the entire sample volume. However, in the nanofluidic TEM liquid cell, the small channel size allows the positioning of a heating electrode in close proximity to the nanochannel. This can be designed to provide uniform heating of the nanochannel over the entire

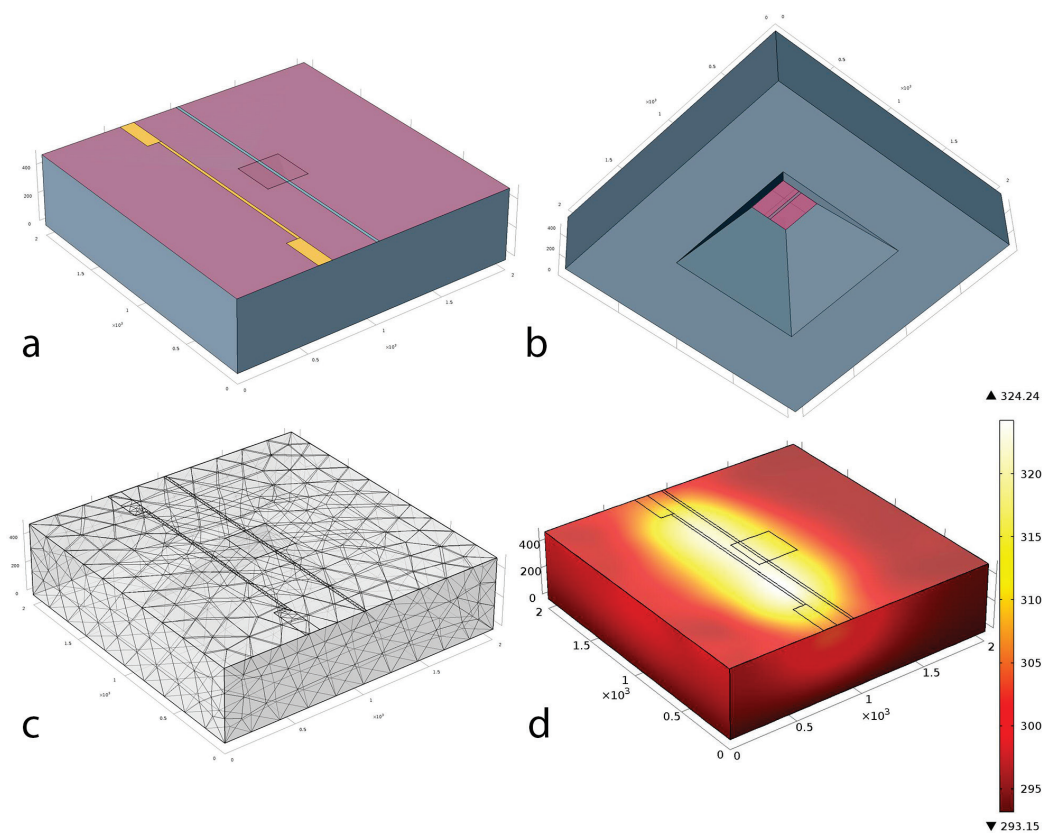


Figure 5.10 COMSOL simulations of the nanofluidic TEM liquid cell with a heating trace next to a water-filled suspended nanochannel showing a) top of the chip, b) bottom of the chip, c) mesh configuration and d) temperature map resulting from Joule heating.

viewing window. To evaluate this approach, finite-element modeling was carried out with COMSOL Multiphysics as shown in Figure 5.10. Joule heating of a gold heater ($50 \text{ nm} \times 20 \text{ }\mu\text{m}$) placed on the silicon nitride surface near the window was implemented. The nanochannel was simulated as a channel of water ($100 \text{ nm} \times 20 \text{ }\mu\text{m}$) placed on the silicon nitride window. The

simulation was configured to model conductive heat transfer, with surface-to-ambient radiation on exposed surfaces. Boundary conditions were set such that the bottom of the chip was at room temperature and the sides of the chip were open boundaries allow heat flux at the edges. The heating current was adjusted to achieve a temperature of about 47 °C. At these conditions, this simple linear heater design demonstrated a temperature uniformity of better than 2 °C in the nanochannel over the silicon nitride window.

5.4 Summary and Outlook

This work highlights the design and implementation of a MEMS-based fluidic cell platform for both SEM and TEM, with potential future application in other complementary and correlative methods. The SEM liquid cell was demonstrated with temperature control within 1 °C, which is critical for characterizing the DNA-nanoparticle systems. Both adsorption (hybridization) and desorption (melting) experiments were successfully executed with the SEM liquid cell. The melting experiments illustrated a two-part melting process whereby edge-bound nanoprisms melt at a lower temperature, a phenomenon not seen during ensemble measurements by UV-Vis. However, while the SEM liquid cell experiments are promising due to the large fluidic reservoir and temperature control, significant challenges remain. In particular, it is clear that the *in situ* studies are not entirely representative of *ex situ* experiments and the exact reason is not clear. For example, many experiments resulted in spontaneous aggregation of the nanoparticles on the membrane, which should have been separated due to steric and electrostatic repulsion. Unlike the TEM liquid cell, there are few detailed experiments of electron beam interactions at low beam energy. While similar mechanisms are at play (radiolysis, charging, etc.), these have not been explored in detail for the SEM. It is important that a more thorough evaluation of the details of

beam effects in the SEM liquid cell be carried out to inform future experiments. In addition, the capability for electrode integration in the SEM liquid cell enables the study of electrochemical processes and the impact of electric fields on nanoparticle assembly.

The nanofluidic TEM liquid cell holds great promise for a critical subset of potential *in situ* studies. Unlike the traditional TEM liquid cell, this approach allows for liquid layers of controlled thickness, allowing detailed investigations of the effects of geometric confinement on fluidic systems. Future integration of electrokinetic pumping, should allow detailed fluid dynamics studies. Through controlled modification of surface chemistry coupled with techniques such as particle image velocimetry, the effects of the electric double layer on fluid flow may be evaluated by direct imaging. This may have significant impact in fields such as energy conversion devices that take advantage of liquid slip in nanochannels.^{322,323} In addition to fundamental nanofluidics studies, this system may also be custom tailored to enable on-chip fluidic mixing of multiple components as well as on-chip heating. Such capabilities could be applied for the study of numerous processes including nanoparticle synthesis and assembly.

5.5 Experimental Methods

5.5.1 MEMS Fabrication

MEMS chips were fabricated for both SEM and TEM liquid cells by the same general process flow, with additional process steps for the nanofluidic TEM liquid cell as described in Figure 5.11. While the full nanofluidic process flow is described below, this can be “short-cut” to produce different versions of the chips. For example, if a simple electrical biasing chip is desired for SEM liquid cell or for high vacuum TEM studies, only the electrode layer (Figure 5.11e) and

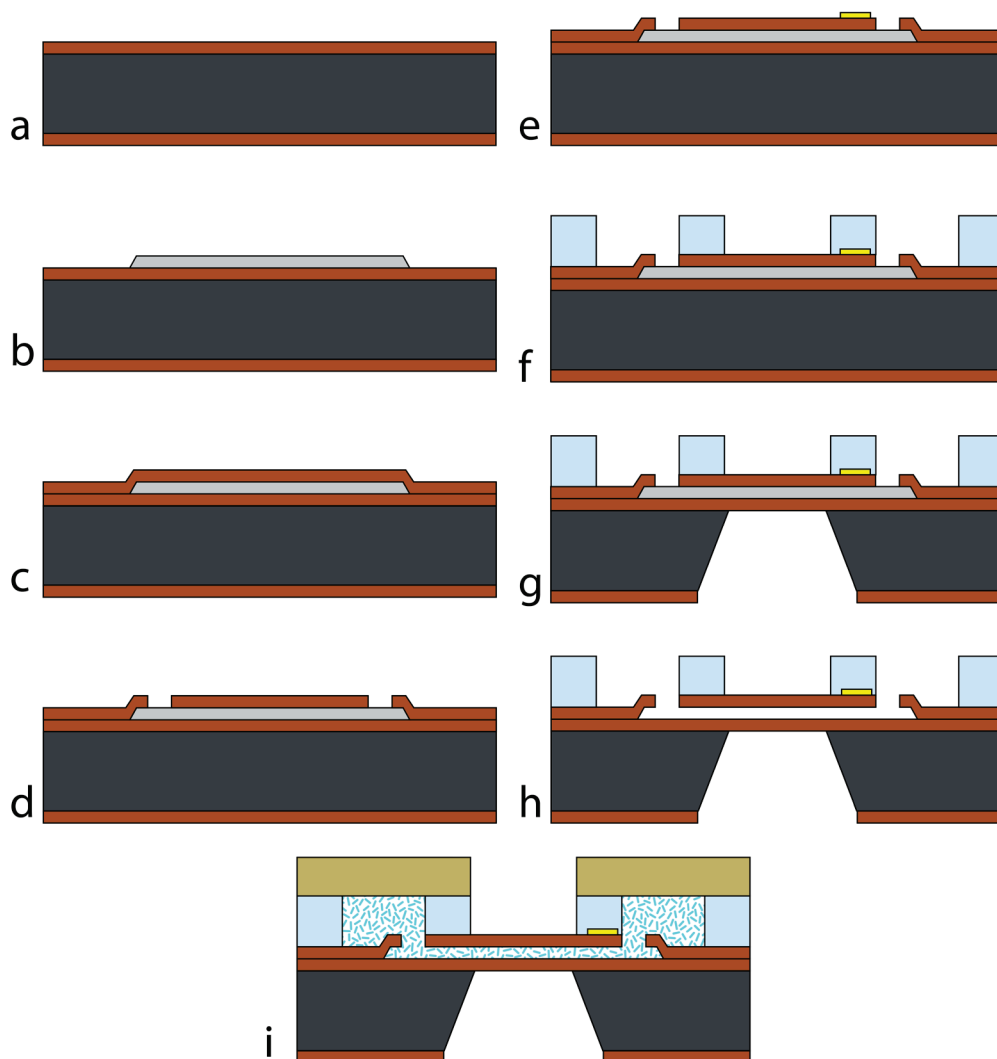


Figure 5.11 MEMS process flow for liquid-cell chips showing a) starting wafer with low-stress silicon nitride, b) sacrificial Cr deposition, c) silicon nitride deposition, d) dry etching silicon nitride for access to nanochannel, e) electrode deposition, f) SU8 microfluidic layer deposition, g) backside etching to release silicon nitride window, h) Cr etching to release nanochannel, i) filling and sealing of microfluidic channels. (Figure adapted with permission from an illustration by Serkan Butun)

backside etching (Figure 5.11g) steps are required. The final steps in this process flow (microfluidic integration) are still under development.

The starting wafers were 500 μm thick, double-side polished, lightly-doped silicon with 50 nm low-stress LPCVD silicon nitride on both sides (Rogue Valley Microdevices). The first step

for the fabrication process was the deposition of the sacrificial chromium layer, which defines the nanochannel(s). This was deposited by electron beam evaporation (AJA) or sputter deposition (AJA Orion) with a thickness that depends on the desired nanochannel height (typically 50 – 200 nm). The channel width and length were defined by a photolithography step (Shipley S1805) using a maskless aligner (Heidelberg μ PG501) followed by wet etching with chromium etchant. The silicon nitride layer that forms the top of the nanochannel was deposited either by mixed-frequency

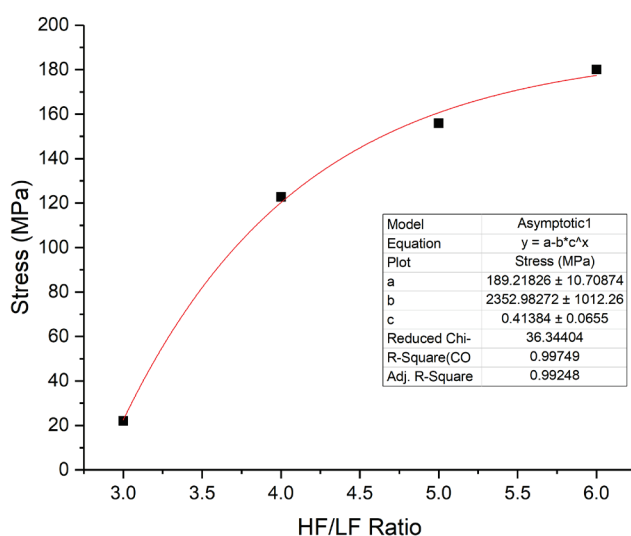


Figure 5.12 PECVD silicon nitride stress-control demonstrated by measurement of wafer curvature and application of Stoney’s formula for different ratios of high and low frequency deposition.

PECVD (STS LpX CVD) or as a low-stress LPCVD (Tystar) film. The PECVD approach allows precise control over the film stress by combined high- and low-frequency depositions, as shown in Figure 5.12, but may suffer from more defects (pinholes) that can negatively influence the channel integrity. Openings in the silicon nitride layer were created by photolithography (Shipley S1813) and RIE (CF_4/O_2) followed by resist strip. A lift-off process (LOR 5A/Shipley S1813) with electron beam evaporation of Cr/Au (5 nm/30 nm) was then used to fabricate the electrode layer. Microfluidic layers (5 – 50 μ m) were defined by SU8 lithography using a contact aligner (Suss

MABA6). The backside release of the silicon nitride window was carried out by DRIE (STS LpX Pegasus) followed by KOH etching (30%, 80 °C with isopropanol). Following backside etching, the sacrificial Cr layer was removed by etching overnight in Cr etchant with photoresist protective layer for electrodes. The sample was then immersed in DI water for an extended period (up to several days) to completely rinse the etchant from the nanochannel(s). The capping/sealing strategy for the microfluidic channels is still under development.

5.5.2 *Liquid-Cell SEM Imaging*

Liquid-cell SEM experiments on DNA-nanoparticle assembly were carried out by first functionalizing the silicon nitride membrane and nanoparticles by the approach outlined in Chapter 2. The solution of interest was loaded into the fluid reservoir with a micropipette and the MEMS chip was loaded by placing it over the o-ring and gently compressing with the top plate. Sealing and membrane integrity were verified by optical microscopy prior to loading in the SEM (FEI Quanta 600F or Quanta 650 FEG). The liquid-cell holder was mounted on the SEM Peltier stage and the resistive heaters were attached to the sides of the holder with carbon tape. A surface-mount PRT (Omega SA1-RTD) was attached to the top plate of the sample holder and both the PRT and resistive heaters were connected to an electrical feedthrough in the SEM. The PRT was connected externally to an external temperature controller (Omega CSi32). For automated temperature control studies, the temperature controller was connected to a solid-state relay, which controlled the output from a variable DC power supply. However, the PID control in this approach resulted in pulsed-DC operation, which is effective for temperature control, but resulted in image interference. As a result, most experiments were conducted with manual temperature control by changing the DC voltage to achieve the desired temperature. The system was actively cooled by

reducing the DC voltage and lowering the temperature of the Peltier stage. The Peltier stage alone does not have sufficient power to heat the sample holder above approximately 35 °C. Imaging was carried out using the solid-state BSE detector with a 30 kV accelerating voltage. Care was taken during imaging to expose each region of the specimen only once and to capture images more than 10 μm apart to minimize beam effects.

5.5.3 *Nanofluidic Liquid-Cell Imaging*

The nanofluidic liquid-cell samples were prepared by filling the released nanochannel with a colloidal suspension of 30 nm citrate-stabilized gold nanoparticles (Nanopartz, Inc.) by capillary action. After the channel filled with fluid, excess fluid was wicked away and the ends of the channels were sealed. The sealing was accomplished by either by means of a standard 5-minute epoxy or by SU8 photoresist followed by UV curing. The nanofluidic liquid cell samples were imaged in by SEM (LEO 1525) using the Robinson BSE detector at 30 kV. The suspended nanochannel samples were imaged by STEM (Hitachi HD2300) in SE, TE/BF and HAADF at 200 kV.

5.5.4 *Thermal Imaging*

Thermal imaging was carried out with an Optotherm Micro Thermal Imaging system. To simulate *in situ* studies, the Peltier stage of this microscope was only used to supplement the resistive heating elements, which were driven at similar voltages as inside the SEM. A polymer tape was applied to the aluminum sample holder match the emissivity of the silicon nitride window and correspondence was verified at room temperature. Measurements were acquired at multiple temperatures and good correspondence between the sample holder and membrane area were seen across the relevant operating range for these experiments (25 – 50 °C).

Chapter 6: Concluding Remarks

While the Summary and Outlook sections of each Chapter in this dissertation contain perspectives on future work in each area, I believe there are a few general areas worth further discussion. First, there is some divergence in opinion about what makes a system “reconfigurable.” One school of thought is that a reconfigurable system is one that should be able to switch, reversibly, from one thermodynamic equilibrium configuration to another.⁹⁶ In fact, much of the research in nanoparticle assembly focuses on developing systems to avoid kinetically trapped configurations, usually because the equilibrium configuration is more ordered. However, I believe this is a rather narrow definition. The reconfigurable systems described in this work do exhibit some properties that likely meet these criteria, but others that do not. While not explicitly evaluated, the size-selective assembly and other examples appear to be in thermodynamic equilibrium. However, some of the nanorod configurations are likely in kinetically trapped states and although these configurations are not directly reversible, one can likely switch between the states by melting and quenching. I would argue that path-independent switching between states, rather than reversibility (path dependent) is a better criterion for reconfigurability. In addition, there are likely quite interesting and distinct properties in many metastable or kinetically trapped configurations in colloidal systems, not to mention dissipative or dynamic configurations. Biological systems would be considered by many to be the ultimate reconfigurable systems and the function of these systems relies heavily on nonequilibrium processes. It therefore seems arbitrary and unnecessarily limiting to focus only on equilibrium configurations. To this end, the types of *in situ* characterization tools outlined in this dissertation will likely play a major role in evaluating such non-equilibrium structures. However, rather than just focusing on *in situ*

characterization to develop a better understanding of *ex situ* experiments and trying to compensate for the (vast) differences in experimental conditions, new research areas can be developed by exploiting this unique environment. Much as the unique properties of nanomaterials are driven by length-scale dependencies, these systems can provide a unique reaction environment due to nanoscale confinement with high surface-to-volume, ultra-high radiation flux with tunable intensity and spatial uniformity, high electric field strength, etc. By exploiting these characteristics, rather than trying to limit their impact, *in situ* microscopy systems can become nanotechnology-enabled laboratories for the creation of new science under extreme conditions.

References

- 1 Kralchevsky, P. A. & Denkov, N. D. Capillary forces and structuring in layers of colloid particles. *Current Opinion in Colloid & Interface Science* **6**, 383-401, (2001).
- 2 Kralchevsky, P. A. & Nagayama, K. Capillary interactions between particles bound to interfaces, liquid films and biomembranes. *Advances in Colloid and Interface Science* **85**, 145-192, (2000).
- 3 Mastrangeli, M. Self-assembly of micro/nanosystems across scales and interfaces. in *2017 19th International Conference on Solid-State Sensors, Actuators and Microsystems (TRANSDUCERS)*. 676-681.
- 4 Sorrenti, A., Leira-Iglesias, J., Markvoort, A. J., de Greef, T. F. A. & Hermans, T. M. Non-equilibrium supramolecular polymerization. *Chemical Society Reviews* **46**, 5476-5490, (2017).
- 5 Bishop, K. J. M., Wilmer, C. E., Soh, S. & Grzybowski, B. A. Nanoscale Forces and Their Uses in Self-Assembly. *Small* **5**, 1600-1630, (2009).
- 6 Nie, Z., Petukhova, A. & Kumacheva, E. Properties and emerging applications of self-assembled structures made from inorganic nanoparticles. *Nature Nanotechnology* **5**, 15, (2009).
- 7 Thorkelsson, K., Bai, P. & Xu, T. Self-assembly and applications of anisotropic nanomaterials: A review. *Nano Today* **10**, 48-66, (2015).
- 8 Grzelczak, M., Vermant, J., Furst, E. M. & Liz-Marzán, L. M. Directed Self-Assembly of Nanoparticles. *ACS Nano* **4**, 3591-3605, (2010).
- 9 Zhang, J., Li, Y., Zhang, X. & Yang, B. Colloidal Self-Assembly Meets Nanofabrication: From Two-Dimensional Colloidal Crystals to Nanostructure Arrays. *Advanced Materials* **22**, 4249-4269, (2010).
- 10 Robert, A. H., Eredzhep, M. & Svetlana, N. When lithography meets self-assembly: a review of recent advances in the directed assembly of complex metal nanostructures on planar and textured surfaces. *Nanotechnology* **28**, 282002, (2017).
- 11 Diaz Fernandez, Y. A., Gschneidner, T. A., Wadell, C., Fornander, L. H., Lara Avila, S., Langhammer, C., Westerlund, F. & Moth-Poulsen, K. The conquest of middle-earth: combining top-down and bottom-up nanofabrication for constructing nanoparticle based devices. *Nanoscale* **6**, 14605-14616, (2014).
- 12 Koh, S. Strategies for Controlled Placement of Nanoscale Building Blocks. *Nanoscale Research Letters* **2**, 519, (2007).
- 13 Grzelczak, M., Perez-Juste, J., Mulvaney, P. & Liz-Marzan, L. M. Shape control in gold nanoparticle synthesis. *Chemical Society Reviews* **37**, 1783-1791, (2008).
- 14 Zhao, P., Li, N. & Astruc, D. State of the art in gold nanoparticle synthesis. *Coordination Chemistry Reviews* **257**, 638-665, (2013).
- 15 Saha, K., Agasti, S. S., Kim, C., Li, X. & Rotello, V. M. Gold Nanoparticles in Chemical and Biological Sensing. *Chemical Reviews* **112**, 2739-2779, (2012).
- 16 Fialkowski, M., Bishop, K. J. M., Klajn, R., Smoukov, S. K., Campbell, C. J. & Grzybowski, B. A. Principles and Implementations of Dissipative (Dynamic) Self-Assembly. *The Journal of Physical Chemistry B* **110**, 2482-2496, (2006).

- 17 Kralchevsky, P. A. & Nagayama, K. Capillary forces between colloidal particles. *Langmuir* **10**, 23-36, (1994).
- 18 Denkov, N., Velev, O., Kralchevski, P., Ivanov, I., Yoshimura, H. & Nagayama, K. Mechanism of formation of two-dimensional crystals from latex particles on substrates. *Langmuir* **8**, 3183-3190, (1992).
- 19 Dimitrov, A. S. & Nagayama, K. Continuous Convective Assembling of Fine Particles into Two-Dimensional Arrays on Solid Surfaces. *Langmuir* **12**, 1303-1311, (1996).
- 20 Sau, T. K. & Murphy, C. J. Self-Assembly Patterns Formed upon Solvent Evaporation of Aqueous Cetyltrimethylammonium Bromide-Coated Gold Nanoparticles of Various Shapes. *Langmuir* **21**, 2923-2929, (2005).
- 21 Liu, S., Zhu, T., Hu, R. & Liu, Z. Evaporation-induced self-assembly of gold nanoparticles into a highly organized two-dimensional array. *Physical Chemistry Chemical Physics* **4**, 6059-6062, (2002).
- 22 Nikoobakht, B., Wang, Z. L. & El-Sayed, M. A. Self-Assembly of Gold Nanorods. *The Journal of Physical Chemistry B* **104**, 8635-8640, (2000).
- 23 Huang, J., Kim, F., Tao, A. R., Connor, S. & Yang, P. Spontaneous formation of nanoparticle stripe patterns through dewetting. *Nature Materials* **4**, 896, (2005).
- 24 Fan, F. & Stebe, K. J. Size-Selective Deposition and Sorting of Lyophilic Colloidal Particles on Surfaces of Patterned Wettability. *Langmuir* **21**, 1149-1152, (2005).
- 25 Fan, F. & Stebe, K. J. Assembly of Colloidal Particles by Evaporation on Surfaces with Patterned Hydrophobicity. *Langmuir* **20**, 3062-3067, (2004).
- 26 Liu, S., Tok, J. B. H., Locklin, J. & Bao, Z. Assembly and Alignment of Metallic Nanorods on Surfaces with Patterned Wettability. *Small* **2**, 1448-1453, (2006).
- 27 Cui, Y., Björk, M. T., Liddle, J. A., Sönnichsen, C., Boussert, B. & Alivisatos, A. P. Integration of Colloidal Nanocrystals into Lithographically Patterned Devices. *Nano Letters* **4**, 1093-1098, (2004).
- 28 Frederic, J., Harun, H. S., Paul, B. & Heinrich, H. Fabrication of large-area ordered arrays of nanoparticles on patterned substrates. *Nanotechnology* **16**, 1311, (2005).
- 29 Liberman, V., Yilmaz, C., Bloomstein, T. M., Somu, S., Echegoyen, Y., Busnaina, A., Cann, S. G., Krohn, K. E., Marchant, M. F. & Rothschild, M. A Nanoparticle Convective Directed Assembly Process for the Fabrication of Periodic Surface Enhanced Raman Spectroscopy Substrates. *Advanced Materials* **22**, 4298-4302, (2010).
- 30 Malaquin, L., Kraus, T., Schmid, H., Delamar, E. & Wolf, H. Controlled Particle Placement through Convective and Capillary Assembly. *Langmuir* **23**, 11513-11521, (2007).
- 31 Kraus, T., Malaquin, L., Schmid, H., Riess, W., Spencer, N. D. & Wolf, H. Nanoparticle printing with single-particle resolution. *Nature Nanotechnology* **2**, 570, (2007).
- 32 Flauraud, V., Mastrangeli, M., Bernasconi, G. D., Butet, J., Alexander, D. T. L., Shahrabi, E., Martin, O. J. F. & Brugger, J. Nanoscale topographical control of capillary assembly of nanoparticles. *Nature Nanotechnology* **12**, 73, (2016).
- 33 Palleau, E., Sangeetha, N. M. & Ressler, L. Quantification of the electrostatic forces involved in the directed assembly of colloidal nanoparticles by AFM nanoxerography. *Nanotechnology* **22**, 325603, (2011).
- 34 Fudouzi, H., Kobayashi, M. & Shinya, N. Assembling 100 nm Scale Particles by an Electrostatic Potential Field. *Journal of Nanoparticle Research* **3**, 193-200, (2001).

- 35 Jones, T. B. *Electromechanics of Particles*. (Cambridge University Press, 1995).
- 36 Giersig, M. & Mulvaney, P. Preparation of ordered colloid monolayers by electrophoretic deposition. *Langmuir* **9**, 3408-3413, (1993).
- 37 Kolíbal, M., Konečný, M., Ligmajer, F., Škoda, D., Vystavěl, T., Zlámal, J., Varga, P. & Šíkola, T. Guided Assembly of Gold Colloidal Nanoparticles on Silicon Substrates Prepatterned by Charged Particle Beams. *ACS Nano* **6**, 10098-10106, (2012).
- 38 Onses, M. S., Pathak, P., Liu, C.-C., Cerrina, F. & Nealey, P. F. Localization of Multiple DNA Sequences on Nanopatterns. *ACS Nano* **5**, 7899-7909, (2011).
- 39 Lin, H. Y., Tsai, L. C. & Chen, C. D. Assembly of Nanoparticle Patterns with Single-Particle Resolution Using DNA-Mediated Charge Trapping Technique: Method and Applications. *Advanced Functional Materials* **17**, 3182-3186, (2007).
- 40 Mendes, P. M., Jacke, S., Critchley, K., Plaza, J., Chen, Y., Nikitin, K., Palmer, R. E., Preece, J. A., Evans, S. D. & Fitzmaurice, D. Gold Nanoparticle Patterning of Silicon Wafers Using Chemical e-Beam Lithography. *Langmuir* **20**, 3766-3768, (2004).
- 41 Jacobs, H. O., Campbell, S. A. & Steward, M. G. Approaching Nanoxerography: The Use of Electrostatic Forces to Position Nanoparticles with 100 nm Scale Resolution. *Advanced Materials* **14**, 1553-1557, (2002).
- 42 Chad, R. B., Michael, G. S., Nyein, Z. L. & Heiko, O. J. Printing nanoparticles from the liquid and gas phases using nanoxerography. *Nanotechnology* **14**, 1057, (2003).
- 43 Barry, C. R., Gu, J. & Jacobs, H. O. Charging Process and Coulomb-Force-Directed Printing of Nanoparticles with Sub-100-nm Lateral Resolution. *Nano Letters* **5**, 2078-2084, (2005).
- 44 Li, Q., Zheng, J. & Liu, Z. Site-Selective Assemblies of Gold Nanoparticles on an AFM Tip-Defined Silicon Template. *Langmuir* **19**, 166-171, (2003).
- 45 Ling, X., Zhu, X., Zhang, J., Zhu, T., Liu, M., Tong, L. & Liu, Z. Reproducible Patterning of Single Au Nanoparticles on Silicon Substrates by Scanning Probe Oxidation and Self-Assembly. *The Journal of Physical Chemistry B* **109**, 2657-2665, (2005).
- 46 Khatri, O. P., Han, J., Ichii, T., Murase, K. & Sugimura, H. Self-Assembly Guided One-Dimensional Arrangement of Gold Nanoparticles: A Facile Approach. *The Journal of Physical Chemistry C* **112**, 16182-16185, (2008).
- 47 Tzeng, S. D., Lin, K. J., Hu, J. C., Chen, L. J. & Gwo, S. Templated Self-Assembly of Colloidal Nanoparticles Controlled by Electrostatic Nanopatterning on a Si₃N₄/SiO₂/Si Electret. *Advanced Materials* **18**, 1147-1151, (2006).
- 48 Ressler, L., Palleau, E., Garcia, C., Viau, G. & Viallet, B. How to Control AFM Nanoxerography for the Templated Monolayered Assembly of 2 nm Colloidal Gold Nanoparticles. *IEEE Transactions on Nanotechnology* **8**, 487-491, (2009).
- 49 Mesquida, P. & Stemmer, A. Attaching Silica Nanoparticles from Suspension onto Surface Charge Patterns Generated by a Conductive Atomic Force Microscope Tip. *Advanced Materials* **13**, 1395-1398, (2001).
- 50 Li, X.-M., Huskens, J. & Reinhoudt, D. N. Reactive self-assembled monolayers on flat and nanoparticle surfaces, and their application in soft and scanning probe lithographic nanofabrication technologies. *Journal of Materials Chemistry* **14**, 2954-2971, (2004).
- 51 Rurack, K. & Martinez-Manez, R. *Supramolecular Chemistry of Organic-Inorganic Hybrid Materials*. (Wiley, 2010).

- 52 Barsotti, J. R. J. & Stellacci, F. Chemically directed assembly of monolayer protected gold nanoparticles on lithographically generated patterns. *Journal of Materials Chemistry* **16**, 962-965, (2006).
- 53 Maury, P., Escalante, M., Reinhoudt, D. N. & Huskens, J. Directed Assembly of Nanoparticles onto Polymer-Imprinted or Chemically Patterned Templates Fabricated by Nanoimprint Lithography. *Advanced Materials* **17**, 2718-2723, (2005).
- 54 Park, M.-H., Ofir, Y., Samanta, B., Arumugam, P., Miranda, O. R. & Rotello, V. M. Nanoparticle Immobilization on Surfaces via Activatable Heterobifunctional Dithiocarbamate Bond Formation. *Advanced Materials* **20**, 4185-4188, (2008).
- 55 Garno, J. C., Yang, Y., Amro, N. A., Cruchon-Dupeyrat, S., Chen, S. & Liu, G.-Y. Precise Positioning of Nanoparticles on Surfaces Using Scanning Probe Lithography. *Nano Letters* **3**, 389-395, (2003).
- 56 Hoepfener, S., Maoz, R., Cohen, S. R., Chi, L. F., Fuchs, H. & Sagiv, J. Metal Nanoparticles, Nanowires, and Contact Electrodes Self-Assembled on Patterned Monolayer Templates—A Bottom-up Chemical Approach. *Advanced Materials* **14**, 1036-1041, (2002).
- 57 Zirbs, R., Kienberger, F., Hinterdorfer, P. & Binder, W. H. Directed Assembly of Au Nanoparticles onto Planar Surfaces via Multiple Hydrogen Bonds. *Langmuir* **21**, 8414-8421, (2005).
- 58 Binder, W. H., Zirbs, R., Kienberger, F. & Hinterdorfer, P. Selective binding of nanoparticles on surfaces and into polymeric matrices via directed hydrogen bonding interactions. *Polymers for Advanced Technologies* **17**, 754-757, (2006).
- 59 Dehlinger, D. A., Sullivan, B. D., Esener, S. & Heller, M. J. Electric-Field-Directed Assembly of Biomolecular-Derivatized Nanoparticles into Higher-Order Structures. *Small* **3**, 1237-1244, (2007).
- 60 Katz, E. & Willner, I. Integrated Nanoparticle–Biomolecule Hybrid Systems: Synthesis, Properties, and Applications. *Angewandte Chemie International Edition* **43**, 6042-6108, (2004).
- 61 Mann, S. Self-assembly and transformation of hybrid nano-objects and nanostructures under equilibrium and non-equilibrium conditions. *Nature Materials* **8**, 781, (2009).
- 62 Srivastava, S. & Kotov, N. A. Nanoparticle assembly for 1D and 2D ordered structures. *Soft Matter* **5**, 1146-1156, (2009).
- 63 Mirkin, C. A., Letsinger, R. L., Mucic, R. C. & Storhoff, J. J. A DNA-based method for rationally assembling nanoparticles into macroscopic materials. *Nature* **382**, 607, (1996).
- 64 Alivisatos, A. P., Johnsson, K. P., Peng, X., Wilson, T. E., Loweth, C. J., Bruchez Jr, M. P. & Schultz, P. G. Organization of nanocrystal molecules using DNA. *Nature* **382**, 609, (1996).
- 65 Jones, M. R., Seeman, N. C. & Mirkin, C. A. Programmable materials and the nature of the DNA bond. *Science* **347**, (2015).
- 66 Li, X., Yang, X., Qi, J. & Seeman, N. C. Antiparallel DNA Double Crossover Molecules As Components for Nanoconstruction. *Journal of the American Chemical Society* **118**, 6131-6140, (1996).
- 67 Rothmund, P. W. K. Folding DNA to create nanoscale shapes and patterns. *Nature* **440**, 297, (2006).

- 68 Hung, A. M., Micheel, C. M., Bozano, L. D., Osterbur, L. W., Wallraff, G. M. & Cha, J. N. Large-area spatially ordered arrays of gold nanoparticles directed by lithographically confined DNA origami. *Nature Nanotechnology* **5**, 121, (2009).
- 69 Mao, C., Sun, W. & Seeman, N. C. Designed Two-Dimensional DNA Holliday Junction Arrays Visualized by Atomic Force Microscopy. *Journal of the American Chemical Society* **121**, 5437-5443, (1999).
- 70 Le, J. D., Pinto, Y., Seeman, N. C., Musier-Forsyth, K., Taton, T. A. & Kiehl, R. A. DNA-Templated Self-Assembly of Metallic Nanocomponent Arrays on a Surface. *Nano Letters* **4**, 2343-2347, (2004).
- 71 Zheng, J., Constantinou, P. E., Micheel, C., Alivisatos, A. P., Kiehl, R. A. & Seeman, N. C. Two-Dimensional Nanoparticle Arrays Show the Organizational Power of Robust DNA Motifs. *Nano Letters* **6**, 1502-1504, (2006).
- 72 Demers, L. M., Mirkin, C. A., Mucic, R. C., Reynolds, R. A., Letsinger, R. L., Elghanian, R. & Viswanadham, G. A Fluorescence-Based Method for Determining the Surface Coverage and Hybridization Efficiency of Thiol-Capped Oligonucleotides Bound to Gold Thin Films and Nanoparticles. *Analytical Chemistry* **72**, 5535-5541, (2000).
- 73 Elghanian, R., Storhoff, J. J., Mucic, R. C., Letsinger, R. L. & Mirkin, C. A. Selective Colorimetric Detection of Polynucleotides Based on the Distance-Dependent Optical Properties of Gold Nanoparticles. *Science* **277**, 1078-1081, (1997).
- 74 Hill, H. D., Millstone, J. E., Banholzer, M. J. & Mirkin, C. A. The Role Radius of Curvature Plays in Thiolated Oligonucleotide Loading on Gold Nanoparticles. *ACS Nano* **3**, 418-424, (2009).
- 75 Hurst, S. J., Lytton-Jean, A. K. R. & Mirkin, C. A. Maximizing DNA Loading on a Range of Gold Nanoparticle Sizes. *Analytical Chemistry* **78**, 8313-8318, (2006).
- 76 Zhang, X., Servos, M. R. & Liu, J. Instantaneous and Quantitative Functionalization of Gold Nanoparticles with Thiolated DNA Using a pH-Assisted and Surfactant-Free Route. *Journal of the American Chemical Society* **134**, 7266-7269, (2012).
- 77 Xu, Q., Lou, X., Wang, L., Ding, X., Yu, H. & Xiao, Y. Rapid, Surfactant-Free, and Quantitative Functionalization of Gold Nanoparticles with Thiolated DNA under Physiological pH and Its Application in Molecular Beacon-Based Biosensor. *ACS Applied Materials & Interfaces* **8**, 27298-27304, (2016).
- 78 Geerts, N. & Eiser, E. DNA-functionalized colloids: Physical properties and applications. *Soft Matter* **6**, 4647-4660, (2010).
- 79 Lukatsky, D. B. & Frenkel, D. Surface and bulk dissolution properties, and selectivity of DNA-linked nanoparticle assemblies. *The Journal of Chemical Physics* **122**, 214904, (2005).
- 80 Dreyfus, R., Leunissen, M. E., Sha, R., Tkachenko, A. V., Seeman, N. C., Pine, D. J. & Chaikin, P. M. Simple Quantitative Model for the Reversible Association of DNA Coated Colloids. *Physical Review Letters* **102**, 048301, (2009).
- 81 Sun, Y., Harris, N. C. & Kiang, C. H. Melting transition of directly linked gold nanoparticle DNA assembly. *Physica A: Statistical Mechanics and its Applications* **350**, 89-94, (2005).
- 82 Jin, R., Wu, G., Li, Z., Mirkin, C. A. & Schatz, G. C. What Controls the Melting Properties of DNA-Linked Gold Nanoparticle Assemblies? *Journal of the American Chemical Society* **125**, 1643-1654, (2003).

- 83 Hurst, S. J., Hill, H. D. & Mirkin, C. A. “Three-Dimensional Hybridization” with Polyvalent DNA–Gold Nanoparticle Conjugates. *Journal of the American Chemical Society* **130**, 12192-12200, (2008).
- 84 Auyeung, E., Li, T. I. N. G., Senesi, A. J., Schmucker, A. L., Pals, B. C., de la Cruz, M. O. & Mirkin, C. A. DNA-mediated nanoparticle crystallization into Wulff polyhedra. *Nature* **505**, 73, (2013).
- 85 Jones, M. R., Macfarlane, R. J., Lee, B., Zhang, J., Young, K. L., Senesi, A. J. & Mirkin, C. A. DNA-nanoparticle superlattices formed from anisotropic building blocks. *Nature Materials* **9**, 913, (2010).
- 86 Macfarlane, R. J., Lee, B., Jones, M. R., Harris, N., Schatz, G. C. & Mirkin, C. A. Nanoparticle Superlattice Engineering with DNA. *Science* **334**, 204-208, (2011).
- 87 Nykypanchuk, D., Maye, M. M., van der Lelie, D. & Gang, O. DNA-guided crystallization of colloidal nanoparticles. *Nature* **451**, 549, (2008).
- 88 Park, S. Y., Lytton-Jean, A. K. R., Lee, B., Weigand, S., Schatz, G. C. & Mirkin, C. A. DNA-programmable nanoparticle crystallization. *Nature* **451**, 553, (2008).
- 89 Liu, W., Tagawa, M., Xin, H. L., Wang, T., Emamy, H., Li, H., Yager, K. G., Starr, F. W., Tkachenko, A. V. & Gang, O. Diamond family of nanoparticle superlattices. *Science* **351**, 582-586, (2016).
- 90 Jones, M. R., Macfarlane, R. J., Prigodich, A. E., Patel, P. C. & Mirkin, C. A. Nanoparticle Shape Anisotropy Dictates the Collective Behavior of Surface-Bound Ligands. *Journal of the American Chemical Society* **133**, 18865-18869, (2011).
- 91 O’Brien, M. N., Jones, M. R., Lee, B. & Mirkin, C. A. Anisotropic nanoparticle complementarity in DNA-mediated co-crystallization. *Nature Materials* **14**, 833, (2015).
- 92 Lin, H., Lee, S., Sun, L., Spellings, M., Engel, M., Glotzer, S. C. & Mirkin, C. A. Clathrate colloidal crystals. *Science* **355**, 931-935, (2017).
- 93 Maye, M. M., Kumara, M. T., Nykypanchuk, D., Sherman, W. B. & Gang, O. Switching binary states of nanoparticle superlattices and dimer clusters by DNA strands. *Nature Nanotechnology* **5**, 116, (2009).
- 94 Sebba, D. S., Mock, J. J., Smith, D. R., LaBean, T. H. & Lazarides, A. A. Reconfigurable Core–Satellite Nanoassemblies as Molecularly-Driven Plasmonic Switches. *Nano Letters* **8**, 1803-1808, (2008).
- 95 Rogers, W. B. & Manoharan, V. N. Programming colloidal phase transitions with DNA strand displacement. *Science* **347**, 639-642, (2015).
- 96 Solomon, M. J. Tools and Functions of Reconfigurable Colloidal Assembly. *Langmuir*, (2018).
- 97 Hartmann, D. M., Heller, M., Esener, S. C., Schwartz, D. & Tu, G. Selective DNA attachment of micro- and nanoscale particles to substrates. *Journal of Materials Research* **17**, 473-478, (2002).
- 98 Kannan, B., Kulkarni, R. P. & Majumdar, A. DNA-Based Programmed Assembly of Gold Nanoparticles on Lithographic Patterns with Extraordinary Specificity. *Nano Letters* **4**, 1521-1524, (2004).
- 99 Noh, H., Hung, A. M. & Cha, J. N. Surface-Driven DNA Assembly of Binary Cubic 3D Nanocrystal Superlattices. *Small* **7**, 3021-3025, (2011).

- 100 Lalander, C. H., Zheng, Y., Dhuey, S., Cabrini, S. & Bach, U. DNA-Directed Self-Assembly of Gold Nanoparticles onto Nanopatterned Surfaces: Controlled Placement of Individual Nanoparticles into Regular Arrays. *ACS Nano* **4**, 6153-6161, (2010).
- 101 Hellstrom, S. L., Kim, Y., Fakonas, J. S., Senesi, A. J., Macfarlane, R. J., Mirkin, C. A. & Atwater, H. A. Epitaxial Growth of DNA-Assembled Nanoparticle Superlattices on Patterned Substrates. *Nano Letters* **13**, 6084-6090, (2013).
- 102 O'Brien, M. N., Radha, B., Brown, K. A., Jones, M. R. & Mirkin, C. A. Langmuir Analysis of Nanoparticle Polyvalency in DNA-Mediated Adsorption. *Angewandte Chemie International Edition* **53**, 9532-9538, (2014).
- 103 Lin, Q.-Y., Li, Z., Brown, K. A., O'Brien, M. N., Ross, M. B., Zhou, Y., Butun, S., Chen, P.-C., Schatz, G. C., Dravid, V. P., Aydin, K. & Mirkin, C. A. Strong Coupling between Plasmonic Gap Modes and Photonic Lattice Modes in DNA-Assembled Gold Nanocube Arrays. *Nano Letters* **15**, 4699-4703, (2015).
- 104 Lin, Q.-Y., Mason, J. A., Li, Z., Zhou, W., O'Brien, M. N., Brown, K. A., Jones, M. R., Butun, S., Lee, B., Dravid, V. P., Aydin, K. & Mirkin, C. A. Building superlattices from individual nanoparticles via template-confined DNA-mediated assembly. *Science*, (2018).
- 105 Litt, D. B., Jones, M. R., Hentschel, M., Wang, Y., Yang, S., Ha, H. D., Zhang, X. & Alivisatos, A. P. Hybrid Lithographic and DNA-Directed Assembly of a Configurable Plasmonic Metamaterial That Exhibits Electromagnetically Induced Transparency. *Nano Letters*, (2018).
- 106 Kim, J., Jones, M. R., Ou, Z. & Chen, Q. In Situ Electron Microscopy Imaging and Quantitative Structural Modulation of Nanoparticle Superlattices. *ACS Nano* **10**, 9801-9808, (2016).
- 107 Li, T., Senesi, A. J. & Lee, B. Small Angle X-ray Scattering for Nanoparticle Research. *Chemical Reviews* **116**, 11128-11180, (2016).
- 108 Senesi, A. J., Eichelsdoerfer, D. J., Brown, K. A., Lee, B., Auyeung, E., Choi, C. H. J., Macfarlane, R. J., Young, K. L. & Mirkin, C. A. Oligonucleotide Flexibility Dictates Crystal Quality in DNA-Programmable Nanoparticle Superlattices. *Advanced Materials* **26**, 7235-7240, (2014).
- 109 Radha, B., Senesi, A. J., O'Brien, M. N., Wang, M. X., Auyeung, E., Lee, B. & Mirkin, C. A. Reconstitutable Nanoparticle Superlattices. *Nano Letters* **14**, 2162-2167, (2014).
- 110 Corricelli, M., Altamura, D., Curri, M. L., Sibillano, T., Siliqi, D., Mazzone, A., Depalo, N., Fanizza, E., Zanchet, D., Giannini, C. & Striccoli, M. GISAXS and GIWAXS study on self-assembling processes of nanoparticle based superlattices. *CrystEngComm* **16**, 9482-9492, (2014).
- 111 Gómez-Graña, S., Hubert, F., Testard, F., Guerrero-Martínez, A., Grillo, I., Liz-Marzán, L. M. & Spalla, O. Surfactant (Bi)Layers on Gold Nanorods. *Langmuir* **28**, 1453-1459, (2012).
- 112 Kwon, S. G., Krylova, G., Phillips, P. J., Klie, R. F., Chattopadhyay, S., Shibata, T., Bunel, E. E., Liu, Y., Prakapenka, V. B., Lee, B. & Shevchenko, E. V. Heterogeneous nucleation and shape transformation of multicomponent metallic nanostructures. *Nature Materials* **14**, 215, (2014).
- 113 Calzolari, D. C., Pontoni, D., Daillant, J. & Reichert, H. An X-ray chamber for in situ structural studies of solvent-mediated nanoparticle self-assembly. *Journal of synchrotron radiation* **20**, 306-315, (2013).

- 114 Ashley, C. E., Dunphy, D. R., Jiang, Z., Carnes, E. C., Yuan, Z., Petsev, D. N., Atanassov, P. B., Velev, O. D., Sprung, M., Wang, J., Peabody, D. S. & Brinker, C. J. Convective Assembly of 2D Lattices of Virus-like Particles Visualized by In-Situ Grazing-Incidence Small-Angle X-Ray Scattering. *Small* **7**, 1043-1050, (2011).
- 115 Choi, J. J., Bian, K., Baumgardner, W. J., Smilgies, D.-M. & Hanrath, T. Interface-Induced Nucleation, Orientational Alignment and Symmetry Transformations in Nanocube Superlattices. *Nano Letters* **12**, 4791-4798, (2012).
- 116 Jiang, Z., Lin, X.-M., Sprung, M., Narayanan, S. & Wang, J. Capturing the Crystalline Phase of Two-Dimensional Nanocrystal Superlattices in Action. *Nano Letters* **10**, 799-803, (2010).
- 117 Pontoni, D., Alvine, K. J., Checco, A., Gang, O., Ocko, B. M. & Pershan, P. S. Equilibrating Nanoparticle Monolayers Using Wetting Films. *Physical Review Letters* **102**, 016101, (2009).
- 118 McMullan, J. M. & Wagner, N. J. Directed self-assembly of colloidal crystals by dielectrophoretic ordering observed with small angle neutron scattering (SANS). *Soft Matter* **6**, 5443-5450, (2010).
- 119 Sonntag, C. v. in *Recent Trends in Radiation Chemistry* 543-562 (WORLD SCIENTIFIC, 2011).
- 120 Becker, D., Adhikary, A. & Sevilla, M. D. in *Recent Trends in Radiation Chemistry* 509-542 (WORLD SCIENTIFIC, 2011).
- 121 Trabattoni, S., Moret, M., Miozzo, L. & Campione, M. Self-assembly of gold nanoparticles on functional organic molecular crystals. *Journal of Colloid and Interface Science* **360**, 422-429, (2011).
- 122 Kim, Y. & Yi, J. In-situ observation of deposition of gold nanoparticles on the amine-functionalized surface by open liquid-AFM. *Korean Journal of Chemical Engineering* **25**, 383-385, (2008).
- 123 Maye, M. M., Luo, J., Han, L. & Zhong, C.-J. Probing pH-Tuned Morphological Changes in Core-Shell Nanoparticle Assembly Using Atomic Force Microscopy. *Nano Letters* **1**, 575-579, (2001).
- 124 Gu, H., Chao, J., Xiao, S.-J. & Seeman, N. C. A proximity-based programmable DNA nanoscale assembly line. *Nature* **465**, 202, (2010).
- 125 Inhee, C., Younghun, K., Jong Ho, K., Young In, Y., Jeongjin, L., Suseung, L., Surin, H. & Jongheop, Y. Fast image scanning method in liquid-AFM without image distortion. *Nanotechnology* **19**, 445701, (2008).
- 126 Fleming, A. J., Kenton, B. J. & Leang, K. K. Bridging the gap between conventional and video-speed scanning probe microscopes. *Ultramicroscopy* **110**, 1205-1214, (2010).
- 127 Weisenhorn, A. L., Hansma, P. K., Albrecht, T. R. & Quate, C. F. Forces in atomic force microscopy in air and water. *Applied Physics Letters* **54**, 2651-2653, (1989).
- 128 Hell, S. W. Far-Field Optical Nanoscopy. *Science* **316**, 1153-1158, (2007).
- 129 Harke, B., Ullal, C. K., Keller, J. & Hell, S. W. Three-Dimensional Nanoscopy of Colloidal Crystals. *Nano Letters* **8**, 1309-1313, (2008).
- 130 Tian, Z., Li, A. D. Q. & Hu, D. Super-resolution fluorescence nanoscopy applied to imaging core-shell photoswitching nanoparticles and their self-assemblies. *Chemical Communications* **47**, 1258-1260, (2011).

- 131 Lauterbach, M. A., Ullal, C. K., Westphal, V. & Hell, S. W. Dynamic Imaging of Colloidal-Crystal Nanostructures at 200 Frames per Second. *Langmuir* **26**, 14400-14404, (2010).
- 132 Nedosekin, D. A., Galanzha, E. I., Dervishi, E., Biris, A. S. & Zharov, V. P. Super-Resolution Nonlinear Photothermal Microscopy. *Small* **10**, 135-142, (2014).
- 133 Ross, F. M. Opportunities and challenges in liquid cell electron microscopy. *Science* **350**, (2015).
- 134 de Jonge, N. & Ross, F. M. Electron microscopy of specimens in liquid. *Nature Nanotechnology* **6**, 695, (2011).
- 135 Hart, J. L., Lang, A. C., Leff, A. C., Longo, P., Trevor, C., Twesten, R. D. & Taheri, M. L. Direct Detection Electron Energy-Loss Spectroscopy: A Method to Push the Limits of Resolution and Sensitivity. *Scientific Reports* **7**, 8243, (2017).
- 136 Stach, E. A., Zakharov, D., Rivas, R. D., Longo, P., Lent, M., Gubbens, A. & Czarnik, C. Exploiting a direct detection camera for in-situ microscopy. *Microscopy and Microanalysis* **19**, 392-393, (2013).
- 137 Park, J., Elmlund, H., Ercius, P., Yuk, J. M., Limmer, D. T., Chen, Q., Kim, K., Han, S. H., Weitz, D. A., Zettl, A. & Alivisatos, A. P. 3D structure of individual nanocrystals in solution by electron microscopy. *Science* **349**, 290-295, (2015).
- 138 Yuk, J. M., Park, J., Ercius, P., Kim, K., Hellebusch, D. J., Crommie, M. F., Lee, J. Y., Zettl, A. & Alivisatos, A. P. High-Resolution EM of Colloidal Nanocrystal Growth Using Graphene Liquid Cells. *Science* **336**, 61-64, (2012).
- 139 Liu, Y., Lin, X.-M., Sun, Y. & Rajh, T. In Situ Visualization of Self-Assembly of Charged Gold Nanoparticles. *Journal of the American Chemical Society* **135**, 3764-3767, (2013).
- 140 Powers, A. S., Liao, H.-G., Raja, S. N., Bronstein, N. D., Alivisatos, A. P. & Zheng, H. Tracking Nanoparticle Diffusion and Interaction during Self-Assembly in a Liquid Cell. *Nano Letters* **17**, 15-20, (2017).
- 141 Luo, B., Smith, J. W., Ou, Z. & Chen, Q. Quantifying the Self-Assembly Behavior of Anisotropic Nanoparticles Using Liquid-Phase Transmission Electron Microscopy. *Accounts of Chemical Research* **50**, 1125-1133, (2017).
- 142 Park, J., Zheng, H., Lee, W. C., Geissler, P. L., Rabani, E. & Alivisatos, A. P. Direct Observation of Nanoparticle Superlattice Formation by Using Liquid Cell Transmission Electron Microscopy. *ACS Nano* **6**, 2078-2085, (2012).
- 143 Sutter, E., Sutter, P., Tkachenko, A. V., Krahne, R., de Graaf, J., Arciniegas, M. & Manna, L. In situ microscopy of the self-assembly of branched nanocrystals in solution. *Nature Communications* **7**, 11213, (2016).
- 144 Chen, Q., Smith, J. M., Park, J., Kim, K., Ho, D., Rasool, H. I., Zettl, A. & Alivisatos, A. P. 3D Motion of DNA-Au Nanoconjugates in Graphene Liquid Cell Electron Microscopy. *Nano Letters* **13**, 4556-4561, (2013).
- 145 Carlson, D. B. & Evans, J. E. in *The transmission electron microscope* (Intech, 2012).
- 146 Frank, J. Single-Particle Imaging of Macromolecules by Cryo-Electron Microscopy. *Annual Review of Biophysics and Biomolecular Structure* **31**, 303-319, (2002).
- 147 Cho, H., Jones, M. R., Nguyen, S. C., Hauwiler, M. R., Zettl, A. & Alivisatos, A. P. The Use of Graphene and Its Derivatives for Liquid-Phase Transmission Electron Microscopy of Radiation-Sensitive Specimens. *Nano Letters* **17**, 414-420, (2017).

- 148 Myers, B. D., Lin, Q.-Y., Wu, H., Luijten, E., Mirkin, C. A. & Dravid, V. P. Size-Selective Nanoparticle Assembly on Substrates by DNA Density Patterning. *ACS Nano* **10**, 5679-5686, (2016).
- 149 Broers, A. N., Harper, J. M. E. & Molzen, W. W. 250-Å linewidths with PMMA electron resist. *Applied Physics Letters* **33**, 392-394, (1978).
- 150 Kim, S. C., Lim, B. O., Lee, H. S., Shin, D. H., Kim, S. K., Park, H. C. & Rhee, J. K. Sub-100nm T-gate fabrication using a positive resist ZEP520/P(MMA-MAA)/PMMA trilayer by double exposure at 50kV e-beam lithography. *Materials Science in Semiconductor Processing* **7**, 7-11, (2004).
- 151 Tada, T. Poly (Trifluoroethyl α -Chloroacrylate as a Highly Sensitive Positive Electron Resist. *Journal of the Electrochemical Society* **126**, 1829-1830, (1979).
- 152 Blum, L., Perkins, M. E. & Liu, H. Y. A study of the effect of key processing variables on the lithographic performance of Microposit SAL601-ER7 resist. *Journal of Vacuum Science & Technology B: Microelectronics Processing and Phenomena* **6**, 2280-2285, (1988).
- 153 Pépin, A., Studer, V., Decanini, D. & Chen, Y. Exploring the high sensitivity of SU-8 resist for high resolution electron beam patterning. *Microelectronic Engineering* **73-74**, 233-237, (2004).
- 154 Namatsu, H., Yamaguchi, T., Nagase, M., Yamazaki, K. & Kurihara, K. Nano-patterning of a hydrogen silsesquioxane resist with reduced linewidth fluctuations. *Microelectronic Engineering* **41-42**, 331-334, (1998).
- 155 Zharnikov, M. & Grunze, M. Modification of thiol-derived self-assembling monolayers by electron and x-ray irradiation: Scientific and lithographic aspects. *Journal of Vacuum Science & Technology B: Microelectronics and Nanometer Structures Processing, Measurement, and Phenomena* **20**, 1793-1807, (2002).
- 156 Geyer, W., Stadler, V., Eck, W., Zharnikov, M., Götzhäuser, A. & Grunze, M. Electron-induced crosslinking of aromatic self-assembled monolayers: Negative resists for nanolithography. *Applied Physics Letters* **75**, 2401-2403, (1999).
- 157 Götzhäuser, A., Eck, W., Geyer, W., Stadler, V., Weimann, T., Hinze, P. & Grunze, M. Chemical Nanolithography with Electron Beams. *Advanced Materials* **13**, 803-806, (2001).
- 158 Ballav, N., Schilp, S. & Zharnikov, M. Electron-Beam Chemical Lithography with Aliphatic Self-Assembled Monolayers. *Angewandte Chemie International Edition* **47**, 1421-1424, (2008).
- 159 Whelan, C. S., Lercel, M. J., Craighead, H. G., Seshadri, K. & Allara, D. L. Improved electron-beam patterning of Si with self-assembled monolayers. *Applied Physics Letters* **69**, 4245-4247, (1996).
- 160 Lercel, M. J., Tiberio, R. C., Chapman, P. F., Craighead, H. G., Sheen, C. W., Parikh, A. N. & Allara, D. L. Self-assembled monolayer electron-beam resists on GaAs and SiO₂. *Journal of Vacuum Science & Technology B: Microelectronics and Nanometer Structures Processing, Measurement, and Phenomena* **11**, 2823-2828, (1993).
- 161 Zhang, G.-J., Tanii, T., Funatsu, T. & Ohdomari, I. Patterning of DNA nanostructures on silicon surface by electron beam lithography of self-assembled monolayer. *Chemical Communications*, 786-787, (2004).

- 162 Tanii, T., Hosaka, T., Miyake, T., Zhang, G.-J., Zako, T., Funatsu, T. & Ohdomari, I. Preferential immobilization of biomolecules on silicon microstructure array by means of electron beam lithography on organosilane self-assembled monolayer resist. *Applied Surface Science* **234**, 102-106, (2004).
- 163 John, P. M. S. & Craighead, H. G. Monolayers of fluorinated silanes as electron-beam resists. *Journal of Vacuum Science & Technology B: Microelectronics and Nanometer Structures Processing, Measurement, and Phenomena* **14**, 69-74, (1996).
- 164 Genzer, J. & Bhat, R. R. Surface-Bound Soft Matter Gradients. *Langmuir* **24**, 2294-2317, (2008).
- 165 Pardo, L., Wilson, W. C. & Boland, T. Characterization of Patterned Self-Assembled Monolayers and Protein Arrays Generated by the Ink-Jet Method. *Langmuir* **19**, 1462-1466, (2003).
- 166 Jeon, N. L., Dertinger, S. K. W., Chiu, D. T., Choi, I. S., Stroock, A. D. & Whitesides, G. M. Generation of Solution and Surface Gradients Using Microfluidic Systems. *Langmuir* **16**, 8311-8316, (2000).
- 167 Jiang, X., Xu, Q., Dertinger, S. K. W., Stroock, A. D., Fu, T.-m. & Whitesides, G. M. A General Method for Patterning Gradients of Biomolecules on Surfaces Using Microfluidic Networks. *Analytical Chemistry* **77**, 2338-2347, (2005).
- 168 Kraus, T., Stutz, R., Balmer, T. E., Schmid, H., Malaquin, L., Spencer, N. D. & Wolf, H. Printing Chemical Gradients. *Langmuir* **21**, 7796-7804, (2005).
- 169 Keenan, T. M. & Folch, A. Biomolecular gradients in cell culture systems. *Lab on a Chip* **8**, 34-57, (2008).
- 170 Yamada, K., Henares, T. G., Suzuki, K. & Citterio, D. Paper-Based Inkjet-Printed Microfluidic Analytical Devices. *Angewandte Chemie International Edition* **54**, 5294-5310, (2015).
- 171 Carroll, K. M., Giordano, A. J., Wang, D., Kodali, V. K., Scrimgeour, J., King, W. P., Marder, S. R., Riedo, E. & Curtis, J. E. Fabricating Nanoscale Chemical Gradients with ThermoChemical NanoLithography. *Langmuir* **29**, 8675-8682, (2013).
- 172 Albisetti, E., Carroll, K. M., Lu, X., Curtis, J. E., Petti, D., Bertacco, R. & Riedo, E. Thermochemical scanning probe lithography of protein gradients at the nanoscale. *Nanotechnology* **27**, 315302, (2016).
- 173 Kim, J., Joy, D. C. & Lee, S. Y. Controlling resist thickness and etch depth for fabrication of 3D structures in electron-beam grayscale lithography. *Microelectronic Engineering* **84**, 2859-2864, (2007).
- 174 Arne, S. & Helmut, S. Fabrication of 3D nanoimprint stamps with continuous reliefs using dose-modulated electron beam lithography and thermal reflow. *Journal of Micromechanics and Microengineering* **20**, 095002, (2010).
- 175 Outi, T., Nguyet, D., Mikhail, E., Harri, L., Kyösti, K. & Babak, P. Building molecular surface gradients with electron beam lithography. *Journal of Micromechanics and Microengineering* **21**, 054025, (2011).
- 176 Ballav, N., Shaporenko, A., Krakert, S., Terfort, A. & Zharnikov, M. Tuning the Exchange Reaction between a Self-assembled Monolayer and Potential Substituents by Electron Irradiation. *The Journal of Physical Chemistry C* **111**, 7772-7782, (2007).
- 177 Ballav, N., Shaporenko, A., Terfort, A. & Zharnikov, M. A Flexible Approach to the Fabrication of Chemical Gradients. *Advanced Materials* **19**, 998-1000, (2007).

- 178 Harnett, C. K., Satyalakshmi, K. M. & Craighead, H. G. Bioactive Templates Fabricated
by Low-Energy Electron Beam Lithography of Self-Assembled Monolayers. *Langmuir* **17**,
178-182, (2001).
- 179 Mesquita, C. H. d., Neto, J. M. F. & Hamada, M. M. Target theory applied in the radiation
damage analysis for organic detectors. in *2007 IEEE Nuclear Science Symposium
Conference Record*. 1313-1317.
- 180 Isaacson, M., Johnson, D. & Crewe, A. V. Electron Beam Excitation and Damage of
Biological Molecules; Its Implications for Specimen Damage in Electron Microscopy.
Radiation Research **55**, 205-224, (1973).
- 181 Baccarelli, I., Bald, I., Gianturco, F. A., Illenberger, E. & Kopyra, J. Electron-induced
damage of DNA and its components: Experiments and theoretical models. *Physics Reports*
508, 1-44, (2011).
- 182 Lett, J. T. & Alexander, P. Crosslinking and Degradation of Deoxyribonucleic Acid Gels
with Varying Water Contents When Irradiated with Electrons. *Radiation Research* **15**, 159-
173, (1961).
- 183 Lett, J. T., Stacey, K. A. & Alexander, P. Crosslinking of Dry Deoxyribonucleic Acids by
Electrons. *Radiation Research* **14**, 349-362, (1961).
- 184 Keller, A., Bald, I., Rotaru, A., Cauët, E., Gothelf, K. V. & Besenbacher, F. Probing
Electron-Induced Bond Cleavage at the Single-Molecule Level Using DNA Origami
Templates. *ACS Nano* **6**, 4392-4399, (2012).
- 185 Luo, X., Zheng, Y. & Sanche, L. DNA strand breaks and crosslinks induced by transient
anions in the range 2-20 eV. *The Journal of Chemical Physics* **140**, 155101, (2014).
- 186 May, C. J., Canavan, H. E. & Castner, D. G. Quantitative X-ray Photoelectron
Spectroscopy and Time-of-Flight Secondary Ion Mass Spectrometry Characterization of
the Components in DNA. *Analytical Chemistry* **76**, 1114-1122, (2004).
- 187 Ptasíńska, S., Styczyńska, A., Nixon, T., Mason, N. J., Klyachko, D. V. & Sanche, L. X-
ray induced damage in DNA monitored by X-ray photoelectron spectroscopy. *The Journal
of Chemical Physics* **129**, 065102, (2008).
- 188 Kanaya, K. & Okayama, S. Penetration and energy-loss theory of electrons in solid targets.
Journal of Physics D: Applied Physics **5**, 43, (1972).
- 189 Lin, Y. & Joy, D. C. A new examination of secondary electron yield data. *Surface and
Interface Analysis* **37**, 895-900, (2005).
- 190 Murata, K., Kyser, D. F. & Ting, C. H. Monte Carlo simulation of fast secondary electron
production in electron beam resists. *Journal of Applied Physics* **52**, 4396-4405, (1981).
- 191 Hovington, P., Drouin, D. & Gauvin, R. CASINO: A new monte carlo code in C language
for electron beam interaction —part I: Description of the program. *Scanning* **19**, 1-14,
(1997).
- 192 Joy, D. C. *Monte Carlo modeling for electron microscopy and microanalysis*. (New York
: Oxford University Press, 1995).
- 193 Demers, H., Poirier-Demers, N., Couture, A. R., Joly, D., Guilmain, M., de Jonge, N. &
Drouin, D. Three-dimensional electron microscopy simulation with the CASINO Monte
Carlo software. *Scanning* **33**, 135-146, (2011).
- 194 Williams, K. R., Gupta, K. & Wasilik, M. Etch rates for micromachining processing-Part
II. *Journal of Microelectromechanical Systems* **12**, 761-778, (2003).

- 195 Jones, M. R. & Mirkin, C. A. Bypassing the Limitations of Classical Chemical Purification with DNA-Programmable Nanoparticle Recrystallization. *Angewandte Chemie* **125**, 2958-2963, (2013).
- 196 Myers, B. D. & Dravid, V. P. Variable Pressure Electron Beam Lithography (VP-eBL): A New Tool for Direct Patterning of Nanometer-Scale Features on Substrates with Low Electrical Conductivity. *Nano Letters* **6**, 963-968, (2006).
- 197 Spectra of DNA-Conjugated Fluorescent Dyes. (Integrated DNA Technologies, 2011).
- 198 Rahul, C., Jaswinder, S., Haining, W., Shengli, Z., Su, L., Hao, Y., Stuart, L. & Yan, L. Distance-dependent interactions between gold nanoparticles and fluorescent molecules with DNA as tunable spacers. *Nanotechnology* **20**, 485201, (2009).
- 199 Shevchenko, E. V., Talapin, D. V., Kotov, N. A., O'Brien, S. & Murray, C. B. Structural diversity in binary nanoparticle superlattices. *Nature* **439**, 55, (2006).
- 200 Kuzyk, A., Schreiber, R., Fan, Z., Pardatscher, G., Roller, E.-M., Högele, A., Simmel, F. C., Govorov, A. O. & Liedl, T. DNA-based self-assembly of chiral plasmonic nanostructures with tailored optical response. *Nature* **483**, 311, (2012).
- 201 Tan, S. J., Campolongo, M. J., Luo, D. & Cheng, W. Building plasmonic nanostructures with DNA. *Nature Nanotechnology* **6**, 268, (2011).
- 202 Park, D. J., Zhang, C., Ku, J. C., Zhou, Y., Schatz, G. C. & Mirkin, C. A. Plasmonic photonic crystals realized through DNA-programmable assembly. *Proceedings of the National Academy of Sciences* **112**, 977-981, (2015).
- 203 Anker, J. N., Hall, W. P., Lyandres, O., Shah, N. C., Zhao, J. & Van Duyne, R. P. Biosensing with plasmonic nanosensors. *Nature Materials* **7**, 442, (2008).
- 204 Park, S.-J., Taton, T. A. & Mirkin, C. A. Array-Based Electrical Detection of DNA with Nanoparticle Probes. *Science* **295**, 1503-1506, (2002).
- 205 Agrios, A. G., Cesar, I., Comte, P., Nazeeruddin, M. K. & Grätzel, M. Nanostructured Composite Films for Dye-Sensitized Solar Cells by Electrostatic Layer-by-Layer Deposition. *Chemistry of Materials* **18**, 5395-5397, (2006).
- 206 Zijlstra, P., Chon, J. W. M. & Gu, M. Five-dimensional optical recording mediated by surface plasmons in gold nanorods. *Nature* **459**, 410, (2009).
- 207 Cargnello, M., Johnston-Peck, A. C., Diroll, B. T., Wong, E., Datta, B., Damodhar, D., Doan-Nguyen, V. V. T., Herzing, A. A., Kagan, C. R. & Murray, C. B. Substitutional doping in nanocrystal superlattices. *Nature* **524**, 450, (2015).
- 208 Boles, M. A. & Talapin, D. V. Many-Body Effects in Nanocrystal Superlattices: Departure from Sphere Packing Explains Stability of Binary Phases. *Journal of the American Chemical Society* **137**, 4494-4502, (2015).
- 209 Senesi, A. J., Eichelsdoerfer, D. J., Macfarlane, R. J., Jones, M. R., Auyeung, E., Lee, B. & Mirkin, C. A. Stepwise Evolution of DNA-Programmable Nanoparticle Superlattices. *Angewandte Chemie International Edition* **52**, 6624-6628, (2013).
- 210 Ku, J. C., Ross, M. B., Schatz, G. C. & Mirkin, C. A. Conformal, Macroscopic Crystalline Nanoparticle Sheets Assembled with DNA. *Advanced Materials* **27**, 3159-3163, (2015).
- 211 Taton, T. A., Mirkin, C. A. & Letsinger, R. L. Scanometric DNA Array Detection with Nanoparticle Probes. *Science* **289**, 1757-1760, (2000).
- 212 Roller, E.-M., Khorashad, L. K., Fedoruk, M., Schreiber, R., Govorov, A. O. & Liedl, T. DNA-Assembled Nanoparticle Rings Exhibit Electric and Magnetic Resonances at Visible Frequencies. *Nano Letters* **15**, 1368-1373, (2015).

- 213 Ross, M. B., Mirkin, C. A. & Schatz, G. C. Optical Properties of One-, Two-, and Three-Dimensional Arrays of Plasmonic Nanostructures. *The Journal of Physical Chemistry C* **120**, 816-830, (2016).
- 214 Storhoff, J. J., Lazarides, A. A., Mucic, R. C., Mirkin, C. A., Letsinger, R. L. & Schatz, G. C. What Controls the Optical Properties of DNA-Linked Gold Nanoparticle Assemblies? *Journal of the American Chemical Society* **122**, 4640-4650, (2000).
- 215 Macfarlane, R. J., Thaner, R. V., Brown, K. A., Zhang, J., Lee, B., Nguyen, S. T. & Mirkin, C. A. Importance of the DNA “bond” in programmable nanoparticle crystallization. *Proceedings of the National Academy of Sciences* **111**, 14995-15000, (2014).
- 216 Donthu, S., Pan, Z., Myers, B., Shekhawat, G., Wu, N. & Dravid, V. Facile Scheme for Fabricating Solid-State Nanostructures Using E-Beam Lithography and Solution Precursors. *Nano Letters* **5**, 1710-1715, (2005).
- 217 Lee, J.-S., Stoeva, S. I. & Mirkin, C. A. DNA-Induced Size-Selective Separation of Mixtures of Gold Nanoparticles. *Journal of the American Chemical Society* **128**, 8899-8903, (2006).
- 218 Hill, H. D., Macfarlane, R. J., Senesi, A. J., Lee, B., Park, S. Y. & Mirkin, C. A. Controlling the Lattice Parameters of Gold Nanoparticle FCC Crystals with Duplex DNA Linkers. *Nano Letters* **8**, 2341-2344, (2008).
- 219 Hill, H. D. & Mirkin, C. A. The bio-barcode assay for the detection of protein and nucleic acid targets using DTT-induced ligand exchange. *Nature Protocols* **1**, 324, (2006).
- 220 Auyeung, E., Macfarlane, R. J., Choi, C. H. J., Cutler, J. I. & Mirkin, C. A. Transitioning DNA-Engineered Nanoparticle Superlattices from Solution to the Solid State. *Advanced Materials* **24**, 5181-5186, (2012).
- 221 Vogel, H. A better way to construct the sunflower head. *Mathematical Biosciences* **44**, 179-189, (1979).
- 222 Li, T. I. N. G., Sknepnek, R., Macfarlane, R. J., Mirkin, C. A. & Olvera de la Cruz, M. Modeling the Crystallization of Spherical Nucleic Acid Nanoparticle Conjugates with Molecular Dynamics Simulations. *Nano Letters* **12**, 2509-2514, (2012).
- 223 Clavero, C. Plasmon-induced hot-electron generation at nanoparticle/metal-oxide interfaces for photovoltaic and photocatalytic devices. *Nature Photonics* **8**, 95, (2014).
- 224 Sankaran, K. J., Kunuku, S., Sundaravel, B., Hsieh, P.-Y., Chen, H.-C., Leou, K.-C., Tai, N.-H. & Lin, I. N. Gold nanoparticle-ultrananocrystalline diamond hybrid structured materials for high-performance optoelectronic device applications. *Nanoscale* **7**, 4377-4385, (2015).
- 225 Zhu, G., Peng, B., Chen, J., Jing, Q. & Lin Wang, Z. Triboelectric nanogenerators as a new energy technology: From fundamentals, devices, to applications. *Nano Energy* **14**, 126-138, (2015).
- 226 Fei Guo, C., Sun, T., Cao, F., Liu, Q. & Ren, Z. Metallic nanostructures for light trapping in energy-harvesting devices. *Light: Science & Applications* **3**, e161, (2014).
- 227 Son, D., Lee, J., Qiao, S., Ghaffari, R., Kim, J., Lee, J. E., Song, C., Kim, S. J., Lee, D. J., Jun, S. W., Yang, S., Park, M., Shin, J., Do, K., Lee, M., Kang, K., Hwang, C. S., Lu, N., Hyeon, T. & Kim, D.-H. Multifunctional wearable devices for diagnosis and therapy of movement disorders. *Nature Nanotechnology* **9**, 397, (2014).
- 228 Yen, C.-W., de Puig, H., Tam, J. O., Gomez-Marquez, J., Bosch, I., Hamad-Schifferli, K. & Gehrke, L. Multicolored silver nanoparticles for multiplexed disease diagnostics:

- distinguishing dengue, yellow fever, and Ebola viruses. *Lab on a Chip* **15**, 1638-1641, (2015).
- 229 Lee, H., Lee, Y., Song, C., Cho, H. R., Ghaffari, R., Choi, T. K., Kim, K. H., Lee, Y. B., Ling, D., Lee, H., Yu, S. J., Choi, S. H., Hyeon, T. & Kim, D.-H. An endoscope with integrated transparent bioelectronics and theranostic nanoparticles for colon cancer treatment. *Nature Communications* **6**, 10059, (2015).
- 230 Li, Z., Palacios, E., Butun, S. & Aydin, K. Visible-frequency metasurfaces for broadband anomalous reflection and high-efficiency spectrum splitting. *Nano letters* **15**, 1615-1621, (2015).
- 231 Butun, S., Palacios, E., Cain, J. D., Liu, Z., Dravid, V. P. & Aydin, K. Quantifying plasmon-enhanced light absorption in monolayer WS₂ films. *ACS applied materials & interfaces* **9**, 15044-15051, (2017).
- 232 Kildishev, A. V., Boltasseva, A. & Shalaev, V. M. Planar Photonics with Metasurfaces. *Science* **339**, (2013).
- 233 Minovich, A. E., Miroshnichenko, A. E., Bykov, A. Y., Murzina, T. V., Neshev, D. N. & Kivshar, Y. S. Functional and nonlinear optical metasurfaces. *Laser & Photonics Reviews* **9**, 195-213, (2015).
- 234 High, A. A., Devlin, R. C., Dibos, A., Polking, M., Wild, D. S., Perczel, J., de Leon, N. P., Lukin, M. D. & Park, H. Visible-frequency hyperbolic metasurface. *Nature* **522**, 192, (2015).
- 235 Devlin, R. C., Khorasaninejad, M., Chen, W. T., Oh, J. & Capasso, F. Broadband high-efficiency dielectric metasurfaces for the visible spectrum. *Proceedings of the National Academy of Sciences* **113**, 10473-10478, (2016).
- 236 Shalaev, V. M., Cai, W., Chettiar, U. K., Yuan, H.-K., Sarychev, A. K., Drachev, V. P. & Kildishev, A. V. Negative index of refraction in optical metamaterials. *Opt. Lett.* **30**, 3356-3358, (2005).
- 237 Liu, Q., Cui, Y., Gardner, D., Li, X., He, S. & Smalyukh, I. I. Self-Alignment of Plasmonic Gold Nanorods in Reconfigurable Anisotropic Fluids for Tunable Bulk Metamaterial Applications. *Nano Letters* **10**, 1347-1353, (2010).
- 238 Huang, L., Chen, X., Mühlenbernd, H., Zhang, H., Chen, S., Bai, B., Tan, Q., Jin, G., Cheah, K.-W., Qiu, C.-W., Li, J., Zentgraf, T. & Zhang, S. Three-dimensional optical holography using a plasmonic metasurface. *Nature Communications* **4**, 2808, (2013).
- 239 Zhao, Y., Belkin, M. A. & Alù, A. Twisted optical metamaterials for planarized ultrathin broadband circular polarizers. *Nature Communications* **3**, 870, (2012).
- 240 Nepal, D., Onses, M. S., Park, K., Jespersen, M., Thode, C. J., Nealey, P. F. & Vaia, R. A. Control over Position, Orientation, and Spacing of Arrays of Gold Nanorods Using Chemically Nanopatterned Surfaces and Tailored Particle–Particle–Surface Interactions. *ACS Nano* **6**, 5693-5701, (2012).
- 241 Kuemin, C., Nowack, L., Bozano, L., Spencer, N. D. & Wolf, H. Oriented Assembly of Gold Nanorods on the Single-Particle Level. *Advanced Functional Materials* **22**, 702-708, (2012).
- 242 Holzner, F., Kuemin, C., Paul, P., Hedrick, J. L., Wolf, H., Spencer, N. D., Duerig, U. & Knoll, A. W. Directed Placement of Gold Nanorods Using a Removable Template for Guided Assembly. *Nano Letters* **11**, 3957-3962, (2011).

- 243 Fengyuan, L., Theodorian, B.-T. & Joel, P. Controlling directed self-assembly of gold
nanorods in patterned PS-b-PMMA thin films. *Nanotechnology* **26**, 055301, (2015).
- 244 Zheludev, N. I. & Kivshar, Y. S. From metamaterials to metadevices. *Nature Materials* **11**,
917, (2012).
- 245 Ou, J.-Y., Plum, E., Zhang, J. & Zheludev, N. I. An electromechanically reconfigurable
plasmonic metamaterial operating in the near-infrared. *Nature Nanotechnology* **8**, 252,
(2013).
- 246 Zhu, W. M., Liu, A. Q., Bourouina, T., Tsai, D. P., Teng, J. H., Zhang, X. H., Lo, G. Q.,
Kwong, D. L. & Zheludev, N. I. Microelectromechanical Maltese-cross metamaterial with
tunable terahertz anisotropy. *Nature Communications* **3**, 1274, (2012).
- 247 Ou, J. Y., Plum, E., Jiang, L. & Zheludev, N. I. Reconfigurable Photonic Metamaterials.
Nano Letters **11**, 2142-2144, (2011).
- 248 Fu, Y. H., Liu, A. Q., Zhu, W. M., Zhang, X. M., Tsai, D. P., Zhang, J. B., Mei, T., Tao, J.
F., Guo, H. C., Zhang, X. H., Teng, J. H., Zheludev, N. I., Lo, G. Q. & Kwong, D. L. A
Micromachined Reconfigurable Metamaterial via Reconfiguration of Asymmetric Split-
Ring Resonators. *Advanced Functional Materials* **21**, 3589-3594, (2011).
- 249 Tao, H., Strikwerda, A. C., Fan, K., Padilla, W. J., Zhang, X. & Averitt, R. D.
Reconfigurable Terahertz Metamaterials. *Physical Review Letters* **103**, 147401, (2009).
- 250 Ma, F., Lin, Y.-S., Zhang, X. & Lee, C. Tunable multiband terahertz metamaterials using
a reconfigurable electric split-ring resonator array. *Light: Science & Applications* **3**,
e171, (2014).
- 251 Pryce, I. M., Aydin, K., Kelaita, Y. A., Briggs, R. M. & Atwater, H. A. Highly Strained
Compliant Optical Metamaterials with Large Frequency Tunability. *Nano Letters* **10**,
4222-4227, (2010).
- 252 Cui, Y., Zhou, J., Tamma, V. A. & Park, W. Dynamic Tuning and Symmetry Lowering of
Fano Resonance in Plasmonic Nanostructure. *ACS Nano* **6**, 2385-2393, (2012).
- 253 Han, J.-H., Kim, I., Ryu, J.-W., Kim, J., Cho, J.-H., Yim, G.-S., Park, H.-S., Min, B. &
Choi, M. Rotationally reconfigurable metamaterials based on moiré phenomenon. *Optics
Express* **23**, 17443-17449, (2015).
- 254 Lapine, M., Powell, D., Gorkunov, M., Shadrivov, I., Marqués, R. & Kivshar, Y. Structural
tunability in metamaterials. *Applied Physics Letters* **95**, 084105, (2009).
- 255 Shadrivov, I. V., Powell, D. A., Morrison, S. K., Kivshar, Y. S. & Milford, G. N. Scattering
of electromagnetic waves in metamaterial superlattices. *Applied Physics Letters* **90**,
201919, (2007).
- 256 Kats, M. A., Sharma, D., Lin, J., Genevet, P., Blanchard, R., Yang, Z., Qazilbash, M. M.,
Basov, D. N., Ramanathan, S. & Capasso, F. Ultra-thin perfect absorber employing a
tunable phase change material. *Applied Physics Letters* **101**, 221101, (2012).
- 257 Cao, T., Wei, C.-w., Simpson, R. E., Zhang, L. & Cryan, M. J. Broadband Polarization-
Independent Perfect Absorber Using a Phase-Change Metamaterial at Visible Frequencies.
Scientific Reports **4**, 3955, (2014).
- 258 Wang, Q., Rogers, E. T. F., Gholipour, B., Wang, C.-M., Yuan, G., Teng, J. & Zheludev,
N. I. Optically reconfigurable metasurfaces and photonic devices based on phase change
materials. *Nature Photonics* **10**, 60, (2015).

- 259 Pourfard, M., Faez, K. & Tabaian, S. H. Autocorrelation-Based Method for Characterization of the Self-Hexagonal Lattice. *The Journal of Physical Chemistry C* **117**, 17225-17236, (2013).
- 260 Pichler, S., Bodnarchuk, M. I., Kovalenko, M. V., Yarema, M., Springholz, G., Talapin, D. V. & Heiss, W. Evaluation of Ordering in Single-Component and Binary Nanocrystal Superlattices by Analysis of Their Autocorrelation Functions. *ACS Nano* **5**, 1703-1712, (2011).
- 261 Wu, C.-K., Hultman, K. L., O'Brien, S. & Koberstein, J. T. Functional Oligomers for the Control and Fixation of Spatial Organization in Nanoparticle Assemblies. *Journal of the American Chemical Society* **130**, 3516-3520, (2008).
- 262 Pauly, M., Pichon, B. P., Albouy, P.-A., Fleutot, S., Leuvrey, C., Trassin, M., Gallani, J.-L. & Begin-Colin, S. Monolayer and multilayer assemblies of spherically and cubic-shaped iron oxide nanoparticles. *Journal of Materials Chemistry* **21**, 16018-16027, (2011).
- 263 Evans, J. W. Random and cooperative sequential adsorption. *Reviews of Modern Physics* **65**, 1281-1329, (1993).
- 264 Bonnier, B., Hontebeyrie, M., Leroyer, Y., Meyers, C. & Pommiers, E. Adsorption of line segments on a square lattice. *Physical Review E* **49**, 305-312, (1994).
- 265 Evans, J. W. Nonequilibrium percolative $c(2 \times 2)$ ordering: Oxygen on Pd(100). *The Journal of Chemical Physics* **87**, 3038-3048, (1987).
- 266 Perino, E. J., Matoz-Fernandez, D. A., Pasinetti, P. M. & Ramirez-Pastor, A. J. Jamming and percolation in random sequential adsorption of straight rigid rods on a two-dimensional triangular lattice. *Journal of Statistical Mechanics: Theory and Experiment* **2017**, 073206, (2017).
- 267 Nord, R. S. Irreversible random sequential filling of lattices by monte carlo simulation. *Journal of Statistical Computation and Simulation* **39**, 231-240, (1991).
- 268 Lukatsky, D. B. & Frenkel, D. Phase Behavior and Selectivity of DNA-Linked Nanoparticle Assemblies. *Physical Review Letters* **92**, 068302, (2004).
- 269 Landau, D. P. & Binder, K. *A guide to Monte Carlo simulations in statistical physics*. (Cambridge university press, 2014).
- 270 Binder, K. Applications of Monte Carlo methods to statistical physics. *Reports on Progress in Physics* **60**, 487, (1997).
- 271 Sandvik, A. W. & Moessner, R. Correlations and confinement in nonplanar two-dimensional dimer models. *Physical Review B* **73**, 144504, (2006).
- 272 Myers, B. D., Lin, Q., O'Brien, M., Mirkin, C. A. & Dravid, V. P. Temperature-Controlled Fluidic-Cell Scanning Electron Microscopy. *Microscopy and Microanalysis* **22**, 764-765, (2016).
- 273 Hujsak, K., Myers, B. D., Roth, E., Li, Y. & Dravid, V. P. Suppressing Electron Exposure Artifacts: An Electron Scanning Paradigm with Bayesian Machine Learning. *Microscopy and Microanalysis* **22**, 778-788, (2016).
- 274 Jungjohann, K. L., Evans, J. E., Aguiar, J. A., Arslan, I. & Browning, N. D. Atomic-Scale Imaging and Spectroscopy for In Situ Liquid Scanning Transmission Electron Microscopy. *Microscopy and Microanalysis* **18**, 621-627, (2012).
- 275 Ahmad, N., Le Bouar, Y., Ricolleau, C. & Alloyeau, D. Growth of dendritic nanostructures by liquid-cell transmission electron microscopy: a reflection of the electron-irradiation history. *Advanced Structural and Chemical Imaging* **2**, 9, (2016).

- 276 Abellan, P., Woehl, T. J., Parent, L. R., Browning, N. D., Evans, J. E. & Arslan, I. Factors influencing quantitative liquid (scanning) transmission electron microscopy. *Chemical Communications* **50**, 4873-4880, (2014).
- 277 Kraus, T. & de Jonge, N. Dendritic Gold Nanowire Growth Observed in Liquid with Transmission Electron Microscopy. *Langmuir* **29**, 8427-8432, (2013).
- 278 Chee, S. W., Baraissov, Z., Loh, N. D., Matsudaira, P. T. & Mirsaidov, U. Desorption-Mediated Motion of Nanoparticles at the Liquid–Solid Interface. *The Journal of Physical Chemistry C* **120**, 20462-20470, (2016).
- 279 White, E. R., Mecklenburg, M., Shevitski, B., Singer, S. B. & Regan, B. C. Charged Nanoparticle Dynamics in Water Induced by Scanning Transmission Electron Microscopy. *Langmuir* **28**, 3695-3698, (2012).
- 280 Mirsaidov, U. M., Zheng, H., Bhattacharya, D., Casana, Y. & Matsudaira, P. Direct observation of stick-slip movements of water nanodroplets induced by an electron beam. *Proceedings of the National Academy of Sciences* **109**, 7187-7190, (2012).
- 281 Grogan, J. M., Schneider, N. M., Ross, F. M. & Bau, H. H. Bubble and Pattern Formation in Liquid Induced by an Electron Beam. *Nano Letters* **14**, 359-364, (2014).
- 282 Schneider, N. M., Norton, M. M., Mendel, B. J., Grogan, J. M., Ross, F. M. & Bau, H. H. Electron–Water Interactions and Implications for Liquid Cell Electron Microscopy. *The Journal of Physical Chemistry C* **118**, 22373-22382, (2014).
- 283 Zheng, H., Claridge, S. A., Minor, A. M., Alivisatos, A. P. & Dahmen, U. Nanocrystal Diffusion in a Liquid Thin Film Observed by in Situ Transmission Electron Microscopy. *Nano Letters* **9**, 2460-2465, (2009).
- 284 Evans, J. E., Jungjohann, K. L., Browning, N. D. & Arslan, I. Controlled Growth of Nanoparticles from Solution with In Situ Liquid Transmission Electron Microscopy. *Nano Letters* **11**, 2809-2813, (2011).
- 285 Grogan, J. M., Rotkina, L. & Bau, H. H. In situ liquid-cell electron microscopy of colloid aggregation and growth dynamics. *Physical Review E* **83**, 061405, (2011).
- 286 Hodnik, N., Dehm, G. & Mayrhofer, K. J. J. Importance and Challenges of Electrochemical in Situ Liquid Cell Electron Microscopy for Energy Conversion Research. *Accounts of Chemical Research* **49**, 2015-2022, (2016).
- 287 Parent, L. R., Bakalis, E., Proetto, M., Li, Y., Park, C., Zerbetto, F. & Gianneschi, N. C. Tackling the Challenges of Dynamic Experiments Using Liquid-Cell Transmission Electron Microscopy. *Accounts of Chemical Research* **51**, 3-11, (2018).
- 288 Rong, G., Zhang, X., Zhao, W., Qiu, Y., Liu, M., Ye, F., Xu, Y., Chen, J., Hou, Y., Li, W., Duan, W. & Zhang, Y. Liquid-Phase Electrochemical Scanning Electron Microscopy for In Situ Investigation of Lithium Dendrite Growth and Dissolution. *Advanced Materials* **29**, 1606187-n/a, (2017).
- 289 Xiao, J., Foray, G. & Masenelli-Varlot, K. Analysis of liquid suspensions using scanning electron microscopy in transmission: estimation of the water film thickness using Monte–Carlo simulations. *Journal of Microscopy* **269**, 151-160, (2018).
- 290 Joshua, D. S. & Andrei, K. Electron transparent graphene windows for environmental scanning electron microscopy in liquids and dense gases. *Nanotechnology* **23**, 505704, (2012).
- 291 Krueger, M., Berg, S., Stone, D. A., Strelcov, E., Dikin, D. A., Kim, J., Cote, L. J., Huang, J. & Kolmakov, A. Drop-Casted Self-Assembling Graphene Oxide Membranes for

- Scanning Electron Microscopy on Wet and Dense Gaseous Samples. *ACS Nano* **5**, 10047-10054, (2011).
- 292 Thiberge, S., Zik, O. & Moses, E. An apparatus for imaging liquids, cells, and other wet samples in the scanning electron microscopy. *Review of Scientific Instruments* **75**, 2280-2289, (2004).
- 293 Egerton, R. F. Mechanisms of radiation damage in beam-sensitive specimens, for TEM accelerating voltages between 10 and 300 kV. *Microscopy Research and Technique* **75**, 1550-1556, (2012).
- 294 Egerton, R. F., McLeod, R., Wang, F. & Malac, M. Basic questions related to electron-induced sputtering in the TEM. *Ultramicroscopy* **110**, 991-997, (2010).
- 295 Jiang, N. & Spence, J. C. H. On the dose-rate threshold of beam damage in TEM. *Ultramicroscopy* **113**, 77-82, (2012).
- 296 Woehl, T. J. & Abellan, P. Defining the radiation chemistry during liquid cell electron microscopy to enable visualization of nanomaterial growth and degradation dynamics. *Journal of Microscopy* **265**, 135-147, (2017).
- 297 Woehl, T. J., Jungjohann, K. L., Evans, J. E., Arslan, I., Ristenpart, W. D. & Browning, N. D. Experimental procedures to mitigate electron beam induced artifacts during in situ fluid imaging of nanomaterials. *Ultramicroscopy* **127**, 53-63, (2013).
- 298 Verch, A., Pfaff, M. & de Jonge, N. Exceptionally Slow Movement of Gold Nanoparticles at a Solid/Liquid Interface Investigated by Scanning Transmission Electron Microscopy. *Langmuir* **31**, 6956-6964, (2015).
- 299 Woehl, T. J. & Prozorov, T. The Mechanisms for Nanoparticle Surface Diffusion and Chain Self-Assembly Determined from Real-Time Nanoscale Kinetics in Liquid. *The Journal of Physical Chemistry C* **119**, 21261-21269, (2015).
- 300 Jiang, N. Note on in situ (scanning) transmission electron microscopy study of liquid samples. *Ultramicroscopy* **179**, 81-83, (2017).
- 301 Jiang, N. On the in situ study of Li ion transport in transmission electron microscope. *Journal of Materials Research* **30**, 424-428, (2015).
- 302 Beld, W. T. E. v. d., Sparreboom, W., Berg, A. v. d. & Eijkel, J. C. T. Frequency dependent AC electroosmotic flow in nanochannels. in *2014 IEEE 27th International Conference on Micro Electro Mechanical Systems (MEMS)*. 1067-1070.
- 303 Haywood, D. G., Harms, Z. D. & Jacobson, S. C. Electroosmotic Flow in Nanofluidic Channels. *Analytical Chemistry* **86**, 11174-11180, (2014).
- 304 Mela, P., Tas, N. R., Berenschot, E. J. W., van Nieuwkastele, J. & van den Berg, A. Electrokinetic pumping and detection of low-volume flows in nanochannels. *Electrophoresis* **25**, 3687-3693, (2004).
- 305 Klein, K. L., Anderson, I. M. & De Jonge, N. Transmission electron microscopy with a liquid flow cell. *Journal of Microscopy* **242**, 117-123, (2011).
- 306 Goriparti, S., Warecki, Z., Harrison, K. L., Leenheer, A., Cumings, J. & Jungjohann, K. L. Liquid-Cell TEM Observations of Sn Lithiation reactions: A Temperature Case Study. *Microscopy and Microanalysis* **23**, 1966-1967, (2017).
- 307 Leenheer, A. J., Jungjohann, K. L. & Thomas Harris, C. Design of a Heated Liquid Cell for in-situ Transmission Electron Microscopy. *Microscopy and Microanalysis* **21**, 1293-1294, (2015).

- 308 Tai, K., Liu, Y. & Dillon, S. J. In Situ Cryogenic Transmission Electron Microscopy for
Characterizing the Evolution of Solidifying Water Ice in Colloidal Systems. *Microscopy
and Microanalysis* **20**, 330-337, (2014).
- 309 Xin, H. L. & Zheng, H. In Situ Observation of Oscillatory Growth of Bismuth
Nanoparticles. *Nano Letters* **12**, 1470-1474, (2012).
- 310 Lando, D. Y., Haroutiunian, S. G., Kul'ba, A. M., Dalian, E. B., Orioli, P., Mangani, S. &
Akhrem, A. A. Theoretical and Experimental Study of DNA Helix-Coil Transition in
Acidic and Alkaline Medium. *Journal of Biomolecular Structure and Dynamics* **12**, 355-
366, (1994).
- 311 Taton, T. A., Mucic, R. C., Mirkin, C. A. & Letsinger, R. L. The DNA-Mediated Formation
of Supramolecular Mono- and Multilayered Nanoparticle Structures. *Journal of the
American Chemical Society* **122**, 6305-6306, (2000).
- 312 Candes, E. J., Romberg, J. & Tao, T. Robust uncertainty principles: exact signal
reconstruction from highly incomplete frequency information. *IEEE Transactions on
Information Theory* **52**, 489-509, (2006).
- 313 Donoho, D. L. Compressed sensing. *IEEE Transactions on Information Theory* **52**, 1289-
1306, (2006).
- 314 Baraniuk, R. G. Compressive Sensing [Lecture Notes]. *IEEE Signal Processing Magazine*
24, 118-121, (2007).
- 315 Trampert, P., Bourghorbel, F., Potocek, P., Peemen, M., Schlinkmann, C., Dahmen, T. &
Slusallek, P. How should a fixed budget of dwell time be spent in scanning electron
microscopy to optimize image quality? *arXiv preprint arXiv:1801.04085*, (2018).
- 316 Bocquet, L. & Tabeling, P. Physics and technological aspects of nanofluidics. *Lab on a
Chip* **14**, 3143-3158, (2014).
- 317 Sparreboom, W., van den Berg, A. & Eijkel, J. C. T. Principles and applications of
nanofluidic transport. *Nature Nanotechnology* **4**, 713, (2009).
- 318 Song, C. & Wang, P. Fabrication of Sub-10 nm Planar Nanofluidic Channels Through
Native Oxide Etch and Anodic Wafer Bonding. *IEEE Transactions on Nanotechnology* **9**,
138-141, (2010).
- 319 Abgrall, P., Low, L.-N. & Nguyen, N.-T. Fabrication of planar nanofluidic channels in a
thermoplastic by hot-embossing and thermal bonding. *Lab on a Chip* **7**, 520-522, (2007).
- 320 Mao, P. & Han, J. Fabrication and characterization of 20 nm planar nanofluidic channels
by glass-glass and glass-silicon bonding. *Lab on a Chip* **5**, 837-844, (2005).
- 321 Sparreboom, W., Eijkel, J. C. T., Bomer, J. & van den Berg, A. Rapid sacrificial layer
etching for the fabrication of nanochannels with integrated metal electrodes. *Lab on a Chip*
8, 402-407, (2008).
- 322 Davidson, C. & Xuan, X. Electrokinetic energy conversion in slip nanochannels. *Journal
of Power Sources* **179**, 297-300, (2008).
- 323 Gillespie, D. High Energy Conversion Efficiency in Nanofluidic Channels. *Nano Letters*
12, 1410-1416, (2012).

Appendix A

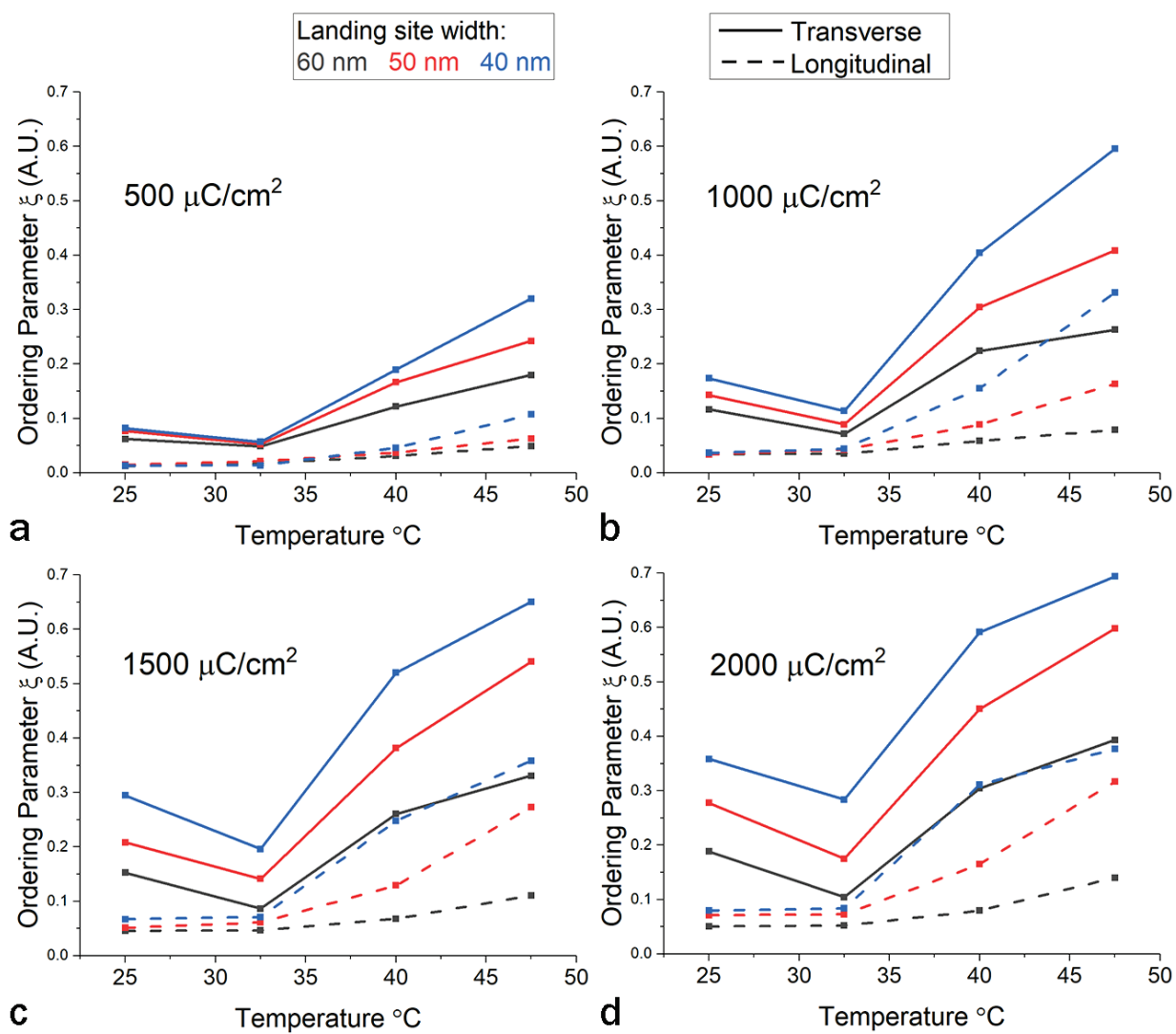


Figure A.1 Ordering parameter as a function of temperature for NR2 on rectangular grid patterns with electron dose of a) 500, b) 1000, c) 1500 and d) 2000 $\mu\text{C}/\text{cm}^2$

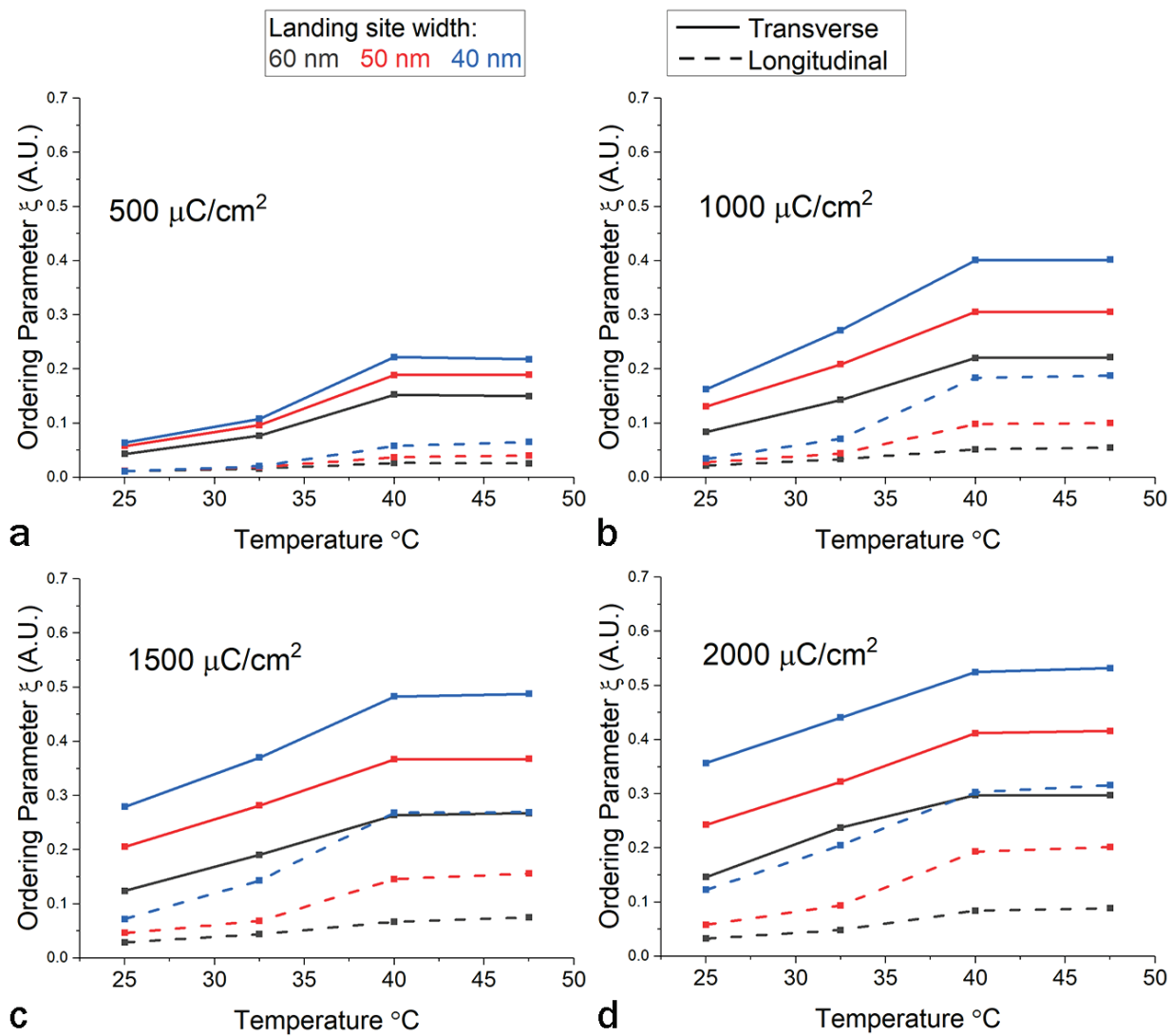


Figure A.2 Ordering parameter as a function of temperature for NR3 on rectangular grid patterns with electron dose of a) 500, b) 1000, c) 1500 and d) 2000 $\mu\text{C}/\text{cm}^2$.

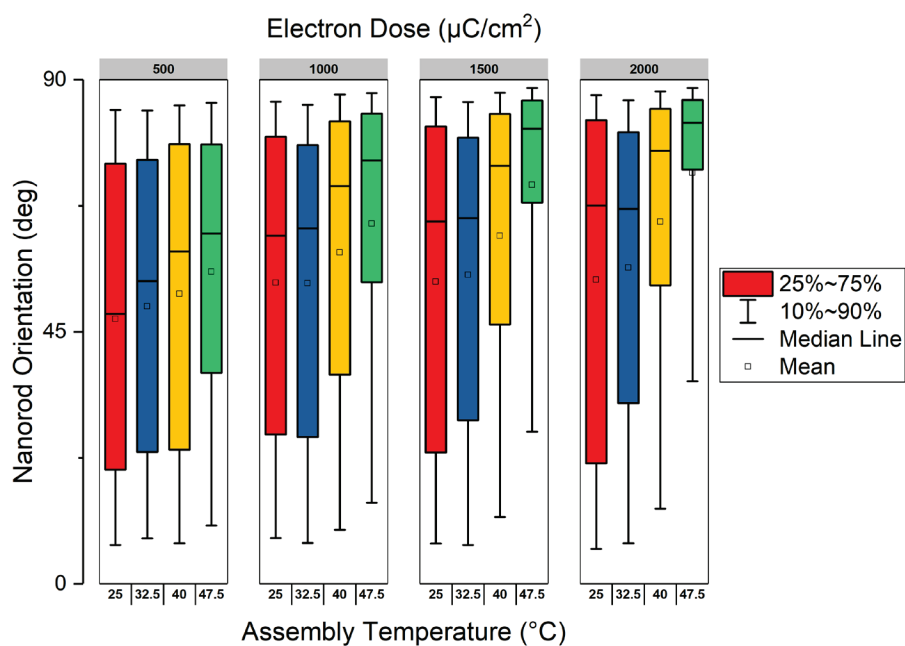


Figure A.3 Box plots of nanorod orientation on rectangular grid patterns for NR2 with 50 nm-wide landing sites.

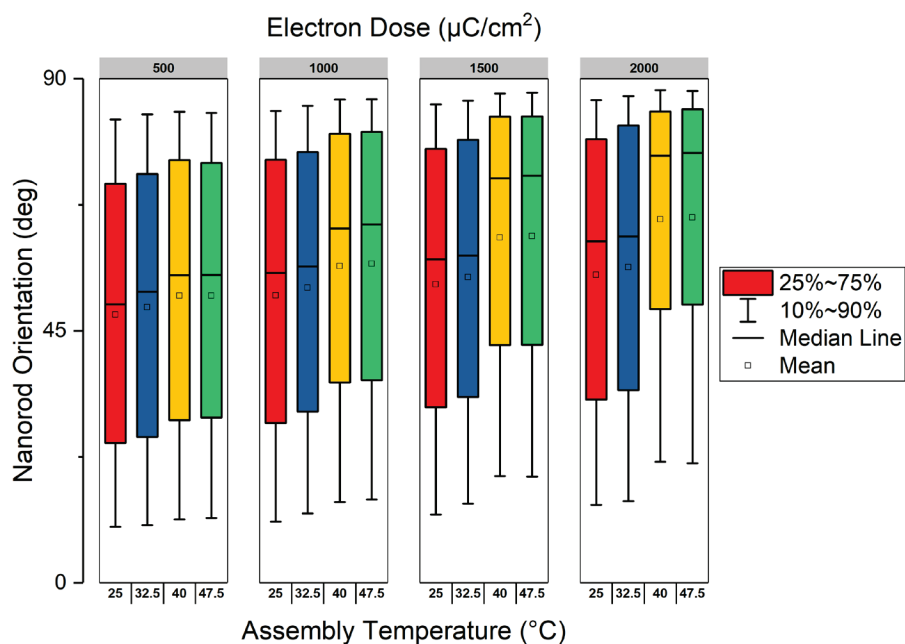


Figure A.4 Box plots of nanorod orientation on rectangular grid patterns for NR3 with 50 nm-wide landing sites.

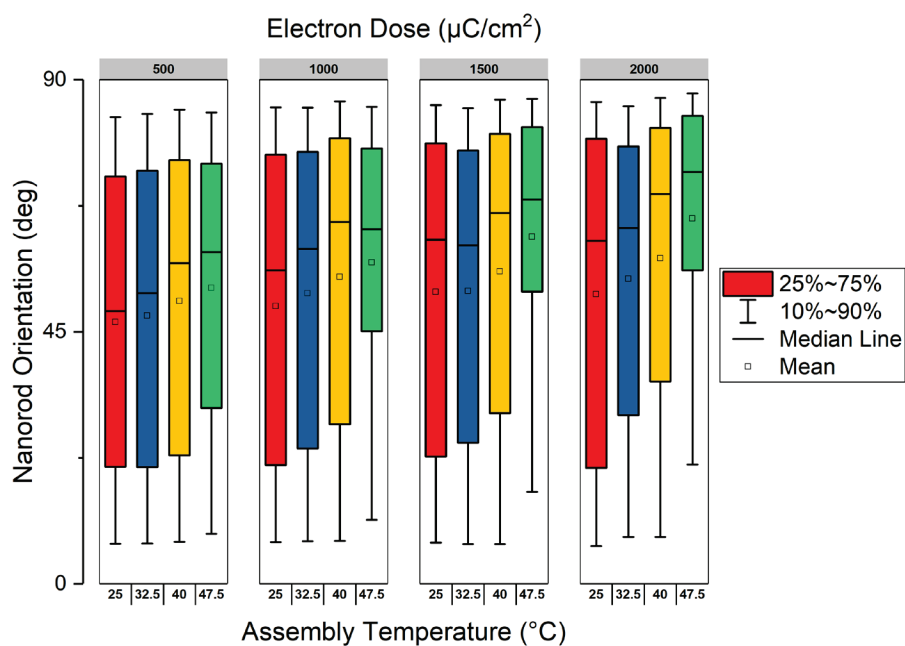


Figure A.5 Box plots of nanorod orientation on rectangular grid patterns for NR2 with 60 nm-wide landing sites.

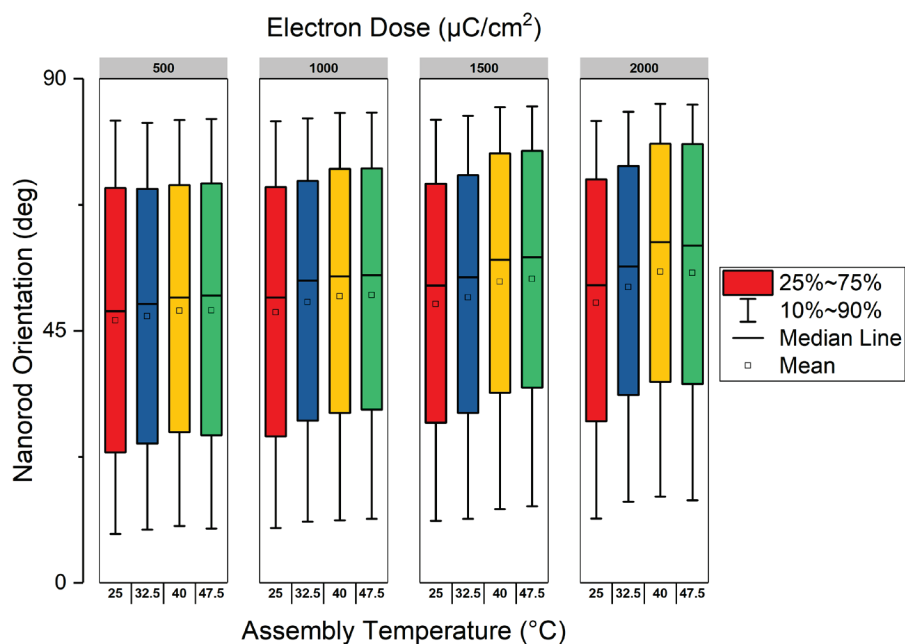


Figure A.6 Box plots of nanorod orientation on rectangular grid patterns for NR3 with 60 nm-wide landing sites.

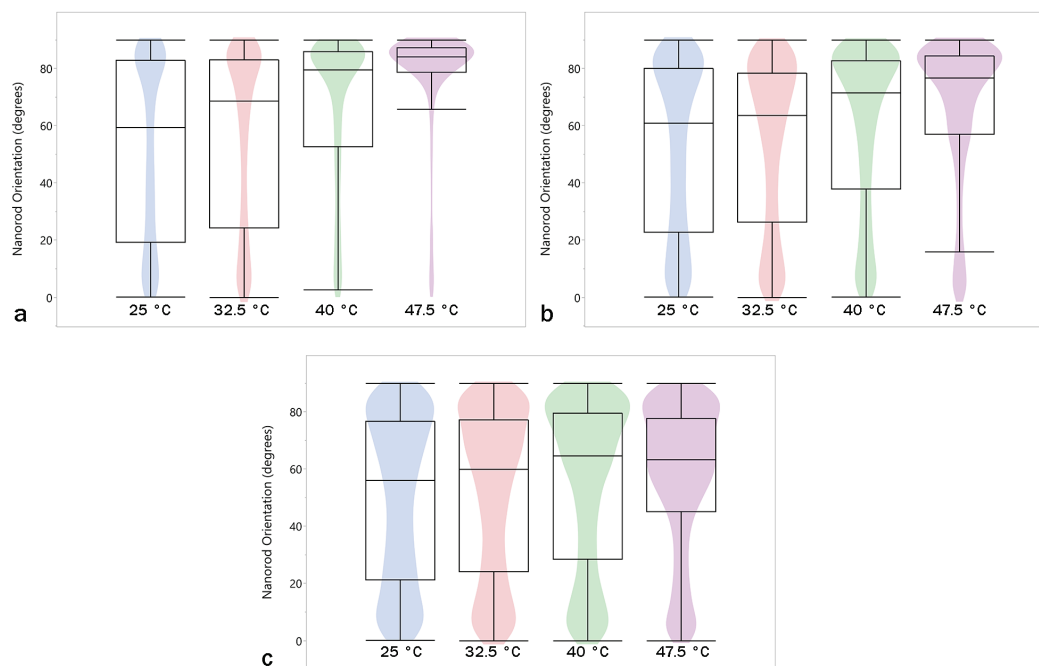


Figure A.7 Violin plots for NR2 assembly on rectangular grid patterns with electron dose of $1000 \mu\text{C}/\text{cm}^2$ and a) 40, b) 50 and c) 60 nm-wide landing sites.

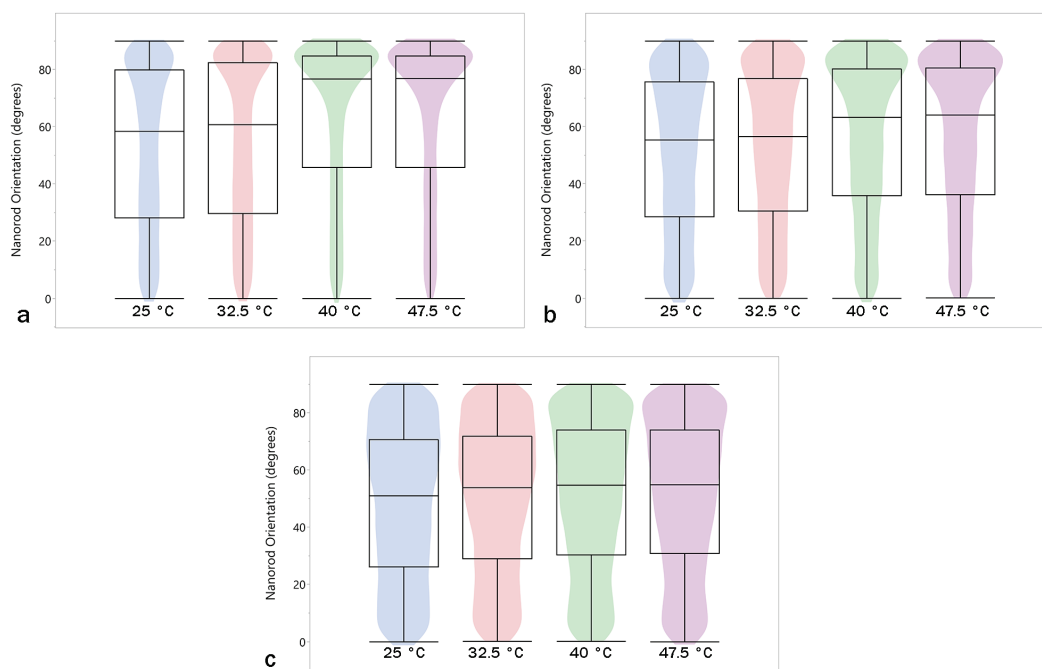


Figure A.8 Violin plots for NR3 assembly on rectangular grid patterns with electron dose of $1000 \mu\text{C}/\text{cm}^2$ and a) 40, b) 50 and c) 60 nm-wide landing sites.

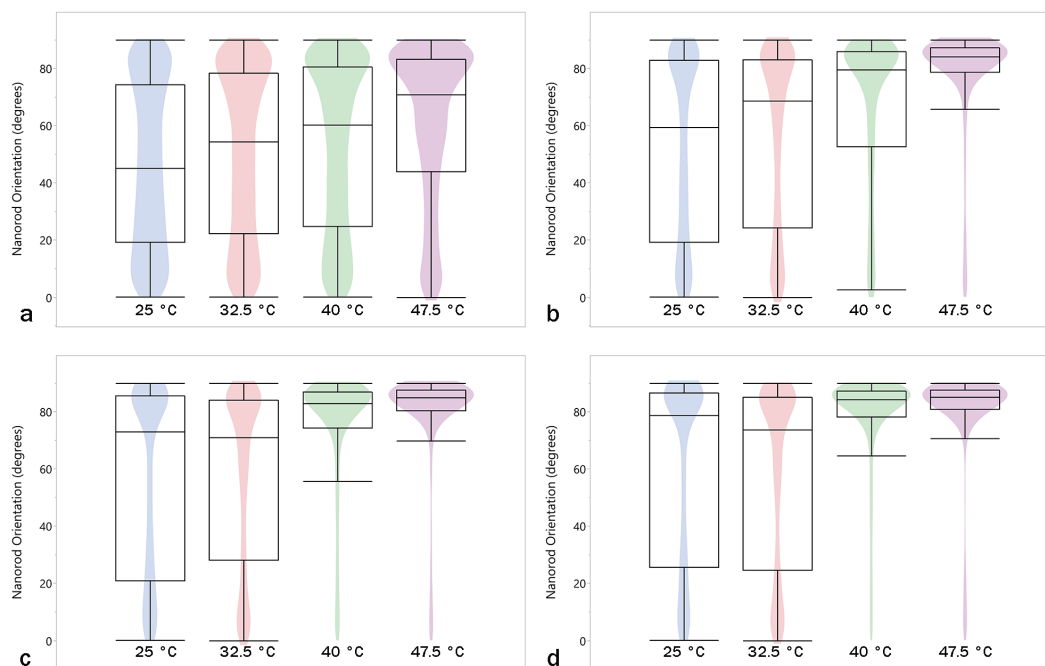


Figure A.9 Violin plots for NR2 assembly on rectangular grid patterns with 40 nm-wide landing sites and a) 500, b) 1000, c) 1500 and d) 2000 $\mu\text{C}/\text{cm}^2$ electron dose.

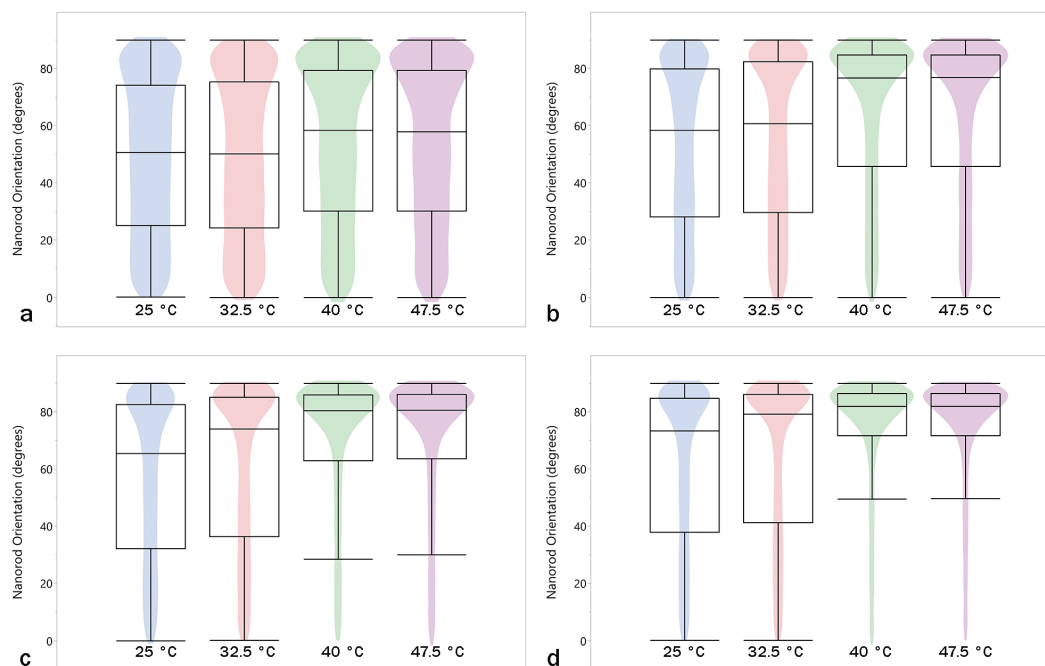


Figure A.10 Violin plots for NR3 assembly on rectangular grid patterns with 40 nm-wide landing sites and a) 500, b) 1000, c) 1500 and d) 2000 $\mu\text{C}/\text{cm}^2$ electron dose.

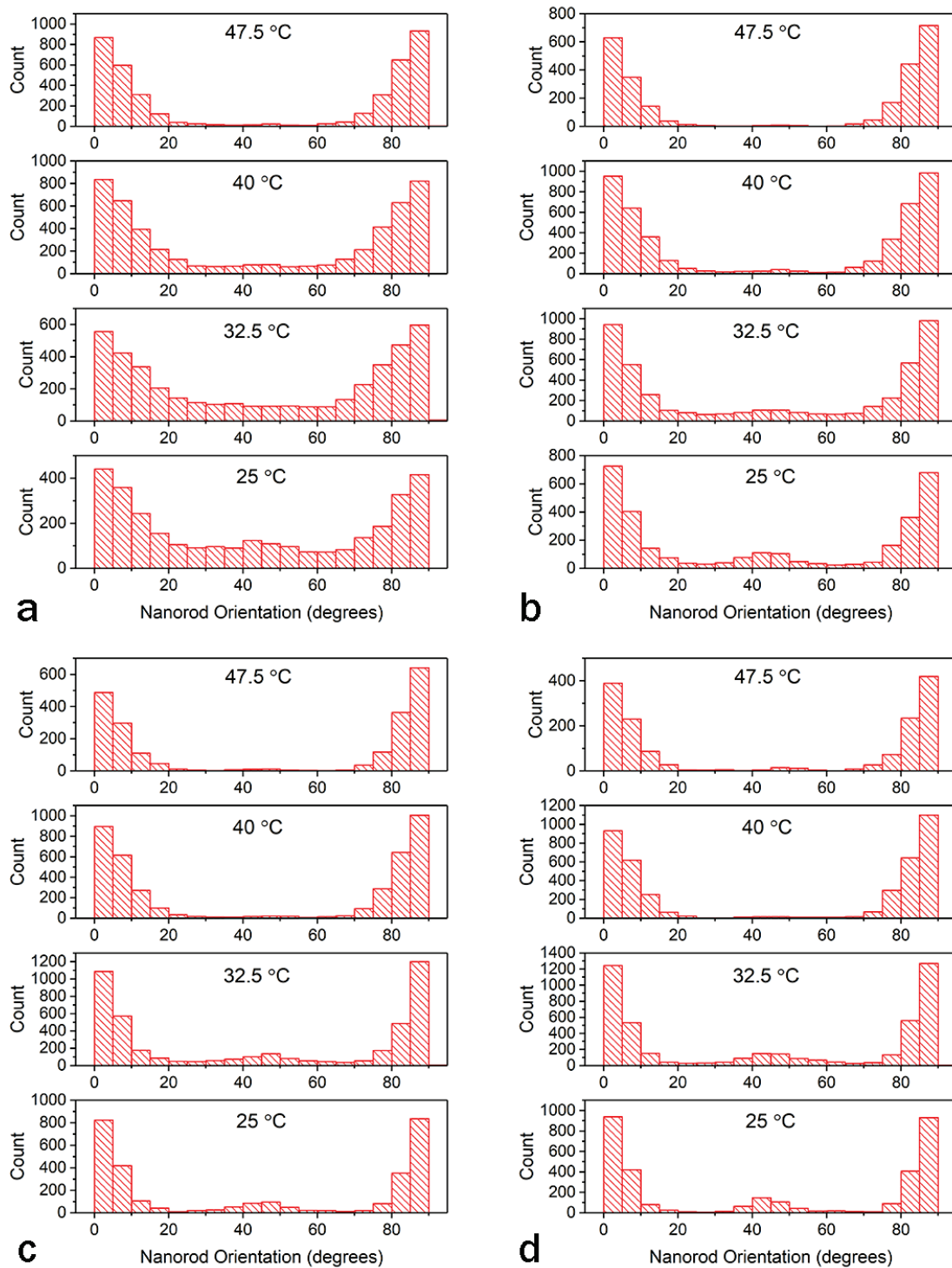


Figure A.11 Histograms of NR2 orientation for square grid patterns with 40 nm-wide landing sites and a) 500, b) 1000, c) 1500 and d) 2000 $\mu\text{C}/\text{cm}^2$ electron dose.

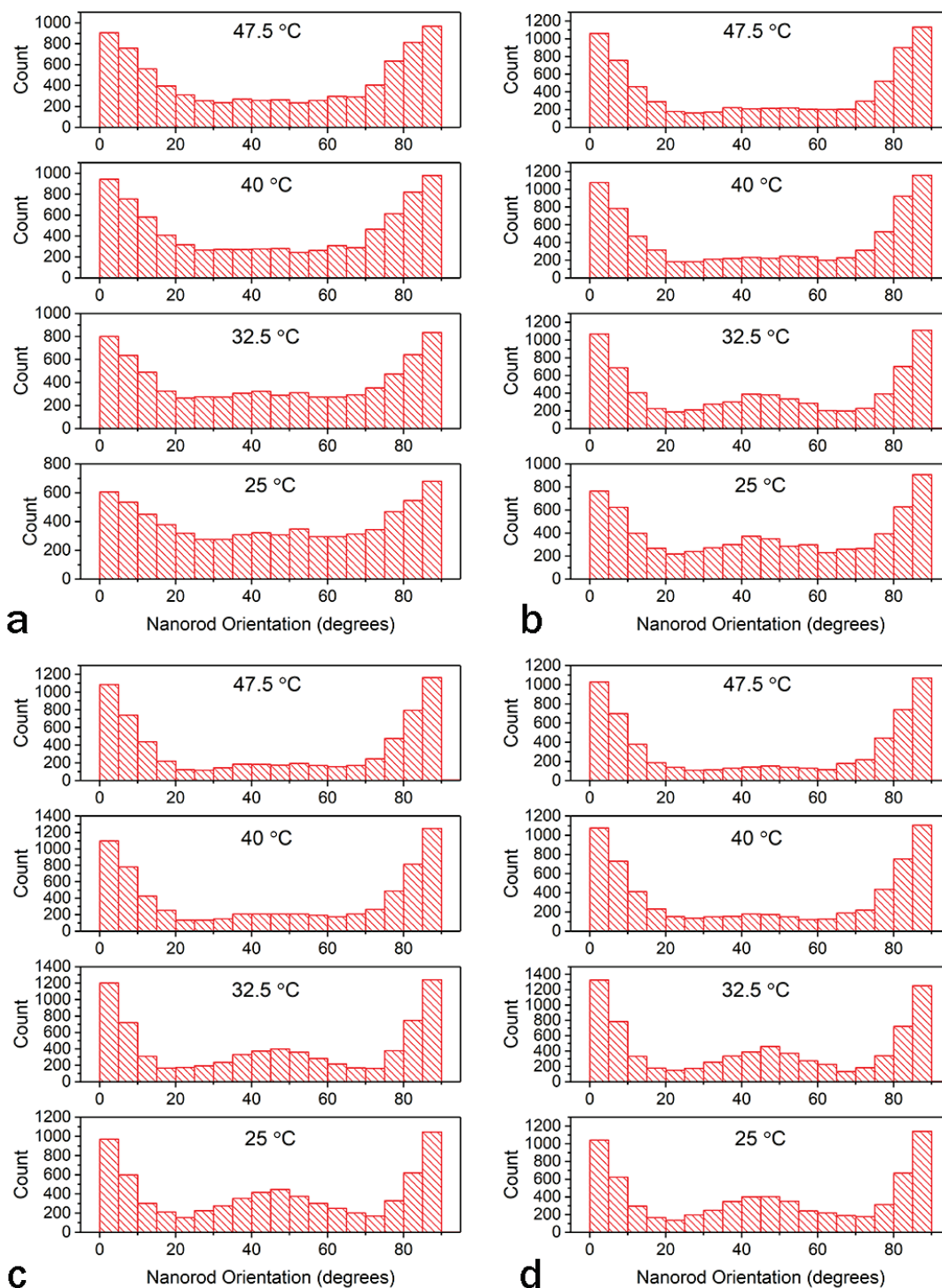


Figure A.12 Histograms of NR3 orientation for square grid patterns with 40 nm-wide landing sites and a) 500, b) 1000, c) 1500 and d) 2000 $\mu\text{C}/\text{cm}^2$ electron dose.

*Curriculum Vitae***Benjamin D. Myers**

EDUCATION

Northwestern University**Ph.D. Materials Science and Engineering** 2018*Patterning and Characterization of Reconfigurable Nanoparticle Assemblies*

Thesis Advisor: Prof. Vinayak P. Dravid

M.S. Materials Science and Engineering 2006*Variable Pressure Electron Beam Lithography (VP-EBL)*

Thesis Advisor: Prof. Vinayak P. Dravid

University of Illinois at Urbana-Champaign**B.S. Materials Science and Engineering** 2000*Concentration in Polymer Science*

EXPERIENCE

Northwestern University

Director of Operations – SHyNE Resource 2015 – Present

SEM Facility Manager - NUANCE Center and Department of Materials Science and Engineering 2002 – 2015

Motorola, Inc.

Process Engineer in Semiconductor Products Sector 2000 – 2002

University of Illinois at Urbana-Champaign

Research Assistant in Aeronautical and Astronautical Engineering 1998 – 2000

PUBLICATIONS

- 1 **Myers, B.D.**, Palacios, E., Butun, S., Myers, D.I., Aydin, K., Dravid, V.P. Programmable Surfaces for Reconfigurable Nanoparticle Assembly. *Manuscript in Preparation*. (2018).
- 2 Zhang, L.*, **Myers, B.D.***, Elupula, R., Grayson, S.M., Torkelson, J.M. and Dravid, V.P. Cyclic Polymers as Negative Resists for Improved Lithographic Performance. *Manuscript in Preparation* (2018). (*equal contribution)
- 3 Hujsak, K. A.*, **Myers, B. D.***, Grovogui, J. & Dravid, V. P. Stage-Rocked Electron Channeling for Crystal Orientation Mapping. *Scientific Reports* **8**, 5175, (2018). (*equal contribution)
- 4 Hanson, E. D., Lajaunie, L., Hao, S., **Myers, B. D.**, Shi, F., Murthy, A. A., Wolverton, C., Arenal, R. & Dravid, V. P. Systematic Study of Oxygen Vacancy Tunable Transport Properties of Few-Layer MoO_{3-x} Enabled by Vapor- Based Synthesis. *Advanced Functional Materials* **27**, 1605380, (2017).
- 5 **Myers, B. D.**, Lin, Q.-Y., Wu, H., Luijten, E., Mirkin, C. A. & Dravid, V. P. Size-Selective Nanoparticle Assembly on Substrates by DNA Density Patterning. *ACS Nano* **10**, 5679-5686, (2016).
- 6 Hujsak, K., **Myers, B. D.**, Roth, E., Li, Y. & Dravid, V. P. Suppressing Electron Exposure Artifacts: An Electron Scanning Paradigm with Bayesian Machine Learning. *Microscopy and*

- Microanalysis* **22**, 778-788, (2016).
- 7 Mannix, A. J., Zhou, X.-F., Kiraly, B., Wood, J. D., Alducin, D., **Myers, B. D.**, Liu, X., Fisher, B. L., Santiago, U., Guest, J. R., Yacaman, M. J., Ponce, A., Oganov, A. R., Hersam, M. C. & Guisinger, N. P. Synthesis of borophenes: Anisotropic, two-dimensional boron polymorphs. *Science* **350**, 1513-1516, (2015).
 - 8 Luo, Z., Jiang, Y., **Myers, B. D.**, Isheim, D., Wu, J., Zimmerman, J. F., Wang, Z., Li, Q., Wang, Y., Chen, X., Dravid, V. P., Seidman, D. N. & Tian, B. Atomic gold-enabled three-dimensional lithography for silicon mesostructures. *Science* **348**, 1451-1455, (2015).
 - 9 Jaber-Ansari, L., Puntambekar, K. P., Kim, S., Aykol, M., Luo, L., Wu, J., **Myers, B. D.**, Iddir, H., Russell, J. T., Saldaña, S. J., Kumar, R., Thackeray, M. M., Curtiss, L. A., Dravid, V. P., Wolverton, C. & Hersam, M. C. Suppressing Manganese Dissolution from Lithium Manganese Oxide Spinel Cathodes with Single-Layer Graphene. *Advanced Energy Materials* **5**, (2015).
 - 10 Wu, J. S., Kim, A. M., Bleher, R., **Myers, B. D.**, Marvin, R. G., Inada, H., Nakamura, K., Zhang, X. F., Roth, E., Li, S. Y., Woodruff, T. K., O'Halloran, T. V. & Dravid, V. P. Imaging and elemental mapping of biological specimens with a dual-EDS dedicated scanning transmission electron microscope. *Ultramicroscopy* **128**, 24-31, (2013).
 - 11 Wang, X., **Myers, B. D.**, Yan, J., Shekhawat, G., Dravid, V. & Lee, P. S. Manganese oxide micro-supercapacitors with ultra-high areal capacitance. *Nanoscale* **5**, 4119-4122, (2013).
 - 12 **Myers, B. D.**, Stevens, B. L., Rożkiewicz, D. I., Barnett, S. A. & Dravid, V. P. Directed assembly in epitaxial zinc oxide films on focused ion beam modified sapphire substrates. *Journal of Vacuum Science & Technology B* **30**, 010605, (2012).
 - 13 Shute, C. J., **Myers, B. D.**, Xie, S., Li, S. Y., Barbee Jr, T. W., Hodge, A. M. & Weertman, J. R. Detwinning, damage and crack initiation during cyclic loading of Cu samples containing aligned nanotwins. *Acta Materialia* **59**, 4569-4577, (2011).
 - 14 Shute, C. J., **Myers, B. D.**, Liao, Y., Li, S. Y., Hodge, A. M., Barbee Jr, T. W., Zhu, Y. T. & Weertman, J. R. High- pressure torsion of copper samples containing columns of highly aligned nanotwins. *Scripta Materialia* **65**, 899-902, (2011).
 - 15 Rożkiewicz, D. I., **Myers, B. D.** & Stupp, S. I. Interfacial Self-Assembly of Cell-like Filamentous Microcapsules. *Angewandte Chemie* **123**, 6448-6451, (2011).
 - 16 Casadio, F., Xie, S., Rukes, S., **Myers, B.**, Gray, K., Warta, R. & Fiedler, I. Electron energy loss spectroscopy elucidates the elusive darkening of zinc potassium chromate in Georges Seurat's A Sunday on La Grande Jatte—1884. *Analytical and Bioanalytical Chemistry* **399**, 2909-2920, (2011).
 - 17 Shute, C. J., **Myers, B. D.**, Xie, S., Barbee Jr, T. W., Hodge, A. M. & Weertman, J. R. Microstructural stability during cyclic loading of multilayer copper/copper samples with nanoscale twinning. *Scripta Materialia* **60**, 1073-1077, (2009).
 - 18 Klajn, R., Gray, T. P., Wesson, P. J., **Myers, B. D.**, Dravid, V. P., Smoukov, S. K. & Grzybowski, B. A. Bulk Synthesis and Surface Patterning of Nanoporous Metals and Alloys from Supraspherical Nanoparticle Aggregates. *Advanced Functional Materials* **18**, 2763-2769, (2008).
 - 19 **Myers, B. D.** & Dravid, V. P. Variable Pressure Electron Beam Lithography (VP-eBL): A New Tool for Direct Patterning of Nanometer-Scale Features on Substrates with Low Electrical Conductivity. *Nano Letters* **6**, 963- 968, (2006).
 - 20 Wu, N., Zhao, M., Zheng, J.-G., Jiang, C., **Myers, B.**, Li, S., Chyu, M. & Mao, S. X. Porous CuO-ZnO nanocomposite for sensing electrode of high-temperature CO solid-state electrochemical sensor. *Nanotechnology* **16**, 2878, (2005).
 - 21 Donthu, S., Pan, Z., **Myers, B.**, Shekhawat, G., Wu, N. & Dravid, V. Facile Scheme for Fabricating Solid-State Nanostructures Using E-Beam Lithography and Solution Precursors. *Nano Letters* **5**, 1710-1715, (2005).

- 22 Whitney, A. V., **Myers, B. D.** & Van Duyne, R. P. Sub-100 nm Triangular Nanopores Fabricated with the Reactive Ion Etching Variant of Nanosphere Lithography and Angle-Resolved Nanosphere Lithography. *Nano Letters* **4**, 1507-1511, (2004).

CONFERENCE PRESENTATIONS

- 1 **Myers, B.**, Butun, S., Kellogg, W. & Dravid, V. Towards Correlative, Multimodal and Adaptive Fluidic-Cell Electron Microscopy in *Liquid Phase Electron Microscopy* (Eindhoven, the Netherlands, 2017).
- 2 **Myers, B. D.**, Lin, Q., O'Brien, M., Mirkin, C. A. & Dravid, V. P. Temperature-Controlled Fluidic-Cell Scanning Electron Microscopy. *Microscopy and Microanalysis* **22**, 764-765, (2016).
- 3 Hujsak, K., **Myers, B. D.**, Roth, E., Li, Y. & Dravid, V. P. Reducing Electron Dose and Sample Damage with Bayesian Machine Learning and Self-Organizing Neural Networks. *Microscopy and Microanalysis* **22**, 1434- 1435, (2016).
- 4 Wu, J., Kim, A., Marvin, R., **Myers, B.**, Woodruff, T., O'Halloran, T., Dravid, V., McIlwrath, K. & Li, S. Imaging and Elemental Mapping of Biological Specimens with the Hitachi HD-2300A Dual-EDS Scanning Transmission Electron Microscope. *Microscopy and Microanalysis* **16**, 884-885, (2010).
- 5 **Myers, B.**, Stevens, B., Barnett, S. & Dravid, V. Lithographically Defined Epitaxy via Focused Ion Beam Induced Lattice Damage. *Microscopy and Microanalysis* **16**, 236-237, (2010).
- 6 **Myers, B.**, McIlwrath, K., Wu, J., Li, S., Inada, H. & Dravid, V. Performance Characterization of Hitachi HD- 2300A STEM with Dual-EDS Configuration. *Microscopy and Microanalysis* **16**, 942-943, (2010).
- 7 **Myers, B.**, Wilson, J., Dravid, V. & Barnett, S. Charge-contrast in SEM imaging with simultaneous ion bombardment. *Microscopy and Microanalysis* **14**, 1012-1013, (2008).
- 8 **Myers, B.**, Pan, Z. & Dravid, V. Beam skirting effects on energy deposition profile in VP-SEM. *Microscopy and Microanalysis* **14**, 1208-1209, (2008).
- 9 **Myers, B.**, Pan, Z., Donthu, S. & Dravid, V. Variable-Pressure Soft-Electron Beam Lithography (VP Soft-eBL). *Microscopy and Microanalysis* **13**, 174-175, (2007).
- 10 **Myers, B.** & Dravid, V. Visualization of the Electron-solid Interaction Volume in Dielectric Materials Under Variable Pressure Conditions. *Microscopy and Microanalysis* **12**, 1498-1499, (2006).

PATENTS

- 1 Provisional Patent Filed US62/624,221, **Myers BD**, Hujsak KA, Dravid, VP, Orientation Determination and Mapping by Stage Rocking Electron Channeling and Imaging Reconstruction, Filed January 31, 2018.
- 2 Patent Application US20170213355A1, Dravid, VP, **Myers, BD**, Hujsak, KA, A method for acquiring intentionally limited data and the machine learning approach to reconstruct it. Filed October 22, 2015
- 3 Kessler MR, White SR, **Myers BD**, Catalyzed Reinforced Polymer Composites, US patent 6,750,272 to Board of Trustees of University of Illinois, 2004.

MEMBERSHIPS

Microscopy Society of America
 Microanalysis Society
 Midwest Microscopy and Microanalysis Society
 Materials Research Society